

Western Kentucky University

TopSCHOLAR®

Masters Theses & Specialist Projects

Graduate School

8-2024

Polygenetic Cave Sedimentation and Speleogenesis in the McCloud Limestone of Northern California

Niles Lathrop

Follow this and additional works at: <https://digitalcommons.wku.edu/theses>



Part of the [Geology Commons](#), [Geomorphology Commons](#), [Sedimentology Commons](#), [Speleology Commons](#), and the [Stratigraphy Commons](#)

This Thesis is brought to you for free and open access by TopSCHOLAR®. It has been accepted for inclusion in Masters Theses & Specialist Projects by an authorized administrator of TopSCHOLAR®. For more information, please contact topscholar@wku.edu.

POLYGENETIC CAVE SEDIMENTATION AND SPELEOGENESIS IN THE
MCCLLOUD LIMESTONE OF NORTHERN CALIFORNIA

A Thesis
Presented to
The Faculty of the Department of Earth, Environmental and Atmospheric Sciences
Western Kentucky University
Bowling Green, Kentucky

In Fulfillment
Of the Requirements for the Degree
Master of Science

By
Niles Lathrop

August, 2024

POLYGENETIC CAVE SEDIMENTATION AND SPELEOGENESIS IN THE
MCCLOUD LIMESTONE OF NORTHERN CALIFORNIA

Defense Date: May 9, 2024

Digitally signed by Patricia
Kambesis
Date: 2024.07.12 00:03:00
-05'00'

Dr. Patricia Kambesis

Digitally signed by Polk, Jason
Date: 2024.07.15 21:54:29 -05'00'

Dr. Jason Polk

Dr. Michael May

Digitally signed by Tinsley, John
C.
Date: 2024.07.13 08:34:08 -07'00'

Dr. John Tinsley

Digitally signed by Joel Despain
Date: 2024.07.15 23:19:55
-05'00'

Joel Despain

Jennifer Hammonds

Executive Director for Graduate Studies

Abstract

POLYGENETIC CAVE SEDIMENTATION AND SPELEOGENESIS IN THE MCCLLOUD LIMESTONE OF NORTHERN CALIFORNIA

Caves in the Permian-aged, McCloud Limestone of the Klamath Mountains of Northern California preserve a diverse range of clastic sediments that represent broad-scale variations in paleo-hydrologic conditions and transport mechanisms that hint at varied modes of speleogenesis through local landscape development. Caves in the McCloud Limestone exhibit a range of cave passage geometries and arrangements that suggests periods of both hypogene and epigene cave development through temporal and spatial scales. This study evaluates the variability in the distribution, mineralogy, and transport mechanisms of clastic-cave sediments in seven hydrologically-distinct caves in the McCloud Limestone to establish relationships between clastic-cave sedimentation and modes of cave genesis and paleo-hydrologic conditions. This study utilizes a combination of detailed cave mapping, sediment facies relationships, particle-size distribution statistics, and mineralogical analysis to differentiate depositional conditions, sediment provenance, and hydrologic control on the deposition of clastic material in a range of suspected polygenetic cave environments. Quantitative techniques such as particle-size statistics, X-ray powder diffraction, scanning electron microscopy, and electron dispersion spectrometry were employed to evaluate sedimentary textures and constituent mineralogy. Samples were collected using percussion-driven core-sampling techniques and grab-sampling. Three primary facies associations are observed that aid in distinguishing depositional and paleo-hydrologic conditions in a polygenetic setting: epikarst-dominated, fluvially-dominated, and autogenic dominated. Relationships between cave genesis and sedimentation are present that elucidate the speleogenetic and geomorphic history of the McCloud Limestone and relationships with regional

volcanism occurring since the Miocene. Multi-stage polygenetic hypogene and epigene cave development is evident along with periods of significant sedimentation, erosion, and extensive in-situ weathering. Correlation of cave sediments with regional stratigraphic markers has yielded a minimum age of cave development at Lake Shasta Caverns of 2.5 to 3.5 Ma. Evaluating sedimentation patterns in a set of seven, hydrologically distinct hypogene and epigene caves has provided insight into the nature of polygenetic cave development and sedimentation. Evaluation of cave sedimentation through facies relationships and mineralogical and grain size trends could be used as a framework for further study on polygenetic karst regions elsewhere.

Keywords: cave sediments, polygenetic karst, hypogene, karst, lithofacies, McCloud Limestone

Acknowledgements

This research was possible through the generous support of many individuals, institutions, entities, and environments. The first to thank are the two individuals, Joel Despain and Heather Veerkamp, who opened my eyes to the endless possibilities of the McCloud Limestone to yield intellectually fascinating polygenetic caves. Exploring, surveying, and studying the caves of the McCloud with CRF Klamath has been an effort I treasure every moment of. The future is bright for cave exploration and science in the McCloud Limestone and I look forward to every coralloid-filled hypogene hole we find.

There are many, many other individuals to thank for contribution to this project, but the next group are the dozens of cavers before us who have worked in these hills to explore and document these unique and geologically diverse caves. Further key individuals to thank are my advisor, Dr. Patricia Kambesis, and committee members for their always helpful support and suggestions. I would also like to extend a huge thank you to Dr. John Andersland at Western Kentucky University for his very generous assistance with the scanning electron microscope and electron dispersive spectrometry analysis. The last individuals to thank are my family and close friends. Much love extends to my parents and brother, you've always been my true inspirations and thank you for your endless support. Thanks to all the great people that have surrounded me and supported me through this project. Especially those who come crawling around underground with me. The institutions I extend very thankful gratification to are Western Kentucky University and the Cave Research Foundation. Without their generous support none of this research would be possible. Lastly, I would like to extend a special thank you to the Whigpistle Cave system in the Mammoth Cave region of Kentucky for its endless emotional support during this endeavor. 42 miles and counting!

Table of Contents

Chapter One: Introduction	1
Chapter Two: Literature Review	5
2.1 Klamath Mountains Geology	5
2.2 Cenozoic Deposits in the Eastern Klamath – Southern Cascade	10
2.3 Cave Sediments.....	15
2.4 Karst and Speleogenesis	35
2.5 Cave-Sediment Sampling.....	29
Chapter Three: Study Area	33
3.1 Geography, Climate, and Flora and Fauna	33
3.2 Geomorphic Features and Stratigraphy	36
3.3 Karst Features	37
3.4 Ellery Creek Cave	39
3.5 Tardis Cave	42
3.6 Pipevine Cave	46
3.7 Ancient Palace Cave	49
3.8 Rileys Cave	53
3.9 Lake Shasta Caverns	56
3.10 January Cave.....	59
Chapter Four: Methods	62
4.1 Split-Spoon Sediment Sampler	64
4.2 Grain-Size Distribution.....	65
4.3 Grain-Size Statistics.....	67

4.4 X-Ray Powder Diffraction	68
4.5 Scanning Electron Microscopy	69
Chapter Five: Results	70
5.1 Ellery Creek Cave	71
5.1.1 Sediment Mineralogy and Grain Size	71
5.1.2 Cave Morphology	75
5.2 Tardis Cave	78
5.2.1 Sediment Mineralogy and Grain Size	87
5.2.2 Cave Morphology	84
5.3 Pipevine Cave	85
5.3.1 Sediment Mineralogy and Grain Size	85
5.3.2 Cave Morphology	90
5.4 Ancient Palace Cave	90
5.4.1 Sediment Mineralogy and Grain Size	90
5.4.2 Cave Morphology	99
5.5 Rileys Cave	99
5.5.1 Sediment Mineralogy and Grain Size	99
5.5.2 Cave Morphology	103
5.6 Lake Shasta Caverns	104
5.6.1 Sediment Mineralogy and Grain Size	104
5.6.2 Cave Morphology	114
5.7 January Cave	115
5.7.1 Sediment Mineralogy and Grain Size	115

5.7.2 Cave Morphology	119
Chapter Six: Discussion	120
6.1 Cave-Sediment Classification.....	121
6.2 Epikarst-Dominated Facies.....	124
6.3 Fluvially-Dominated Facies.....	126
6.4 Autogenic-Dominated Facies.....	132
6.5 Lithofacies Associations and Paleo-Depositional Environments	136
6.6 Trends in Clay Mineralogy	138
6.7 Trends in Grain-Size Distribution.....	141
6.8 Multi-stage Polygenetic Development.....	148
6.9 Regional Context	153
6.10 Limitations	158
Conclusions.....	160
Works Cited	163
Appendix I: EDS Results	177
Appendix II: Radiocarbon Dates from EC13.....	180
Appendix III: Standard Operating Procedure for Clay Mineral XRD Analysis with a Bruker D2 Phaser XRPD	182
Appendix IV: Median Grain Size Data	201

List of Figures
GSD (grain-size distribution)
XRD (x-ray diffraction)

Figure 1.1: Modified map of the extent of the McCloud Limestone	3
Figure 2.1: Eastern Klamath Terrane stratigraphic column.....	6
Figure 2.2: Hjulström diagram.....	18
Figure 2.3: Schematic diagram of cave sediment storage zones and inputs and outputs	21
Figure 2.4: Schematic diagram of hydrothermal hypogene development	29
Figure 2.5: Schematic diagram for split-spoon sampler and sampling equipment.....	32
Figure 3.1: McCloud River drainage basin and Shasta Lake.....	34
Figure 3.2: Photo looking south over the McCloud River.....	35
Figure 3.3: Topographic elevation profiles of the seven cave sites	36
Figure 3.4: Map of Ellery Creek Cave with sample locations marked.	39
Figure 3.5: Photos of the Sump Room passage fill and associated stratigraphy	41
Figure 3.6: Map of Tardis Cave with sample locations marked	42
Figure 3.7: Paragenetic notch in Tardis Cave.....	44
Figure 3.8: Joint-controlled passage in Tardis Cave with wall notches	44
Figure 3.9: Map of Pipevine Cave with sample locations marked.	46
Figure 3.10: Photo of descending pit series in Pipevine Cave	47
Figure 3.11: Exposed stratigraphy at the north end of the Pipevine Cave lower chamber....	47
Figure 3.12: Map of Ancient Palace Cave with sample locations marked	48
Figure 3.13: Photo of the lower chamber in APC.....	50
Figure 3.14: Photo of the very-fine grained red clay in APC	51
Figure 3.15: Map of Rileys Cave with sample locations marked.	53

Figure 3.16: Photos of ceiling pendants and calcified paleofill in Rileys Cave	54
Figure 3.17: Map of Lake Shasta Caverns with sample locations marked	57
Figure 3.18: Well-stratified and altered tephra and fine clastics in LSC.....	58
Figure 3.19: Map of January Cave with sample locations marked.....	59
Figure 3.20: Photos of the lower chamber and upper entrance passage in January Cave	61
Figure 5.1: Composite XRD scan of EC1 Entrance	72
Figure 5.2: Composite XRD scan of Ellery Cr B13 at 43-60 cm	73
Figure 5.3: Composite XRD scan of Ellery Cr Boring 13 at 183-193 cm.....	74
Figure 5.4: Boring log of Ellery Creek Cave Boring 13.....	75
Figure 5.5: Ellery Cr Cave Boring 13 at 43-60 cm GSD.....	76
Figure 5.6: Ellery Cr Cave Boring 13 at 183-193 cm GSD.....	76
Figure 5.7: Ellery Creek Cave EC1 Lower Entrance Passage GSD	77
Figure 5.8: Boring log of Tardis Cave Boring.....	79
Figure 5.9: Composite XRD scan of Tardis TH5 Dome Infiltrate	80
Figure 5.10: Composite XRD scan of Tardis Boring at 96-101 cm	81
Figure 5.11: Composite XRD scan of Tardis Boring at 61-81 cm	82
Figure 5.12: Tardis TH5 Dome Infiltrate GSD.....	82
Figure 5.13: Tardis Boring at 61-81 cm GSD.....	83
Figure 5.14: Tardis Boring at 96-101 cm GSD.....	83
Figure 5.15: Joint-controlled paragenetic passage in Tardis Cave	84
Figure 5.16: Composite XRD scan of P1 Entrance Room.....	86
Figure 5.17: Composite XRD scan of Pipevine P8 Laminated Brown Fines.....	87
Figure 5.18: Composite XRD scan of Pipevine P10 Fines.....	87

Figure 5.19: Composite XRD scan of Pipevine P3 White Fines	88
Figure 5.20: Pipevine P1 Entrance Room GSD.....	89
Figure 5.21: Pipevine P8 Laminated Brown Fines GSD	89
Figure 5.22: Pipevine P3 White Fines GSD	89
Figure 5.23: Ferromanganese deposit in APC	99
Figure 5.24: Composite XRD scan of APC1 Entrance.....	92
Figure 5.25: Composite XRD scan of APC4 Borning Room Fines	92
Figure 5.26: XRD scan of powdered ferromanganese corrosion residue in APC	94
Figure 5.27: SEM-EDS images of ferromanganese corrosion residue in APC	95
Figure 5.28: SEM image of manganese-oxide fabric and opal-A	96
Figure 5.29: SEM images of well-faceted fayalite in APC	96
Figure 5.30: APC1 Entrance Passage GSD	97
Figure 5.31: APC2 Jaded River Fines GSD.....	98
Figure 5.32: APC4 Borning Room Fines GSD.....	98
Figure 5.33: APC3 Black Fines GSD	99
Figure 5.34: Composite XRD scan of Rileys R5 Surface.....	100
Figure 5.35: Composite XRD scan of Rileys R3 Lower Chamber Sink	101
Figure 5.36: Rileys R5 Surface GSD.....	102
Figure 5.37: Rileys R3 Lower Chamber GSD	102
Figure 5.38: Rileys R4 Calcified Paleofill GSD.....	104
Figure 5.39: Altered yellow tephra in LSC.....	104
Figure 5.40: Composite XRD scan of powdered LSC1 Entrance Slope	105
Figure 5.41: Composite XRD scan of powdered LSC2 Signature Room.....	106

Figure 5.42: Composite XRD scan of powdered LSC3 Yellow Fines	106
Figure 5.43: SEM image of altered tephra shards.....	108
Figure 5.44: SEM image of altered tephra to halloysite and allophane.....	108
Figure 5.45: Surface corrosion texture on the face a kaolinized tephra shard	109
Figure 5.46: Fe-Mn imogolite-allophane nodule in LSC.....	110
Figure 5.47: Fe-Mn imogolite-allophane nodule in LSC.....	111
Figure 5.48: Agglomeration of altered tephra shards	111
Figure 5.49: Fe-Mn imogolite-allophane nodule in LSC.....	112
Figure 5.50: LSC1 Natural Entrance GSD	113
Figure 5.51: LSC2 Signature Room GSD.....	113
Figure 5.52: LSC3 Yellow Tephra GSD.....	114
Figure 5.53: LSC4 Stratified Tephra GSD	114
Figure 5.54: Composite XRD scan of January J3 Entrance Room.....	116
Figure 5.55: Composite XRD scan of January Cave J-C9 Lower Chamber	116
Figure 5.56: View of an agglomeration of platy clay from January Cave.....	117
Figure 5.57: January J-C9 Lower Chamber GSD.....	118
Figure 5.58: January J3 Entrance Room GSD	118
Figure 6.1: Sand-silt-clay ternary plot	143
Figure 6.2: Bivariate plot of mean grain size (ϕ) vs sorting (ϕ)	146
Figure 6.3: Condensation corrosion ablation rim in LSC.....	151
Figure 6.4: Modified map of regional volcanic centers in relation to Shasta Lake	153
Figure 6.5: Modified map of the extent of the Tuscan Formation.....	156

List of Tables

Table 5.1: Table of samples analyzed for grain size distribution and mineralogy	61
Table 6.1: Lithofacies associations present at each cave site	128
Table 6.2: Clay species present in surface and in-cave samples.....	131
Table 6.3: Statistical results from KW, Dunn's, and MWU tests.....	139

List of Equations

Equation 2.1: Stokes' law of settling velocity for particle in fluid.....	19
---	----

Chapter One: Introduction

Karst landscapes develop through myriad interactions between surface and subsurface processes and are commonly described as hypogenic or epigenic: hypogenic is development from recharge that is independent of immediately overlying or adjacent processes, and epigenic is development from meteoric, surface-derived processes. Karst landscapes that exhibit both hypogenic and epigenic processes are described as polygenetic (Palmer, 2006); however, polygenetic karst landscapes are seldom described in detail and characteristic sedimentary patterns and facies far less so. The study of cave sedimentation is important because it is intrinsically linked to paleo-hydrogeologic regimes in both epigenic (Bosch and White, 2015; Herman et al., 2012; Trappe, 2010; Springer and Kite, 1997; Gillieson, 1986) and hypogenic settings (Klimchouk, 2017; Palmer, 2011; Foos et al., 2001; Polyak and Guven, 2000). The caves of the McCloud Limestone in the Klamath Mountains of Northern California provide a unique setting to study the origin of cave sediments and relationships to cave genesis and associated landscape development.

Caves of the McCloud Limestone exhibit evidence for hypogenic and epigenic morphologies and are situated at elevations ranging from zero meters to 325 meters above current river base level (Despain et al., 2022). Many of the caves exist as relict, dry passages that preserve evidence of paleo-hydrologic conditions manifested in a diverse range of speleogens, passage morphologies, and clastic cave deposits. One subset of McCloud caves exhibits epigenic characteristics such as paragenetic flood mazes and fluvially-derived clastic sediments. The other subset exhibits hypogenic characteristics such as ramiform morphologies, intensely varied passage sizes, irregular roof pendants, and exclusively fine-grained sediment deposits (Despain et al., 2022; Klimchouk, 2017). Caves of the McCloud Limestone of northern California are ideal

natural laboratories to study the variability and paleo-hydrogeologic origin of cave sediments in a polygenetic setting.

Caves throughout the McCloud Limestone preserve a range of deposits consisting of well-rounded, poorly sorted, fluvially-derived sediments to well-sorted fine clays associated with low transport energies. Some of the caves preserve exclusively well-sorted, fine-grained sediments, whereas others preserve a range of poorly sorted and well-rounded clastic sediments; however, the relationship between the distribution, mineralogical origin, and transport mechanisms of cave sediments in hypogene and epigene caves in the McCloud has not been resolved or described.

For this study, seven caves in the McCloud Limestone were chosen to represent the spectrum of observed cave morphologies and sedimentary repositories observed in the McCloud Limestone karst. The studied caves range in elevations from river level (~280 meters above sea level) to up to 325 meters above river (base) level (~680 meters above sea level). The chosen caves and the clastic deposits within them suggest a history of dynamic paleo-hydrologic regimes ranging from high-energy fluvial influence and low-energy depositional environments. From lowest to highest elevation, the chosen cave sites are as follows: Ellery Creek Cave, Tardis Cave, Pipevine Cave, Ancient Palace Cave, Rileys Cave, Lake Shasta Caverns, January Cave (Figure 1.1). The research questions addressed in this study are as follows:

1. What is the relationship between mode of cave development and the distribution, source, and transport mechanisms of clastic deposits of the caves of the McCloud Limestone?
2. Can previously devised cave-sediment classifications systems be used to characterize and classify the suites of sediments observed in the caves of the McCloud Limestone?

3. How does karstification and cave sedimentation in the McCloud Limestone relate to regional geologic context and geomorphic development?

In order to address the objectives of this study, cave-sedimentology techniques such as clay mineralogy and grain-size distribution were used to evaluate paleo-hydrogeologic regimes and sedimentary provenance in a polygenetic karst setting. Analysis of clastic cave sediments through facies relationships, color study, grain-size distribution, and mineralogical identification

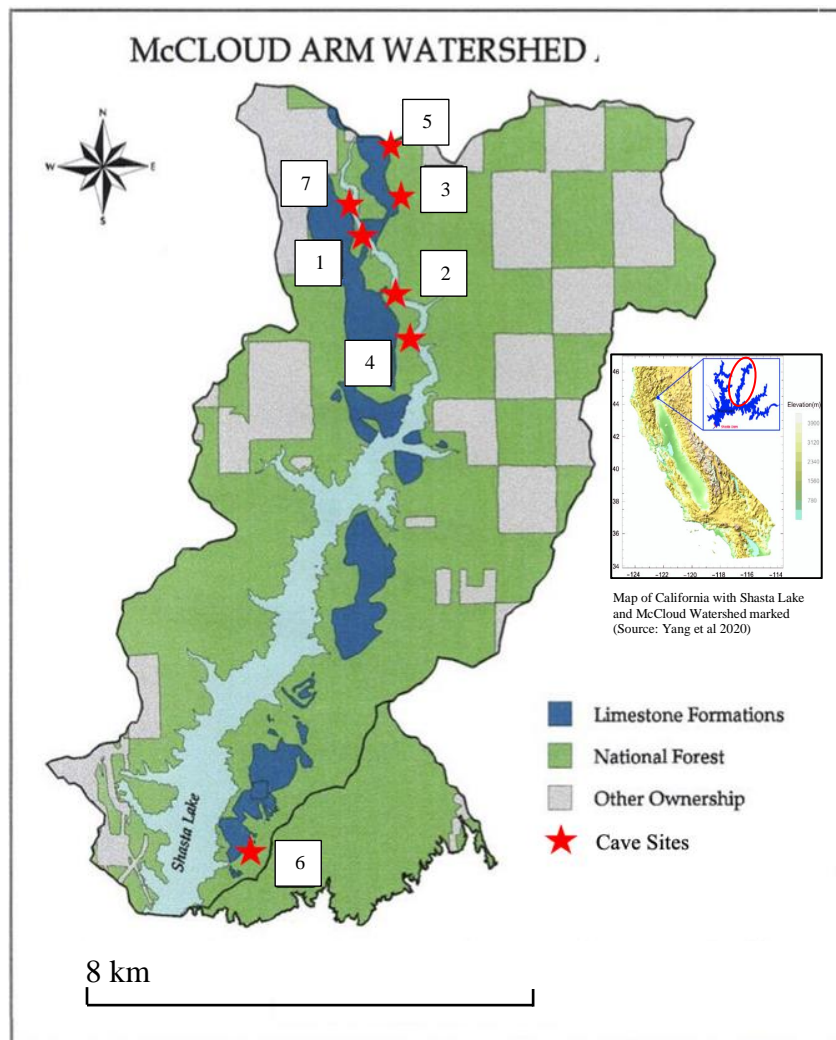


Figure 1.1: Modified map of the extent of the McCloud Limestone along the McCloud River at Shasta Lake with seven study sites marked 1 – Ellery Creek Cave (cored), 2- Tardis Cave (cored), 3 – Pipevine Cave, 4 – Ancient Palace Cave, 5 – Rileys Cave, 6 – Lake Shasta Caverns, 7 – January Cave (Source: USDA, 1998; Yang et al., 2020).

were used to determine the history of paleo-hydrologic conditions and pathways. As exposures of thick clastic deposits are rare, portable core sampling techniques were utilized to retrieve relatively undisturbed samples from depth. Multiple instruments and analytical techniques were used to characterize clay mineralogy and grain size distribution. Instruments and techniques employed in this study were laser diffractometer grain-size analysis, X-ray powder diffraction (XRD), scanning electron microscopy (SEM), and electron dispersive spectrometry (EDS). Folk and Ward (1957) grain-size statistics were generated using GratiStat v8 and bivariate plots were generated in OriginPro (Blott and Ply, 2001; OrginLabs, 1992). Clay mineral XRD methods were based on sample preparation procedures and data interpretation methods described by Poppe et al. (2001) and Moore and Reynolds (1997). Core sampling was conducted with a self-driven split-spoon core sampler and cores were either described in the field or transported for analysis in sealed plastic liners. Samples were analyzed for clay mineralogy, grain size distribution, and nano-morphology at Western Kentucky University in the fall of 2023 and spring of 2024.

Chapter Two: Literature Review

2.1 Klamath Mountains Geology

The Klamath Mountains of Northern California are a complex of accretionary terranes, or tectonic fragments, primarily made up of an amalgamation of sedimentary, metamorphic, and igneous rocks. The oceanic crust and volcanic arc sequences that make up the terranes of the Klamath Mountains rode on the Farallon Plate as it was subducted under the North American Plate during the early Mesozoic (Irwin, 1989). The masses of oceanic and volcanic arc sequences collided with the North American plate from the late Jurassic to the early Cretaceous, forming the ancestral Klamath Mountains during what is called the Nevadan Orogeny (Hacker et al., 1995; Irwin, 1989; Harper and Wright, 1984). During the post-orogeny time, the Klamath Mountains experienced a long period of erosion and uplift, creating the steep valleys and deep river canyons typical of the region (Irwin, 1989; Albers and Robertson, 1961). The rocks that make up the western portion of the Klamath Mountains are primarily intensely metamorphosed oceanic sediments and volcanics. The terranes that compose the eastern Klamath region are comparatively undeformed, and the rock units within them are mostly stratigraphically intact (Irwin, 1989; Albers and Robertson, 1961).

The Eastern Klamath Terrane is composed of three subdivisions or subterranes – the Trinity, Yreka, and Redding subterranes. The Trinity and Yreka subterranes are chiefly made up of ultramafic and metamorphic rocks. The Redding subterrane constitutes sixteen formations of volcanic and sedimentary rock that represents island-arc depositional environments from the early Paleozoic through to the Quaternary (Figure 2.1) (Irwin, 1989; Albers and Robertson, 1961; Trask, 1855). Formations within the Redding subterrane range from the volcanoclastic

Formation	Age	Thickness in feet	Lithologic description	Economic value	Number on diagrammatic section	Diagrammatic section
Unconsolidated deposits	Quaternary	0-100	Includes alluvial material in stream valleys, rock and soil mantle on hill slopes, talus, local terrace deposits, and landslide debris.	None	16	
Basalt	UNCONFORMITY Pleistocene or Pliocene	0-200	Small bodies of basalt that locally cap hilltops and ridges in southeastern part of the map area.	None	15	
Tuscan formation	UNCONFORMITY(?) Pliocene	0-360	Tuff breccia, consisting of poorly lithified aggregate of blocks, lapilli, and volcanic ash.	None	14	
Quartz diorite and related rocks	UNCONFORMITY Early Cretaceous(?) or Late Jurassic(?)		Includes fine-grained mafic quartz diorite, medium-grained augite quartz diorite, fine-grained diorite, albite diabase, and minor granodiorite.	None	13	
Igneous rocks of the Pit River stock	UNCONFORMITY Early Cretaceous(?) or Late Jurassic(?)		Leucocratic granodiorite, albite granite and quartz diorite, with minor aplite.	None	12	
Hosselkus limestone	Late Triassic	0-250	Thick- to thin-bedded light-gray limestone containing abundant fossils.	Potential source of lime products.	11	
Pit formation	Middle and Late Triassic	2000-4400	Predominantly medium-gray to black shale and siltstone, with abundant lenses of metadacite tuff and quartz keratophyre tuff. Also includes lenses of limestone and lava flows.	Host rock for sulfide deposits.	10	
Bully Hill rhyolite	Triassic	100-2500	Chiefly quartz keratophyre lava flows and pyroclastic rocks but includes metadacite, keratophyre, and shaly tuff. Also includes quartz keratophyre dikes in the Dekkas andesite.	Host rock for sulfide deposits.	9	
Dekkas andesite	Permian	1000-3500	Chiefly keratophyre and spilite lava flows and pyroclastic rocks, with lenses of siliceous mudstone and quartz keratophyre in upper part.	None	8	
Nosoni formation	UNCONFORMITY(?) Permian (Leonard or Guadalupe)	0-2000	Chiefly tuffaceous mudstone and tuff interlayered with subordinate tuff breccia. Fossils abundant in some tuffaceous mudstone beds.	None	7	
McCloud limestone	UNCONFORMITY Permian (Hueco and Leonard?)	500-2500	Thin- to very thick-bedded light-gray limestone, with local layers of chert and chert nodules. Many beds contain abundant fossils.	Host for contact metamorphic magnetite deposits. Potential source of lime products.	6	
Baird formation	UNCONFORMITY(?) Mississippian	3000-5000	Lower part consists dominantly of pyroclastic rock with subordinate mudstone and keratophyre flows; middle part chiefly siliceous mudstone, with subordinate tuff and minor limestone; upper part is keratophyre, lava and volcanic breccia.	None	5	
Bragdon formation	UNCONFORMITY Mississippian	0-3000	Mainly shale and mudstone, with numerous lenses of grit and chert conglomerate; locally a few lenses of tuff and sandstone.	None	4	
Kennett formation	UNCONFORMITY Middle Devonian	0-400	Chiefly dark gray siliceous mudstone, tuff, and brownish-gray tuffaceous mudstone containing fossils; small lenses of light gray limestone in upper part.	Potential source of lime products.	3	
Balaklala rhyolite	Middle Devonian	1000±	Quartz keratophyre lava flows and pyroclastic rocks.	Host for massive sulfide deposits in West Shasta copper-zinc district.	2	
Copley greenstone	Devonian(?)	2000±	Keratophyre and spilite lava flows and breccias; includes minor quartz keratophyre tuff.	None	1	

Figure 2.1: Eastern Klamath Terrane stratigraphic column with Tuscan Formation (orange), McCloud Limestone (blue), Bully Hill and Balaklala Rhyolite (red) highlighted (Source: Albers and Robertson, 1961)

debris-flows of the Tuscan Formation to the massive-sulfide rich Balaklala Rhyolite and Bully Hill Rhyolite. The Balaklala and Bully Hill Rhyolites are particularly important for mineral resources as they harbor large deposits of pyrite, gold, silver, and copper (Albers and Robertson, 1961). The ore deposit at Iron Mountain in the Balaklala Rhyolite is up to 60 meters thick and composed of 95% pyrite and averaging 1% copper and 2% zinc. The massive sulfide deposits are also known to produce notable low pH acid- mine-drainage (AMD) conditions both naturally and artificially. The Iron Mountain Mine in the West Shasta Mining District was the site of the lowest naturally occurring pH from AMD ever recorded at -3.7 (Nordstrom and Alpers, 1999). Massive sulfide deposits do not come in contact with the McCloud Limestone directly, but regional faults may connect between the formations. The prominent, cliff-forming formation in the Redding subterrane of the Eastern Klamath Terrane is the cave-forming McCloud Limestone of early Permian age (Diller, 1902).

The McCloud Limestone, forming a major physiographic component of the Redding subterrane, crops out in a relatively thin, disjointed band between Redding and approximately 40 kilometers south of Mt. Shasta, CA (Figure 1.1) (Albers and Robertson, 1961). In this band, the McCloud Limestone stands out in the landscape as a dominant, resistant, cliff-forming outcrop. The McCloud Limestone varies significantly in thickness with a maximum thickness of 760 meters in the central portion of the approximate north-south exposure. Extensive faulting has caused intense displacement and offsets in the exposure with the most distinct discontinuity in the thinner, southern and northern ends. In general, beds in the McCloud Limestone dip steeply to the east with a general north-south strike direction. Disjunct blocks of McCloud Limestone are rarely thicker than 500 meters and are typically less than 300 meters thick (Skinner and Wilde, 1965). Where the McCloud Limestone is exposed, it is generally heavily karstified exhibiting

well developed epikarst and high cave density (DOI 2013, Despain et al., 2022). Caves of the McCloud Limestone have been studied through the lenses of paleontology, archeology, and climatic reconstruction since the early 20th century (Oster et al., 2020; Feranec, 2009; Furlong, 1906; Sinclair 1904). However, little research has focused on the speleogenetic history of the McCloud and how it relates to regional geomorphic development (Despain et al., 2022).

Previous research on the McCloud Limestone has emphasized carbonate depositional setting, paleontology, and economic viability (Demirmen and Harbaugh, 1965; Skinner and Wilde, 1965; Evans, 1977; Smith, 1894; Trask, 1855). Sediments comprising the McCloud Limestone were deposited in a warm shallow sea setting that possessed strong wave action. Paleomagnetic research suggests the limestone is indicative of an environment of deposition at a low latitude that has since rotated 109 degrees before colliding with the North American plate (Mankinen et al., 1989). The limestone is mostly free of allogenic siliciclastics and volcanic clasts, implying deposition in relatively clear water with little to no eolian or volcanic material input from the atmosphere. Organisms that occupied warm shallow waters such as crinoids, fusulinids, byozoans, gastropods, etc. are common in the McCloud Limestone (Demirmen and Harbaugh, 1965). The McCloud Limestone was divided into seven chemo-lithologic units by Evans (1977) based on relative percentages of limestone, dolomite, and silica. Evans (1977) estimated that only 20 percent of the formation is made up of carbonate with at least 90 percent limestone purity. The remaining percentage is primarily made up of high-magnesium limestone (dolostone). In general, the McCloud Limestone is composed of relatively pure, light-to-dark gray massively bedded calcarenite that has been locally dolomitized and silicified (Miller, 1989; Evans, 1977, Demirmen and Harbaugh, 1965). Skinner and Wilde (1965) conducted an exhaustive study on fusulinid and lithologic zonation in the McCloud Limestone and established

a set of biostratigraphic sections along the north-south exposure of the formation. The study on fusulinid zonation and biostratigraphy established a Wolfcampian-age for the McCloud Limestone (Skinner and Wilde, 1965). Almost all outcrops of the McCloud Limestone are bounded and intruded by augite quartz diorite dikes and sills of late-Jurassic age and iron and magnesium-rich skarn deposits are common throughout the contacts (Evans, 1977; Albers and Robertson, 1961).

Contacts between the McCloud Limestone and underlying and overlying formations, the Baird and Nosoni, are almost everywhere intruded by altered augite-quartz diorite and associated skarn deposits (Albers and Robertson, 1961; Smith, 1894). In some cases, the intrusive material has caused contact alteration of the limestone to low-grade marble (Skinner and Wilde, 1965). Plutonic intrusions were widespread during the formation of the Klamath Mountains and many terranes of sedimentary and metamorphic rocks were intruded by dikes and sills of various chemistries (Irwin, 1989). Through extensive geologic mapping of the region, Albers and Robertson (1961) concluded that the intrusive bodies encompassing the McCloud Limestone are likely late Jurassic in age due to cross-cutting relationships with a nearby Jurassic-age plutonic body, the Pit River Stock. Karstification and cave development appears to be closely associated with intrusive bodies of augite quartz diorite, as caves are commonly exposed along contacts with intrusive bodies, and intrusive bodies are frequently observed inside cave passages (Despain et al., 2022; Spain, 2022). Since primary orogenic and intrusive events in the Jurassic, the Klamath Mountains region has been subject to erosion, and uplift creating a diverse and complex range of Cretaceous to Cenozoic age deposits.

The post-Nevadan orogeny period in the Klamath Mountains was dominated by erosion, glaciation, and regional uplift that began in the Cretaceous and continued through to the

Cenozoic (Irwin, 1989; Albers and Robertson, 1961). Large portions of the western Klamath Mountains were flattened to a broad, flat surface composed of marine and fluvial sediments by the start of the Miocene Epoch (Anderson, 2008; Aalto, 2006; Diller, 1902). The widely distributed and laterally continuous paleo-surfaces were coined the 'Klamath Peneplain' by Diller (1902). The surfaces marked a level of regional erosion and deposition of marine and fluvial sediments (Anderson, 2008). Regional uplift resumed in the Klamath Mountains during early Pliocene, resulting in river incision and erosion through the erosional peneplain surfaces. Recent research has used relationships between the peneplain surfaces and river downcutting to resolve questions relating to river incision rates in the western Klamath Mountains, but river incision rates and paleo-topographic characteristics in the eastern Klamath Mountains are not as well defined or described (Anderson, 2008). Irwin (1989) suggests that paleo-topographic relief in the Siskiyou Mountains of the east-central Klamath Mountains was greater than 1000 meters due to the relative lack of exposed peneplain erosional surfaces. A lack of described peneplain or paleo-topographic deposits in the eastern Klamaths suggests a paleo-topographic evolution that is poorly understood (Anderson, 2008). Eastern Klamath Mountain uplift rates and Cenozoic evolution has not been well resolved due to the relative lack of deposits and research on them (Anderson, 2008; Albers and Robertson, 1961). Study of cave-sediment deposits in the eastern Klamath Mountains can reveal insights into paleo-topographic evolution by preserving shifts in paleo-hydrologic and depositional environment influences or controls.

2.2 Cenozoic Deposits in the Eastern Klamath – Southern Cascade

Post-orogenic deposits in the eastern Klamath Mountains and Shasta Lake region are relatively rare with little to no exposures of late Mesozoic or early Cenozoic age rocks in the

region. After major orogenic events in the Jurassic, erosion dominated in the Klamath Mountains and rivers incised through the landscape while transporting material to the Pacific Ocean and 'Sacramento River Valley' basins (Anderson, 2008, Aalto, 1992 Haggart, 1986). The oldest Cenozoic formation forms outcrops adjacent to the Shasta Lake region is the Montgomery Creek fluvial conglomerates of Eocene age (Renne et al., 1990, Albers and Robertson, 1961, Sanborn, 1960). The Montgomery Creek Formation is widely distributed in a region between the Shasta Lake physiographic region and the Southern Cascade Volcanic range and Northern Sierra Nevada range. The broad depression between the two physiographic regions was called the 'Lassen Strait' by Diller (1902). The Lassen Strait was a broad depression inundated with marine and fluvial sediments and records fluvial deposition from the late Cretaceous to early – middle Cenozoic (Haggart, 1986; Diller, 1902). Renne et al. (1990) found that the fluvial sediments of the Montgomery Creek Formation in the Lassen Strait were transported by a fluvial system originating in the Idaho Batholith region during the early to middle Eocene epoch (~34 - 48 Ma). The paleo-drainage transported sediments from Idaho, Oregon, and northwestern California to the Sacramento Valley basin and Pacific Ocean (Aalto, 1992). The Montgomery Creek Formation records the earliest deposition of Cenozoic sediments in the eastern Klamath Mountains region and study of them can elucidate how the region has evolved since orogenic events in the Jurassic. The lack of exposed sediments or volcanics between the Eocene to Miocene in the eastern Klamath Mountain-Shasta Lake region suggests a period of erosion and regional uplift (Albers and Robertson, 1961). This period of relative quiescence was interrupted as Southern Cascade Volcanism began in the late Miocene and continued into the Holocene. Voluminous and widespread eruptive events from Southern Cascade Volcanics resulted in the accumulation of thick and widely distributed volcanic deposits between the eastern Klamath and

northern Sierra Nevada Mountains, known as the Lassen Segment, as well as the broad volcanic center north of Lassen, the Shasta Segment (Hildreth, 2007).

The Shasta Segment is defined as the broad volcanic region between the Mt. Shasta eruptive center and Medicine Lake Volcanic Field. The entire segment stretches 50 km north-south and 120 km east-west. Volcanism in the Shasta Segment began in the Late Pliocene and continued into the Holocene. Shasta Segment volcanism in the Pliocene consisted primarily of mafic shield volcanoes and fissure-fed plateau capping basalts that constructed the modern physiographic character of the region (Hildreth, 2007). Mt. Shasta is the dominant, modern volcanic edifice in the segment and is the most voluminous stratovolcano of the Quaternary Cascades. Older volcanic edifices like the similarly voluminous early Pleistocene Rainbow Mountain stratovolcano erupted large volumes of andesite-dacite that contributed to the modern topographic regime (Hildreth, 2007; Gardner, 1964). Mt. Shasta began erupting approximately 0.6 Ma and is composed of one primary volcanic edifice (Hildreth, 2007). The accumulation of Shasta Segment volcanics created a topographic high in the region. The overall Shasta Segment and Mt. Shasta topographic highs are the headwaters of the McCloud River (USDA, 1998). In between the Shasta Segment and Lassen Segment is a 50 km gap of little to no volcanic vents and primarily Paleozoic metamorphic and sedimentary rocks (Blakely et al., 1985; Hildreth, 2007).

The Lassen Segment is the southernmost extent of the Cascade volcanic range and has produced the largest volume of silicic magma in the range. The segment is a complex volcanic center composed of overlapping volcanic edifices ranging from as young as 26 ka to as old as 7 Ma that stretches approximately 80 km north-south and 110 km east-west. The Lassen Segment is composed of the remnants of five, large volume silicic volcanic peaks that erupted from the

late Pliocene to the Quaternary. These volcanic centers include Dittmar (1.5 – 2.5 Ma), Snow Mountain (1 – 2 Ma), Maidu (1 – 2.4 Ma), Yana (2 – 3 Ma), and Lassen (< 0.8 Ma). The five centers in Lassen were long lived, erupting periodically over hundreds of thousands of years. (Hildreth, 2007). Adjacent to the five, long-lived voluminous eruptive centers are hundreds of shorter-lived more mafic eruptive vents in the Lassen Segment (Guffanti et al., 1990). In total there are approximately 597 late-Cenozoic volcanic vents that make up the Lassen volcanic center. Of these 597 vents, at least 476 vents erupted within the last 2 Ma. The remaining 121 vents erupted from approximately 7 to 2 Ma (Clynne and Muffler, 2017; Hildreth, 2007). Geographically, the Lassen Segment is the closest volcanic center to the Shasta Lake – eastern Klamath Mountains region, with Snow Mountain (1 – 2 Ma) being within approximately 40 km of the McCloud Limestone and the Shasta Lake physiographic region. The Mt. Shasta eruptive center, in comparison, is approximately 60 km from the McCloud Limestone karst region (Hildreth, 2007).

Concurrently during the eruption of Southern Cascade Volcanics in the Shasta and Lassen Segments beginning in the Miocene, paleo high-stand sediment and volcanic deposits were developing at distinct, laterally continuous elevations in the Shasta Lake physiographic region. The high-stand markers are defined by flat-topped spurs with common elevations, river transported gravels, late Cenozoic volcanics, and stream transported limonite clasts of varying size. The most distinct high-stand markers are positioned at approximately 312, 381, and 500 - 530 meters and can be traced across large distances in the Shasta Lake – eastern Klamath Mountain region (Albers and Robertson, 1961). The deposits are similar to those of the peneplains of Diller (1902) but were not studied or described in recent in-depth studies on Klamath Peneplain surfaces in the central and western Klamath regions (Anderson, 2007; Aalto,

2006). The highest elevation paleo base-level sediment deposits are distributed in the 500–530-meter range and consist primarily of thin terrace deposits of transported, spongy limonite and angular rock fragments (Albers and Robertson, 1961). The limonite deposits are only mapped in a small portion of the Shasta Lake region adjacent to the Bully Hill Mine between First and Second Creeks. Albers and Robertson (1961) describe the deposit as being a thin, discontinuous layer stretching for roughly 300 meters along a steep hillside and only approaching 7 meters thick. At a similar elevation of the limonite deposits, Albers and Robertson (1961) describe a distribution of flat-topped spurs and small peaks that apparently mark old valley levels. Another such deposit at a similar elevation to the limonite deposit is the relatively well studied volcanic tuff breccia of the Tuscan Formation.

The Tuscan Formation is a regionally widespread deposit of Pliocene age possessing volcanic debris-flows, air-fall tuffs, minor basaltic to andesite lava flows, and siliciclastic sediments. The Tuscan Formation covers an area of 5,000 km² along the western margin of the Sierra Nevada mountains and extends from just south of the Pit River to south of Oroville, California (Clynne and Muffler, 2017; Gonzalez, 2014). The primary source of the Tuscan Formation are the Yana and Latour volcanic centers of the Lassen Segment. The Tuscan Formation was dated to as young as approximately 2.5 Ma and to as old as 3.5 Ma (Clynne and Muffler, 2017). The Tuscan outcrops at its northernmost extent along the southern boundary of Shasta Lake and is exposed along Backbone Ridge and in discontinuous outcrops north and south of the ridge. The exposures of the Tuscan Formation in the Backbone Ridge area are primarily made up of soft, friable tuff breccia. The exposure in this area is undeformed and lies unconformably over deformed rocks of Paleozoic and Mesozoic rocks of the Eastern Klamath Terrane (Albers and Robertson, 1961). Through detailed mapping of Tuscan exposures, Albers

and Robertson (1961) concluded that pre-Tuscan topography, where it is exposed at Backbone Ridge at Shasta Lake, was characterized by low relief south of the ridge and high relief north of the ridge. The evidence cited for a pre-Tuscan low relief south of the ridge were that the uplands on either side of Little Cow Creek are broad regions of low relief, the base of the Tuscan slopes gently southwestward and can be traced between discrete masses, and the fact that Tuscan thickness south of the ridge is relatively uniform beneath of a basalt cap. Evidence for a region of pre-Tuscan, high relief north of the ridge is that the distribution of discrete Tuscan masses appears to have been guided by valleys similar in orientation to Sugarpine Canyon and the Pit River (Albers and Robertson, 1961).

2.3 Cave Sediments

Unlike depositional environments on the surface, caves offer a stable environment for long-term storage and preservation of sediments that may reveal paleo-depositional and climatic conditions. Cave sediments record detailed information on past water flow conditions, paleo-climatic insight, and dateable proxies that shed light on the history and conditions of speleogenesis and environmental change (i.e. Kurecic et al., 2021;; Nehme et al., 2014; Polk et al., 2013; Bosch and White, 2007; White, 2007; Sasowsky, 2007; Stock, 2005; Polyak et al., 1998; Gillieson, 1986). Cave sediments can be divided into two genetic categories – autogenic (autochthonous) and allogenic (allochthonous) (Sasowsky, 2007; Ford and Williams, 2007; White, 2007). Autogenic sediments can be divided further into clastic and chemical deposits. Autogenic sediments are those that originate in the cave environment, such as authigenic mineral precipitates or bedrock residuum. Allogenic sediments are those that are carried into the cave environment via a transport system. Clastic sediments are defined by fragments of weathered

rock that are transported away from the source rock to an area of storage, whether it be within a basin or fluvial channel. Clastic sediments are particularly useful for reconstructing paleohydrologic conditions because parameters such as grain-size distribution and absolute sediment size are directly correlated to flow velocity in a transport system (Woodside et al., 2015; Nehme et al., 2014; Herman et al., 2012; Springer and Kite, 1997). Many researchers have investigated cave sediments to examine their origins and potential for proxy usage and several facies classification systems have been proposed. The facies terms describe patterns in sedimentary sequences based on mechanical characteristics such as grain size sorting and depositional energies (Bosch and White, 2015; White, 2007; Gillieson, 1996; Kukla and Ložek, 1958). Facies classification systems primarily describe allogenic fluvial sediments as they transport the bulk of clastic sediments in caves (Springer, 2019; Herman et al., 2012; Gillieson, 1996). By applying facies system descriptions along with study of grain size and mineralogical distributions, studies of cave sedimentology have elucidated paleo-depositional conditions and depositional age in a range of cave environments.

Clastic cave sediments have provided ideal material for studying paleo-environmental change and time constraints through the study of numerous proxies from grain size distribution to cosmogenic burial dating. Studies on grain size distribution of clastic cave sediments has allowed for the relative differentiation of stratigraphic units representing varying sedimentary processes (Entrena et al., 2022; Hauselmann et al., 2010; Gillieson, 1986; Butzger, 1981) and shifts in hydrodynamic flow regimes by evaluation of skewness and sorting indices and boundary shear stress models (Nehme et al., 2014; Herman et al., 2012). Studies have also revealed insight into the river incision rates through radionuclide signatures preserved during the burial process (Laureano et al., 2016; Stock, 2006; Granger et al., 2001) or paleomagnetic

signatures preserved in iron-rich sediments (Parés et al., 2020; Stock et al., 2005). Statistical analysis of grain size data using moment statistics formulae modified by Folk and Ward (1957) have been standardized in cave sedimentology and comparison of parameters such as skewness and kurtosis are commonly employed in these studies (Nehme et al., 2014; Shackley, 1972; Gillieson, 1986; Butzger, 1981). For instance, Shackley (1972) provides a summary of grain size distribution characteristics in cave sediments and notes that distributions are commonly bimodal and exhibit very high or low kurtosis. Shackley (1972) attributes this to high degrees of mixing of materials with relatively unchanged size characteristics. Shackley (1972) further notes that unimodality is rare in cave sediments because of common mixing. In order to study the transport and deposition of clastic sediments in an aqueous setting, research has necessitated the understanding of key principles in sedimentology such as Hjulström's diagram and the principle of Stokes Law of settling (Hjulström, 1955; Lamb, 1895).

Clastic sediments move through a cave stream as suspended particles (suspended load) or rolling and saltating (bed load) and are subject to deposition as water velocity decreases. After deposition, subsequent incision may entrain the deposits sediment load depending on water velocity and grain size. Hjulström's diagram explains the relationship between water velocity, grain size, sediment deposition, and sediment entrainment (Figure 2.2) (Springer, 2019; Hjulström, 1955). The key phenomena that the Hjulström diagram shows is that higher velocities are required for the entrainment of silt to clay-sized particles relative to coarser material such as sand. This results in a phenomena whereby very-fine particles and coarse-grained particles require higher water velocities to entrain compared to mid-range grain sizes such as sand and pebble-size (Springer, 2019; Hjulström, 1955). Stokes Law of settling similarly describes a

relationship between grain size and deposition although focuses on settling velocity of particles in suspension (Lamb, 1895). Once sediments are entrained in suspension, they will

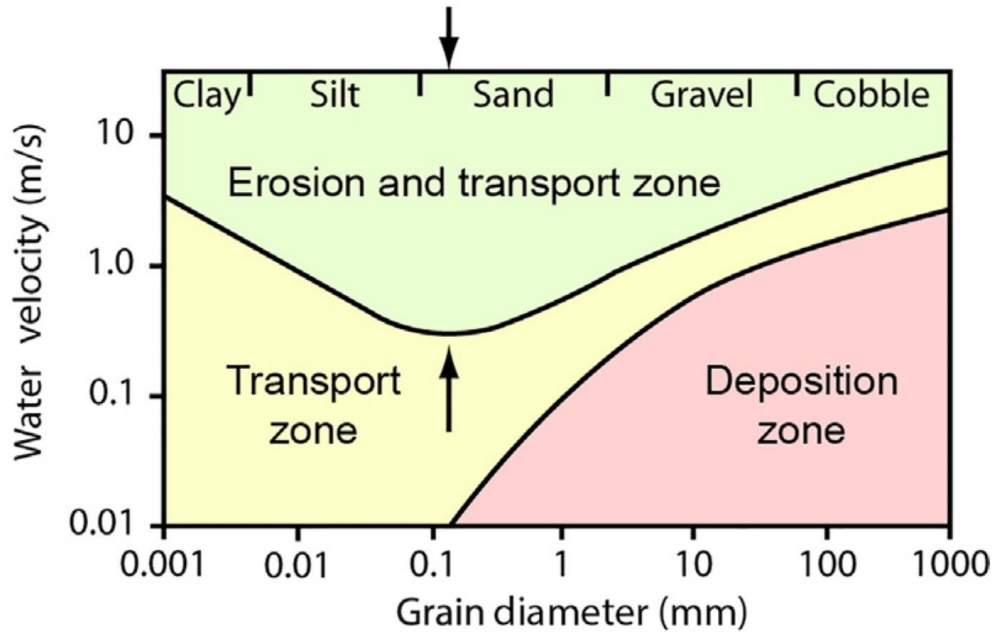


Figure 2.2: Hjulström diagram with a mark at the lowest water velocity for erosion (Source: Springer, 2019)

remain in suspension as long as they are being transported by turbulent lift forces in any direction. As water velocity decreases and turbulent forces decline, sediments will fall out of suspension at a fall velocity that is dependent on particle size, particle density, and viscosity of the fluid. The relationship between these parameters and the resulting fall velocity is shown by Stokes law (Equation 2.1) (Herman et al., 2012; Lamb, 1895). A majority of clastic sediments that are transported and deposited in cave systems are allogenic in origin and typically originate from surface drainages (Springer, 2019; Herman et al., 2012; Gillieson, 1986).

(Eq. 2.1)

$$V = \frac{2r^2 (\rho_{sphere} - \rho_{fluid}) g}{9\mu}$$

Equation 2.1: Settling velocity based on Stokes Law relationships, where

r = particle radius (m)

ρ_{sphere} = particle density (kg/m³)

ρ_{fluid} = fluid density (kg/m³)

μ = fluid viscosity (kg/m.s)

g = gravity (m/s²)

Allogenic transport of clastic sediments into karst systems involves input source that affect facies characteristics and distributions. Allogenic sediment transport into karst systems occurs through active hydrology and/or gravity-driven processes. Researchers have defined and studied these input sources and devised systems for understanding their transport mechanisms and importance in the cave sediment budget (Bosch and White, 2015; Herman et al., 2012; Trappe, 2010; Ford and Williams, 2007; Sasowsky and Mylorie, 2003; Gillieson, 1996; White and White, 1968, Kukla and Ložek, 1958). The primary input sources of clastic sediments include fluvial transport by sinking streams, storm runoff through sinkholes, infiltration through epikarst fractures and fissures, sinkhole drainage and collapse, sediments brought in by surface stream backflushing, and entrance sedimentation (Figure 2.3) (Bosch and White 2015; Trappe 2010; Gillieson 1996). Allogenic transport is dominant in fluviokarst settings due to the great sediment input from sinking streams and high-energy flood events. Clastic sediments in a

fluviokarst transport system behave similar to fluvial systems in gorges and floodplains and deposit similar facies. The primary difference, however, is that cave fluvial systems are confined to conduits of varying geometries. Water levels and velocity can therefore shift dramatically during flood events, resulting in chaotic sedimentation and erosion. Rapidly changing velocities and associated depositional energy can affect lateral continuity of sediment beds and make it difficult to reconstruct depositional conditions (Bosch and White, 2015; Gillieson, 1996). Sediments also enter a cave through relatively low velocity transport mechanisms such as epikarst seepage, sinkhole washdown and entrance infiltration. Epikarst sediments tend to be fine grained and may contain weathering residuum and regolith. Entrance deposits consist of a mixture of organic-rich soil and surface debris and rock fragments from entrance collapse from surface weathering processes such as results from freeze-thaw cycles. Entrance facies deposits

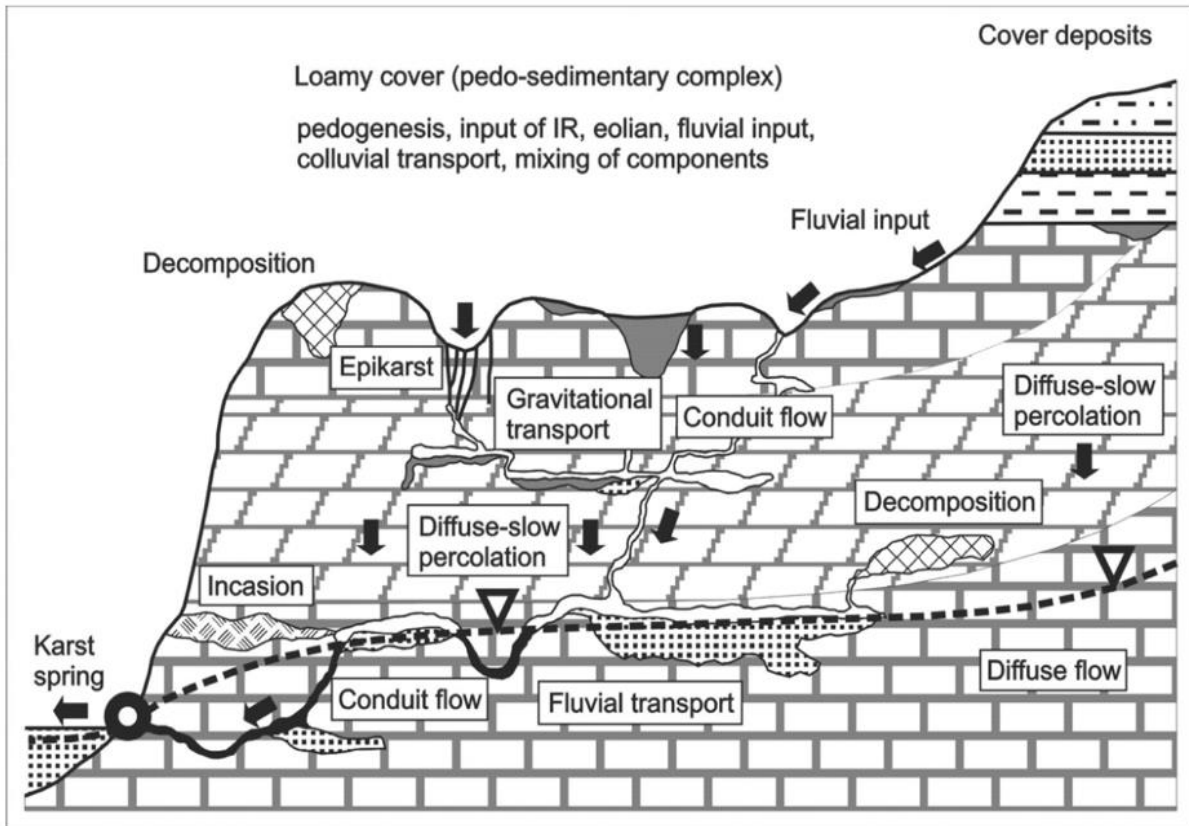


Figure 2.3: Schematic diagram of cave sediment storage zones and inputs and outputs (Source: Trappe, 2010)

are not necessarily deposited by a hydrologic control and are not transported long distances into the cave (Herman et al., 2012; Trappe, 2010; Kukla and Ložek, 1958). Cave sediments that are not typically transported long distances and originate from the cave environment are defined as autogenic in character.

Autogenic sediments are those that originate in the cave environment and remain there until transport out of the cave-storage system. Clastic autogenic sediments are primarily gravity-driven deposits such as breakdown and the clastic products that breakdown produce. Another clastic autogenic sediment that can contribute large quantities of fine-grained material is weathering residuum. In non-fluviokarst settings possessing low transport energy, weathering

residuum can accumulate large volumes of fine-grained sediment (Herman et al., 2012). Chemical sediments are primarily authigenic and are composed of chemical precipitates and evaporites, such as travertine and sulfates. Chemical sediments are diverse and complex with some 250 recognized minerals forming in cave environments around the world commonly forming under in unique environmental conditions. Calcite is the most abundant chemical sediment, but chemical deposits, such as phosphates, water ice, sulphates, nitrates, silicates, and metal oxides, are common in most cave environments although typically in small quantities (White, 2007; Ford and Williams, 2007). Researchers have studied authigenic deposits in detail for their use in paleoclimate and speleogenesis research (Oster et al., 2020; Polyak et al., 1998). Chemical sediments are not contained in most cave-sediment facies classification system.

Many classification systems have been proposed to describe sedimentary facies and particle characteristics, but a unified facies classification that is broadly applicable and mechanically descriptive is lacking (White, 2007). Early classification systems that sought to describe clastic sediments and transport were devised by Springer and Kite (1997), Gillieson (1986), Pickle (1985), White and White (1968), and Kukla and Ložek (1958). These systems either fall short of providing classification for all facies types or focus too narrowly on depositional energy and flow regime (Bosch and White, 2007). This is partially because cave sediments are idiosyncratic and depositional conditions commonly vary wildly (Sasowsky, 2007). Building on previous work, Bosch and White (2007) attempted to establish a classification system for sediments in fluviokarst settings that focuses primarily on particle size, sorting, and sedimentary structures. The classification system is most like that of Gillieson (1986) in that it describes facies as products of depositional energy and sorting characteristics. Bosch and White (2007) establish five principal sedimentary facies in their classification system.

Previous workers (Trappe, 2010; Pickle, 1985; Gillieson, 1986; Springer and Kite, 1997, and Kukla and Ložek, 1958) introduced select facies concepts in their work, but Bosch and White (2007) provided a summation and refinement of the classification systems.

Bosch and White (2007) describe five facies commonly encountered in fluviokarst settings: 1) channel facies, 2) thalweg facies, 3) slackwater facies, 4) diamicton facies, and 5) backswamp facies. Channel facies is a broad description of sediments that have been sorted through fluvial transport in a conduit. In stratigraphic section, channel facies exhibit distinct stratification of silts, sands, and gravels. Further, grain size and sorting characteristics in channel facies sediments typically shift dramatically in the stratigraphic section dependent on the depositional energy in the channel at any given location and the source material. Because of this, Bosch and White (2007) suggest that channel facies can often be further separated into sub-facies dependent on variations in sorting and grain-size characteristics. The thalweg facies describes a particular sedimentary condition whereby an active, flood-prone stream either cuts into a channel facies sequence forming a secondary stream channel or a primarily coarse-grained sequence is deposited in a localized area. The material transported in the secondary channel is commonly coarse-grained gravel, cobbles, and boulders due to the high flow velocities required to scour channel facies deposits and create a secondary channel. The slackwater facies is defined by fine-grained, laminated deposits that are transported as suspended load and dropped out of suspension as flow-velocity decreases (Bosch and White, 2007; Herman et al., 2012; Gillieson, 1986). Floodwaters laden with fine-grained suspended load may be transported into smaller side-passages where flow velocities decrease due to potential blockages or shrinkage of passage size. Fine-grained suspended load will then drop out of suspension according to Stokes law of settling. Diamicton facies, originally proposed by Gillieson (1986) for use in cave sedimentology,

describes sedimentary facies consisting of unbedded and unsorted mixtures of all grain sizes. Gillieson (1986) interpreted the cave diamicton facies as being the result of debris flows and mass movement events that do not sort or stratify sediment. The diamicton facies is different than gravity-driven deposits, such as talus, because the diamicton facies exhibits a wider range of grain sizes and larger grain sizes suspended in a matrix of fine clays or silt. Finally, the backswamp facies describes sediments that are deposited with little-to-no lateral transport and primarily consist of weathering residuum and fissure infiltrates. Bosch and White (2015) chose the term 'backswamp' to describe the process whereby some caves act like hydrologic swamps with large volumes of slow-moving water. Because of low transport energy, backswamp facies are typically fine-grained and made up of clay and silt-sized grains and clasts of insoluble material such as chert and fossils (Bosch and White, 2007). Backswamp facies is the only facies described by Bosch and White (2007) that consists primarily of autogenic sediments, where a majority of the sediments originate from weathering residuum. Autogenic sediments make up a large portion of sediments entrained in a karst system, and in non-fluviokarst settings autogenic sediments make up the largest component (Springer 2019; Herman et al. 2012; Onac and Forti, 2011).

Trappe (2010) recognized the complexity and heterogeneity of allogenic sediments and developed a facies system for describing depositional conditions whereby clastic sediments accumulate (Figure 2.1). The facies associations include surface-karst sediments, crack-filling facies, cave-entrance facies, and inner-cave facies (Trappe, 2010). These are described as surface-sediments as the products of corrosive, erosive, gravitate, and pedological processes that form the clastic sediments that overlay karst systems. These clastic sediments may eventually move into the karst system via cracks and fissures in the karstified rock, creating the crack-filling

facies. Trappe (2010) suggests that allogenic processes can contribute sediments to the crack-filling facies by in-situ weathering of the karstic rock at the karst-sediment contact and subsequent release of weathering residuum. The concept of a cave-entrance facies is described as sedimentary deposits made up of superficial material transported into the cave environment through colluvial or alluvial processes (Trappe, 2010; Kukla and Ložek, 1958). The cave entrance facies is commonly the focus of archeological and paleontological investigations due to the ability to preserve superficial deposits that have not been heavily altered by the cave environment (Farrand, 2001). The final facies domain described by Trappe (2010) is the inner-cave facies that is largely controlled by hydrologic conditions. The details of these inner-cave facies generally correlate with the facies classification system devised by Bosch and White (2007). This study will use facies terms from all of the aforementioned system components of Trappe (2010) and Kukla and Ložek (1958) facies will be utilized to describe sedimentary facies that are not expressly described by Bosch and White (2007).

2.4 Karst and Speleogenesis

Karst landscapes form as the result of acidified water interacting with soluble bedrock. Broadly, karst can be defined in three genetic categories, syngenetic/eogenetic, hypogenic, and epigenetic (Klimchouk, 2015; Gillieson, 1996). Each genetic category describes the source of karstification, or the set of reactions that dissolves soluble bedrock creating karst landforms. Syngenetic/eogenetic karst describes the karstification process occurring in the littoral zone, or coastal or oceanic settings, and forms through mixing reactions in the halocline zone. Syngenetic/eogenetic karstified rock generally possesses high porosity and includes young carbonates. Hypogenic karst is defined by karstification by deep seated waters and/or non-

meteoric acid sources that have little-to-no influence from surface processes (Klimchouk, 2017; Palmer, 2006). Volcanogenic cave genesis is a process of hypogene karstification involving interactions between deep-seated water and volcanically derived sulfuric and carbonic acid sources (Palmer, 2006; Gary and Sharp, 2006). Hypogene and volcanogenic karstification is generally disconnected from surface processes. Epigenic karst is defined by karstification occurring from interactions between soluble rock and meteoric water and surface processes (Klimchouk, 2017; Ford and Williams, 2007; Palmer, 2006). Epigene karst landforms define the epigene karst landscape and are generally composed of sinkholes and closed depressions, sinking streams, poljes, etc. (Ford and Williams, 2007; Palmer, 2006; Gillieson, 1996). Epigenetic karst makes up a considerable portion of the karst environments studied to date, and Palmer (2006, 1991) suggests 80-85% of karst landscapes form epigenetically.

Epigenetic caves are those that develop through the dissolution of soluble bedrock by acids that originate from surface processes and meteoric water infiltration through soil and epikarst (Gillieson, 1996; Palmer, 1991). Epigene karst develops with a strong relationship with the overlying landscape and development is directly affected by surface hydrology and recharge. Karst development in epigene settings initiates as a direct result of hydraulic gradients and groundwater flow. Epigene development is intrinsically linked to landscape development and processes occurring on the surface through hydrologic control. Acid source in epigene settings is a major distinguishing factor that separates epigene from hypogene karst (Palmer, 2013; Palmer, 2006). The most common and abundant source of acidity in karst aquifers is carbonic acid forming from dissolved carbon dioxide. Average levels of carbon dioxide in the atmosphere are around 0.04 percent, but in soils in certain climates with rich biodiversity carbon dioxide levels can be as much as ten percent (White et al., 1995). Epigenetic karst aquifers are sourced with

carbonic-acid laden water through two primary input processes, autogenic and allogenic recharge zones (Palmer, 2006; Gillieson 1996; White et al., 1995).

Autogenic recharge occurs through the bedrock surface through water-rock interactions in the epikarst and in sinkholes. At first, autogenic recharge is slow because chemical aggression (i.e CaCO_3 undersaturation) is quickly used at the surface in widening joints and fractures in the epikarst. Over time, those widened joints and fractures become large enough to supply chemically aggressive water to a conduit system below (Williams, 2008; Palmer, 2006, Gillieson, 1996). Two major components make up the autogenic recharge – diffuse input through widened joints and fissures in the epikarst and runoff captured by closed depressions, or sinkholes. Allogenic recharge describes input through sinking streams and channelized flow originating from hydrologic systems flowing over relatively insoluble bedrock. Channelized flow can enter the karst aquifer with chemically aggressive water through interactions with insoluble rock. Allogenic flow also carries suspended and bedload sediments into the karst aquifer and can be a major player in physical weathering processes (Gillieson, 1996; White et al., 1995; Palmer, 1991). In contrast to epigene karst aquifers, hypogene karst aquifers do not receive direct recharge through allogenic sources and do not need to have a direct relationship with geomorphic features on the surface (Klimchouk, 2017; Palmer, 2013; Palmer, 2006).

Hypogene karst is broadly defined by karstification and speleogenesis that occurs with no direct relationship with surface geomorphology, and the acid source for karstification is not directly related to surface processes. Hypogenic caves form as deep, typically confined phreatic systems as well as near or above the water table with condensation corrosion and mixing with meteoric waters (Audra and Palmer, 2015; Klimchouk, 2017; Palmer, 2013, Palmer, 1991). Researchers have proposed multiple definitions of hypogene karst since the late 20th century that

have described the primary mechanisms and conditions necessary for dissolution in hypogene settings. Klimchouk (2017) suggests hypogene karstification typically occurs at depth in confined aquifers with recharge from deep-seated sources or through rejuvenation of epigenic acid sources by deep-seated processes. Deep-seated fluid sources that recharge the karst aquifer originate from hydro-stratigraphically lower rock units and aquifers (Klimchouk, 2017). Palmer (2013, 1991) defines hypogene karstification with a focus on the source and transport of chemical dissolution and aggressiveness. The sources of chemical aggressiveness in hypogene settings are not directly tied to surface sources such as soil carbon dioxide or organic acids. Instead, hypogene acid sources may originate from sulfide oxidation, rising thermal waters, and/or volcanically derived carbon dioxide (Klimchouk, 2023; Audra and Palmer, 2015; Gilli, 2014; Palmer, 2013, Piccini et al., 2007; Gary and Sharp, 2006; Salomon, 2003; Audra et al., 2003; Dublyansky, 1995; Palmer, 1991). Broadly, the oxidation of pyrite and sulfide-rich sedimentary rocks leads to the formation of sulfuric acid and the increased chemical aggressiveness of karstic water in both vadose and phreatic settings (Klimchouk, 2017; Audra and Palmer, 2015; Audra et al. 2003; Palmer 2013). Rising thermal waters from hydrothermal or volcanogenic sources results in the thermal convection of fluids through pre-existing rock structure (Figure 2.4). Rising fluids can be confined and/or transported along intrusive volcanic features to form hydrologically-confined hydrothermal karst (Klimchouk et al., 2023). In many instances, increased groundwater flux and associated endogenic carbon dioxide and hydrogen sulfide has led to aggressive karstification and resulting hypogenic morphologies (Gilli, 2014; Piccini et al., 2007; Gary and Sharp, 2006; Salomon, 2003; Dublyansky, 1995).

2.5 Cave-Sediment Sampling

Cave-sediment sampling techniques have traditionally employed resource intensive trenching excavations or rudimentary soil sampling techniques such as shallow PVC (poly vinyl chloride) coring (Temovski et al., 2016; Stratford, 2011; Tobin, 2007). Trenching requires many days of hard labor and often takes months of careful planning to execute safely and efficiently. Traditional archeological sediment sampling has employed destructive and time-consuming equipment such as hydraulic drills, hammers, picks, and explosives (Stratford, 2011). Researchers have long recognized the challenges of sampling in cave environments (Stratford, 2011; Sasowsky, 2007), but new methods of efficient sampling are rarely proposed. Previous workers in archeology or pedology have utilized mechanical coring techniques such as used in this study (Canti and Meddens, 1998), but very few researchers have used percussion-driven soil sampling techniques in a cave setting (Bailey and Thomas, 1987; Jenkinson et al., 1983).

Bailey and Thomas (1987) recognized the need for quick and effective sampling to depth in cave research settings and tested a self-driven, percussion apparatus to a maximum depth of eight meters. They demonstrated that percussion-driven sampling can be quick and effective in retrieving continuous, relatively undisturbed samples from depth for use in archeological research; however, researchers involved in the study noted that the sampler is best used in fine sediments with little to no coarse fraction. In addition, they note that the sampler is best used with steel liners and sand shoes for sediment retention. They believe that coring to depths of 10 – 15 meters would be possible with liners and retention shoes (Bailey and Thomas, 1987). Jenkinson et al. (1983) investigated the use of a similar technique called hydraulic ram sampling to retrieve undisturbed samples of cave sediments. Hydraulic ram sampling is done by driving a sampling core tube into a sediment section by applying an opposite force to the cave ceiling. The sampling method requires a small enough cave passage for the hydraulic ram to be placed upon

the ceiling to apply a resistive force. The researchers demonstrated that the technique retrieved relatively undisturbed samples from depths of 0.5 – 1.6 meters, but limitations included the need for short ceilings and measurable displacement of the sediment samples in the core (Jenkinson et al., 1983). Other percussion-driven geotechnical and environmental techniques such as standard penetration testing (SPT) have not been utilized in a cave setting and could prove to be an efficient and practical sampling method.

Geotechnical and environmental consultants have successfully used SPT split-spoon sampling for decades and have proven it to be an effective sampling system compared to other methods. The use of a split-spoon sampler allows the user to evaluate soil samples in the field with minimum disturbance to the sample (Carter and Bentley, 2016). Use of a split-spoon sampler is a central component of the SPT procedure often utilized by geotechnical engineers and soil scientists (Kasich et al., 2017; Moss and Merguerian, 2010). The SPT procedure with the use of a split spoon sampler was developed by engineers at the Raymond Concrete Pile Company in 1927 and has since been performed globally in a variety of site conditions (USBR, 2001). The test was standardized by ASTM international and is conducted under standard methods described by ASTM D1586-11 (ASTM, 2014). Standardization of the test has allowed researchers to quantify the mechanics of the test and relate them to various soil properties.

The SPT procedure is used by engineers to determine the relative density of subsurface materials through the counting of successive hammer blows (i.e blow counts) that progress the sampler. Blow counts are recorded during sampler progression and are used to calculate various engineering properties such as shear strength and compressibility (Carter and Bentley, 2016). Traditionally, as standardized by the ASTM, the split-spoon sampler is progressed into the subsurface by a drop-hammer of standard weight and drop distance. The split-spoon sampler

itself is made up of the driving shoe at the tip of the sampler, two components of the split barrel, and a coupling device at the top connected to extension rods and ultimately the slide hammer

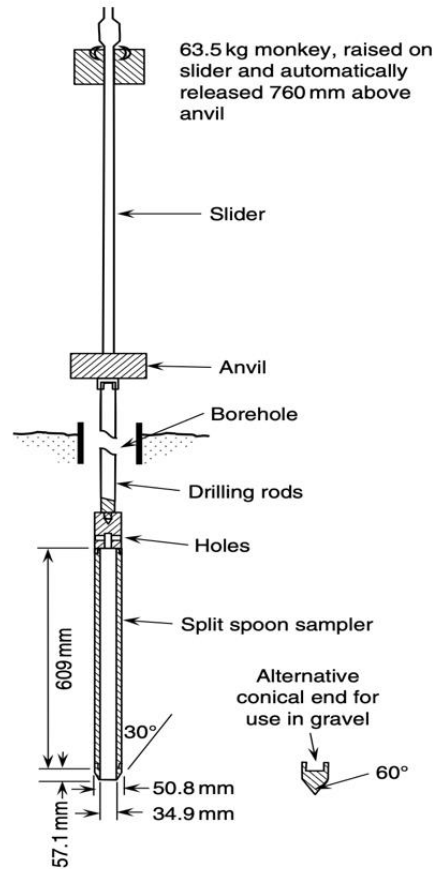


Figure 2.5: Schematic diagram for split-spoon sampler and associated sampling equipment (Source: Carter and Bentley, 2016).

(Figure 2.5). The split-barrel nature of the sampler allows the user to disassemble the sampler as it's retrieved from the subsurface and evaluate the contents with minimal disturbance to the sample. Compared to other methods, the use of split spoon sampling creates minimal disturbance to the sample (Horton et al., 2015).

Other sampling methods that retrieve samples from depth such as hollow stem augers or thin-walled sampler tubes require the use of an extractor method to remove material from the sampler because one cannot open the sampler during the field test. This process results in notable

disturbance to the sample and can result in inaccurate depth correlation from the extraction process. Researchers have tested the level of disturbance between various subsurface sampling methods and determined that split-spoon sampling is reliable for retrieving relatively undisturbed samples that are not broken down by the sampling or evaluation process (Horton et al., 2015)

Chapter Three: Study Area

3.1 Geography, Climate, and Flora and Fauna

The McCloud River is a prominent arm of Shasta Lake and forms regional base-level hydrology for the development of karst in the McCloud Limestone (Figure 3.1). Five major drainages flow into Shasta Lake: the Sacramento River, the McCloud River, the Pit River, Backbone Creek, and Squaw Creek. Shasta Lake is an artificial lake and is impounded by Shasta Dam. It is the largest reservoir in the state of California with a maximum storage perimeter of 111 kilometers. Shasta Lake is composed of five arms that correspond to major drainages dammed at Shasta Dam. The five arms are named by their respective drainages, with the Sacramento River arm and McCloud River arm being two prominent arms (DOI, 2013). Flowing south from Shasta Lake at Shasta Dam is the lower Sacramento River. The lower Sacramento River flows south through the Central Valley through the high population centers of Redding and Sacramento before ultimately flowing into the Pacific Ocean at the Sacramento River Delta. Redding, California at 85,000 residences is the closest population center to Shasta Lake being approximately 30 km south of the lake. Primary uses for the lake include water resources and recreation, with boating and hunting being the most popular (DOI, 2013).

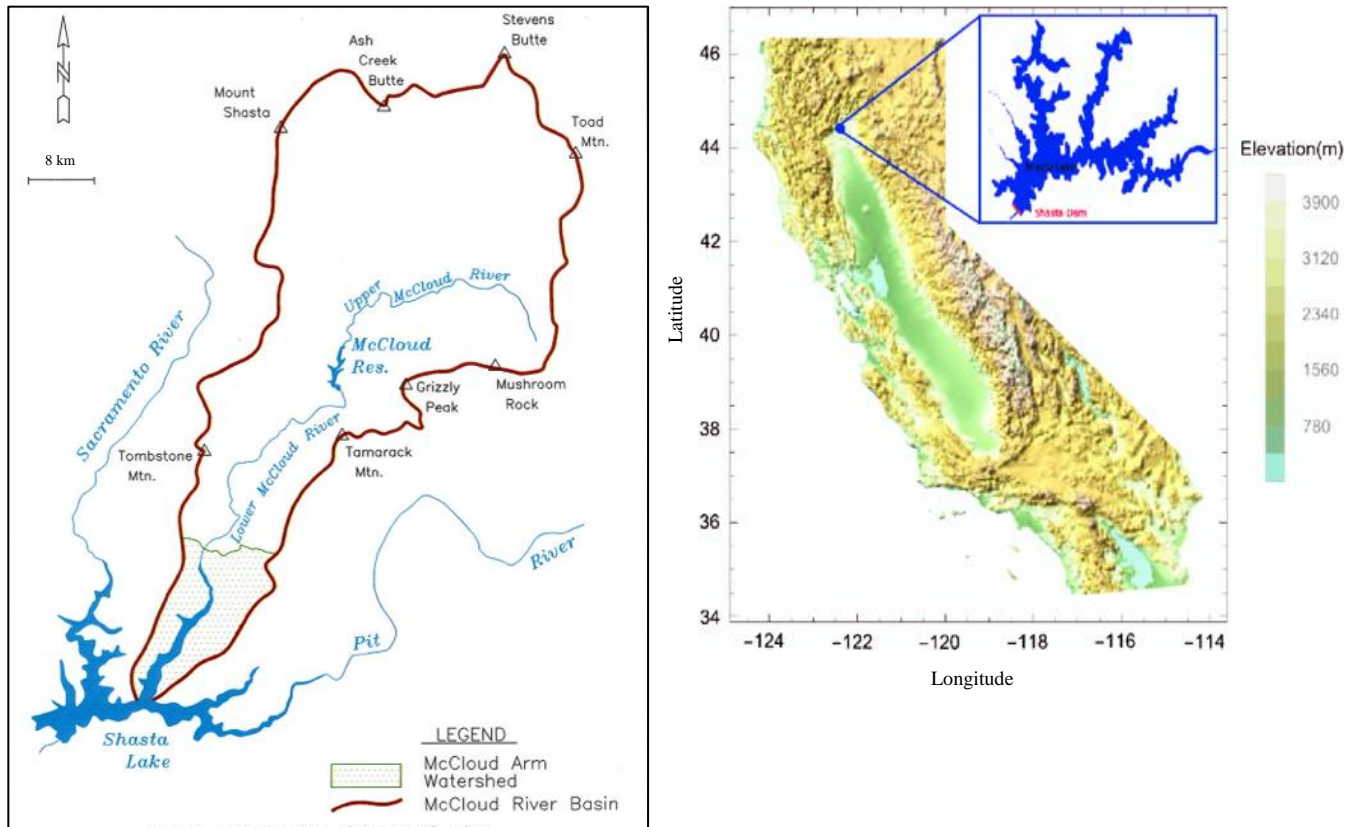


Figure 3.1: Left - McCloud River drainage basin and Shasta Lake (Source: USDA, 1998). Right - Shasta Lake in context with California geography (Source: Yang et al., 2020).

The terrain around Shasta Lake is rugged and highly dissected with steep forested hillsides (Figure 3.2). Approximately half of the slopes in the middle Sacramento River – Shasta Lake region exceed 15 percent grade (Sawyer, 2006). The Shasta Lake region is characterized by hot summers (frequently exceeding 40 degrees C) and wet, cool winters with average 1.5-2 meters of rain per year (DOI, 2013). The steep canyons and secluded forests of the Shasta Lake – McCloud River region harbor a rich biodiversity with many endemic flora and fauna (USDA, 1998). The Shasta Lake geomorphic region is composed of several vegetation types with dominant assemblages being mixed conifer, black oak and canyon live oak, and chaparral. Mixed

conifer vegetation types dominant in ponderosa pine and Douglas-fir are the most common covering approximately 40% of the landscape. Black oak and canyon live oak cover approximately 44% of the landscape in often dense, tree-sized stands (USDA, 1998). The McCloud Limestone harbors a diverse set of endemic flora and fauna including the Shasta Salamander and the Shasta Fawn Lily (North State Resources, Inc., 2010). The Shasta Salamander is only found proximal to the caves and karst landscapes of Shasta Lake and is listed as a federally endangered species. Among the Shasta Salamander and Shasta Fawn Lily, eleven bat species occupy the caves, mines, and abandoned infrastructure in the Shasta Lake region (USDA, 1998).



Figure 3.2: Photo looking south over the McCloud River approximately 200 m above Rileys Cave (Source: Author).

3.2 Geomorphic Features and Stratigraphy

Shasta Lake is positioned at the intersection of four major geomorphic provinces in Northern California - the Trinity and Klamath Mountains to the west, the Southern Cascades to the north and east, the Central Valley to the south, and Yolla Bolly and Coast Range mountains to the southwest. The Shasta Lake geomorphic region is underlain by rocks of the Eastern Klamath Terrane. Rocks of the Eastern Klamath Terrane consist of strata representing sedimentary and volcanic deposition in island arc settings from the Ordovician (~490 Ma) to the Jurassic (~145 Ma) (Albers and Robertson, 1961). The McCloud Limestone is a prominent carbonate unit in the eastern Klamath Terrane and forms outcrops in thin disjointed bands from 5 km north of Redding to 30 km south of Mt. Shasta. The McCloud Limestone predominately crops out along or adjacent to the McCloud River as it originates at the south face of Mt. Shasta and drains into Shasta Lake. The McCloud Limestone forms a major physiographic feature of the eastern Klamath Mountain terrain at Shasta Lake with the formation of well-developed epikarst and 300-meter cliffs (Albers and Robertson, 1961). Caves and karst features are common in the McCloud Limestone and are a major component of the past and current hydrogeology. Lying unconformably beneath the McCloud Limestone is the greatly deformed pyroclastic flows and tuffaceous shales, sandstones, and minor limestones of the Baird Formation of Mississippian age. The Baird Formation is almost everywhere separated by the McCloud by dikes of augite quartz diorite. Laying unconformably over the McCloud Limestone, and are commonly intruded with mafic quartz diorite, are the tuffaceous sandstones and conglomerates of the Nosoni Formation of Permian age (Albers and Robertson, 1961). The McCloud Limestone, bounded by intrusives and relatively impermeable rock, forms well developed karst and cave features at a wide range of elevations and lateral distribution.

3.3 Karst Features

Caves and karst features are widespread and well developed in the McCloud Limestone with approximately 35 known caves in a 40 square kilometer region (Despain et al., 2022). Caves in the McCloud Limestone are primarily situated above current hydrologic baselevel and are not major components of the active hydrologic regime. Caves of the McCloud Limestone generally exhibit strong phreatic and hypogene morphologies reflecting formation in both epiphreatic and bathyphreatic settings. Many of the caves exist as relict dry caves disconnected from channelized vadose action and very rarely exhibit stream-channel morphologies such as canyon-style passages. Caves in the McCloud commonly develop hypogene and phreatic morphologies such as sponge-work passage networks, broad scallops, dissolution rims, intensely varied passage size, cupolas, and isolated pendants (Despain et al., 2022; Klimchouk, 2017). Seven caves of such character are the focus of this study: Ellery Creek Cave, Tardis Cave, Pipevine Cave, Ancient Palace Cave, Rileys Cave, Lake Shasta Caverns, January Cave (Figure 1.1). The seven caves were chosen as a representative distribution of the types of passage morphologies and clastic deposits found in caves of the McCloud. This subset of caves also represents the drastic vertical distribution of cave and karst features seen in the McCloud Limestone (Figure 3.3). All the caves are hydrologically inactive except Ellery Creek Cave. Since many of the caves are hydrologically inactive, allogenic and autogenic sediments readily fill open conduits and terminate cave passages.

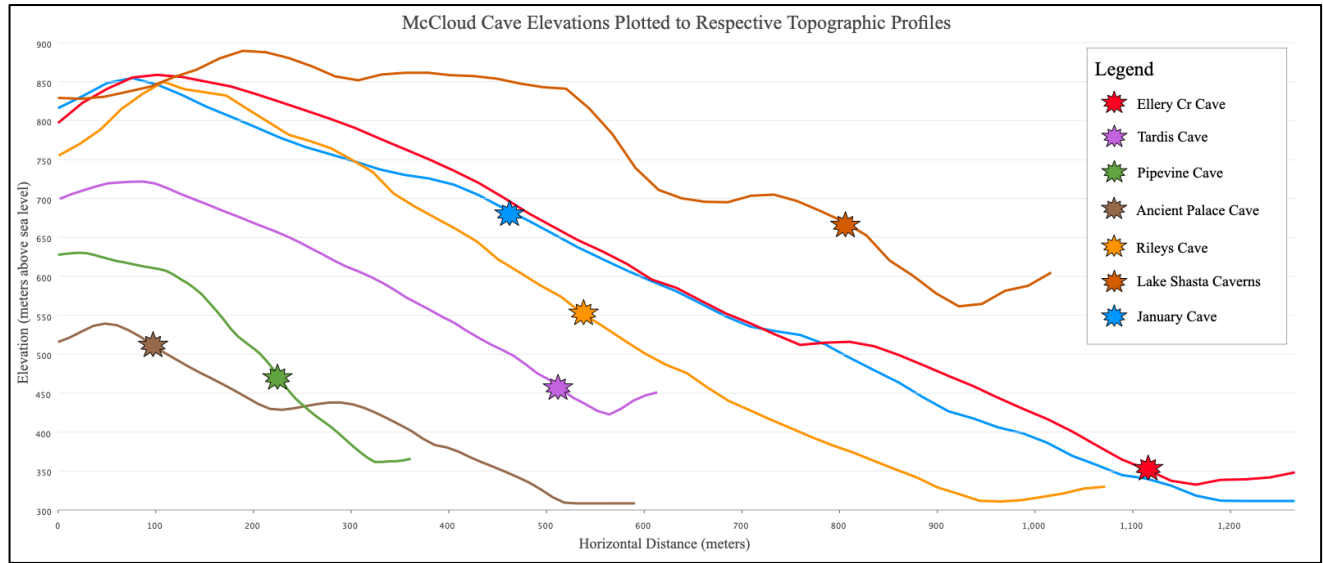


Figure 3.3: Elevations of all seven cave sites plotted to respective topographic profiles. The topographical profiles represent horizontal transects that extend from local base level of the McCloud River or pertinent tributary drainage to the crest of the adjacent ridge. The adjacent ridge represents the highest hydrology in the respective basin of each cave site (Source: Author).

3.4 Ellery Creek Cave

Ellery Creek Cave is an active flood-dominated epigene cave developed at the local base-level (~355 meters above sea level). Ellery Creek Cave is currently surveyed to 243 meters long and 18 meters deep (Figure 3.4). The cave has developed primarily phreatic flood-morphologies

such as flood-maze pockets and broad scours as well as vadose canyon incision. Clastic sediments are well distributed in Ellery Creek Cave with at least 2-meter thick fine-grained passage fills and numerous ledge and pocket fills. Ellery Creek Cave has two known entrances, numerous impassable in-feeder passages trending towards the surface, and an active fluvial input.

The upper entrance passage trends upwards from the surface and does not preserve any significant fine material. The lower entrance, however, descends steeply from surface and transports significant amount of fine-grained colluvium into the cave. The coarse fraction in the

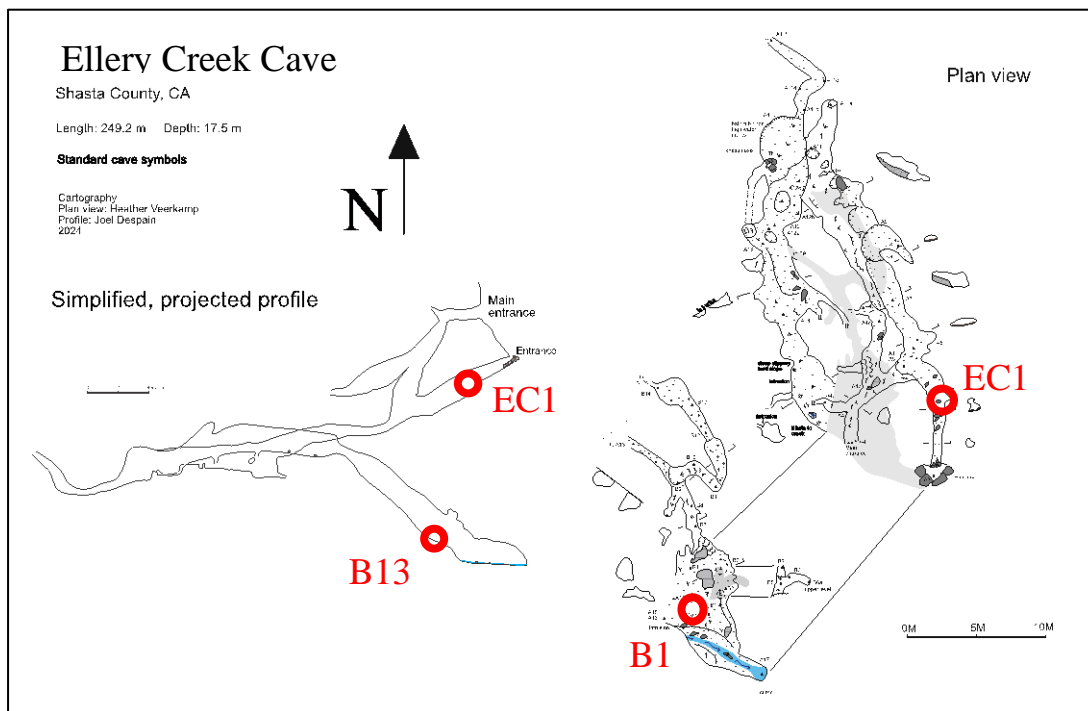


Figure 3.4: Map of Ellery Creek Cave with sample locations marked (Source: Veerkamp and Despain, 2024b).
entrance colluvium is highly angular and predominately limestone. From the entrance to the terminal sump room are numerous impassable ceiling inlets that are depositing fine-grained alluvial fans of various sizes. The constriction passage in-between the diorite passage and sump

room is floored and walled with poorly-sorted, well-rounded and strongly imbricated sands and gravels. The direction of imbrication suggests flow from the diorite passage to the sump room.

Sedimentation in the Sump Room is defined by a fine-grained passage fill that ranges from 30 cm to at least 2.3 meters thick. The total thickness is unknown. The passage fill slopes steeply (32 degrees) from the imbricated gravel deposit to the sump pool and associated drainage. In the ceiling of the sump room are two, 1-m wide, 2-3 m tall ceiling in-feeders that terminate in fine-grained sediment plug. A small drainage enters the sump room out of numerous small holes along the western wall and flows for ~4 meters across the floor of the passage until forming a sump-pool. The bed of the stream is cut into a fine-grained passage fill that is at least two meters thick where the stream enters the passage. Suspended and bedload transport is likely entering the passage through the numerous wall inlets. A ~10 cm bed of charcoal is exposed at the base of the sump room fill adjacent to where the channelized flow has incised into the fill (Figure 3.5).

The channelized flow appears to be incising into the charcoal bed and redistributing material throughout the passage during floods. The two primary outlets for the cave are the downstream sump in the sump room and impassable floor drains at the base of a bedding headwall in the heavily bedding-controlled pothole passage. Large floods in the sump room are likely eroding the fill at a faster rate than is being deposited. Organic material is common in the entrance passages as surface detritus intermixed with colluvial debris. Organic material including

charcoal and woody fragments are common in the lower sump room and are discussed in detail in the later sections.

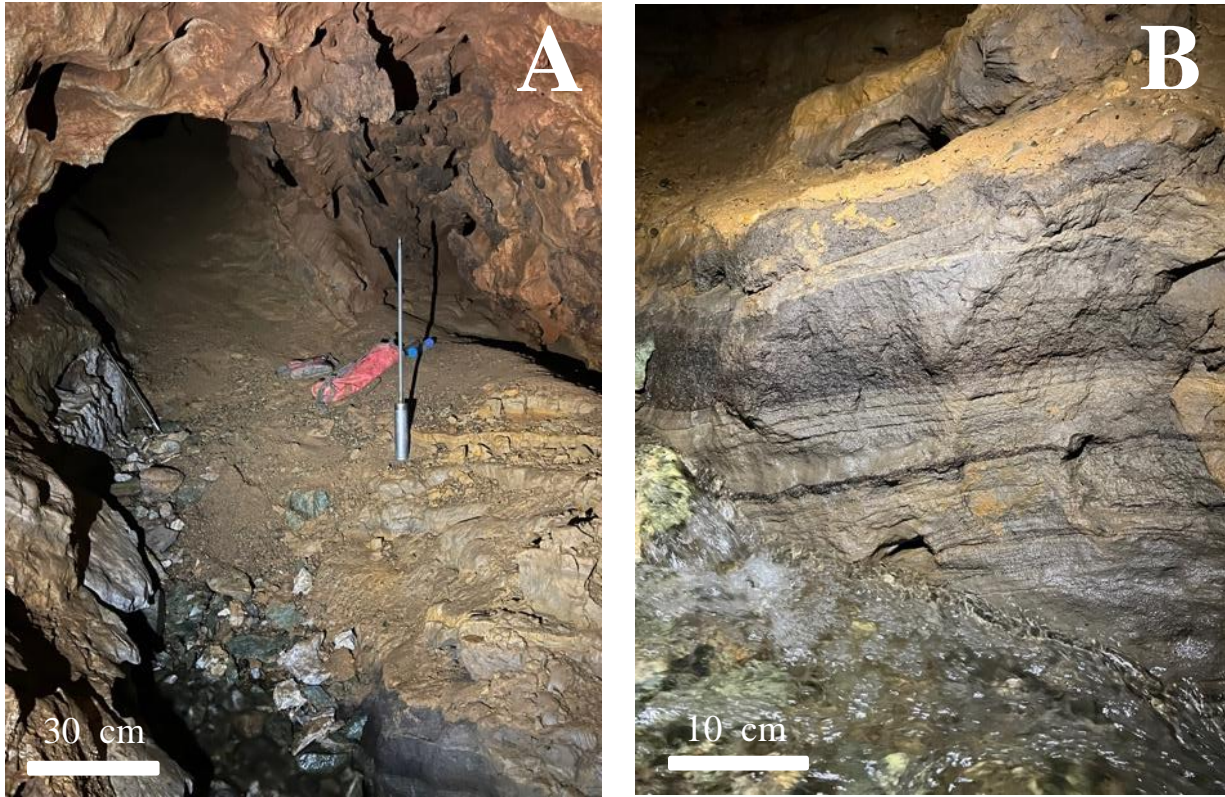


Figure 3.5: A – Sump room passage fill and Boring 13 location. B – Massively bedded and thinly-laminated 1-8 cm charcoal beds at the base of the passage fill (Source: Author).

3.5 Tardis Cave

Tardis Cave is a single-level, bedding and joint controlled maze cave situated approximately 50 meters above local base level (~455 meters above sea level). The cave is currently surveyed to 866 meters and 5 meters deep (Figure 3.6). Tardis exhibits many morphologic features that suggests fluvial influence through stream piracy, paragenetic shielding, and anastomotic flood development. Paragenetic shielding occurs in Tardis Cave as clastic sediments shield bedrock from downwards incision (Farrant and Smart, 2011). Sedimentation in Tardis is ubiquitous and diverse in texture with rounded-gravel wall pockets and 1-2-m thick sequences of silt-sand passage fills. Tardis Cave has two open entrances and at least two suspected collapsed or plugged entrances.

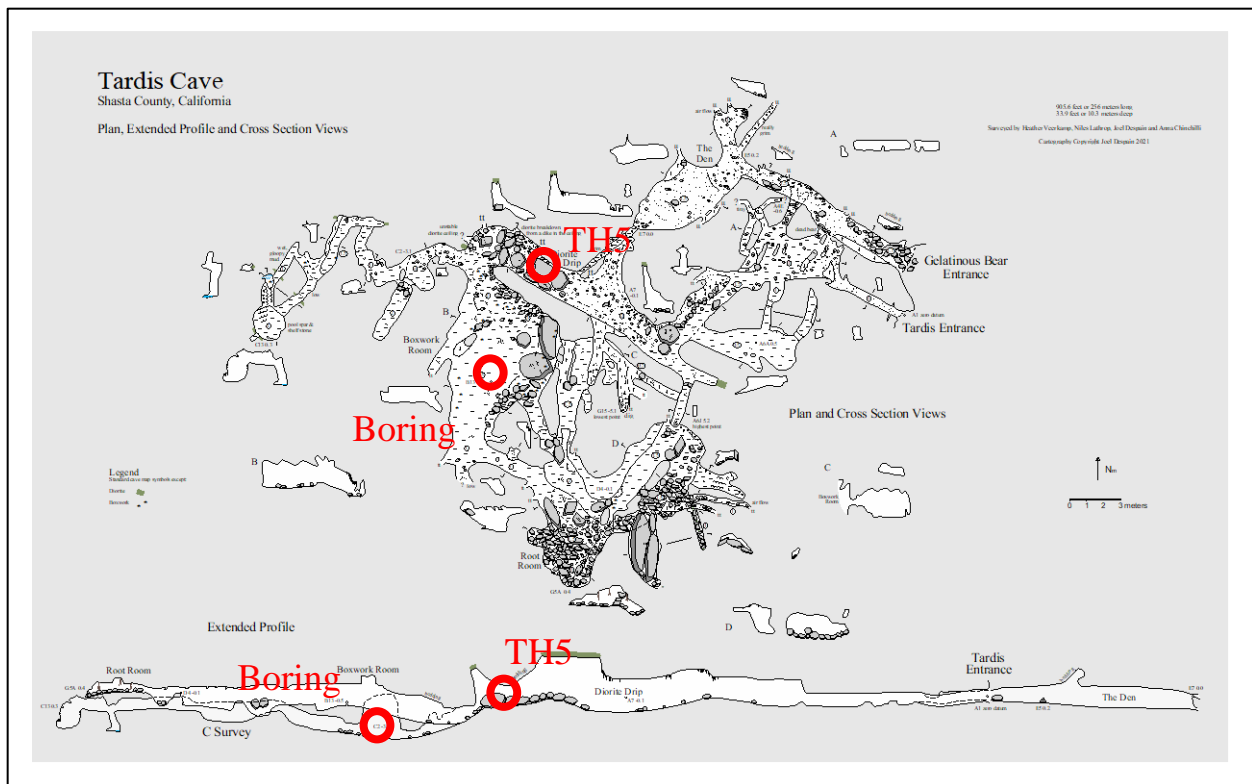


Figure 3.6: Map of Tardis Cave with sample locations marked (Source: Despain, 2022c).

Passages in Tardis are shallow with most passages forming within 30-50 m from the surface. Above the cave is a relatively flat bench with well-developed clints and grikes and moderate soil-cover. Multiple impassable voids exist that appear to trend down towards the cave. The epikarst drains express in the cave as ceiling inlets depositing alluvial fans throughout the cave. Material in the fans is predominately angular, poorly-sorted, organic-rich, and mostly altered diorite and chert.

Sedimentary outlets are common throughout the cave, with the primary active outlet being at the southern end of the Boxwork Room. The outlet in the Boxwork Room funnels down to an impassable bedrock drain. Paleo-outlets are present throughout the eastern and southeastern edges of the cave through the two current entrances and numerous impassable voids at the eastern margin. Outlets are numerous but do not appear to be focused or concentrated.

Epikarst inlets provide angular, poorly sorted material that form alluvial fans and mounds and paleo flood inlets. Clean bedrock floor is uncommon in the cave. Passages nearest to the entrances and the suspected collapsed western entrance are partially broken-down and floored with cobble to boulder-sized breakdown. The central dike room preserves primarily epikarstic infiltrate from two impassable domes and eroded fragments of a diorite intrusion. The alluvial room immediately west of the dike room is floored and partially filled with a 3-5 m wide, 1-meter-deep alluvial fan.

Primarily along the western wall of the Boxwork Room and progressing westward are ledge deposits of imbricated and well-rounded sand and gravel (Figure 3.7) The ledge deposits range in thickness from a few centimeters to a meter thick and extend from the alluvial room to

the southwestern breakdown room. The ledge deposits are typically associated with horizontal paragenetic notches that can extend upwards of a meter into the bedrock.



Figure 3.7: Paragenetic notch with associated rounded and imbricated sand and gravel (Source: Author).



Figure 3.8: Joint-controlled passage with horizontal notches at multiple levels (Source: Author).

The paragenetic notches form at multiple levels in the central portion of the cave (Figure 3.8). Suspected paleo-flow direction based on imbrication direction is approximately southwest to northeast.

The southwestern passages terminate in the root room and breakdown collapse. The root room is characterized by dense root infiltration through enlarged joints and fractures in the ceiling. At the opposite end of the cave, clastic material is intermixed with cobble-sized limestone breakdown. The fine clastic material in the bear den room is hard-packed and minimally disturbed and partially coated in calcite and organic crusts. Organics are common throughout Tardis Cave as root thickets, entrance and epikarst debris, and animal refuse.

3.6 Pipevine Cave

Pipevine is a joint-controlled and steeply-dipping fissure cave situated 75 meters above local base-level (~470 meters above sea level). Pipevine Cave is currently surveyed to 98-meters long and 56-meters deep (Figure 3.9). Pipevine is made up of three large-volume, steeply descending chambers connected by near body-size passages (Figure 3.10). Most of Pipevine Cave is devoid of clastic sediment besides a 4+ meters thick deposit of well-stratified clay, silt, and sand in the lower chamber. The exposed deposit is made up of a stratigraphically and structurally complex assemblage of multi-facies fine sediments. Soft-sediment deformation and micro-faulting is common in the exposure and sediment facies vary dramatically by color and fine-particle texture (Figure 3.11). The few pocket deposits throughout the pit series are made of fine-grained allogenic material and calcite fragments.

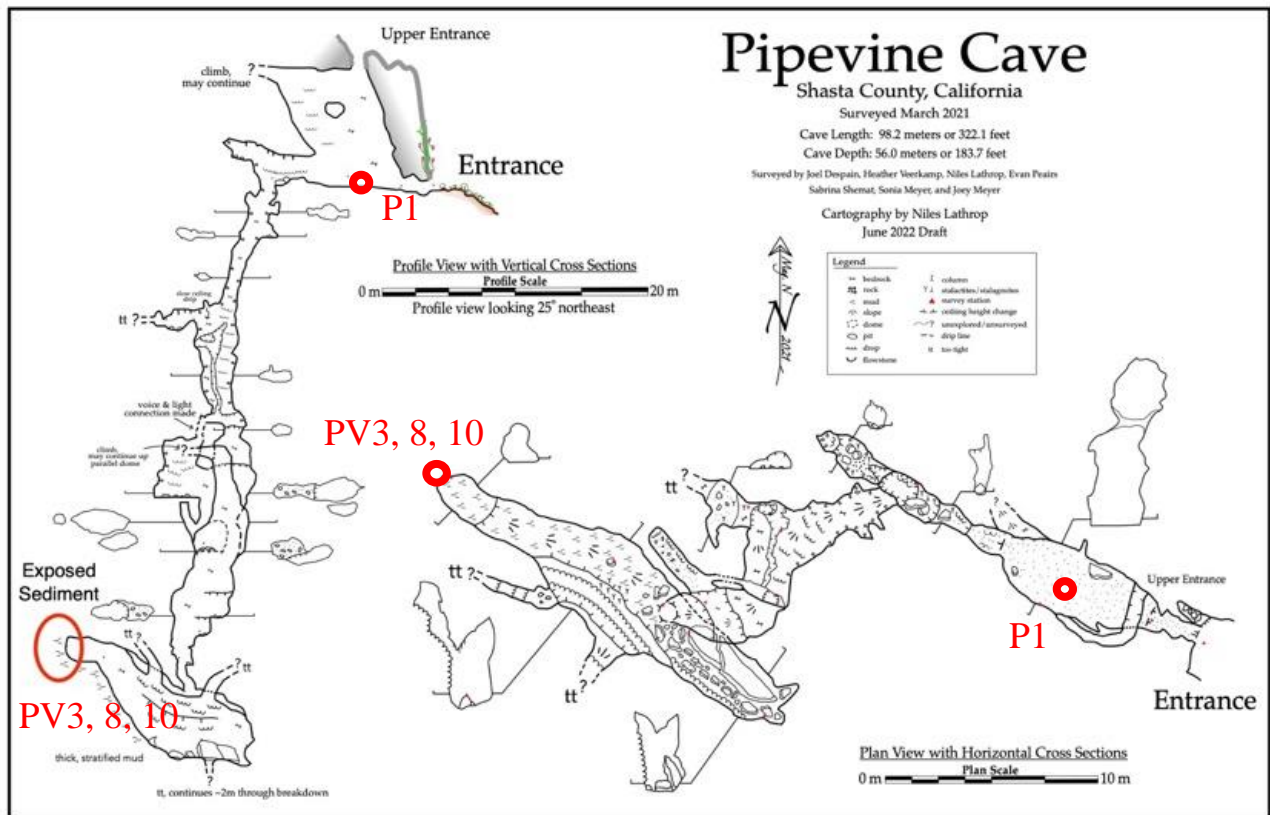


Figure 3.9: Map of Pipevine Cave with sample locations marked (Source: Author).



Figure 3.10: Photo of descending pit series and thin bedrock partition in-between ceiling rises. (Source: Author).

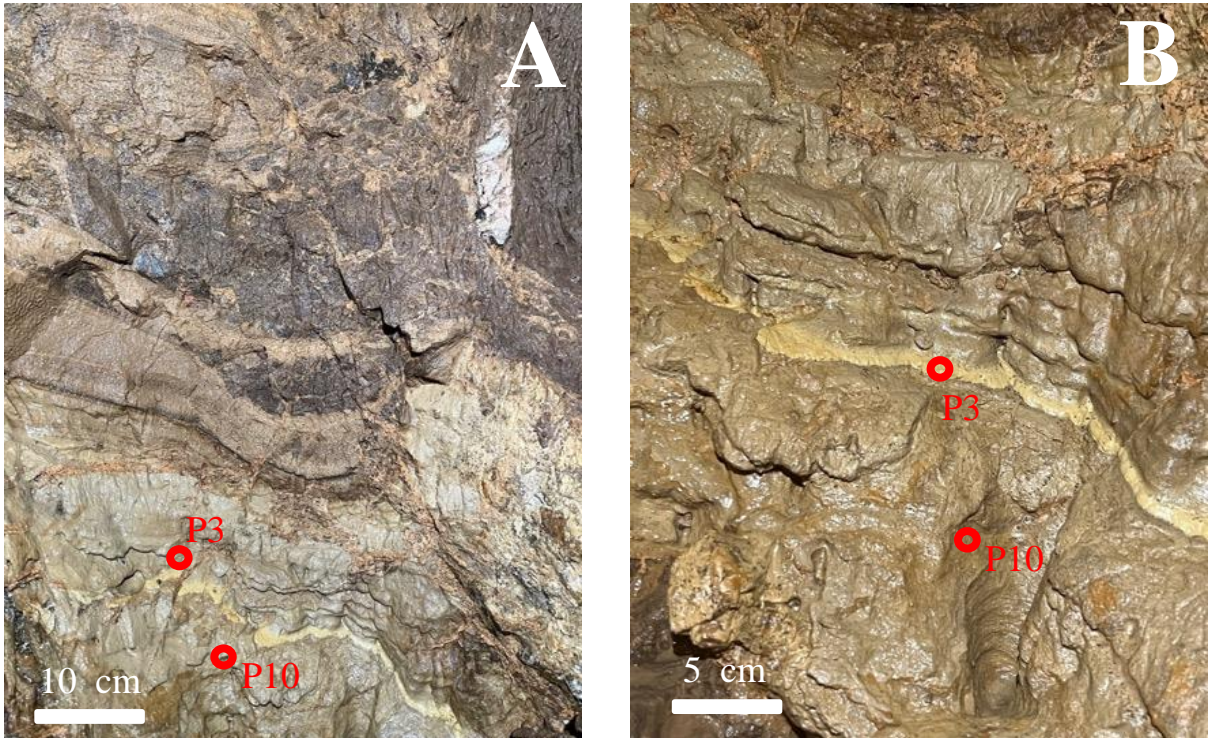


Figure 3.11: A – Exposed stratigraphy at the north end of the lower chamber with sample locations marked, B – Close-up of the P3 white fines and P10 yellowish brown fines (Source: Author).

Current sedimentation in the cave is dominated by epikarst fissure infiltration and entrance colluvium. The cave-entrance room is situated in a cliff-forming knob with up to 3-meter-deep epikarst fissures above the cave. The highest entrance to the cave developed between epikarst pinnacles approximately 10m above the primary entrance. Entrance-room sedimentation is predominantly organic-rich, sandy silt with a of trace limestone breakdown. Minor epikarst overprinting is apparent in the first pit with a series of 20-40 cm-deep, stair-stepping incisions on the floor of the down-trending phreatic passage. No other inputs for clastic sediment are apparent in the remaining depth of the cave other than a high ceiling passage in the lower chamber, although this passage ends in calcite plug and input significance is unclear.

The primary output for the cave is at the lowest point in the lower chamber through multiple drain points below and adjacent to the breakdown floor. Accommodation below this output must be significant enough to have stored the volume of fine-grained material that existed in the lower room, assuming it was full to the point where horizontal beds are exposed at the top, northern end of the deposit. The cave does not have obvious resurgence point(s) on the surface. Organics are uncommon throughout the cave except for minor roots and animal refuse material in the entrance room.

3.7 Ancient Palace Cave

Ancient Palace Cave (APC) is a large-volume cave situated 210 meters above local base level (~510 meters above sea level). The cave is currently surveyed to 714 meters long and 34 meters deep (Figure 3.12). APC is composed primarily of one large (150 m x 50m footprint) chamber and dispersed side passages of varying sizes (Figure 3.13). The cave exhibits hypogene morphologies such as ramiform passage geometry, broad scallops, drastic passage-size differences, and sudden large-scale passage terminations.

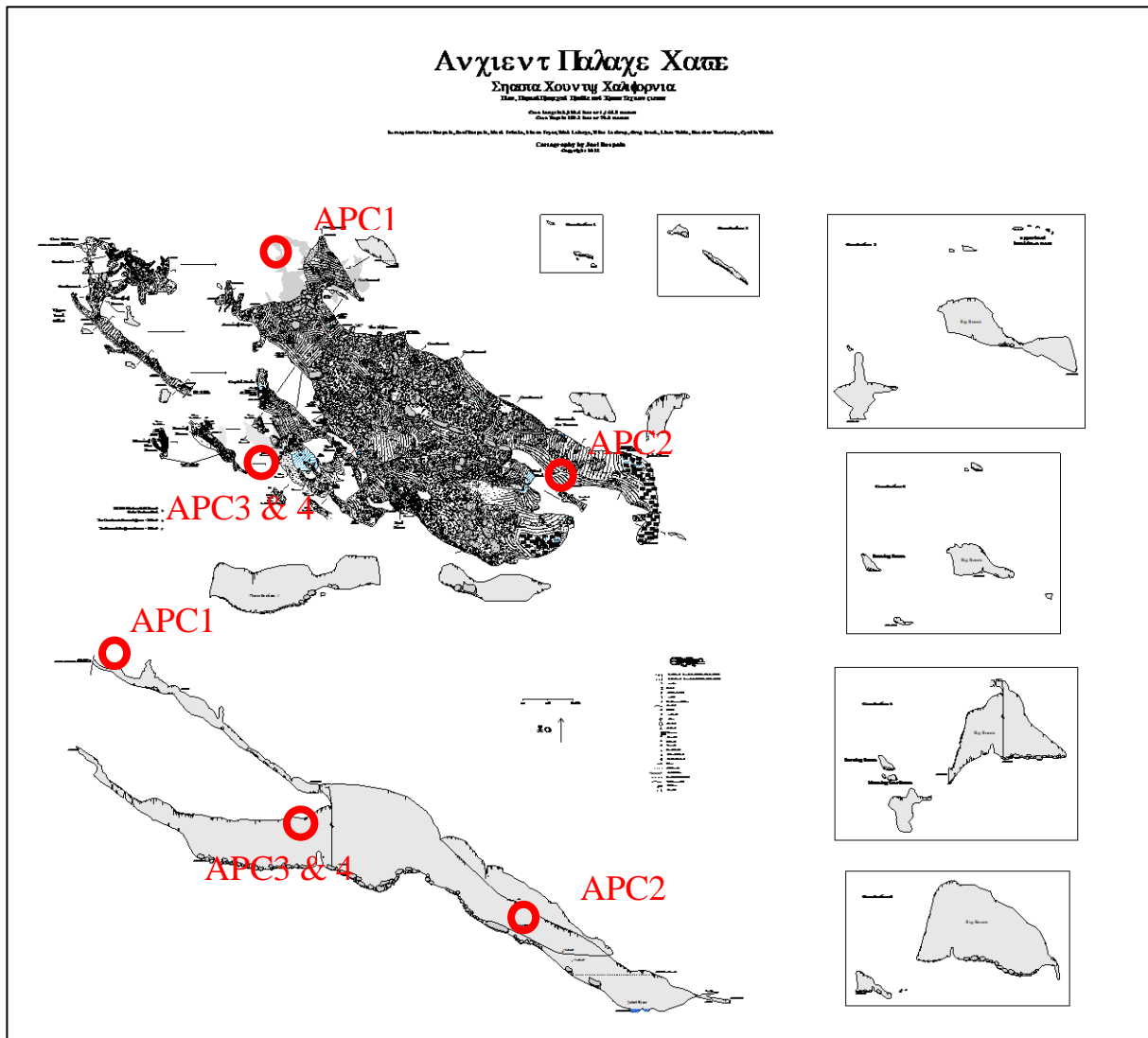


Figure 3.12: Map of Ancient Palace Cave with sample locations marked (Source: Despain 2022a)



Figure 3.13: Photo of the large-volume lower chamber with extensively calcified breakdown. (Source: Dave Bunnell, 2022).

Besides cave-entrance infiltrate, APC preserves exclusively very-fine grained sediment deposits and extensively calcified breakdown (3.14). Ancient Palace Cave has one known inlet from the surface and no obvious outlet. Entrance passages quickly trend into the outcrop and clastic sediment coming in from the entrance and remains within 30 m of the entrance. The upper levels of the cave do not appear to have any current or paleo-inputs for clastic material. The lower-level chamber and associated side passages have no known active inputs or outlets. The lower portions of the main chamber in the Jaded River and southwestern branch terminate in bedrock closure, stagnant pools, and/or calcite blockage. The stagnant pool at the Jaded River



Figure 3.14: Photo of ubiquitous red clay and calcified breakdown in the lower chamber of Ancient Palace Cave (Source: Author).

passage forms a sump-like termination, but the passage does not appear to continue. The northern section of the room trends towards the surface and breakdowns but there are no clear signs that it is a collapsed entrance. Void space within the breakdown could lead to unknown outlets for clastic sediments but there are no clear signs of this.

Clastic sediments in APC are primarily distributed in the entrance passage and throughout the margins of the lower chamber room. Sediments are predominately silt to sand-sized in the entrance passage and clay to silt sized in the lower chamber room. There are no clear deposits of material coarser than sand in the cave other than cave breakdown. The fine-grained clastics in the lower chambers and adjacent rooms are predominately clay-sized and well-laminated. The bulk of the fine-grained clay is well distributed throughout the lower portions of the cave and forms breakdown coating and massive deposits upwards of 15 cm thick.

The calcite-coated breakdown in the lower chamber is commonly coated in thinly laminated dark red clay that can be upwards of eight cm thick. The central portion of the breakdown floor, however, does not preserve any fine-clastic material on the surface. It appears epikarstic drips from the central portion of the ceiling is transporting clay coatings below the breakdown. This is substantiated by the fact that thickest clay deposits are preserved within and below the breakdown.

3.8 Rileys Cave

Rileys Cave is a relict maze cave situated approximately 235 meters above current base level (~550 meters above sea level). Rileys Cave is currently surveyed to 316 meters long and 20 meters deep (Figure 3.15). The cave exhibits many prominent roof pendants and anastomoses, sediment false floors, channelized epikarst vadose flow, and in-cave sediment sinks, indicating a dynamic sedimentation history (Figure 3.16). Clastic deposits in Rileys Cave are present in almost all known passages and range from well-sorted fines to poorly sorted sands and gravels.

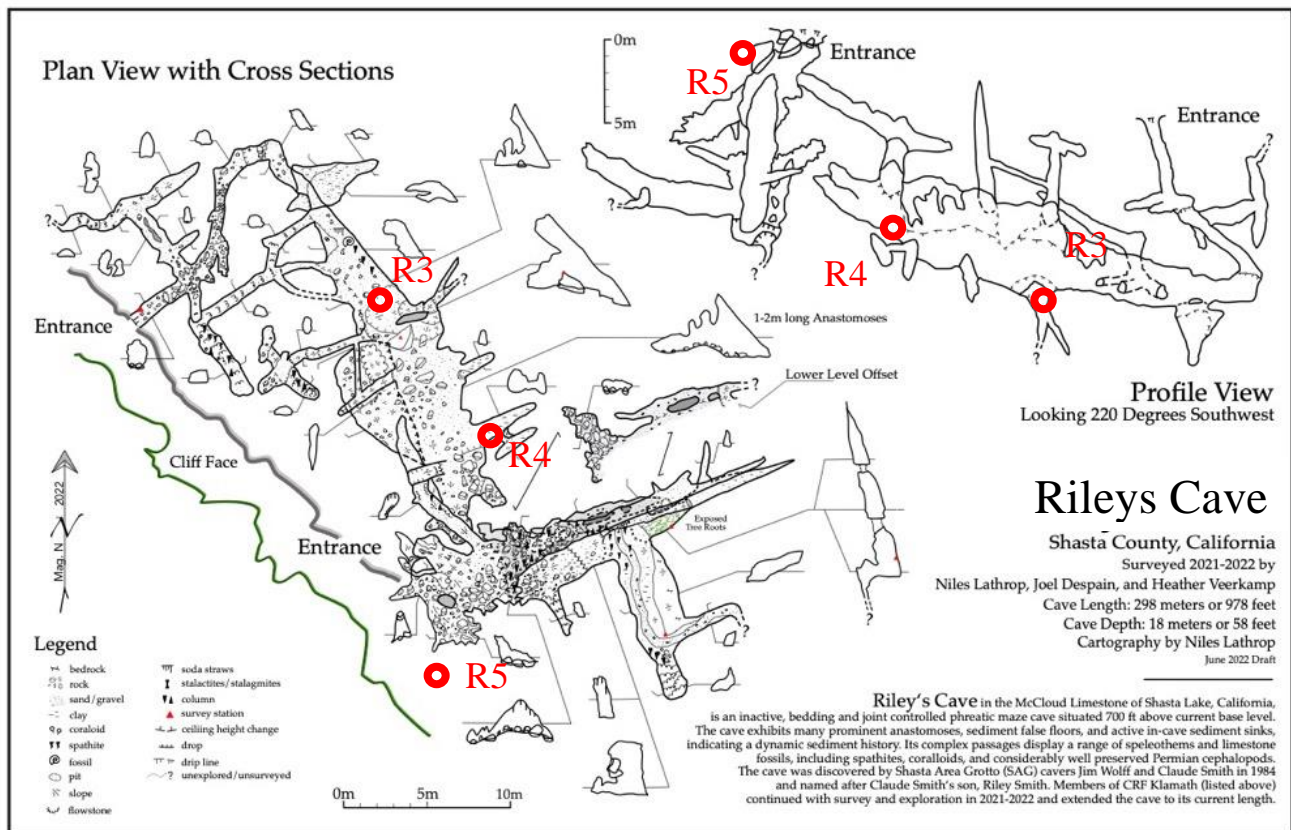


Figure 3.15: Map of Rileys Cave with sample locations marked (Source: Author).

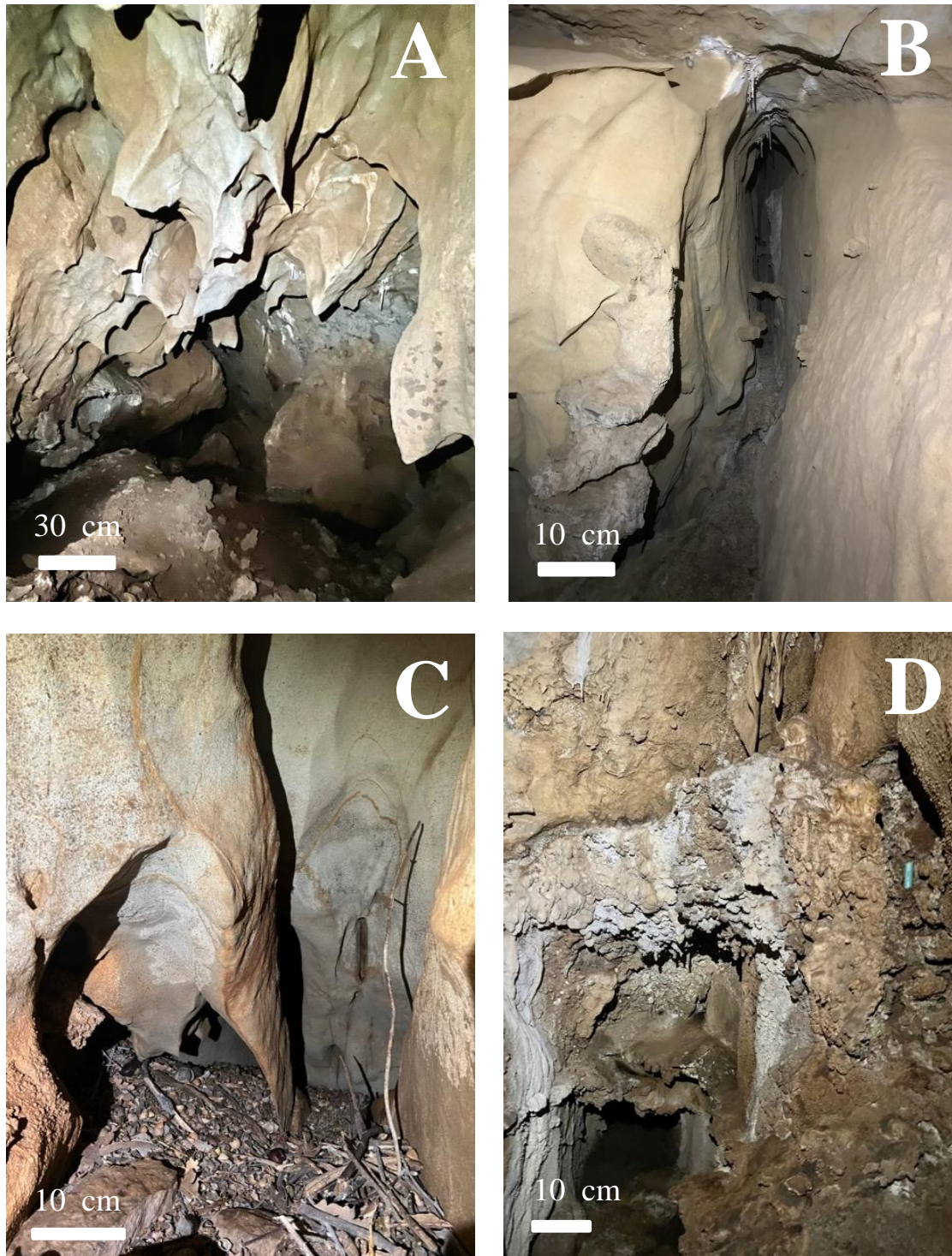


Figure 3.16: A – 1-2-m-deep roof pendants at southern end of central chamber. B – Joint-controlled elliptical passage in the ceiling of the longer chamber. C – Roof pendant/ceiling fin in the northern passages. D – Heavily calcified wall pocket and sample R4 sampling location (Source: Author).

Very little exposed bedrock floor is common in the cave and passages often terminate in passage fills with silt to sand-sized sediment.

Grain transport and sorting is apparent in the southern and central chambers by channelization of epikarstic water. Two channelized flows end in passage-sized in-cave sinks that actively provide clastic sediment to underlying voids with accommodation space. The sediment sinks have accommodated a significant amount of clastic material as numerous high paleo-fill levels are present throughout the cave. The southern rift passages preserve three separate sediment 'false floors' representing three distinct paleo-fill levels.

Sedimentary outputs on the surface are unclear as there are no clear springs or resurgence points of channelized epigenic flow. Clastic input is present through multiple active and collapsed entrances leading to widespread colluvial sedimentation. The upper level, bedrock-collapse sinkhole entrance provides colluvial input to the southern and central passages. Organic material is common in the cave but is generally limited to fragments of vegetation and animal refuse. Weathering products and/or authigenic sediments are not readily visible throughout the cave.

3.9 Lake Shasta Caverns

Lake Shasta Caverns (LSC) is an extensively modified multi-cave system situated approximately 340 meters above base-level (~662 meters above sea level). The cave is currently surveyed to 1,440 meters long and 68 meters deep (Figure 3.17). LSC is largely composed of at least three separate large-scale voids connected through a series of man-made tunnels excavated for show cave infrastructure. The cave preserves both well-rounded, poorly-sorted and imbricated gravels as well as fine-grained weathering products and pocket deposits of predominately fine-grained material.

The cave has one known natural entrance and no obvious current or paleo outlets. Below the current natural entrance is a potential collapsed entrance. The collapsed entrance area preserves higher volumes and diversity of clastic material compared to the remaining portions of the cave. In the upper portions of the cave, enlarged joints and impassable ceiling inlets could extend up to the epikarst and provide clastic material to the cave, but these inlets are unclear. Overall, the cave descends steeply from the natural entrance and passages are often 50 to 80-meters below the surface.

Clastic sediments in Lake Shasta Caverns are varied in mineralogy and texture. The dramatic modification that has occurred in the cave has both disturbed and redistributed some of the fine-grained clastic materials, although many undisturbed deposits still exist. A vast majority of the clastic material in the cave is preserved in the Signature Room, Basement Room, and Spider Complex. Very little clastic material is preserved elsewhere. The material preserved in these areas is predominately well-rounded and poorly-sorted sand and gravel and well-stratified silt. In many cases the sand and gravel deposits are well-stratified and imbricated in a consistent

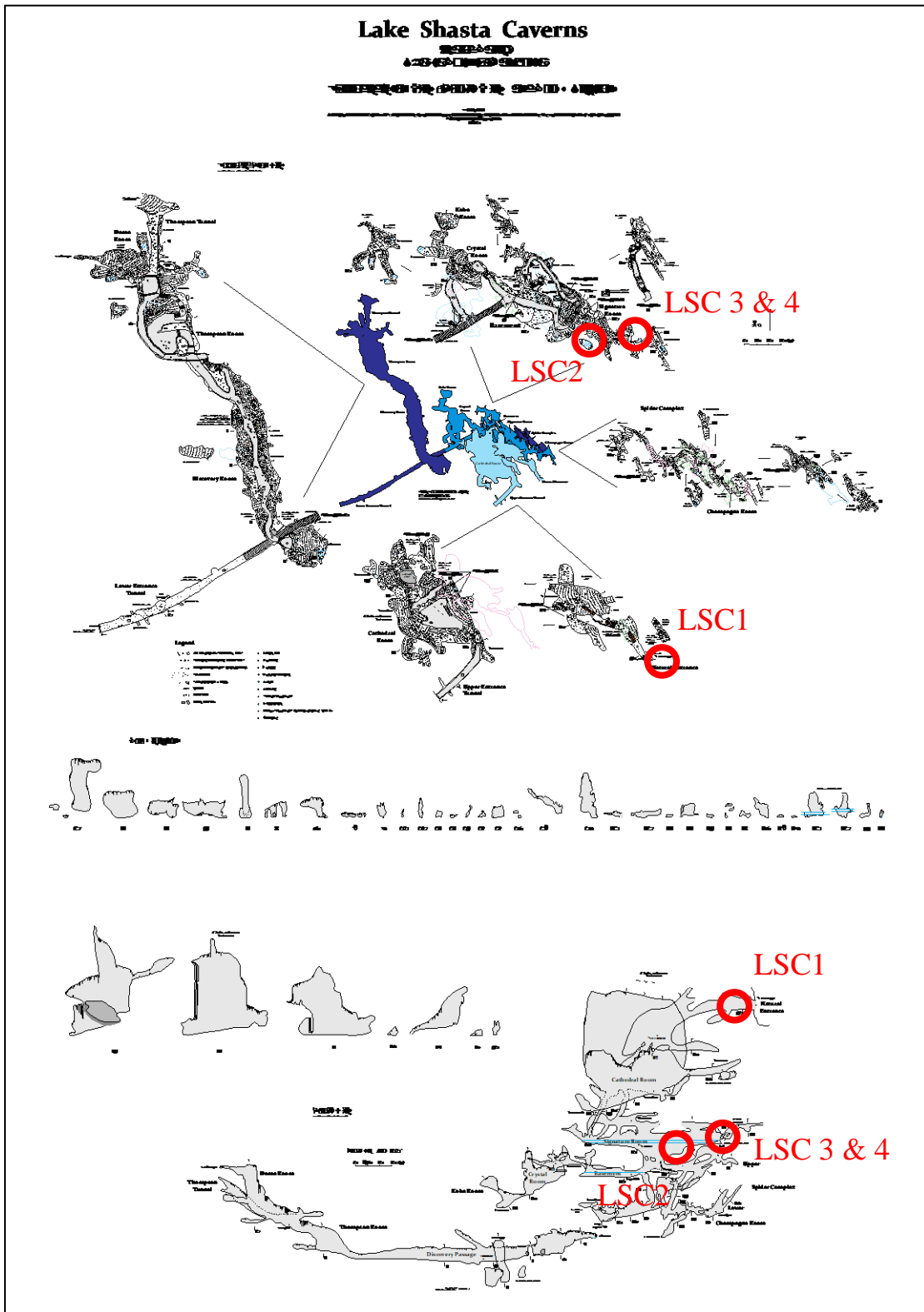


Figure 3.17: Map of Lake Shasta Caverns with sample locations marked (Source: Despain, 2022b).

direction (Figure 3.18). The direction of imbrication is generally southeast to northwest and from the potential collapsed entrance towards the interior portion of the cave.

The largest volumes of coarse, gravel-sized material are in the Signature Room and ceiling of the Champagne Room in the Spider Complex, is directly below the Signature Room. Coarse material in these rooms is typically capped by well-stratified, silt-sized material. In two observable instances, the silt-sized material is predominately tephra that has altered to halloysite and Fe-Mn imogolite-allophane. The tephra is strongly associated and interbedded with fluvial sediments so was therefore likely transported via fluvial processes (Figure 3.18).



Figure 3.18: Well-stratified and kaolinized tephra and fine clastics deposited over well-imbricated and well-rounded sand and gravel (Source: Author).

3.10 January Cave

January Cave is a hydrologically inactive cave developed at approximately 365 meters above local base level (~687 meters above sea level). January Cave is currently surveyed to 186 meters long and 31 meters deep (Figure 3.19). The cave exhibits many prominent phreatic and hypogene speleogens and preserves exclusively fine, stratified clay deposits similar to those encountered in Ancient Palace Cave. Sedimentation is dominated by entrance colluvial input and minor epikarst infiltration. No obvious inputs are apparent in the lower portion of the cave. The primary entrance for input was collapsed at the time of discovery and a small open hole was excavated to form the passable entrance.

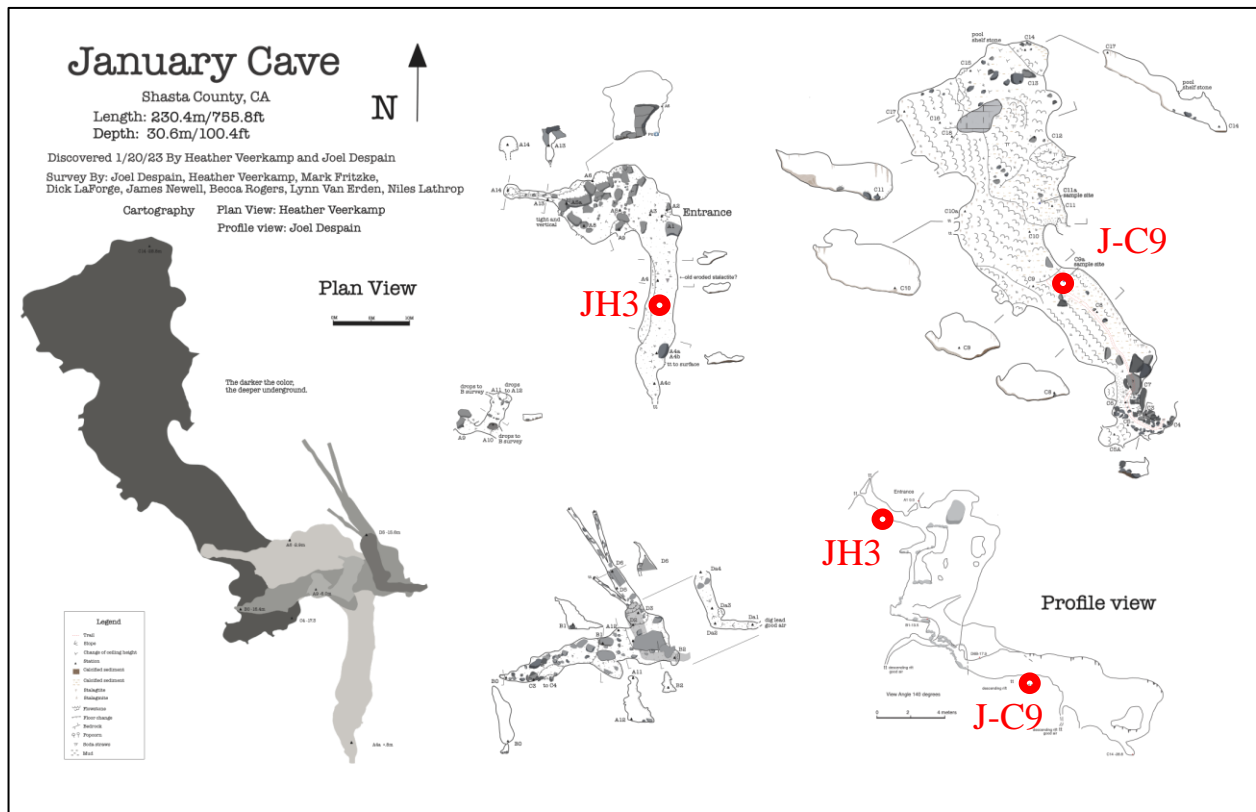


Figure 3.19: Map of January Cave with sample locations marked (Source: Despain and Veerkamp, 2024a).

Clastic material is well-distributed throughout the collapsed entrance room and lower chamber with only minor clastic materials observable throughout the middle-level passages. Clastic material in the entrance room is primarily coarse grained and angular and composed of angular limestone gravel and cobbles (Figure 3.20A). Fine-grained material is present as a matrix and is mostly coarser silt to sand-sized. The volume of clastic material in the collapsed entrance room is minimal compared to the high volume of clay and silt-sized clastic material in the lower chamber (Figure 3.20B).

The fine-grained, predominantly clay-sized fill in the lower chamber is well-laminated and often heavily coated in calcite and structurally disturbed. Cobble-sized fragments are often rotated and out-of-place from original horizontal deposition (Figure 3.20C and D). The lower chamber descends steeply to the north and terminates in passage fill. Two outlet points are apparent in the lower chamber although one is entirely bedrock and does not appear to be providing considerable accommodation. The other is small scale and does not appear to be active. Organic material is prevalent in the southern portion of the lower chamber as thinly-spaced root masses.



Figure 3.20: A – Angular limestone and diorite gravel and cobble in the entrance passage. B – Lower chamber with heavily-calcified and deformed dark red fine clay. C & D – Finely-laminated dark red clay in the lower chamber (Source: Author).

Chapter Four: Methods

A variety of field and lab methods are employed in this study to characterize the provenance, distribution, and transport mechanisms of clastic sediments in caves of the McCloud Limestone. Clastic sediment provenance was studied by applying clay mineral XRD to entrance, surface, and in-cave samples and establishing source relationships and trends. The distribution of clastic material was studied through detailed cave mapping and georeferencing of sample locations, as well as a detailed evaluation of inputs and outputs of each cave study site. Lastly, the transport mechanisms of clastic material were studied using grain size distribution characteristics, stokes law, and statistical relationships to evaluate the significance of median grain sizes between groups of samples. Core-sampling and grab sampling techniques were utilized to retrieve samples prior to analysis.

Samples were extracted using a combination of core-sampling techniques and traditional stratigraphic methods such as grab-sampling. Core sampling was conducted using a self-driven split-spoon sampler to depths of one to two meters and hand sampling included grab sampling. Core sampling was conducted in Ellery Creek Cave and Tardis Cave. Sub-samples were taken from the cores for investigating specific strata or representative sections. Sub-samples were taken from cores in a systematic manner. Sub-sampling generally occurred at the base of the boring and towards the middle of the boring for each boring selected for in-depth study. Grab-sampling at exposed sediment faces was conducted in the remaining five caves (Rileys Cave, January Cave, Ancient Palace Cave, Tardis Cave, and Lake Shasta Caverns) with heavy-duty plastic sample bags and clean sampling implements. Core and grab sampling locations were chosen to represent the gross sedimentological character of a particular deposit. The author chose sampling locations that appeared representative of sediment grain size and texture, apparent

mineralogy, color, and sedimentary structures. In general, sampling locations between each cave represented similar depositional environments, whether it be from clear deposits of entrance facies or clear deposits of interior facies. Munsell color notation was noted on all wet samples during the in-field sample description process (Munsell, 2020). After sample collection, sample locations were surveyed and georeferenced using a high-accuracy laser distometer. Samples were taken to Western Kentucky University at the end of the Summer 2023 for grain size analysis and mineralogical study.

Lab techniques employed in this study were grain-size analysis, X-ray powder diffraction (XRD), and scanning and transmission electron microscope (SEM) with electron dispersive spectrometry (EDS) capability. Clastic-sediment mineralogy was evaluated using clay mineral XRD and SEM-EDS. Clay mineral XRD samples preparation procedures and data interpretation followed methods outlined by Poppe et al. (2001) and Moore and Reynolds (1997). Clastic sediment transport mechanisms and paleo-hydrologic conditions were studied using particle-size distribution and related statistical analysis. Particle-size distribution was conducted on the <2 mm fraction using a Malvern Mastersizer 2000 and ASTM sieve methods were employed for the >2 mm fraction (Gee and Or, 2002). Particle-size statistics as described by Folk and Ward (1957) were employed using Gratistat v8 to describe depositional conditions and transport mechanisms (Blott and Pye, 2001). Gratistat v8 is an excel-based program for calculating grain size statistics such as mean, median, sorting, skewness, and kurtosis using moment and Folk and Ward methods.

Grain size relationships were evaluated for statistical significance using the non-parametric Kruskal-Wallis ANOVA (KW) and Dunn's and Mann-Whittney U (MWU) tests calculated in OriginPro (Blott and Pye, 2001; Dunn, 1964; Kruskal and Wallis, 1952; Mann and

Whitney, 1947). Detailed cave maps were generated as a framework for evaluating clastic-sediment distribution and to evaluate cave morphology. Through comprehensive mineralogical and particle-size analysis on clastic cave sediments in the McCloud, patterns of depositional energies and paleo-hydrologic conditions emerged that characterized the paleo-hydrologic controls on speleogenesis in the polygenetic karst of the McCloud Limestone.

The set of chosen methodologies complement each other to characterize clastic-cave sedimentation and develop relationships between cave genesis and sedimentation source and process. These relationships aid in understanding the links between deposits of clastic material to modes of paleohydrology and cave development. Statistical and qualitative data were used in combination to determine classifications, sediment origin, and speleogenetic interpretation.

4.1 Split-Spoon Sediment Sampler

This sample retrieval method utilizes a hand-driven split-spoon core sampler to retrieve minimally disturbed cave sediment cores from depth. This method is in contrast to invasive and time-intensive trenching techniques as often used in cave sediment research (Stratford, 2011; Sasowsky, 2007). In addition, these methods aid in the extraction of deeply-buried sediments when exposed stratigraphic sections are not present. The goal with this type of sampler was to retrieve samples quickly and efficiently from depths of 2+ m with minimal disturbance. The sampler itself is a 61-cm long, 6.3-cm outside diameter split-spoon sampler fit with plastic liners. The sampler is self-driven using a 9 kg direct-cone penetration slide-hammer with 1 m extension rods. To remove the sampler from depth, the operator uses the slide-hammer and assorted hand tools. To advance the sampler further and maintain the integrity of the boring hole, a hand-driven auger with extension rods is used. The sampler is lined with plastic sleeves for retrieving sealed,

undisturbed samples for subsequent lab analysis. The general procedure for this style of hand-driven sampling is well understood and utilized across many disciplines (Carter and Bentley, 2016; Black and Raines, 1978), but little research exists on use of percussion-style sampling in a cave setting (Bailey and Thomas, 1987). The use of split-spoon sampling facilitated the retrieval of undisturbed samples from depth and allowed for the evaluation and logging of cave sediment materials during in-field sampling.

4.2 Grain-Size Distribution

This study utilized laser diffractometer and grain size analysis via standard sieving to aid in interpretation of the depositional energy and paleo-hydrologic patterns between cave deposits. Cumulative grain-distribution plots are commonly used by geologists and engineers to evaluate sedimentological processes and strength of materials (Gee and Or, 2002). Grain-size distribution has been utilized in cave-sediment research to reconstruct paleo-hydrologic conditions and flood recurrence intervals (Herman et al., 2012). Bivariate plots are commonly used in classical sedimentology and cave sedimentology to evaluate patterns of deposition and transport (Nehme et al., 2014; Trappe, 2010; Myceilska and Ludwikowska, 2011; Shackley M., 1972; Folk and Ward, 1957). Grain size or particle-size analysis is a measure of the size and distribution of grain sizes in a sediment sample. Grain sizes in a sediment sample can vary dramatically from submicron clay particles (<1 micron) to boulder size (>0.25 meters). Fine particles less than 2000 microns are subdivided into three categories – sand, silt, and clay. Grain-size distribution is traditionally conducted by sieve analysis, pipette, and hydrometer testing, although modern techniques such as laser-diffraction are now common-place in particle-size analysis (Gee and Or, 2002; Jilavenkatesa et al., 2001). Regardless of the method, proper sample preparation and

pretreatment is paramount. Many sediments have aggregates that are not easily dispersed or contain carbonate coatings and oxides that act as particle cement. Aggregates and cements can alter the accuracy of a grain-size distribution by over-representing the total percentage of fines or coarse material. Standard grain-size methods require that samples be treated in an aqueous solution to physically and chemically separate aggregates (Gee and Or, 2002). The process of sieve analysis is described in detail by Gee and Or (2002) and Jilianvenkatesa and others (2001).

Samples collected from exposed sediments and core samples from depth were analyzed for grain-size distribution using a Malvern Mastersizer 2000 laser-diffractometer at Western Kentucky University. The Malvern Mastersizer 2000 laser-diffractometer detects particles in the range from 0.02 microns to 2000 microns. The Malvern was operated using a modified standard operating procedure based on the Malvern Mastersizer 2000 operating manual. Grain-size distribution plots were generated using the Malvern 2000 software, and subsequent statistical analysis was conducted using Grainstrat v8 software by Blott and Pye (2001). The statistical analysis was conducted using Folk and Ward (1957) formulae on the primary mode and included mean and median grain size, skewness, and kurtosis. Results are shown in logarithmic phi (ϕ) units and microns. Grain-size statistics generated in Gradistat v8 were plotted in OriginPro to generate a bivariate plot of mean grain size and sorting and a sand-silt-clay ternary diagram. Bivariate plots are commonly used in classical sedimentology and cave sedimentology to evaluate patterns of deposition and transport (Nehme et al., 2014; Trappe, 2010; Myceilska and Ludwikowska, 2011; Shackley M., 1972; Folk and Ward, 1957). Analyzing grain size distribution of samples from the seven cave site allows for the evaluation of transport mechanisms between caves and between groups of samples. These relationships further aid in

understanding the relationships between clastic sediments and paleohydrology and modes of cave genesis.

4.4 Grain-Size Statistics

Grain size data for 57 samples were collected and analyzed for determining the statistical significance between median values of three separate facies groups. Prior to running the tests, data normality was evaluated and the data was determined to be non-parametric; therefore, non-parametric tests, including the KW, Dunn's, and MWU tests were utilized. The KW test and ad-hoc Dunn's test were used on all three facies groups and MWU test was performed on two facies groups at a time to test the null hypothesis that the populations (groups) are similar. The analyses involved the use of the MWU test in addition to the KW test in an effort to reduce Type I errors. Type I errors would arise during the KW test due to differences in population size and intervariation between median values across the entire sample set. The MWU test was conducted in an effort to reduce errors by evaluating pairwise relationships as opposed to the sample set as a whole. The Dunn's test was utilized an ad-hoc, pairwise analysis following the KW test to determine how different each group is from each other. The KW, Dunn's, and MWU tests were conducted using a p -value of 0.05 as a threshold for rejecting the null hypothesis. The null hypothesis in this case is that the medians in the given groups are the same and the samples come from the same population. If the calculated p -value is below the chosen 0.05 value, then the null hypothesis is rejected, meaning the samples are statistically different and do not come from the same population (Lomuscio, 2021; Dunn, 1964; Kruskal and Wallis, 1952; Mann and Whitney, 1947). Evaluating statistical relationships between groups of samples further solidifies the differentiation of groups of samples by the degree and type of transport and deposition. The

degree and type of transport and deposition that acts of cave sedimentation is directly-tied to paleo-hydrology and cave development (Palmer, 2007; Gillieson, 1996).

4.3 X-Ray Powder Diffraction

X-ray powder diffraction (XRD) was employed in this study to characterize the mineral provenance of cave deposits and surface samples. X-ray powder diffraction is a rapid, minimally destructive scientific method that utilizes x-ray diffraction to identify structural information of powder and microcrystalline materials. Structural information, or atomic spacing, is determined by the diffraction of x-rays through a crystal lattice. Researchers in cave sediment science have utilized XRD to evaluate mineralogical constituents and provenance of chemical and clastic sediments (Entrena et al., 2022; Foos et al., 2000; Polyak and Guven, 2000). This study utilized XRD to identify the mineralogical provenance of fine-grained clastic sediment samples collected in seven separate caves in the McCloud Limestone. Sample preparation was conducted at Western Kentucky University using procedures outlined by Poppe and others (2001) and Moore and Reynolds (1997).

Sample preparation methods for clay minerals required special preparation of glass slide mounts and heat and ethylene glycol treatment. Heat and chemical treatment affect atomic spacing by collapsing or swelling the crystal structure in characteristic manners. Behavior of clay mineral spacing through heat and chemical treatment is well documented and summarized by Poppe et al. (2001) and Moore and Reynolds (1997). Glass slide mounts and loose powder material were analyzed at Western Kentucky University with a Bruker D2 Phaser. Glass slide mounts were scanned from 3-40 degrees 2theta using a step size of 0.8 seconds, step increment of 0.02 degrees, and PSD opening of 1.5. Powdered material was scanned from 3-70 degrees 2

theta using identical scan parameters. XRD data was analyzed using the Match! (Putz and Brandenburg, 2024) and Bruker Diffrac.Eva softwares (Bruker, 2018). General operating procedures for sample preparation methods and equipment operation are summarized in Appendix III. Overall, trends in cave mineralogy between each cave site and between in-cave and entrance samples allowed for evaluation of clay provenance and degrees of pedogenic weathering. Relationships between the clay minerals present or absent in a particular cave environment can reveal insight into the mode of cave genesis and paleo-hydrology (Northup and Lovoie, 2001; Polyak and Guven, 2000).

4.4 Scanning Electron Microscopy

Scanning electron microscopy (SEM) and electron dispersive spectrometry (EDS) analysis were used in this study for determining nanoscale grain morphology and mineral phase identification. Samples were prepared and analyzed at Western Kentucky University using a JEOL JSM 6510-LV Scanning Electron Microscope with a MOXTEK 550i thin film coated IXRF energy dispersive spectrometer. Samples were analyzed at a magnification range of 600-25,000x at 20kV. The sample APC3 (Ancient Palace Cave) black fines samples were sputter-coated with a gold coating in a vacuum chamber. SEM-EDS results were interpreted by the author using online mineralogical databases and well-regarded textbooks on cave mineralogy (RRUF, 2021; Hill and Forti, 1986). SEM-EDS was utilized herein to further evaluate mineral provenance for samples that could not be identified through XRD.

Chapter Five: Results

This study analyzed 23 samples from seven cave sites for grain size distribution, x-ray diffraction, scanning electron microscopy, and electron dispersive spectrometry (Table 5.1). In addition, 34 more subsamples were analyzed from the cores EC13 and T1 for use in grain size distribution analyses. Results from grain size and mineralogical analyses are in the following sections of this chapter.

Table 5.1: Core and grab samples analyzed for grain size and mineralogy (Source: Author).

Cave	Sample	Type	Depth	Analyses
Ellery Cr	EC1	Grab	0-5 cm	GSD, XRD
Ellery Cr	EC13	Core	43-60 cm	GSD, XRD
Ellery Cr	EC13	Core	183-193 cm	GSD, XRD
Tardis	TH5	Grab	0-5 cm	GSD, XRD
Tardis	T1	Core	61-81 cm	GSD, XRD
Tardis	T1	Core	96-101 cm	GSD, XRD
Pipevine	P1	Grab	0-5 cm	GSD, XRD
Pipevine	P3	Grab	0-5 cm	GSD, XRD
Pipevine	P8	Grab	0-5 cm	GSD, XRD
Pipevine	P10	Grab	0-5 cm	GSD, XRD
APC	APC1	Grab	0-5 cm	GSD, XRD
APC	APC2	Grab	0-5 cm	GSD, XRD, SEM
APC	APC3	Grab	0-5 cm	GSD, XRD, SEM-EDS
APC	APC4	Grab	0-5 cm	GSD, XRD, SEM
Rileys	R5	Grab	0-5 cm	GSD, XRD
Rileys	R3	Grab	0-5 cm	GSD, XRD
Rileys	R4	Grab	0-5 cm	GSD, XRD
LSC	LSC1	Grab	0-5 cm	GSD, XRD
LSC	LSC2	Grab	0-5 cm	GSD, XRD, SEM-EDS
LSC	LSC3	Grab	0-5 cm	GSD, XRD

LSC	LSC4	Grab	0-5 cm	GSD, XRD, SEM-EDS
January	JH3	Grab	0-5 cm	GSD, XRD
January	J-C9	Grab	0-5 cm	GSD, XRD, SEM-EDS

5.1 Ellery Creek Cave

5.1.1 Sediment Mineralogy and Grain Size

Numerous grab and boring samples were collected from Ellery Creek Cave for grain-size distribution and clay mineral XRD analysis (Figure 5.1). Samples were collected to represent characteristic clastic deposits in the cave and careful attention was taken to retrieve samples that would be representative of the depositional conditions observed. The study conducted eleven borings in the cave primarily in the lower sump room fill slope. The ten borings in the lower sump room were conducted to characterize the stratigraphic variability of a thick deposit that does not have an exposed erosional face for study. Stratigraphy was logged in the field and further refined with grain-size distribution. The deposit preserves prominent charcoal beds are an average of 1-3 cm thick, but are up to 12 cm thick lower in the section. The EC1 entrance sample was taken from the lower entrance colluvial slope towards the base of the primary descending passage.

Three subsamples (EC1, EC13 43-60 cm, EC13 183-193 cm) from Ellery Creek Cave were analyzed with XRD for constituent mineralogy, including one subsample from the entrance passage, EC1, and two from further inside the cave from the Sump Room passage fill. The passage fill samples for XRD were retrieved from prominent beds in the 2.3-meter-deep Boring 13 conducted in the sump room. The entrance room sample, EC1, consists of clinochlore (Mg-chlorite), illite, and quartz (Figure 5.1). The high relative intensity of the chlorite 14A peak after

heating to 550C suggests the presence of the Mg-rich form, clinochlore (Moore and Reynolds 1997).

The two boring sub-samples obtained from EC13 at the 43-60 cm and 183-193 cm intervals represent two locations in the core sample that either characterize apparent gross mineralogy or investigate distinct strata. The sub-sample from 43-60 cm represents strata with a common color, texture, and plasticity. This sample taken from 43-60 cm contains vermiculite, interstratified chlorite-illite, and quartz (Figure 5.2). Interstratification (I/S) is seen as a less intense and broader 14A peak after heating to 550c (Moore and Reynolds 1997).

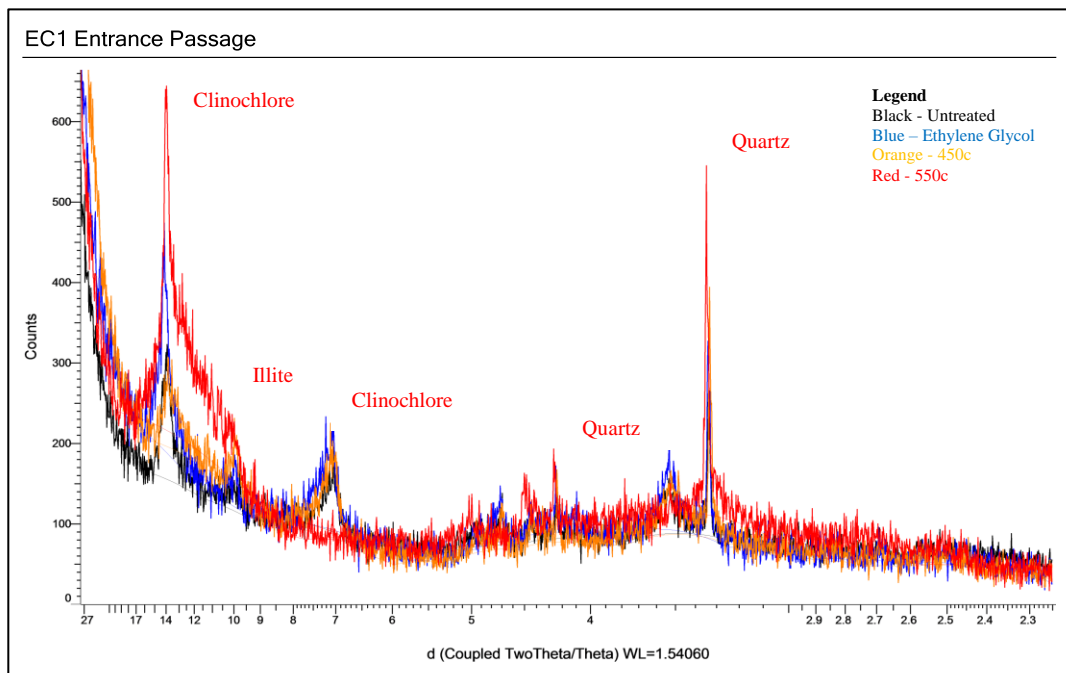


Figure 5.1: Composite XRD scan of EC1 Entrance; 14A – clinochlore; 10A – illite. Quartz peaks are present as sharp peaks at 3.34Å and 4.26Å (Source: Author).

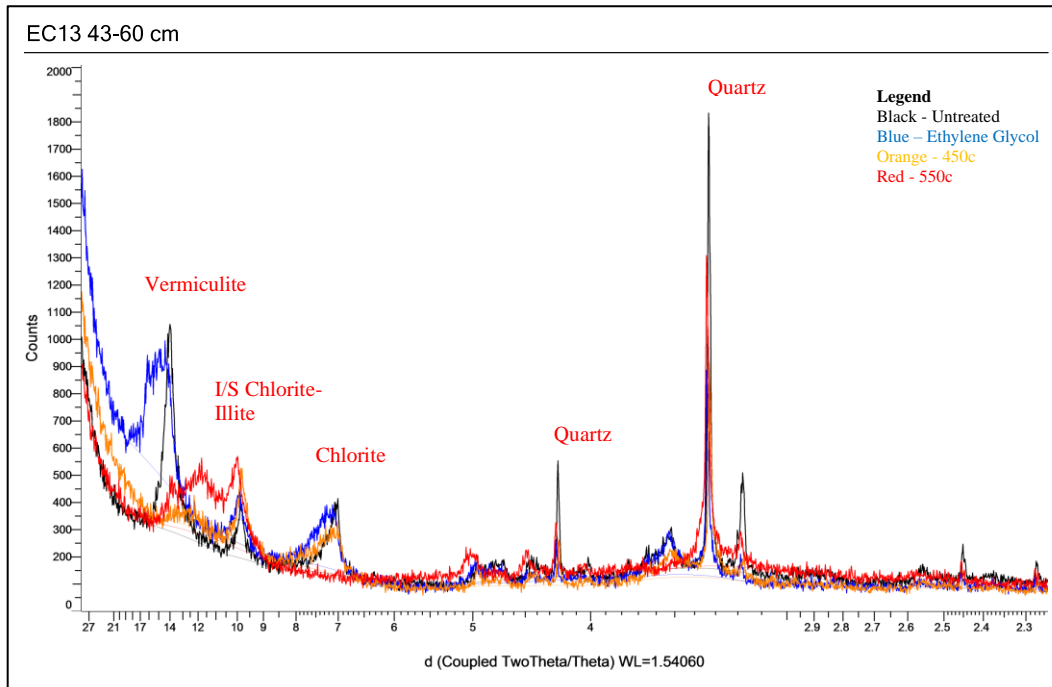


Figure 5.2: Composite XRD scan of Ellery Cr B13 at 43-60 cm. 14A – vermiculite; 14A – I/S chlorite-illite, 10A – illite. Quartz peaks are present as sharp peaks at 3.34A and 4.26A (Source: Author).

sample retrieved from 183-193 cm from a distinct bed of yellow (10YR 8/8) clayey silt that is underlain and overlain by beds of gray sandy silt. The sample taken from 183-193cm contains vermiculite, illite, chamosite (Fe-chlorite), and quartz (Figure 5.3). Vermiculite is present as a progressively collapsing 14A peak through heating to 550c and slight expansion of the 14A peak after treatment with ethylene glycol. Illite is present as a stable 10A peak and kaolinite is present as a 7A peak that collapses through heating at 550c. Quartz peaks are present as sharp peaks at 3.34A and 4.26A (Poppe et al., 2001; Moore and Reynolds, 1997).

Numerous hand and boring samples were analyzed from Ellery Creek Cave for grain-size distribution. Grain size-distribution of the samples indicates a wide range in mean grain size from coarse sand and gravel to clayey silt and sorting from poorly sorted to very poorly sorted.

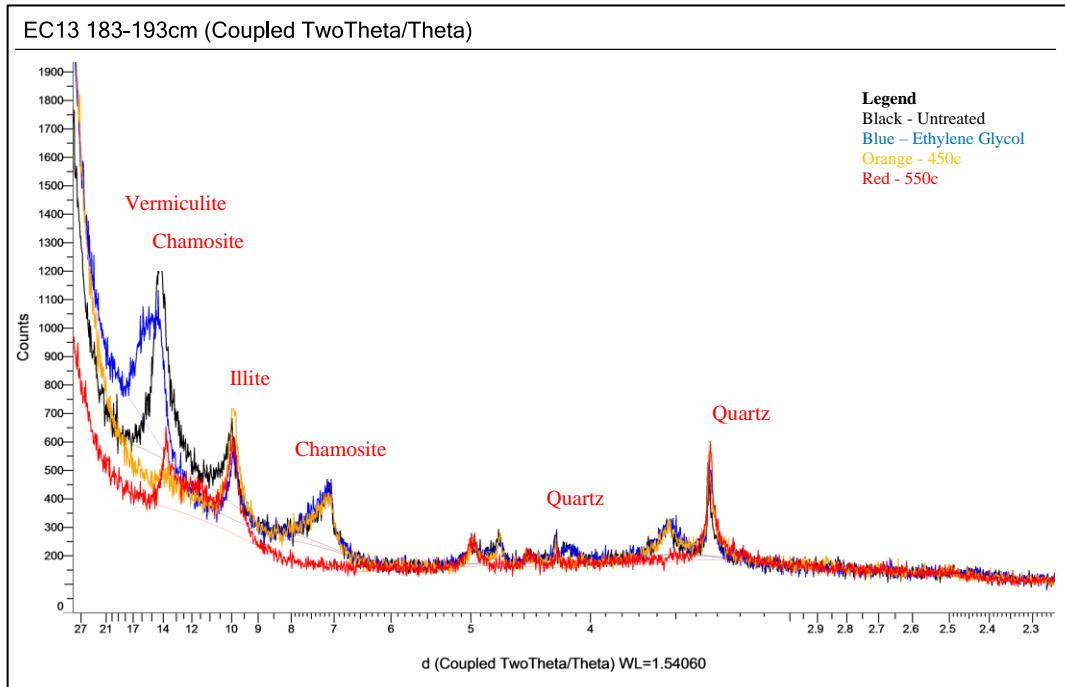


Figure 5.3: Composite XRD scan of Ellery Cr Boring 13 at 183-193 cm; 14A – vermiculite, 14A – chamosite, 10A– illite. Quartz peaks are present as sharp peaks at 3.34Å and 4.26Å (Source: Author).

The Sump Room passage fill preserves the largest volume of sediment in the cave and exhibits the widest range of grain sizes and sorting. The deepest boring conducted at 2.3-meters encountered a range of grain-size distributions and stratigraphic structures (Figures 5.4 – 5.6). The material recovered consists primarily of sandy silt with a mean grain size between ~4 and 80 microns with sand interbeds upwards of a 15 cm thick. Four distinct interbeds of silty sand to sand with gravel are situated at intervals of 40-50 cm apart (Figure 5.4). The silt and clay sized material is often finely laminated although silt-rich beds can be massive. Where clay was

detected in Boring 13, clay content was at least 16% and upwards of 23%. Strata that did not preserve clay had a clay content near zero or at zero. The entrance passage sample, EC1, contain minimal clay and consists primarily of very poorly sorted sandy silt (Figure 5.7).

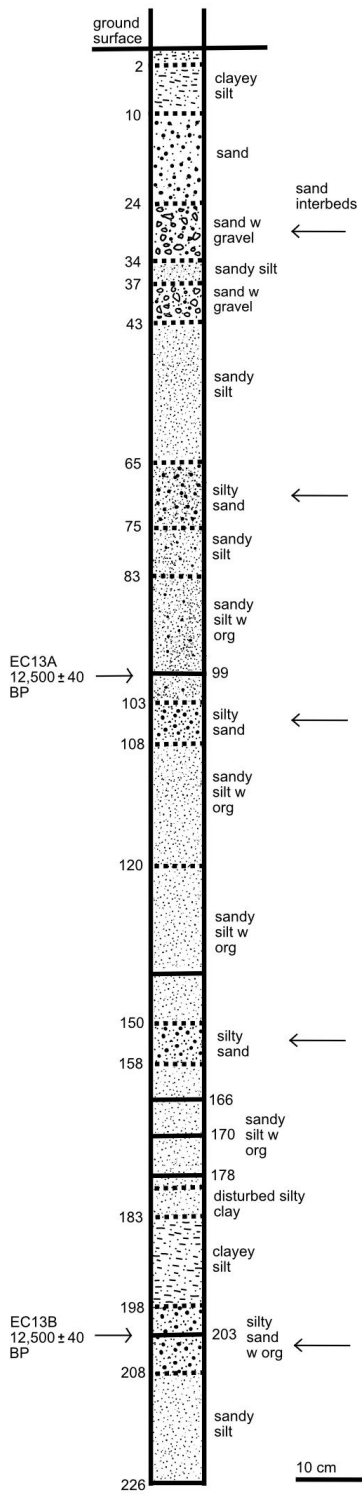
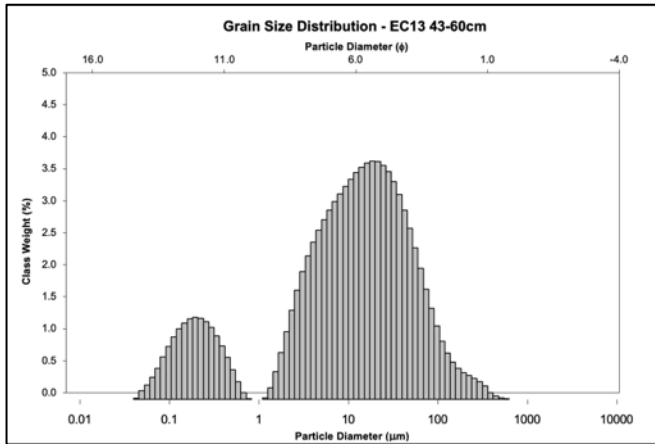
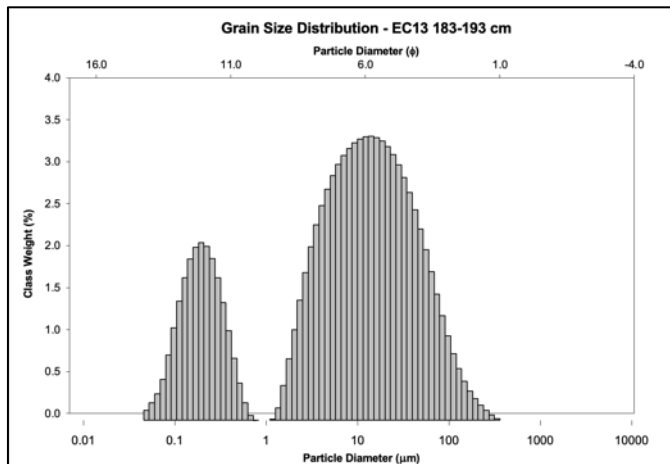


Figure 5.4: Boring log of Ellery Creek Cave Boring 13 with charcoal sampling locations marked on left and sand interbeds marked on right (Source: Author).



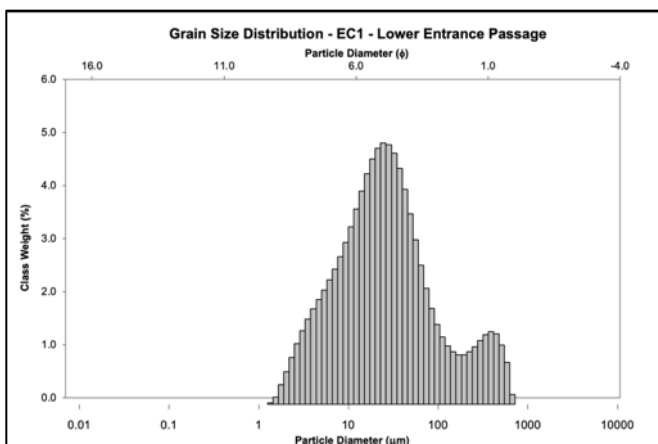
Mean (mm/ ϕ)	15.68/ 6.0	Coarse silt
Sorting (ϕ)	1.68	Poorly Sorted
Skewness (ϕ)	-0.002	Symmetrical
Kurtosis (ϕ)	0.916	Mesokurtic

Figure 5.5: Ellery Creek Cave Boring 13 at 43-60 cm; very fine sandy coarse silt, grayish brown (10YR 5/2), slight laminations with darker fine material, trace charcoal (Source: Author).



Mean (mm/ ϕ)	14.11/ 6.15	Coarse silt
Sorting (ϕ)	1.64	Poorly Sorted
Skewness (f)	-0.035	Fine Skewed
Kurtosis (f)	0.884	Platykurtic

Figure 5.6: Ellery Creek Cave Boring 13 at 183-193 cm; medium silt, yellow (10YR 8/8), slight fining upwards present, sharp contact with charcoal below (Source: Author).



Mean (mm/φ)	25.32/ 5.30	Fine silt
Sorting (φ)	1.93	Poorly Sorted
Skewness (φ)	-0.095	Symmetrical
Kurtosis (φ)	1.185	Leptokurtic

Figure 5.7: Ellery Creek Cave EC1 Lower Entrance Passage; very fine sandy coarse silt, dark yellowish brown (10YR 5/4), minor angular limestone gravel, trace organics (roots, animal refuse) (Source: Author)

Charcoal and wood fragments are ubiquitous throughout Boring 13 and occur as individual fragments or distinct beds and laminations ranging from 0.5 to 10mm thick. Two samples of charcoal and wood fragments were collected from 98 cm and 203 cm for radiocarbon dating and results indicate that both samples lay within the same approximate age range of 12,500 ± 40 BP (see Appendix II).

5.1.2 Cave Morphology

Ellery Creek Cave is made up of a series of horizontal, bedding and lithology-controlled passages that are predominantly phreatic. Passage development in Ellery Creek Cave is dense and often is overlapping with lower-level passages developing directly below the entrance. The upper entrance passage developed as a bedding-controlled phreatic-loop as evident by development along and up-dip of strike direction. The pothole passage in-between the entrance passages and the junction room is strongly situated on a bedding surface oriented at

approximately 340/35 degrees NE. The junction room is a rounded, elliptical-shaped passage with a 2m-deep, ephemeral eddy pool making up the floor.

The diorite passage immediately after the junction room is strongly situated on a steeply dipping diorite intrusion with the southern wall and ceiling being entirely diorite. The northern wall of the diorite passage is limestone and is characterized by three impassable inlets that are providing chemical and clastic sediments to the passage. The sump room is predominately formed in limestone and is strongly phreatic with broad scalloped walls and an elliptical cross section. A small portion of the southeastern bedrock wall is composed of altered diorite.

5.2 Tardis Cave

5.2.1 Sediment Mineralogy and Grain Size

Two hand samples were collected and one boring was advanced in Tardis Cave. Sample TH5 was collected from a ledge of fine-grain material at the base of an epikarst dome drain in the dike room. Two sub-samples were retrieved from the T1 core conducted in the passage-filling alluvial fan in the Boxwork Room. One sub-sample was collected at a representative interval towards the middle of the boring at 61-81 cm and the other sub-sample was retrieved at 96-101 cm from the basal bed of the one-meter-long boring. The boring conducted in Tardis Cave revealed an alternating sequence of well-sorted sand and clayey silt with an overall fining downwards sequence (Figure 5.8). Silt and clay content ranged dramatically between near zero in the thickest sand bed at 12-32 cm and 67% in the basal bed between 96-101cm.

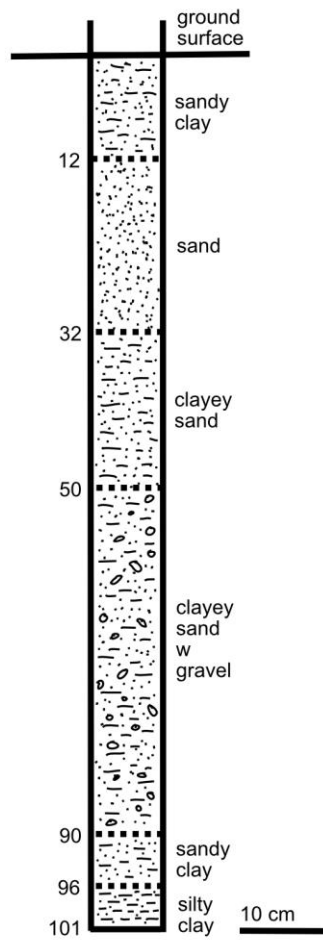


Figure 5.8: Boring log of the core taken in Tardis Cave (Source: Author).

All three samples were analyzed with XRD to evaluate constituent mineralogy. Sample TH5 collected from a deposit of dome infiltrate contains chamosite (Fe-rich chlorite), illite, and quartz (Figure 5.9). The Fe-rich form, chamosite, is likely present based on observation of the low relative intensity of the basal reflection and relative high intensity of the second order reflection at 7A (Moore and Reynolds, 1997). The overall presence of chlorite is shown by the increase in intensity of the 14A peak after heating to 550c. The two samples collected from the Boxwork Room boring both contain illite and quartz but differ in the behavior and geometry of the 14A peak. The sub-sample collected from the basal bed 96-101 cm contains smectite,

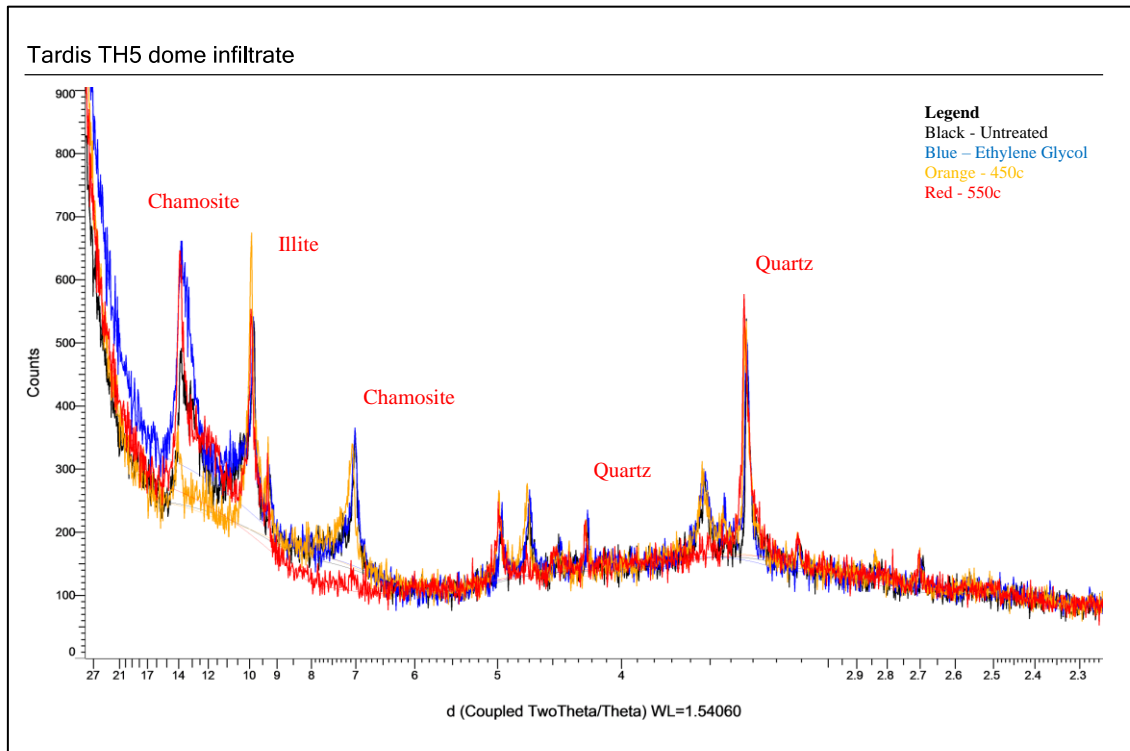


Figure 5.9: Composite XRD scan of Tardis TH5 Dome Infiltrate; 14A – chamosite, 10A – illite. Quartz peaks are present as sharp peaks at 3.34Å and 4.26Å (Source: Author).

chamosite (Fe-chlorite), illite, and quartz (Figure 5.10). Smectite is present as a 14A peak that shifts towards 17A after treatment with ethylene glycol. Chamosite is present in the sample from the relative increase in intensity of the 14A peak through heat treatment to 550c. The sample taken from 61-81 cm contains the same clay species but overall possesses more smectite and less Fe-chlorite due to the higher and lower relative intensities of relative peaks (Figure 5.11). The relative proportion of clay species is suggested by the relative behavior of the 14A peak through heating to 550c. The 14A peak of 96-101 cm sample shows more relative intensity after heating to 550c and the 14A peak of the 61-81 cm peak shows very little increase in intensity. Illite is

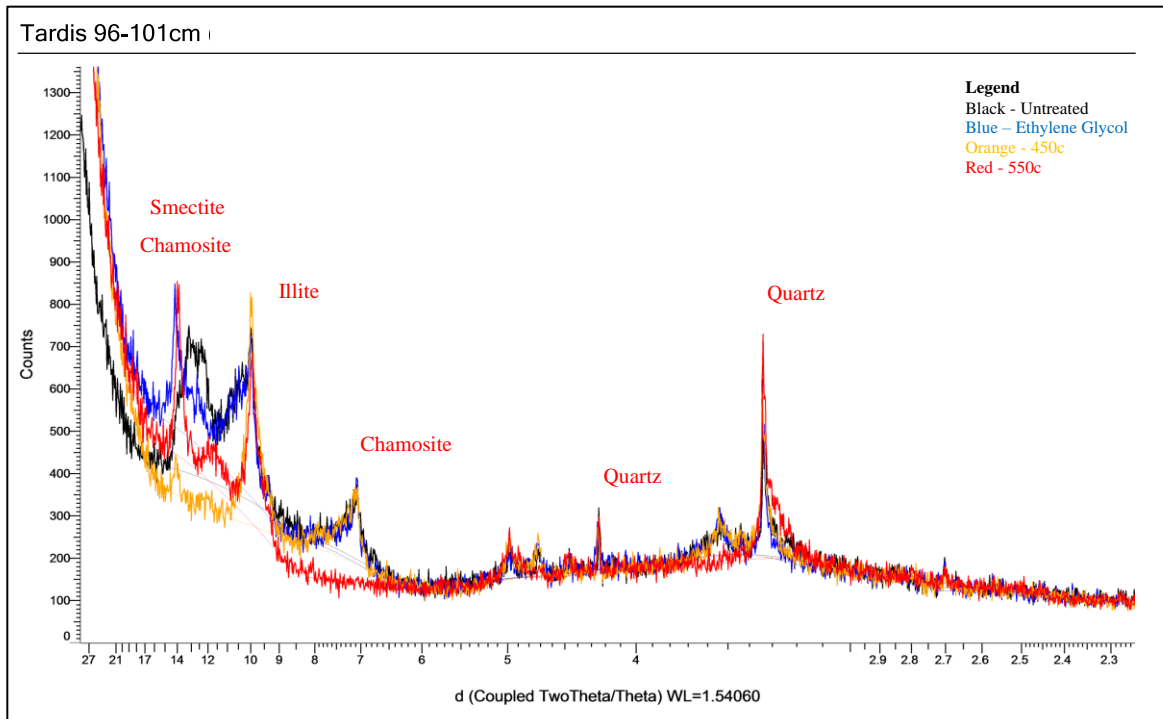


Figure 5.10: Composite XRD scan of Tardis Boring at 96-101 cm; 14A – smectite; 14A – chamosite, 10A – illite. Quartz peaks are present as sharp peaks at 3.34Å and 4.26Å (Source: Author).

present in all samples as a stable 10A peak. Quartz peaks are present as sharp peaks at 3.34Å and 4.26Å (Poppe et al., 2001; Moore and Reynolds, 1997).

Grain-size distribution was conducted on all hand and boring samples. Results indicate overall similarities in poor sorting but a range in mean grain size and peak geometry. Grain size distribution of the TH5 dome infiltrate sample indicates a high clay content (39%) and very poor sorting (Figure 5.12). Grain-size distribution of boring interval samples indicates an overall fining downward through the depth of the one-meter boring. Mean grain size and clay content at the basal bed is 1.35 microns and 67% and the overlying beds generally coarsen upwards with a grain size and clay content of 13.4 mm and 14% (Figure 5.13 and 5.14).

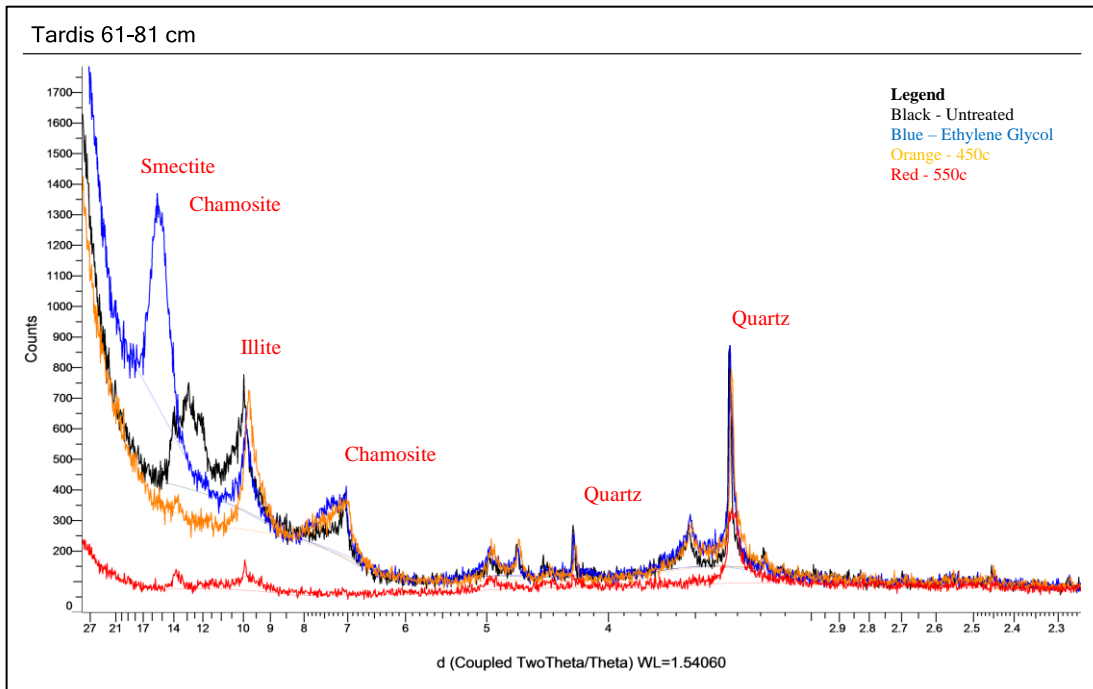
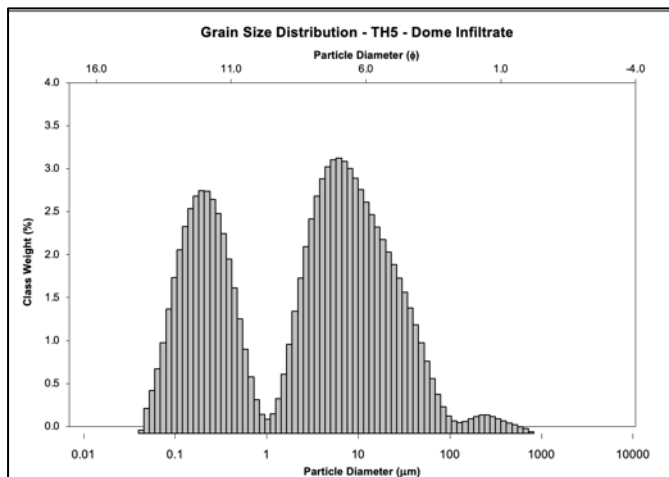
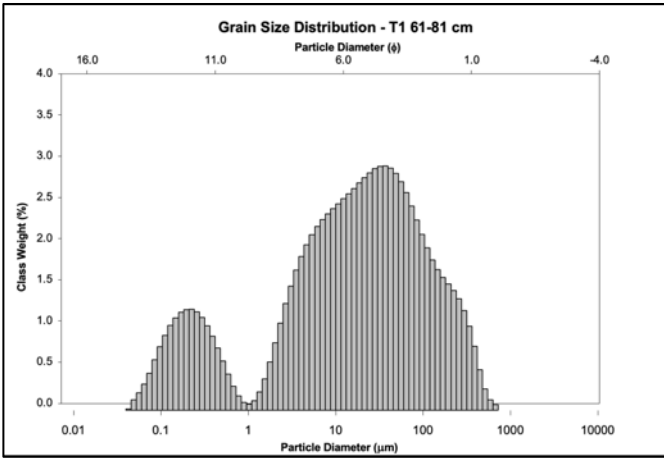


Figure 5.11: Composite XRD scan of Tardis Boring at 61-81 cm. 14A – smectite; 14A - chamosite; 10A – illite. Quartz peaks are present as sharp peaks at 3.34A and 4.26A (Source: Author).



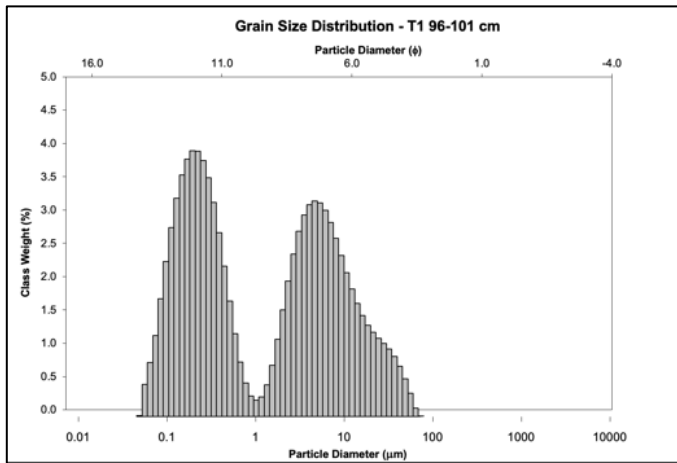
Mean (mm/ φ)	2.42/ 8.70	Very Fine Silt
Sorting (φ)	3.05	Very Poorly Sorted
Skewness (φ)	-0.146	Coarse skewed
Kurtosis (φ)	0.938	Mesokurtic

Figure 5.12: Tardis TH5 Dome Infiltrate; silty clay, reddish brown (2.5YR 4/3), trace angular to subrounded diorite and limestone gravels, trace organics (husks, mycelium, bones) (Source: Author).



Mean (mm/ ϕ)	13.40/ 6.22	Medium silt
Sorting (ϕ)	3.18	Very Poorly Sorted
Skewness (ϕ)	0.25	Fine Skewed
Kurtosis (ϕ)	1.15	Platykurtic

Figure 5.13: Tardis Boring at 61-81 cm; medium silt, dark yellowish brown (10YR 5/6) (Source: Author).



Mean (mm/ ϕ)	1.35/ 9.53	Clay
Sorting (ϕ)	2.72	Very Poorly Sorted
Skewness (ϕ)	0.06	Symmetrical
Kurtosis (ϕ)	0.68	Platykurtic

Figure 5.14: Tardis Boring at 96-101 cm; medium silt, dark yellowish brown (10YR 5/6) (Source: Author).

5.2.2 Cave Morphology

Passages in Tardis are strongly controlled by joints and intrusive material and most passages show evidence of paragenetic development (Figure 5.15). Paragenetic notches and upwards migrating pockets and cupulas suggests bedrock shielding from deposits of densely packed clastics and fine sediments (Farrant and Smart, 2011; Renault, 1958). Passages in the southwestern and northeastern portion of the cave have one or two distinct paragenetic notches that are typically within 30 centimeters of the ceiling. In the central, larger portion of the cave, paragenetic notches form at multiple levels. Where exposed bedrock floor is common the bedrock is scoured with potholes and eddy pockets. Potholes and pockets can range from a few centimeters deep to 1.5 meters deep.



Figure 5.15: Strongly joint-controlled passage with a horizontal paragenetic notch (Source: Bunnell, 2023).

5.3 Pipevine Cave

5.3.1 Sediment Mineralogy and Grain Size

Multiple grab samples were collected throughout Pipevine Cave and analyzed using grain-size distribution and clay mineral XRD. The P1 sample was collected as a bulk sample of the entrance room fines. The P8 laminated brown fines, P10 yellowish brown fines, and P3 white fines samples were collected from the approximately 2-meter tall, 1-meter wide exposed face at the north end of lower chamber. The exposed face is the only exposed stratigraphy present in a 1-2 meter-wide, 8-meter tall passage fill. The exposed face is well-stratified with 1-3 mm laminations and up to 15 cm thick beds of massive clayey silt. Sample P8 was collected from a package of finely laminated brown (7.5YR 4/3) and yellowish-brown (10YR 5/4) fine silts and clay. Sample P10 was retrieved from a relatively massive, 15-cm thick yellowish brown (10YR 5/6) silt bed. Sample P3 was retrieved from a singular and distinct 2-4 mm layer of light brownish gray (2.5YR 6/2) clayey silt that lay in-between two massive beds of yellowish-brown silt. Sample P10 was collected from the underlying yellowish-brown silt bed below P3.

All samples collected were analyzed with XRD to evaluate constituent mineralogy. The P1 sample collected in the entrance room contains clinochlore (Mg-chlorite), illite, and quartz (Figure 5.16). The P8 laminated brown and P10 fines sample contains interstratified illite-chlorite and quartz (Figure 5.17 and 5.18). Interstratification (I/S) is seen as a less intense and broader 14A peak after heating to 550c (Moore and Reynolds, 1997). Sample P3 of the 2-4 mm layer of white clayey silt contains vermiculite, illite, and quartz (Figure 5.19). The vermiculite 14A peak is distinct from the chlorite peak by progressively collapsing to 10A through heating to 550c. The 14A peak of chlorite increases in intensity through heating to 550c. Illite is present in

all samples as a stable 10A peak. Quartz peaks are present as sharp peaks at 3.34Å and 4.26Å (Moore and Reynolds, 1997).

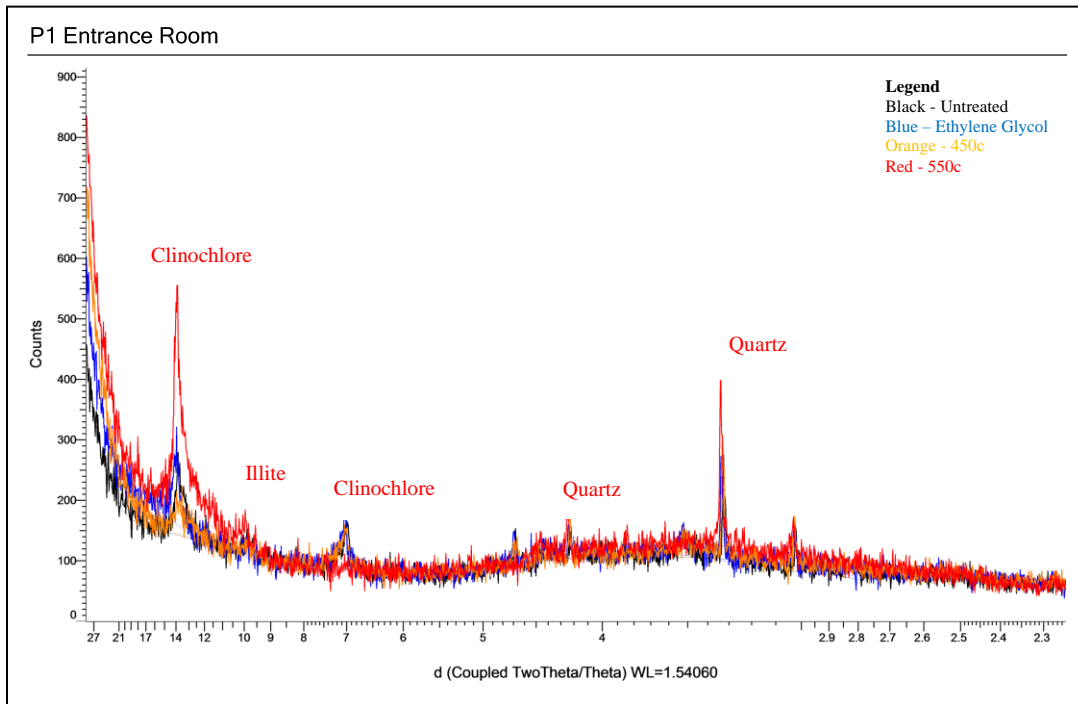


Figure 5.16: Composite XRD scan of P1 Entrance Room; 14Å – clinochlore, 10Å – illite. Quartz peaks are present as sharp peaks at 3.34Å and 4.26Å (Source: Author).

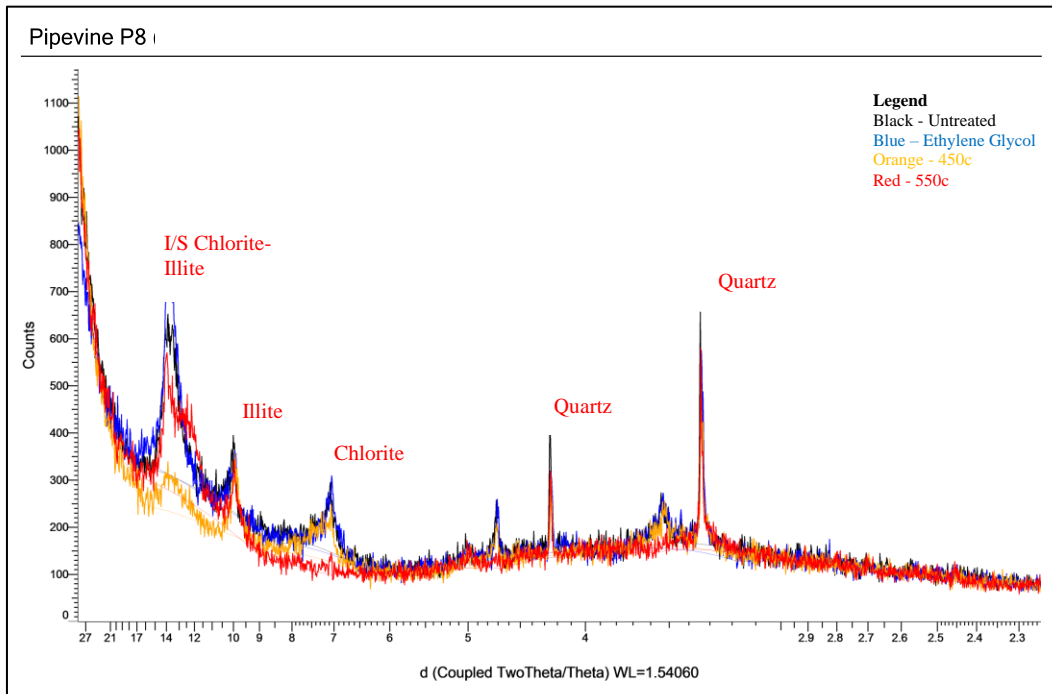


Figure 5.17: Composite XRD scan of Pipevine P8 Laminated Brown Fines; 14A – I/S chlorite-illite; 10A – illite. Quartz peaks are present as sharp peaks at 3.34Å and 4.26Å (Source: Author).

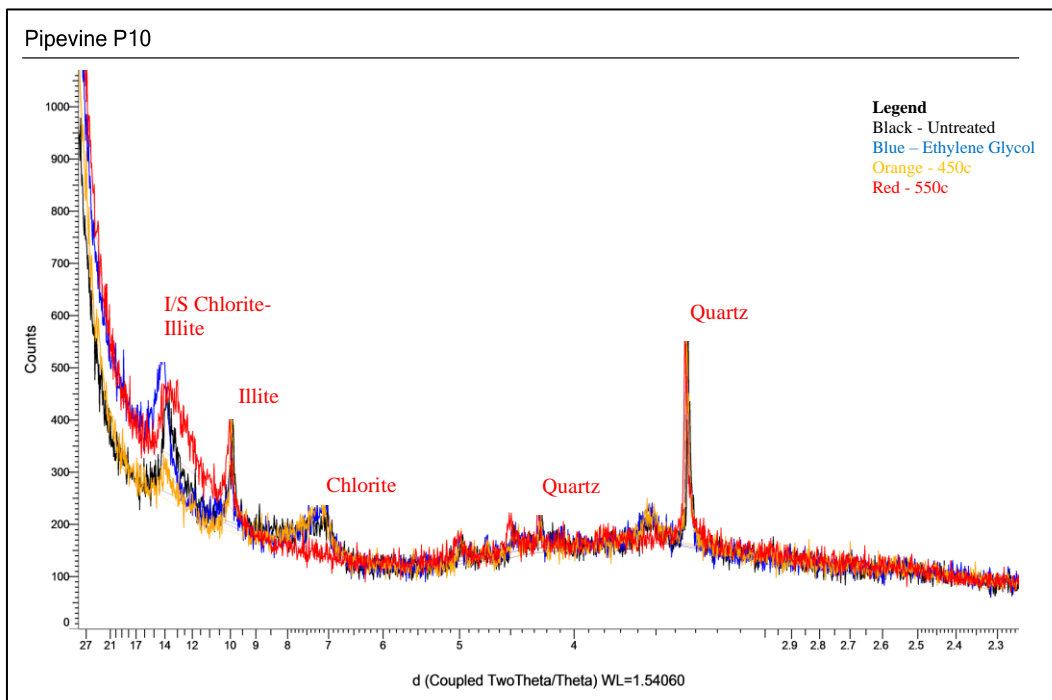


Figure 5.18: Composite XRD scan of Pipevine P10 Fines; 14A – I/S illite-chlorite; 10A – illite. Quartz peaks are present as sharp peaks at 3.34Å and 4.26Å (Source: Author).

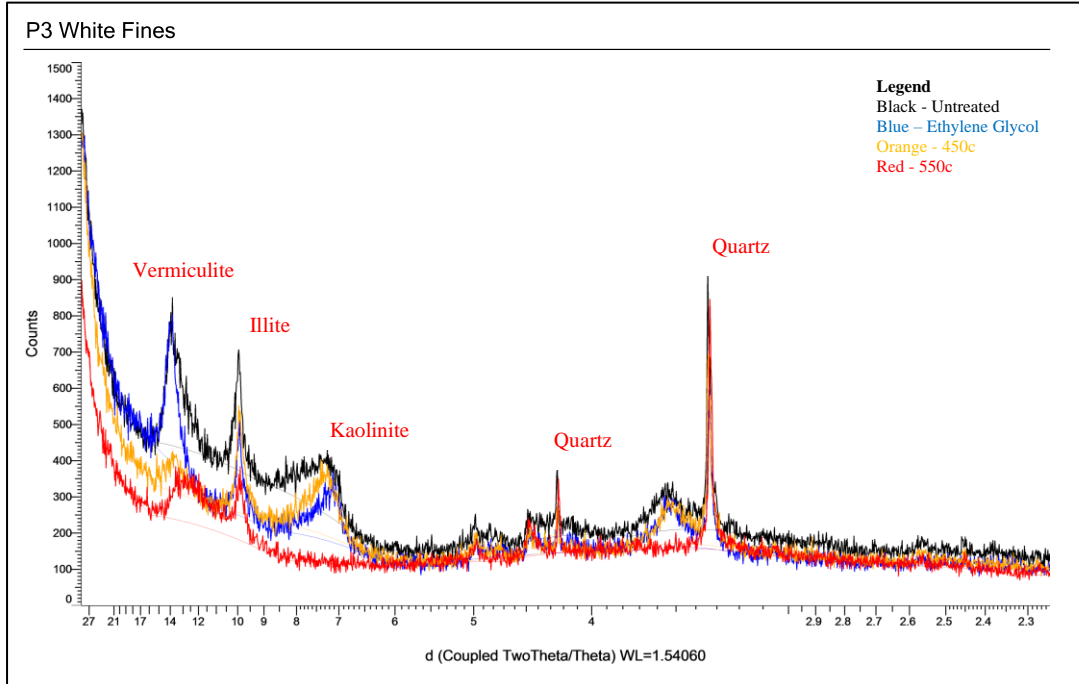
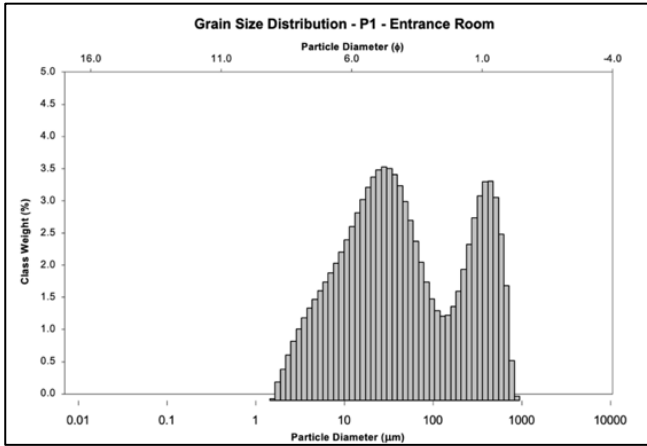


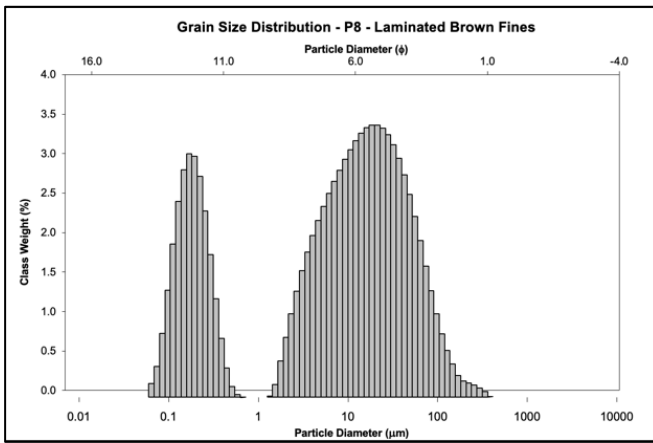
Figure 5.19: Composite XRD scan of Pipevine P3 White Fines; 14A – vermiculite; 10A – illite, 7A – kaolinite. Quartz peaks are present as sharp peaks at 3.34Å and 4.26Å (Source: Author).

Grain-size distribution of the analyzed samples indicates similar grain size and peak geometry in the lower chamber samples and distinct grain size and sorting in the upper-level entrance passage (Figures 5.20 – 5.22). Grain-size distributions for material collected from the lower chamber passage fill are fine to coarse, silt-sized sediments and are bimodal with a distinct clay-sized mode. The entrance fines sample, PV1, is coarser than the material in the lower chamber by a factor of 10x. The entrance fines material does not have a clay mode, but rather a leptokurtic fine-sand mode (Figures 5.20 – 5.22).



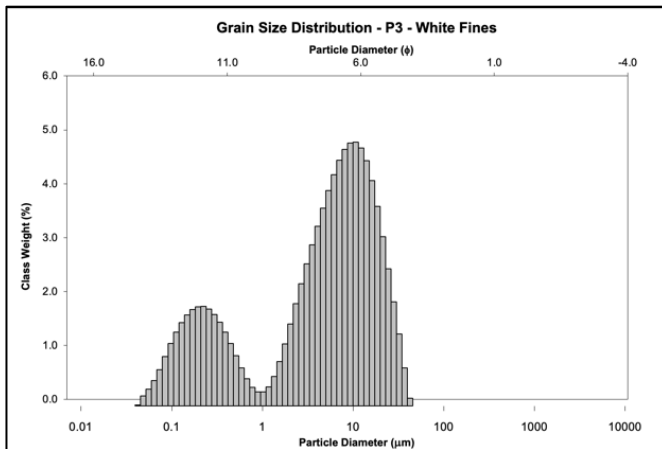
Mean (mm/ ϕ)	49.87/ 4.33	Very Coarse Silt
Sorting (ϕ)	2.40	Very Poorly Sorted
Skewness (ϕ)	-0.13	Coarse Skewed
Kurtosis (ϕ)	0.75	Platykurtic

Figure 5.20: Pipevine P1 Entrance Room; medium sandy coarse silt, yellowish brown (10YR 5/4), minor angular limestone gravel, trace organics (roots, animal refuse, mycelium) (Source: Author).



Mean (mm/ ϕ)	16.29/ 5.94	Coarse silt
Sorting (ϕ)	1.583	Poorly Sorted
Skewness (ϕ)	0.025	Symmetrical
Kurtosis (ϕ)	0.89	Platykurtic

Figure 5.21: Pipevine P8 Laminated Brown Fines; coarse silt, dark yellowish brown (7.5YR 4/3), 1-2 mm laminations throughout. (Source: Author).



Mean (mm/ ϕ)	8.08/ 6.95	Medium silt
Sorting (ϕ)	1.17	Poorly Sorted
Skewness (ϕ)	0.09	Symmetrical
Kurtosis (ϕ)	0.92	Mesokurtic

Figure 5.22: Pipevine P3 White Fines; medium silt, tannish white (2.5YR 6/2) (Source: Author).

5.3.2 Cave Morphology

Pipevine is made up of a series of down-trending elliptical passages, that range in volume from body-sized to 3-4 meters in diameter. Passages are well developed on a major, 80-degree dipping joint with occasional conjugate joints. No major structural displacement is apparent on the walls of the joint-controlled passages. Flat ceilings and stationary water level indicators are rare in the cave with only one identified. The three primary chambers in the cave develop cupula-like ceiling rises that appear to form on conjugate joints. The ceiling rise in the central portion of the cave forms a thin (10-30 cm) partition between the adjacent passage that extends most of the length of the 8-m tall ceiling rise. The rising ceiling passages terminate in carbonate bedrock.

5.4 Ancient Palace Cave

5.4.1 Sediment Mineralogy and Grain Size

Four grab samples were retrieved throughout Ancient Palace Cave for grain size distribution and clay mineral XRD analysis. The APC1 sample was collected as a bulk sample of the entrance slope colluvium. The APC2 sample was retrieved as a bulk sample from coatings of dark red (2.5YR 3/6) clay on calcified breakdown blocks approximately 30-meters upslope from the Jaded River. The clay coating ranges from 0.5-6 cm thick and forms abundant surface coating in many places. The APC3 black fines sample was collected from a ~3-cm thick wall deposit in the Borning Room side passage at the western edge of the lower levels. The APC3 black fines (2.5YR 2.1/1) material forms wall, pocket, and floor coatings and massive deposits (Figure 5.23). The material is closely associated with a heavily-altered diorite intrusion

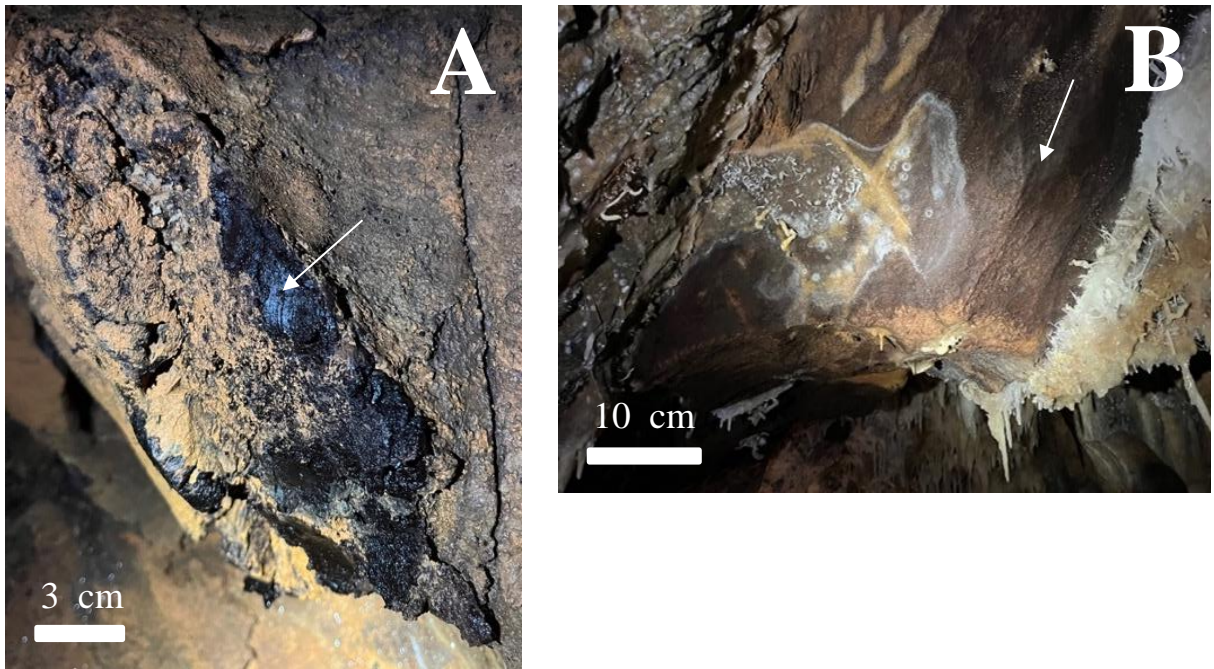


Figure 5.23: A - Ferromanganese deposit forming massive wall deposit. B – Ferromanganese deposit as a thin wall coating (Source: Despain, 2024).

that forms one wall and the ceiling of the passage. So far as what's known, the black fines deposit is isolated to the one, more-remote side passage that is partially formed in altered diorite. The APC4 sample was collected from a floor coating of dark red (2.5YR 3/6) clay in the Borning Room passage. The APC4 sample was retrieved in relative proximity to the APC3 sample.

All four samples were analyzed with XRD to evaluate constituent mineralogy. The entrance passage sample, APC1, contains chamosite, illite, and quartz (Figure 5.24). The two samples of the ubiquitous dark red clay-rich material both contain smectite, illite, and disordered kaolinite (Figure 5.25). Smectite is present as a 14A peak expands towards 17A through ethylene glycol treatment and collapse through heating to 400c and 550c. Kaolinite is present in both red

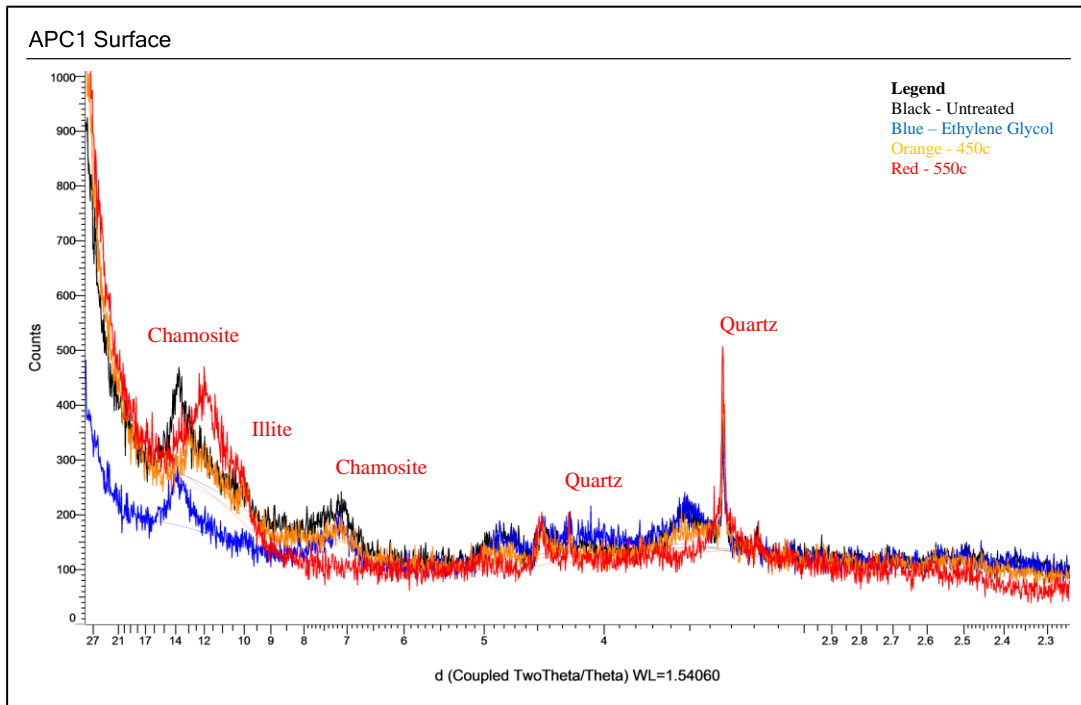


Figure 5.24: Composite XRD scan of APC1 Entrance; 14A – chamosite; 10A – illite. Quartz peaks are present as sharp peaks at 3.34Å and 4.26Å (Source: Author).

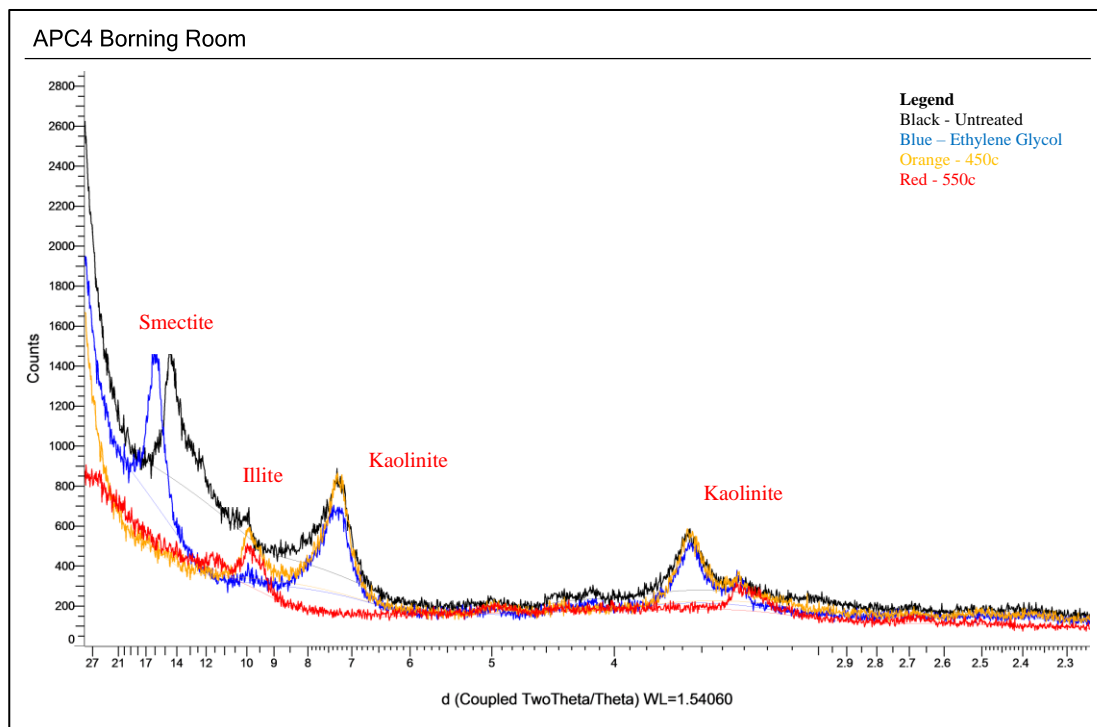


Figure 5.25: Composite XRD scan of APC4 Borning Room; 14A – smectite, 10A – illite, 7A – disordered kaolinite. Quartz peaks are not present (Source: Author).

clay samples as a broad peak at 7A that collapses through heating to 550c. The presence of disordered kaolinite (fireclay) is likely due to the observed relatively broad 7A peak (Poppe et al., 2001; Moore and Reynolds, 1997). The APC3 sample of black fines material contains predominately quartz, manganese-oxide, and likely smectite and kaolinite (Figure 5.26). The sample was too non-plastic to prepare oriented slide mounts, so the clay species remains unconfirmed.

The APC3 sample was analyzed with SEM-EDX to further identify mineral phases/constituents. The material was identified as a ferromanganese deposit (FMD) as similarly identified in hypogenic caves in New Mexico and South Dakota (Spilde et al., 2006; Northup and Lovoie, 2001; Dotson et al., 1999; Hill and Forti, 1997). SEM images and EDX analysis revealed the presence of pitted and corroded quartz, opal-A, manganese-oxide/hydroxides, iron-oxides/hydroxides, and minor authigenic calcite and alunite and trace allogenic fayalite (Figure 27 - 29). Fayalite (Fe_2SiO_4) in this setting is presumed to be allogenic, as fayalite is a high-temperature Olivine-group mineral that occurs in predominately ultramafic volcanic and plutonic rocks or in metamorphosed iron-rich sediments and impure carbonates (RRUF, 2021). XRD and SEM-EDX results suggests the material is an authigenic corrosion residue of both the altered diorite and limestone bedrock. The allogenic fayalite is assumed to be residuum from the diorite or limestone.

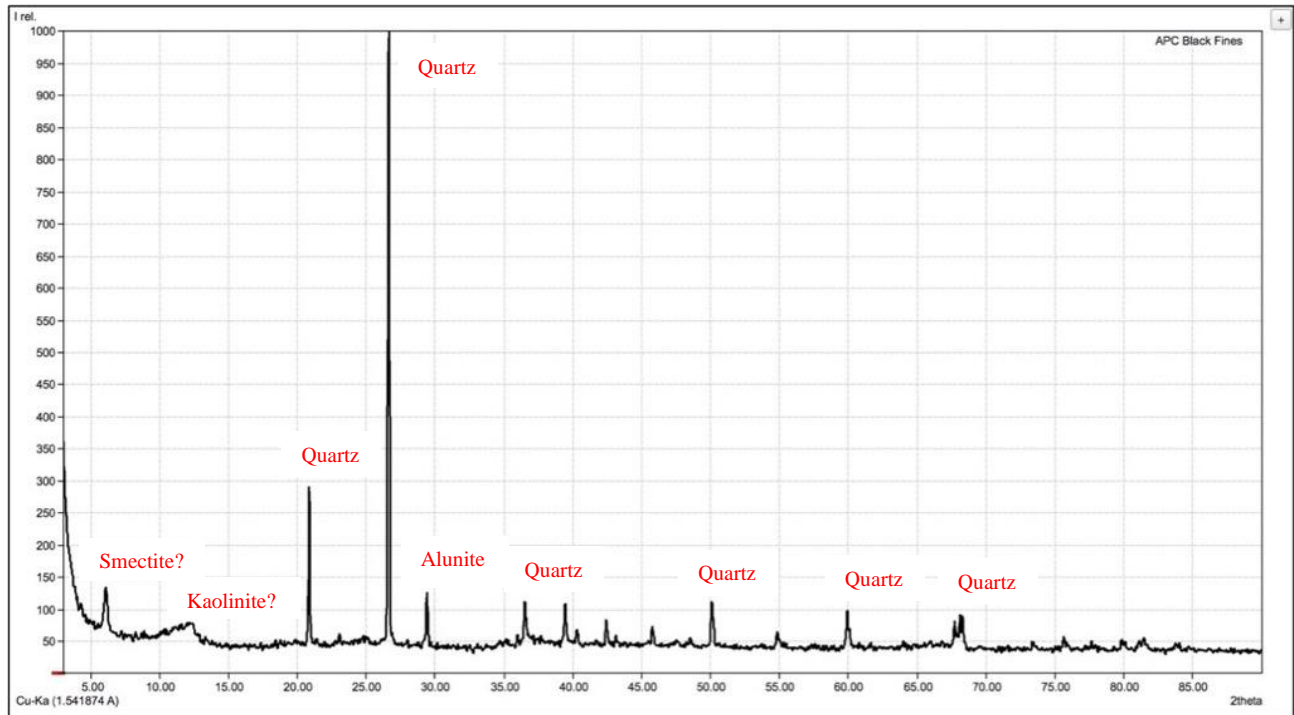


Figure 5.26: XRD scan of powdered corrosion residue at 3-90 2 theta angle, 1s step time, 0.02 deg increment. Quartz peaks are present along with alunite and likely smectite and kaolinite (Source: Author).

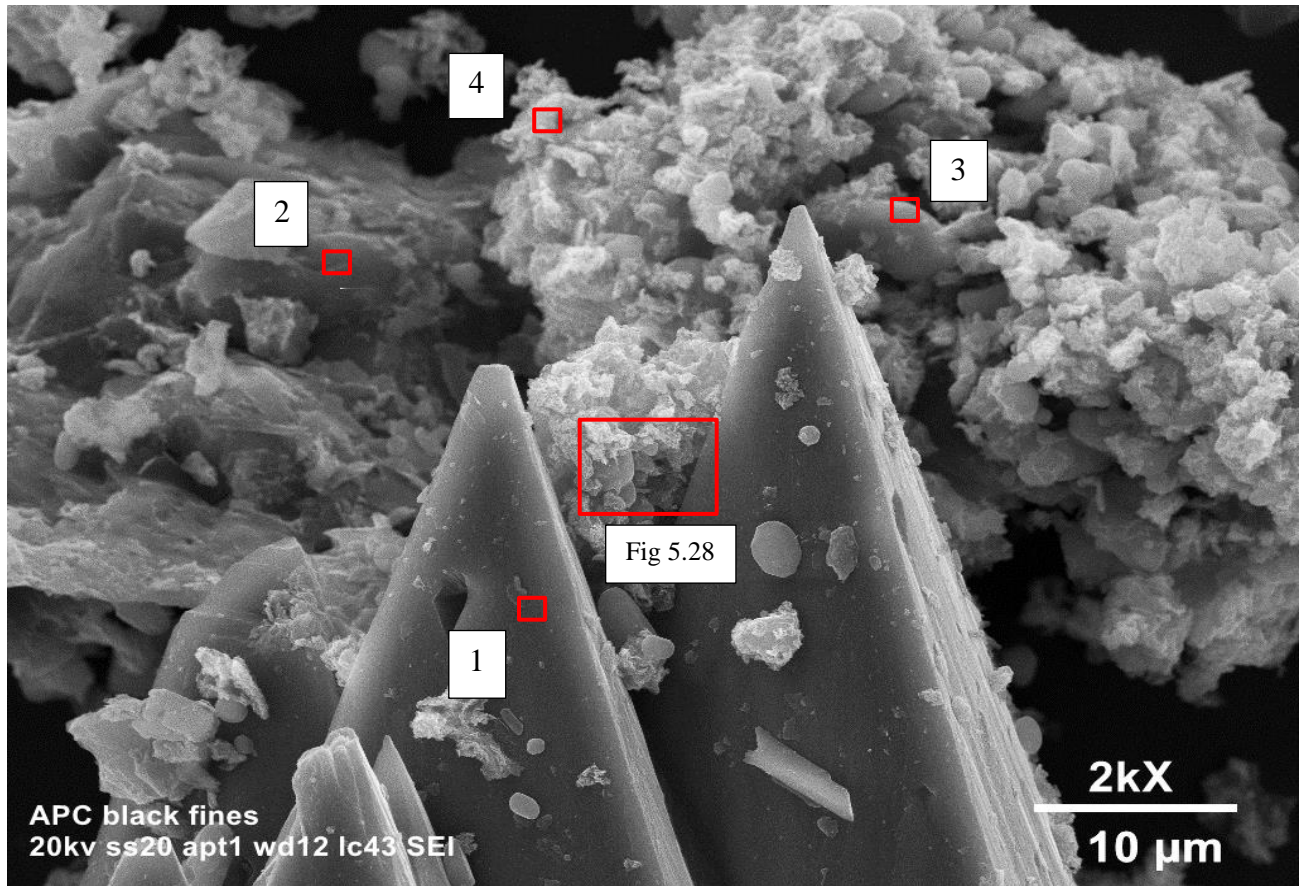


Figure 5.27: Well faceted and striated authigenic calcite with pitted and opalized quartz and Mn-hydroxide fabric. Scan 1: Calcite; Scan 2: Pitted Quartz; Scan 3: Opal-A; Scan 4: Manganese-oxide corrosion residue (see Appendix I for EDS results) (Source: Author).

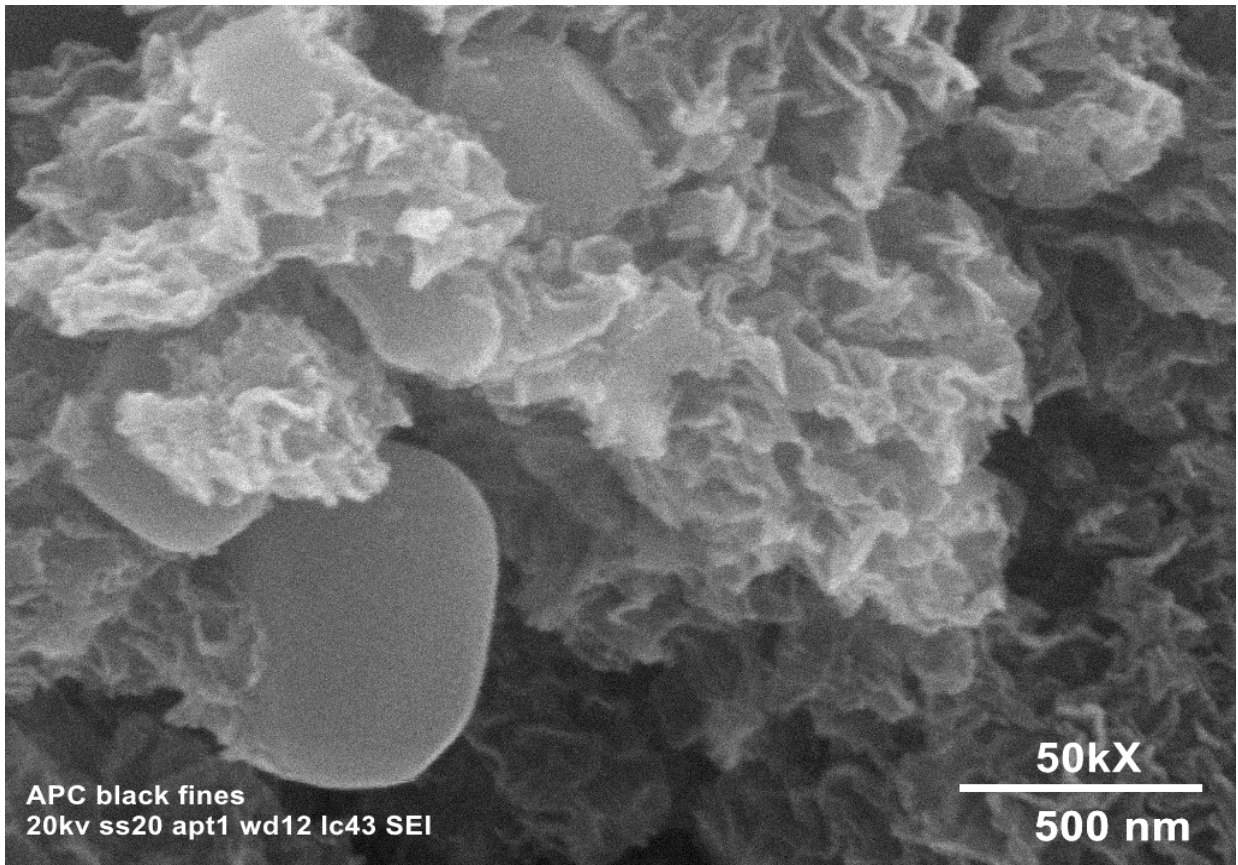


Figure 5.28: Close-up of wispy and furrowed manganese-oxide/hydroxide fabric and opal-A (Source: Author).

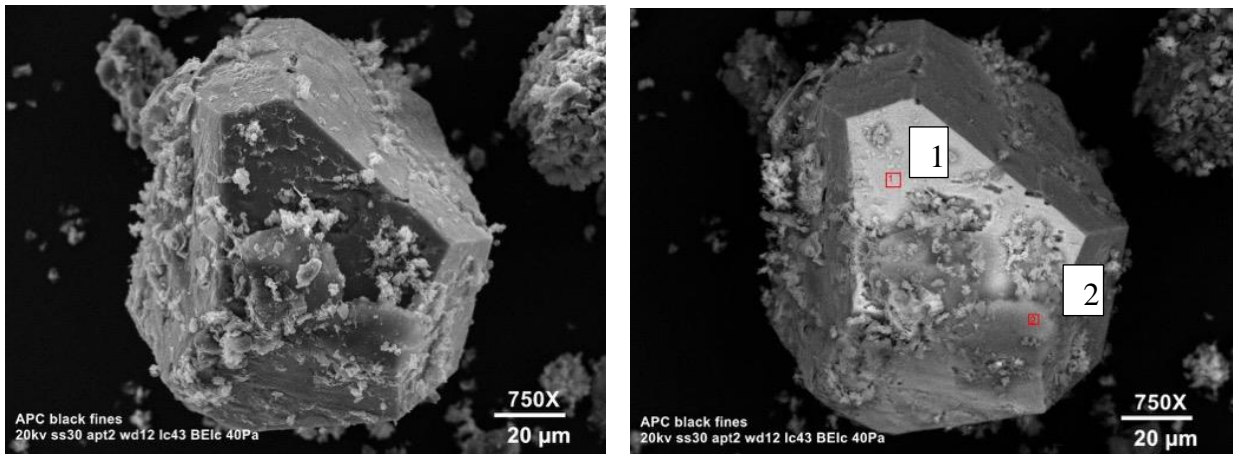
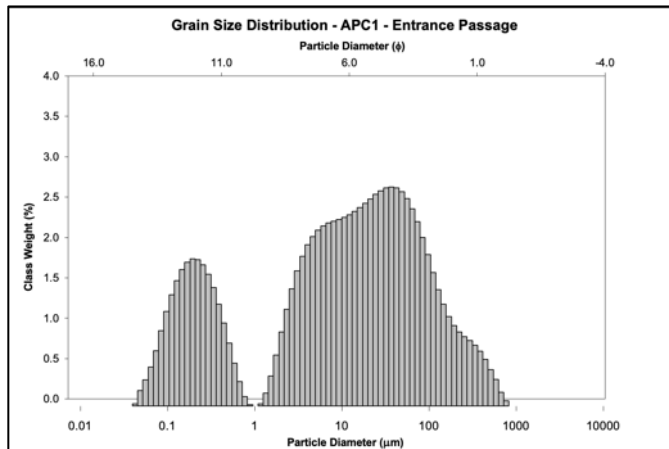


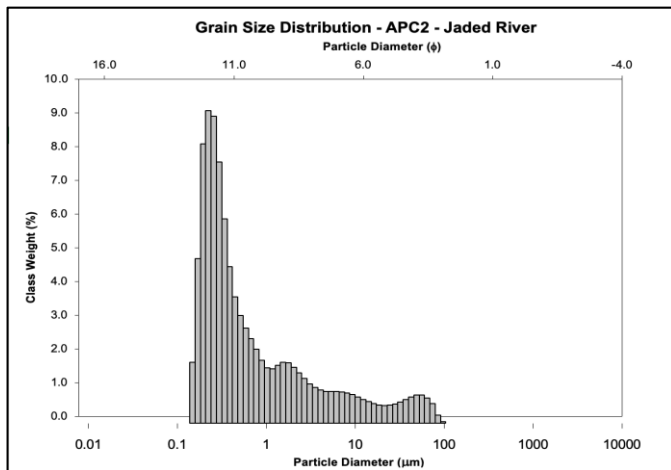
Figure 5.29: Well-faceted fayalite with manganese-oxide/hydroxide coating and opal-A. Scan 1: Fayalite; Scan 2: Weathered alunite rhomboid (see Appendix I for EDS results) (Source: Author).

Grain-size distribution of the four samples reveals notable differences in mean grain size, sorting, and skewness and kurtosis. The APC1 entrance-passage sample consists of very-fine sandy coarse silt that is very poorly sorted, fine skewed, and mesokurtic (Figure 5.30). The dark red clay samples (APC2 and APC4) are considerably fine-grained and exhibit differing sorting, skewness and kurtosis. Both APC2 and APC4 samples are very coarse skewed and very leptokurtic with mean grain sizes of 0.22 and 0.62 microns, respectively. The dark red clay samples are better sorted with leptokurtic peaks (Figure 5.31 and 5.32). The APC3 sample of the black fines material is notably different from the three other samples by being moderately sorted, symmetrical, mesokurtic and with a mean grain size of 11.25 microns (Figure 5.33).



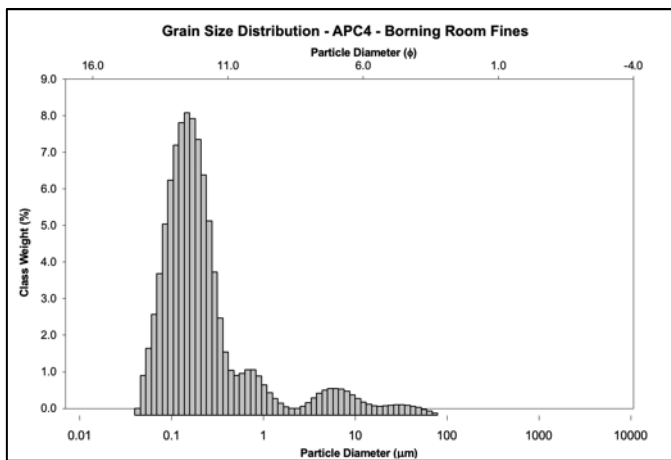
Mean (mm/φ)	6.58/ 7.25	Fine Silt
Sorting (φ)	3.68	Very Poorly Sorted
Skewness (φ)	0.29	Fine Skewed
Kurtosis (φ)	1.02	Mesokurtic

Figure 5.30: APC1 Entrance Passage; very fine sandy coarse silt, dark reddish brown (2.5YR 2.5/4), trace angular limestone gravel, trace organics (roots and animal refuse) (Source: Author).



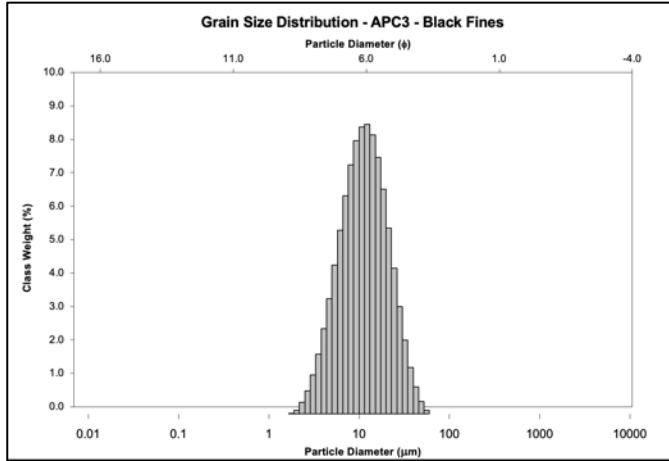
Mean (mm/φ)	0.71/ 10.47	Clay
Sorting (φ)	2.22	Poorly Sorted
Skew. (φ)	-0.63	Very Coarse Skewed
Kurt. (φ)	1.12	Very Leptokurtic

Figure 5.31: APC2 Jaded River Fines; clay, dark red (2.5YR 3/6), slight laminations throughout with black fine-grain material (Source: Author).



Mean (mm/φ)	0.22/ 12.18	Clay
Sorting (φ)	1.72	Poorly Sorted
Skew. (φ)	-0.47	Very Coarse Skewed
Kurt. (φ)	1.96	Very Leptokurtic

Figure 5.32: APC4 Boring Room Fines; clay, dark red (2.5YR 3/6), slight laminations throughout with black fine-grain material (Source: Author).



Mean (mm/φ)	11.25/ 6.74	Medium Silt
Sorting (φ)	0.89	Moderately Sorted
Skew. (φ)	0.03	Symmetrical
Kurt. (φ)	0.97	Mesokurtic

Figure 5.33: APC3 Black Fines; medium silt, black (2.5YR 1.5/1) (Source: Author).

5.4.2 Cave Morphology

The upper-level passages in Ancient Palace Cave are exclusively phreatic with rounded, elliptical cross sections and broad-scalloped scours and ceiling pockets. Original bedrock surfaces are poorly exposed in the lower-level chamber from extensive ceiling breakdown. Side passages off the lower chamber expose strongly phreatic morphology with broadly scoured walls and overall ramiform geometry. Dead-end rising passages and cupolas are common in the upper and lower portions of the cave.

5.5 Rileys Cave

5.5.1 Sediment Mineralogy and Grain Size

Three grab samples were collected at the cave entrance and inside the cave and were analyzed for grain size distribution and clay mineralogy. Sample R3 was retrieved from the in-cave sediment sink as a representative sample of the passage fill at that location. Sample R4 was collected from a calcite-coated 0.6x2 m pocket/ledge paleo-fill ledge approximately 1.5-meters

above the floor. Sample R5 was taken on the surface approximately 15-meters up-slope from the upper sinkhole entrance.

The sample R5 collected from the cave entrance slope was analyzed via XRD clay-mineral procedures and contains clinochlore (Mg-chlorite), illite, and quartz (Figure 5.34). The two samples collected in-cave, R3 and R4 (R4 figure not shown), were analyzed with XRD and both contain clinochlore, illite, and quartz (Figure 5.35). The high relative intensity of the chlorite 14A peak after heating to 550C suggests the presence of the Mg-rich form, clinochlore. The surface sample, Illite is present in all samples as a stable 10A peak. Quartz peaks are present as sharp peaks at 3.34A and 4.26A (Poppe et al., 2001; Moore and Reynolds, 1997).

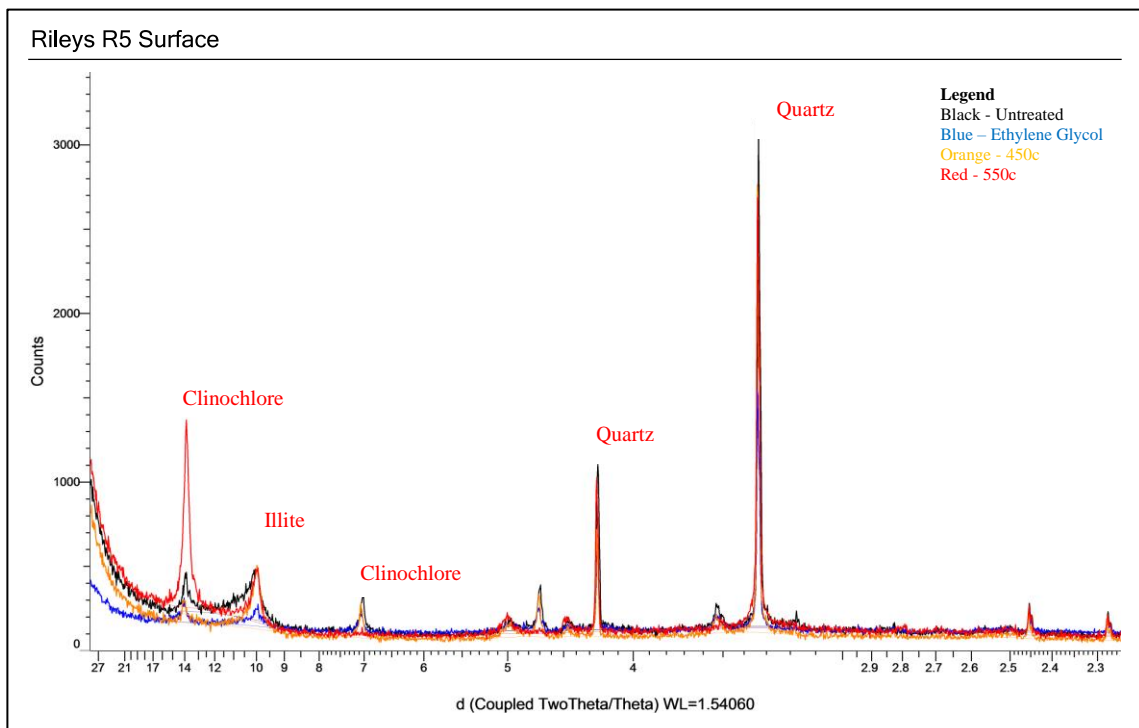


Figure 5.34: Composite XRD scan of Rileys R5 Surface; 14A – clinochlore; 10A – illite. Quartz peaks are present as sharp peaks at 3.34A and 4.26A (Source: Author).

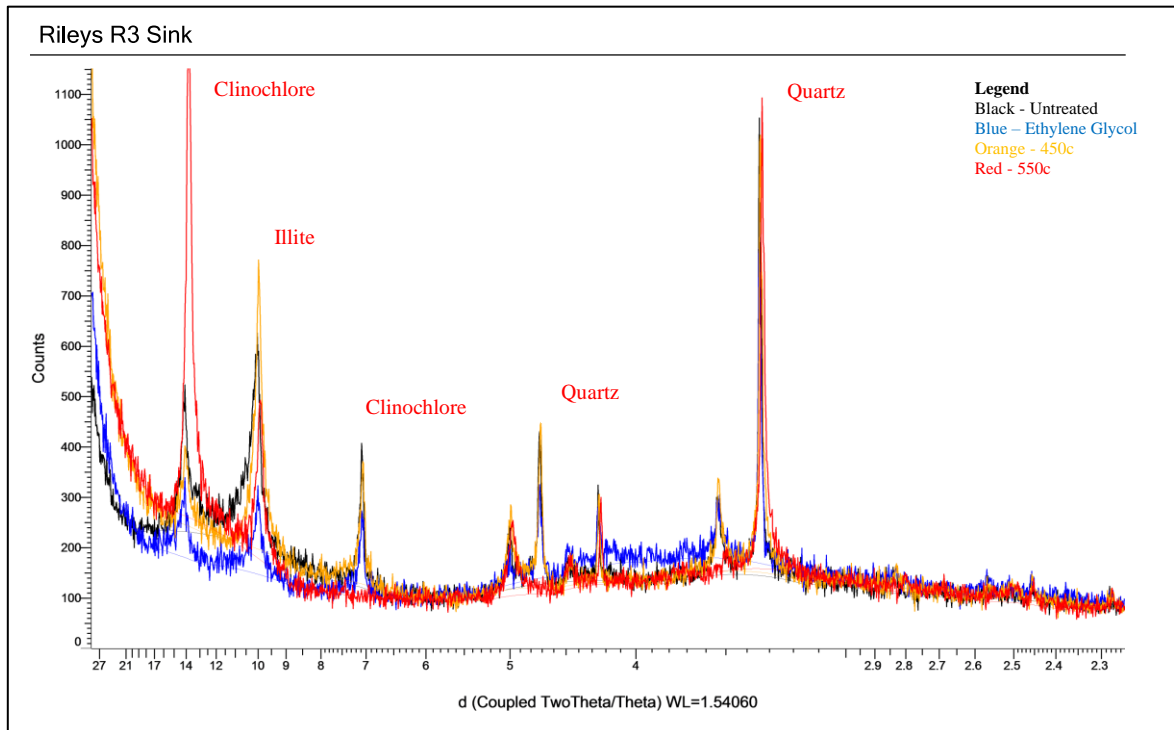
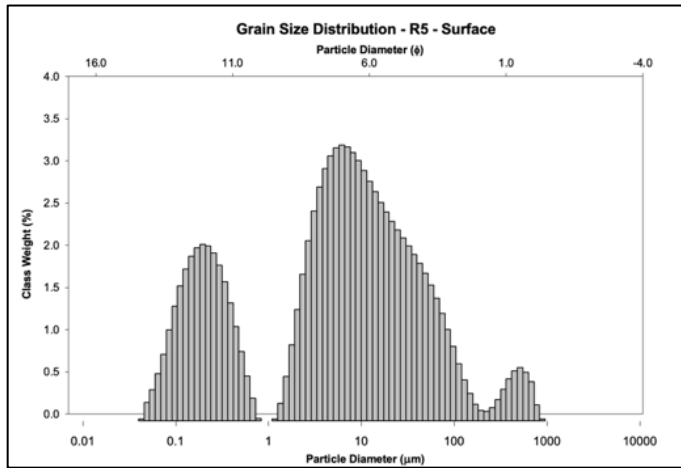


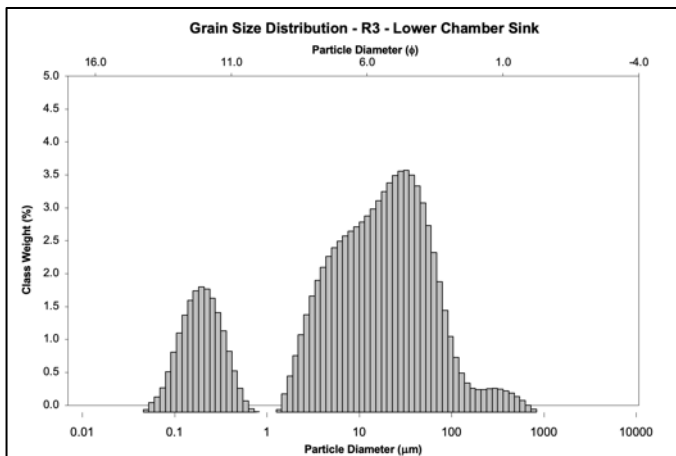
Figure 5.35: Composite XRD scan of Rileys R3 Lower Chamber Sink; 14A – clinochlore; 10A – illite. Quartz peaks are present as sharp peaks at 3.34Å and 4.26Å (Source: Author).

Grain-size distribution of the five samples shows a range from coarse silt to very fine sandy coarse silt and all samples are very poorly sorted and bimodal. All samples share a clay fraction mode with clay content ranging from 7-22%. The two samples collected in-cave, R3 and R4, showed similar peak geometry and presence of a clay-sized mode of similar percentage (19 and 22%). Both samples are very fine skewed and are leptokurtic (positive kurtosis larger than that of a normal distribution) with near identical distribution statistics (Figure 5.36 – 5.38).



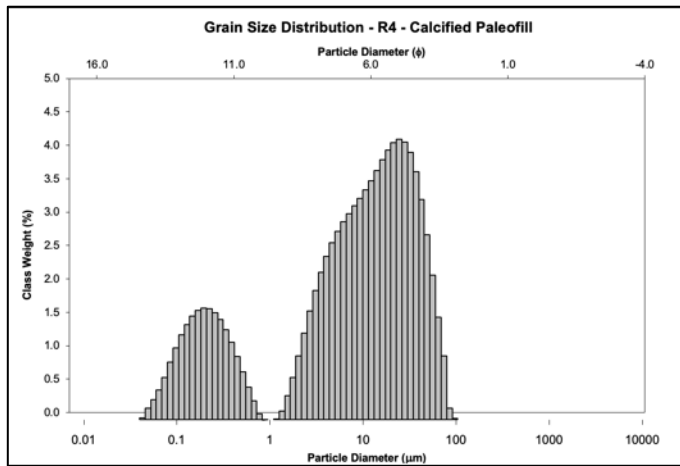
Mean (mm/φ)	13.16/ 6.25	Medium silt
Sorting (φ)	1.98	Very Poorly Sorted
Skewness (φ)	-0.238	Coarse Skewed
Kurtosis (φ)	1.04	Mesokurtic

Figure 5.36: Rileys R5 Surface; very fine sandy fine silt, dark reddish brown (5YR 3/2), minor organics (roots, leaf fragments, mycelium) (Source: Author).



Mean (mm/φ)	17.84/ 5.81	Fine Silt
Sorting (φ)	3.36	Very Poorly Sorted
Skewness (φ)	0.05	Symmetrical
Kurtosis (φ)	0.91	Mesokurtic

Figure 5.37: Rileys R3 Lower Chamber Sink; very fine sandy coarse silt, dark yellowish brown (10YR 3/4), trace angular limestone gravel, trace calcite coralloid fragments, minor organics (roots and animal refuse) (Source: Author).



Mean (mm/ ϕ)	13.65/ 6.20	Coarse silt
Sorting (ϕ)	1.42	Poorly Sorted
Skewness (ϕ)	0.12	Very Fine Skewed
Kurtosis (ϕ)	0.84	Platykurtic

Figure 5.38: Rileys R4 Calcified Paleo-fill; coarse silt, dark yellowish brown (10YR 5/6), trace limestone gravel, trace organics (root and leaf fragments) (Source: Author).

5.5.2 Cave Morphology

Passages in Rileys Cave are heavily joint and bedding controlled and are commonly phreatic. Joints are predominantly perpendicular to the surface slope and bedding strike and bedding strike/dip is approximately 320/20 degrees NE. Cross sections vary from bedding to joint controlled but are primarily elliptical and broadly scalloped. Multiple passages form on a set of parallel, vertical joints that trend near perpendicular to the adjacent cliff face.

The two active entrances and apparent collapsed entrances form on the parallel vertical joints. The southern ceiling of the central chamber is characterized by up to 1.5 m long roof pendants and anastomotic ceiling channels. The pendants and ceiling channels are developed on both sides of a ceiling inlet passage that connects the upper and lower levels of the cave.

Pendants and prominent ceiling channels are primarily exposed in the southern portion of the main chamber.

5.6 Lake Shasta Caverns

5.6.1 Sediment Mineralogy and Grain Size

Four samples were collected at Lake Shasta Caverns and were analyzed for clay mineral composition via XRD and for grain-size distribution. Two samples, LSC3 and LSC4, were analyzed with SEM-EDX to further evaluate constituent mineralogy. The LSC1 sample was retrieved from the slope closely adjacent to the one natural entrance to the cave. The LSC2 sample was collected from a light olive brown (2.5Y 5/4) finely-laminated ledge deposit along the southern wall of the Signature Room approximately 1.6 meters above the current floor surface. The LSC3 sample was collected from an approximately 12 cm thick bed of well-stratified, light gray (10YR 7/2) fine-grained material laying stratigraphically above an 80-cm thick bed of poorly-sorted and well-imbricated sand and gravel. The LSC4 sample was collected from an approximately 10-cm thick floor deposit of yellow (10YR 8/8) fine-grained material coated in two to three-cm of calcite coating and coralloid growth (Figure 5.39). The LSC4 sample was collected approximately three meters away from the LSC3 sample on the floor of the

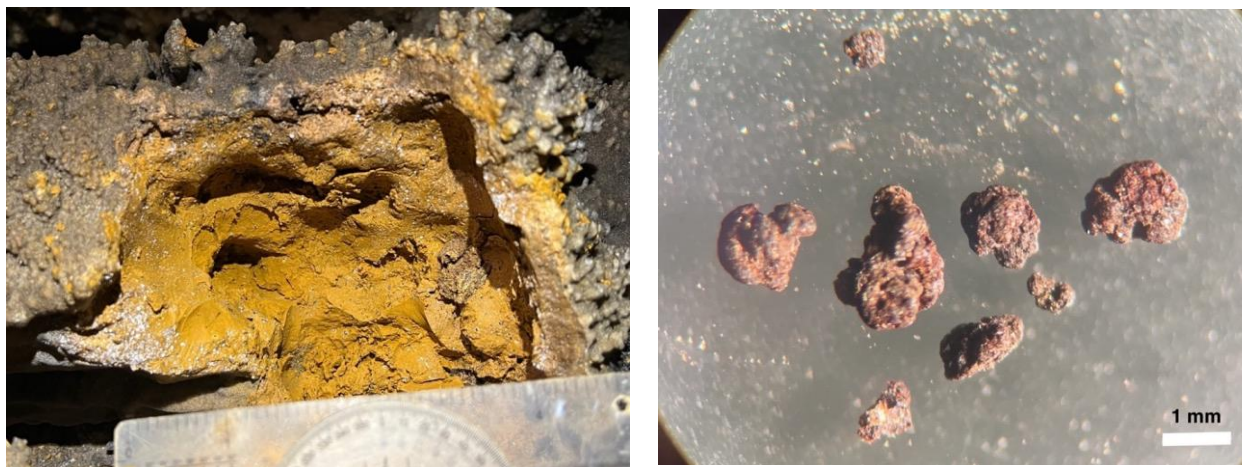


Figure 5.39: Left - Poorly stratified and calcite-coated kaolinized tephra with trace Fe-Mn imogolite-allophane nodules. Right – Optical microscope view (reflected light) of Fe-Mn imogolite-allophane nodules (Source: Author).

passage that they are both preserved. The four samples collected at Lake Shasta Caverns were analyzed with XRD to evaluate constituent mineralogy. The entrance sample, LSC1, contains vermiculite, chamosite, illite, and quartz (Figure 5.40). Vermiculite is present as a 14A peak that progressively collapses through heating from 400c to 550c. Illite is present in minor quantities, and presents as a weak 10A peak that remains stable through heating and EG treatment (Pope et al., 2001; Moore and Reynolds, 1997). Sample LSC2 was retrieved from the finely-laminated ledge deposit in the Signature Room and contains chamosite, illite, and quartz (Figure 5.41). Chlorite is present as a 14A peak that increases in intensity through heating to 550c. The Fe-rich form of chlorite, chamosite, is likely present based on the low relative intensity of the 14A peak and relative high intensity of the 7A peak (Moore and Reynolds, 1997).

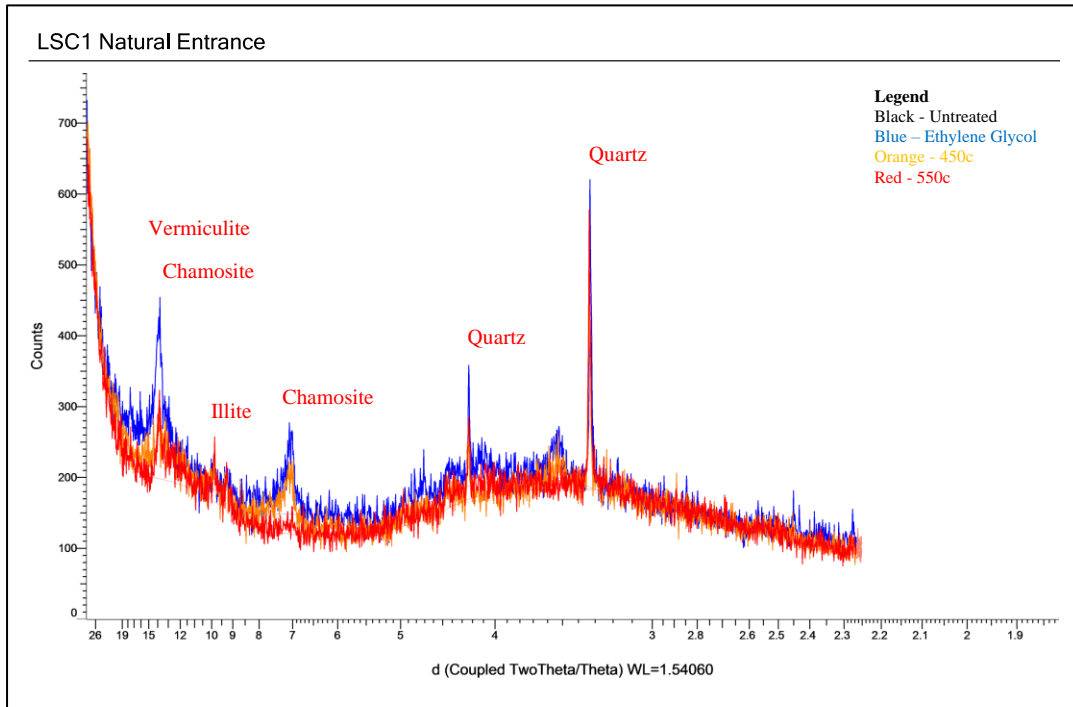


Figure 5.40: Composite XRD scan of LSC1 Entrance Slope; 14A – vermiculite; 14A – chamosite; 10A – illite. Quartz peaks are present as sharp peaks at 3.34Å and 4.26Å (Source: Author).

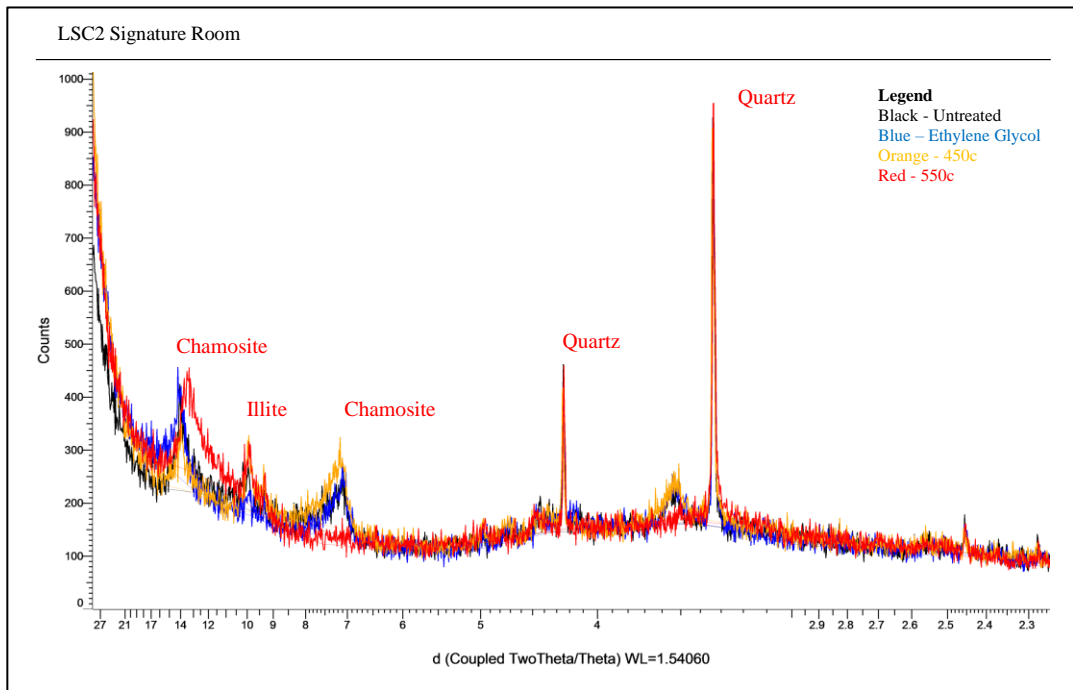


Figure 5.41: Composite XRD scan of LSC2 Signature Room; 14Å – chamosite, 10Å – illite
 Quartz peaks are present as sharp peaks at 3.34Å and 4.26Å (Source: Author).

Illite is present as a stable 10Å peak that remains stable through heating and EG treatment.

Quartz is present in both LSC1 and LSC2 samples as sharp peaks at 3.34Å and 4.26Å. Two samples, LSC3 and LSC4, are not plastic enough to make oriented slide mounts so powdered samples were prepared for XRD. The produced XRD pattern closely resembles that of halloysite, allophane, and quartz (Figure 5.42) (La Ba, 2020). SEM-EDS was used to further evaluate constituent mineralogy and grain morphology.

SEM-EDS analyses on LSC3 and LSC4 suggests the material is a corroded and devitrified tephra that has been altered in-situ to a suite of short and long-range order aluminosilicates. Short order mineraloids being material with local crystalline order and broad disorder, making them amorphous. Long-order minerals being broadly ordered and with more defined crystal structure. SEM of samples LSC3 and LSC4 shows that both samples are

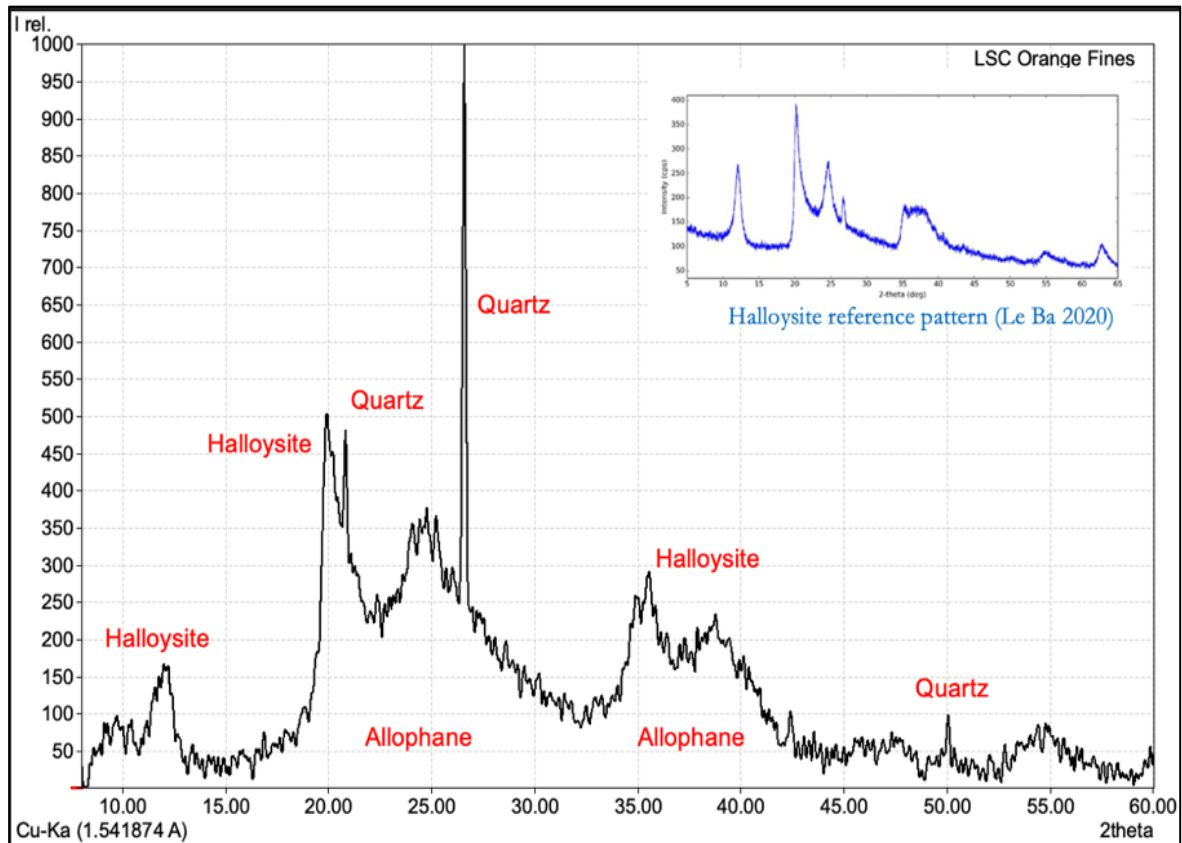


Figure 5.42: XRD scan of powdered LSC3 Yellow Fines at 3-90 2theta, 1s step time, 0.02 deg increment. 7A - Quartz peaks are present as sharp peaks at 3.34Å and 4.26Å (Source: Author).

primarily made up of irregular, vesiculated shards with trace sand-sized nodules. The shards are mostly elongate and/or broadly curved and often show vesiculation (Figure 5.43). An EDS analysis on the tephra shards in both samples suggests the tephra shards have weathered to a near 1:1 Al:Si aluminosilicate (Figure 5.44). Tephra in soil deposits weather from silica pumice glass to halloysite, allophane, and imogolite depending on depositional environment and elemental constituents (Fieldes, 1955). The presence of near 1:1 Al:Si altered tephra glass in all EDS scans suggests that halloysite and allophane has formed inside weathered tephra fragments (Figure 5.44) (Lowe, 1986). The LSC3 yellow tephra sample contains nodules of Fe-Mn aluminosilicate with Al:Si of near 2:1, suggesting the presence of proto-imogolite and allophane (Lowe, 1986).

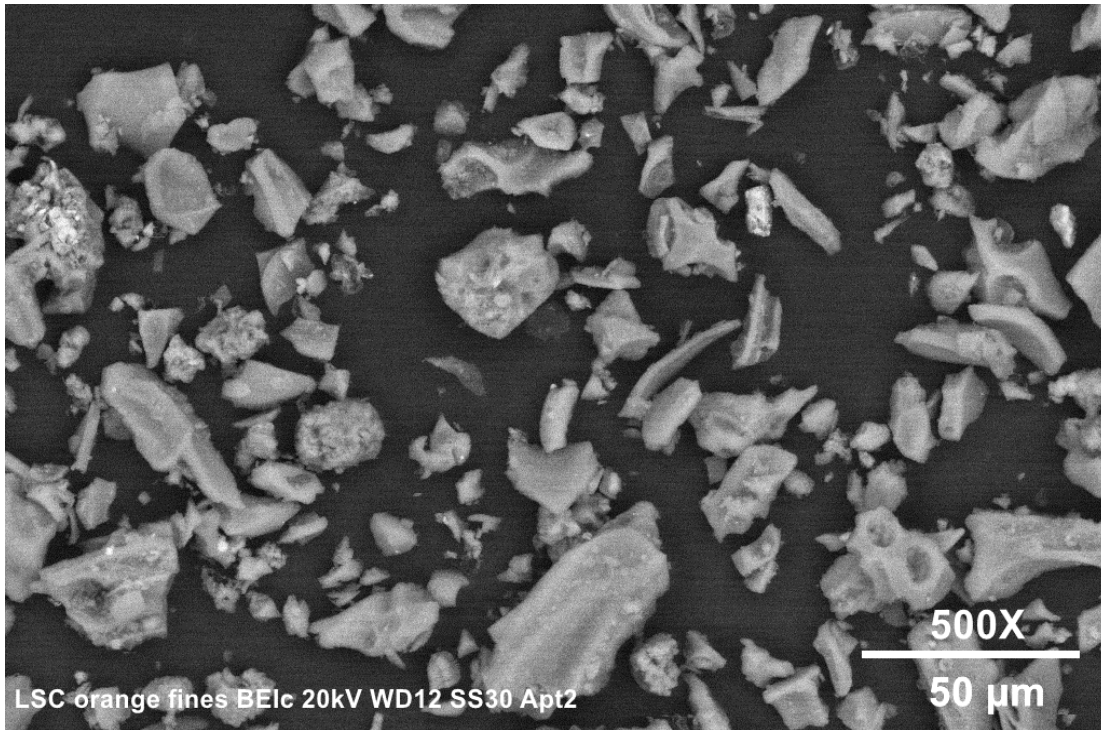


Figure 5.43: SEM image of altered tephra shards (Source: Author).

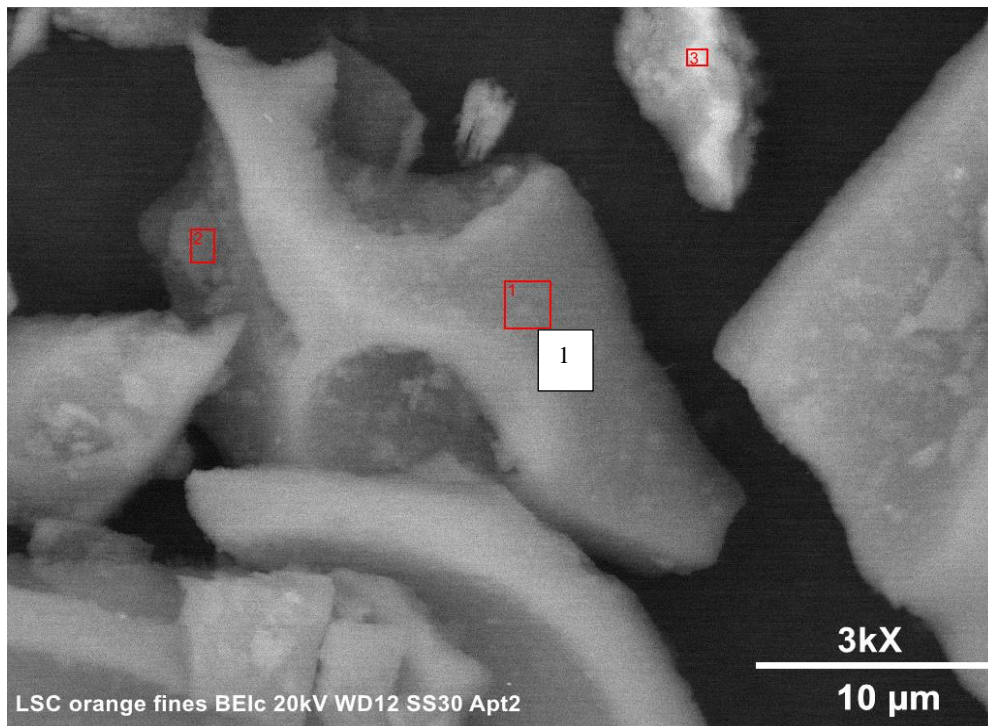


Figure 5.44: Angular tephra shard altered to halloysite and allophane (see Appendix I for EDS results) (Source: Author).

The presence of near 1:1 Al:Si aluminosilicates in the two LSC3 and LSC4 samples suggests in-situ alteration to allophane and imogolite and formation of authigenic halloysite (Dowd, 2017; Churchman et al., 2016; Almquist, 2011; Fieldes, 1955). Platy clay morphology is seen filling in the angular voids of the Fe-Mn nodules, suggesting the presence of authigenic platy halloysite (Almquist, 2011; Lowe, 1986) Tubular halloysite morphology is not apparent in SEM images. Surface corrosion texture is present on the flat face of a tephra plate in the LSC4 sample (Figure 5.45).

Sand-sized nodules of Fe-Mn imogolite-allophane are present in the orange LSC3 sample and exhibit angular and irregular, commonly clay-filled voids that resemble shard molds (Figure 5.46). The sharp angularity and irregular nature of the brecciated matrix suggests that nodules formed around an agglomeration of tephra shards filling in the interstitial pore-space

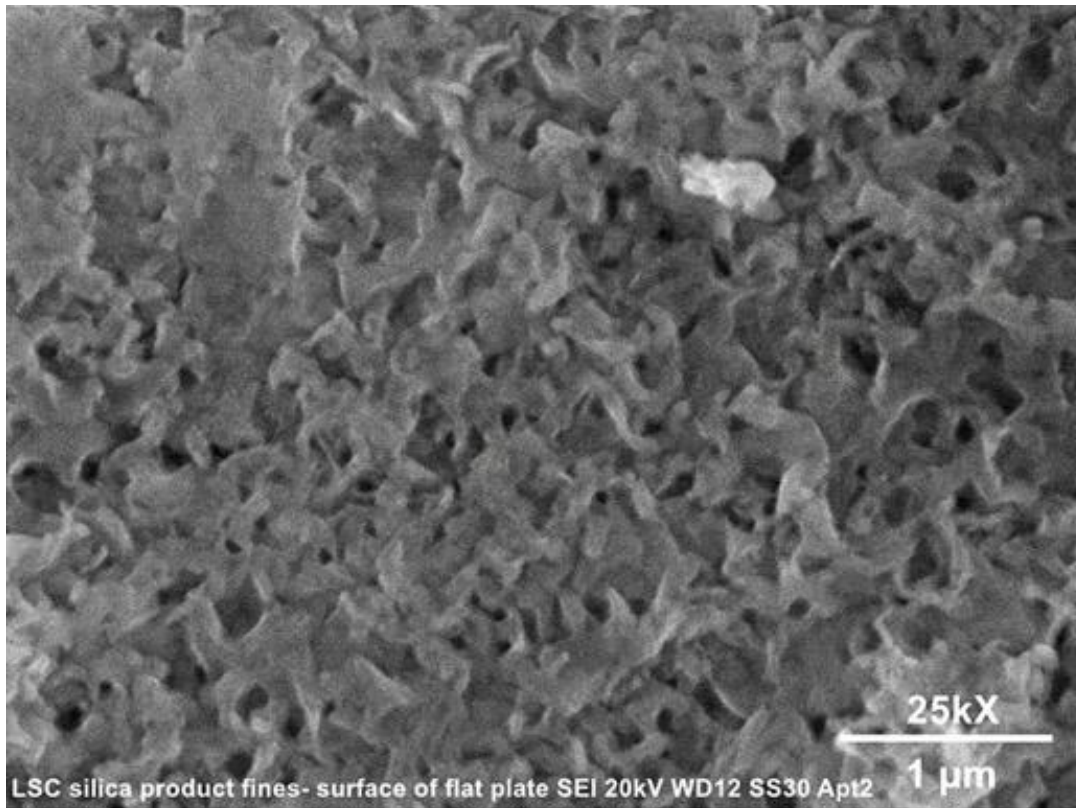


Figure 5.45: Surface corrosion texture on the face a de-vitrified tephra shard (Source: Author).

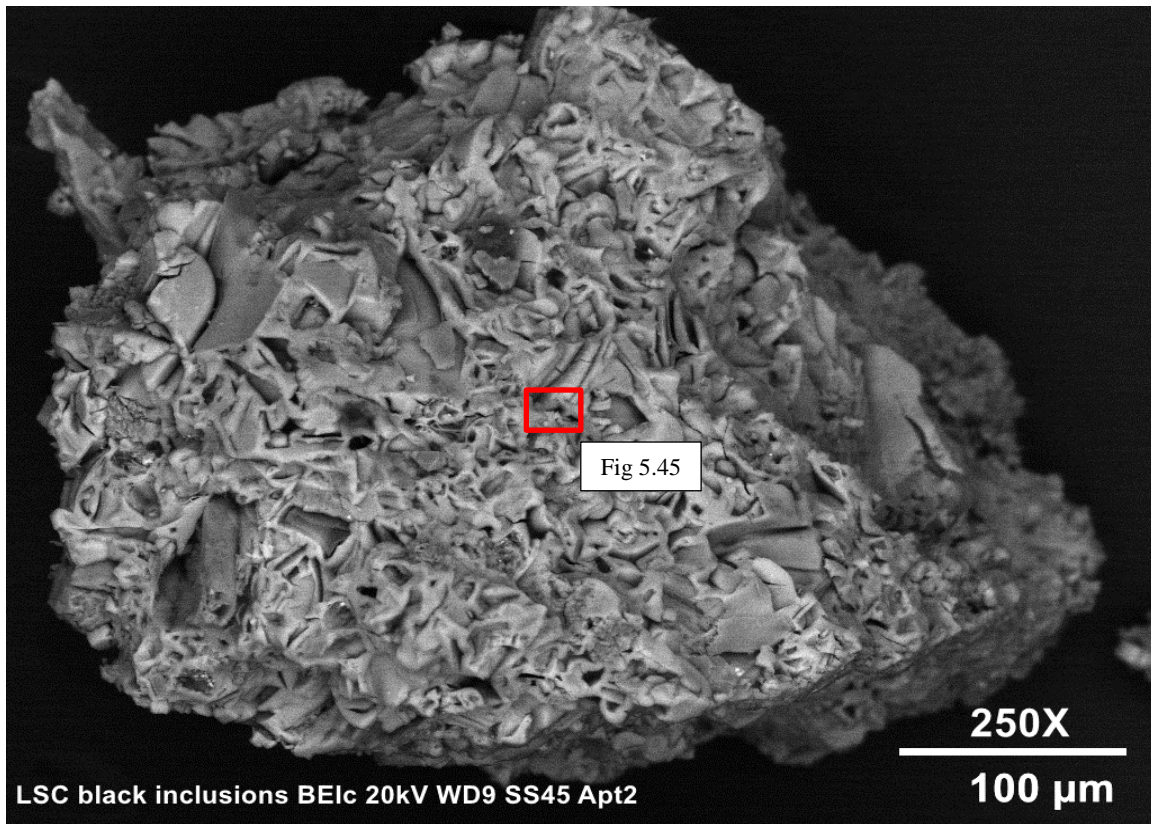


Figure 5.46: Fe-Mn imogolite-allophane nodule with irregular angular voids and amorphous surface texture (Source: Author).

between grains (Figure 5.47). Agglomerations with similar void space geometry are seen in sample LSC4 (Figure 5.48). The botryoidal texture and apparent banding suggest microcrystalline or amorphous mineral growth in the allophane (Figure 5.49). Titanium is present as a trace element and is likely forming ilmenite (see Appendix I for EDS results).

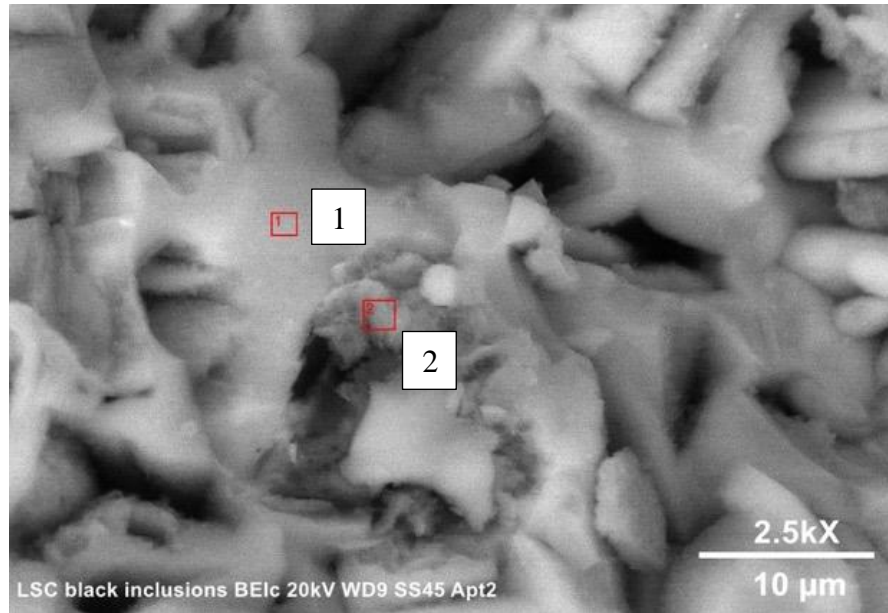


Figure 5.47: Scan 1: Fe-Mn imogolite-allophane with titanium oxide and calcium carbonate;
Scan 2: Angular void fill of near 1:1 Al:Si aluminosilicate, likely platy halloysite
(see Appendix I for EDS results) (Source: Author).

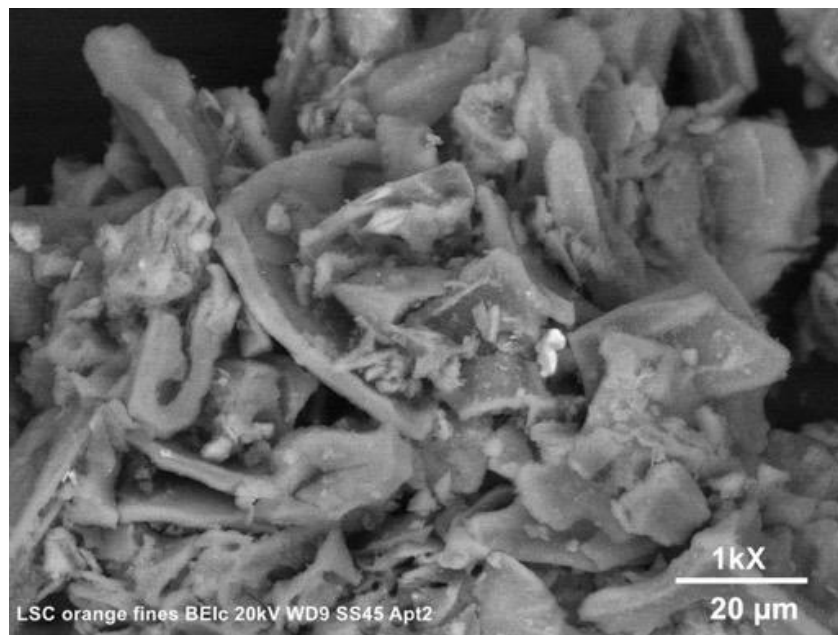


Figure 5.48: Agglomeration of de-vitrified tephra shards (Source: Author).

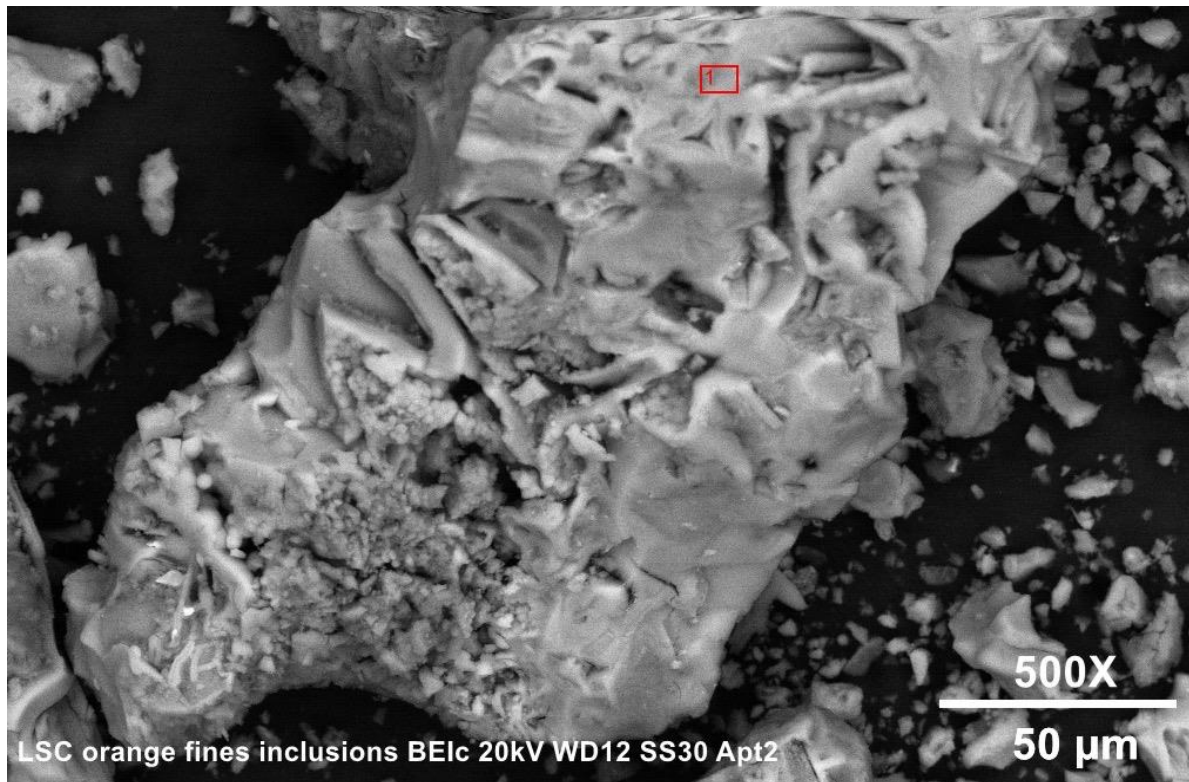
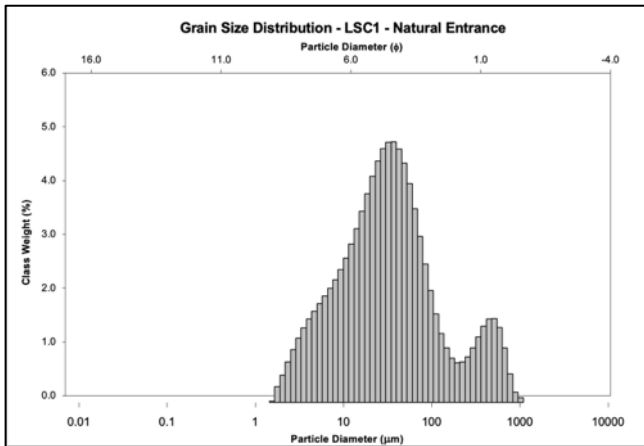


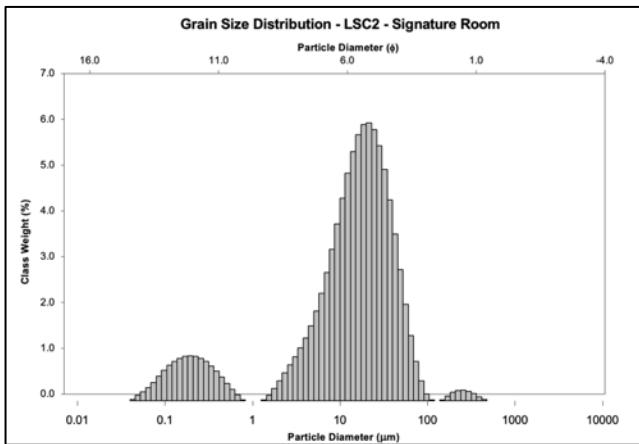
Figure 5.49: Fe-Mn imogolite-allophane nodule with botryoidal surface texture, amorphous banding, and angular molds from agglomerated tephra (Source: Author).

Grain-size distribution was conducted on all four samples and results indicate that mean grain size, sorting, skewness, and kurtosis are similar throughout. All four samples are medium to coarse silt-sized and exhibit similar sorting, skewness, and kurtosis. Of note are the similar mean grain size between LSC3 and LSC4 as well as the overall moderate sorting and mesokurtic nature of all four distributions. Both tephra samples, LSC3 and LSC4, are coarse silt sized (21.76 and 24.65 micron) and moderately sorted. All four samples are medium to coarse silt-sized and are moderately to poorly sorted (Figure 5.50 – 5.53).



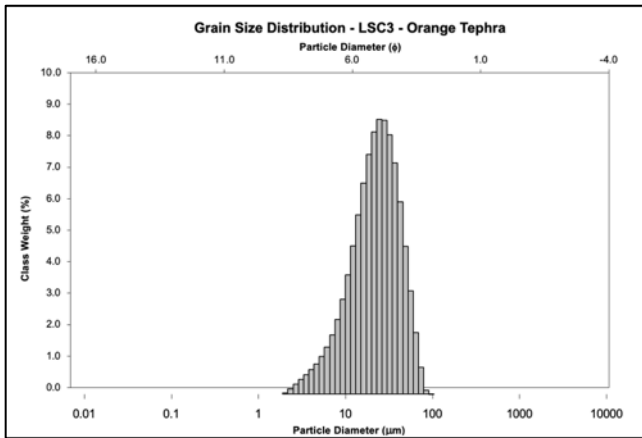
Mean (mm/φ)	31.10/ 5.0	Coarse Silt
Sorting (φ)	1.99	Poorly Sorted
Skewness (φ)	-0.057	Symmetrical
Kurtosis (φ)	1.21	Leptokurtic

Figure 5.50: LSC1 Natural Entrance; very fine sandy coarse silt, light yellowish brown (10YR 6/4), minor angular limestone and diorite gravel, trace organics (roots, leaves, animal refuse) (Source: Author).



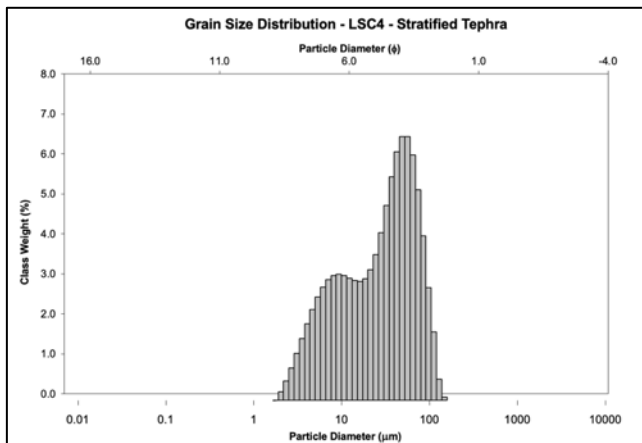
Mean (mm/φ)	16.94/ 5.88	Coarse silt
Sorting (φ)	1.16	Poorly Sorted
Skewness (φ)	0.13	Fine Skewed
Kurtosis (φ)	1.01	Mesokurtic

Figure 5.51: LSC2 Signature Room; coarse silt, light yellowish brown (10YR 6/4), slight stratification with whitish fines (Source: Author).



Mean (mm/ ϕ)	21.76/ 5.22	Coarse Silt
Sorting (ϕ)	0.95	Moderately Sorted
Skewness (ϕ)	0.16	Fine Skewed
Kurtosis (ϕ)	1.04	Mesokurtic

Figure 5.52: LSC3 Yellow Tephra; coarse silt, yellow (10YR 8/8), trace sand-sized Fe-Mn nodules throughout (Source: Author).



Mean (mm/ ϕ)	24.65/ 5.34	Coarse Silt
Sorting (ϕ)	1.48	Moderately Sorted
Skewness (ϕ)	0.30	Fine Skewed
Kurtosis (ϕ)	0.79	Mesokurtic

Figure 5.53: LSC4 Stratified Tephra; coarse silt, light gray (10YR 7/2), slight laminations throughout with yellowish brown fines, trace silt-sized Fe-oxides throughout (Source: Author).

5.6.2 Cave Morphology

Passages in Lake Shasta Caverns are joint and fault controlled and exhibit strong phreatic morphologies. Passage cross-section geometry and scale varies dramatically, and cross sections are commonly elliptical and rounded. Bedrock wall and ceiling surfaces are typically broadly scalloped and form pockets and cupulas of varying sizes. Horizontal notches are cut into the

bedrock in the Signature and Basement Rooms and are continuous around the circumference of the rooms.

The notches in the Signature Room are developed in a pair and both notches are situated within two meters of the floor in a four- to five-meter-tall chamber. The notches are incised approximately 20-30 cm horizontally into the bedrock and are situated approximately 50-80 cm from one another vertically. Cupulas and ceiling pockets are common in the cave and can form spongework-like networks of rising passages that intersect to form windows and archways. The best example of this morphology is in the ceiling of the Basement Room.

5.7 January Cave

5.7.1 Sediment Mineralogy and Grain Size

Two grab samples were collected from January Cave for grain-size distribution and clay mineral XRD analysis. The J3 sample was collected as a bulk sample from the entrance room and represents colluvial material from the surface. The J-C9 sample was taken from the floor of the lower-level chamber towards the middle of the room.

Both samples were analyzed with XRD and grain-size distribution and are markedly different in both mineralogy and texture. The J3 Entrance Room sample contains predominately vermiculite, illite, kaolinite, and quartz (Figure 5.54). The lower chamber sample, J-C9, in contrast contains smectite/montmorillonite, illite, and disordered kaolinite (Figure 5.55). Smectite is evident by its expansive behavior of the 14A peak towards 17A after treatment with ethylene glycol. In addition, the smectite 14A peak will progressively collapse to 10A through heat treatment to 550c. Quartz peaks are lacking in the J-C9 sample from the lower chamber.

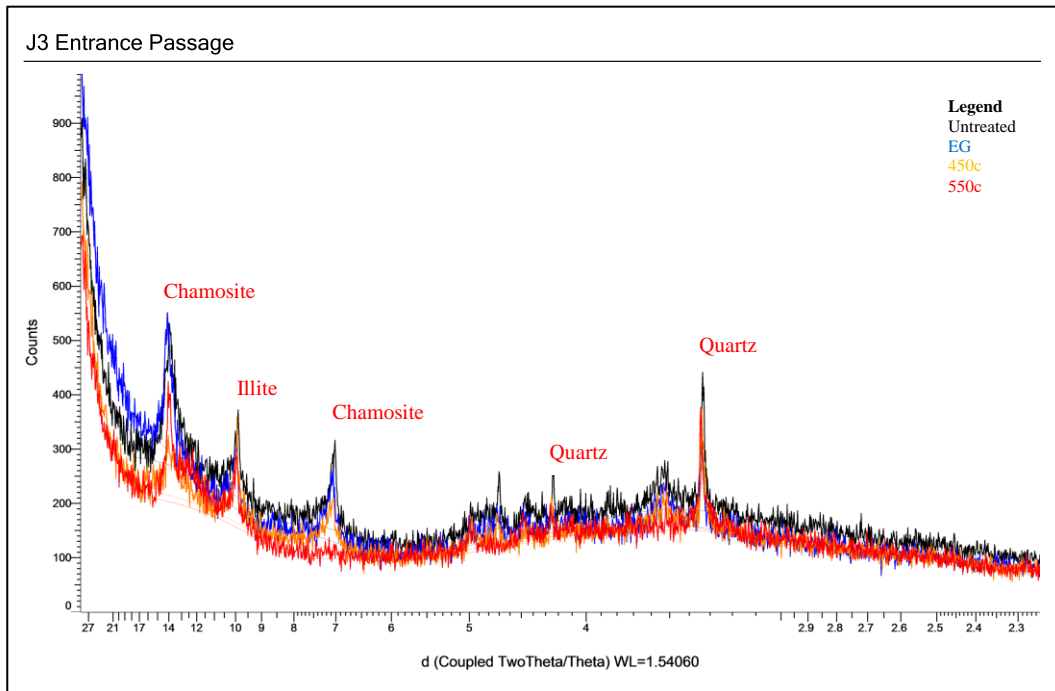


Figure 5.54: Composite XRD scan of January J3 Entrance Room. 14 – chamosite, 10A – illite. Quartz peaks are present as sharp peaks at 3.34Å and 4.26Å (Source: Author).

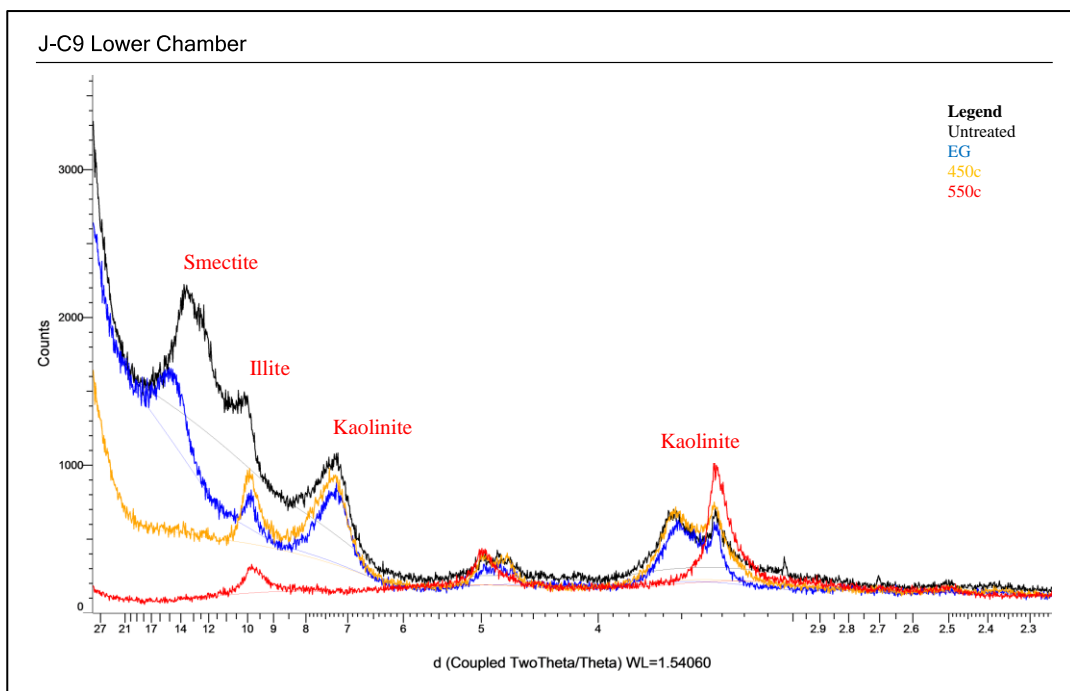


Figure 5.55: Composite XRD scan of January Cave J-C9 Lower Chamber. 14A – smectite; 10A – illite, 7A – disordered kaolinite. Quartz peaks are not present (Source: Author).

Illite is present in both samples by the stable 10A peaks. However, the 10A illite peak in the J-C9 lower chamber sample is conspicuously less intense. The disordered kaolinite is present as broader XRD peaks and generally plaiter crystalline structure rather than hexagonal (Figure 5.55 and 5.56) (Moore and Reynolds, 1997). Quartz peaks are present in the J3 entrance room sample as sharp peaks at 3.34A and 4.26A (Poppe et al. 2001; Moore and Reynolds 1997).

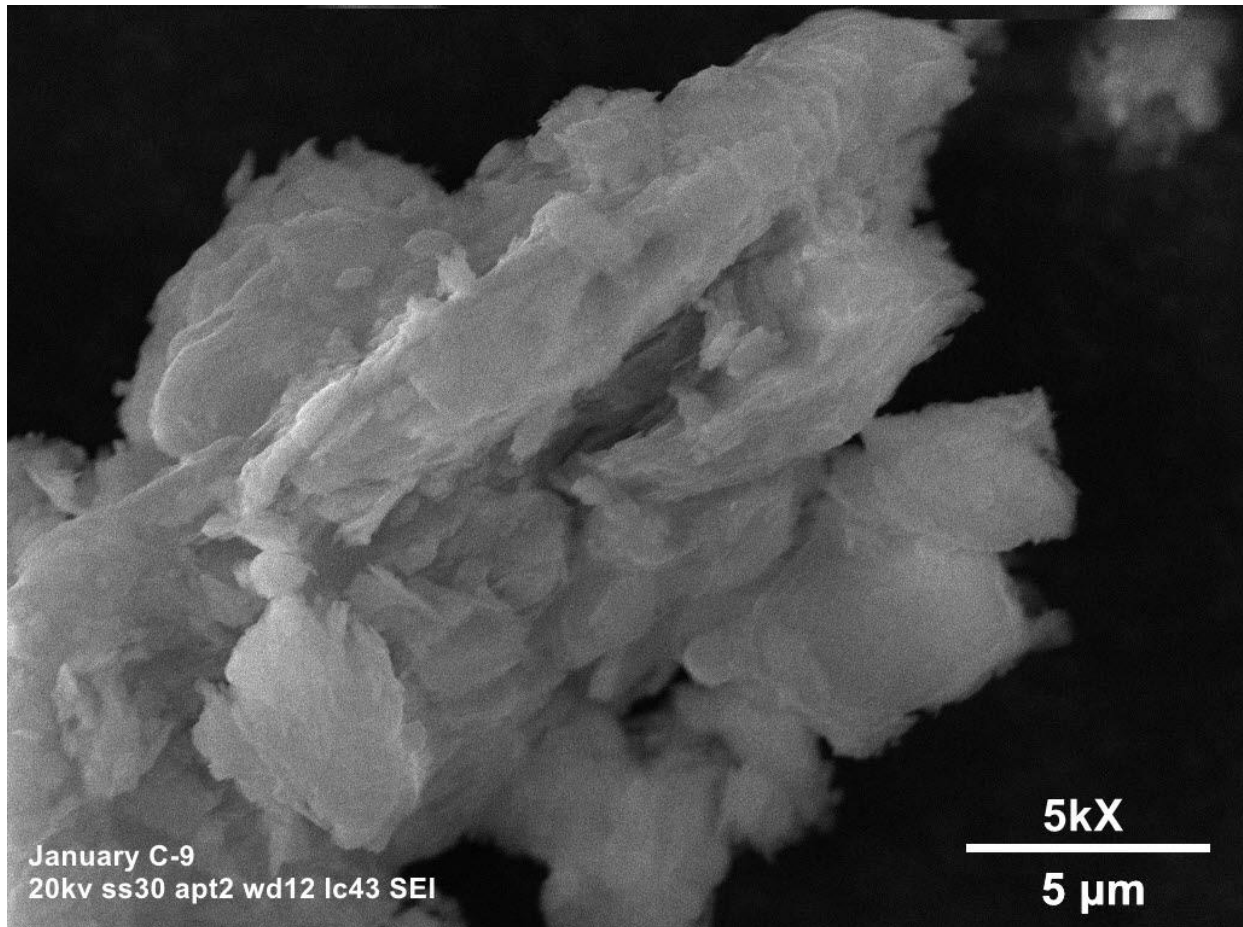
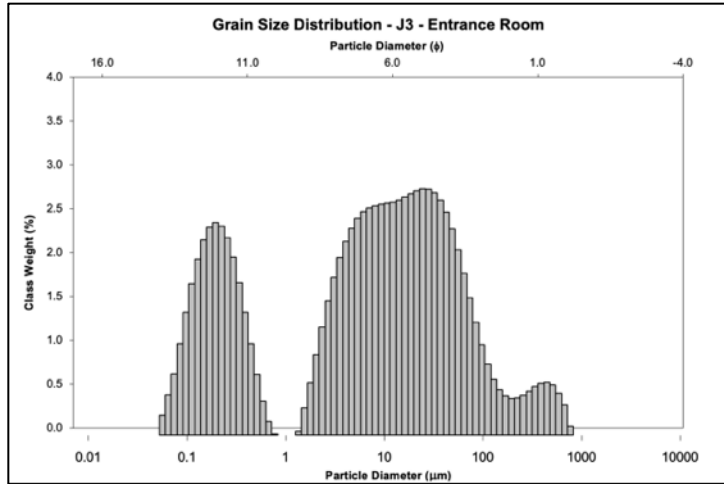


Figure 5.56: View of an agglomeration of platy clay from January Cave J-C9 Lower Chamber. (Source: Author).

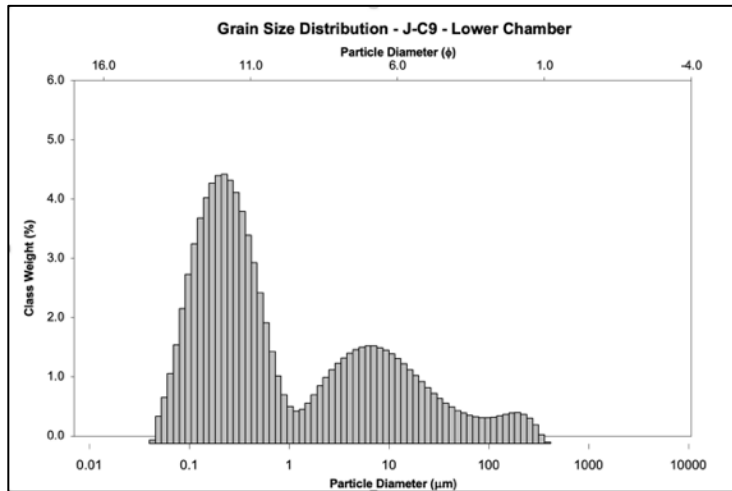
Grain size distribution of both samples indicates similar sorting and kurtosis but notable difference in mean grain size and skewness. The entrance room sample, J3, consists primarily of dark yellowish brown (10YR 3/6) very poorly sorted, very-fine sandy coarse silt that is fine

skewed (Figure 5.57). The lower chamber sample, J-C9, consists of dark red (10R 3/6) very poorly sorted clay with a trace of silt to sand nodules (Figure 5.58). The J-C9 sample is very coarse skewed and bimodal with a mean grain size of 0.89 microns compared to a mean grain size of 4.64 microns for the J3 sample collected in the entrance passage.



Mean (mm/φ)	4.64/ 7.75	Fine silt
Sorting (φ)	3.56	Very Poorly Sorted
Skewness (φ)	-0.1	Symmetrical
Kurtosis (φ)	1.02	Mesokurtic

Figure 5.57: January J3 Entrance Room; very fine sandy coarse silt dark yellowish brown (10YR 3/6), trace angular limestone gravel, trace organics (roots, animal refuse) (Source: Author).



Mean (mm/φ)	0.89/ 10.14	Clay
Sorting (φ)	3.10	Very Poorly Sorted
Skewness (φ)	-0.52	Very Coarse Skewed
Kurtosis (φ)	0.81	Platykurtic

Figure 5.58: January J-C9 Lower Chamber; clay, dark red (10R 3/6), slight stratification with 1-2mm black laminations, trace silt to sand-sized black nodules (Source: Author).

5.7.2 Cave Morphology

January Cave is made up of three primary levels with a steeply dipping joint-controlled rift connecting the levels. The upper and lower levels are made up of gently dipping phreatic chambers with near-circular cross sections. The upper and lower levels are joined by an approximately 20-meter-tall joint-controlled fissure dipping at approximately 80 degrees. Passages in January are commonly phreatic and elliptical with broad scallops and cupulas. Scallops can range from one-half to two-meters wide and cupulas can be up to one-meter deep.

Chapter Six: Discussion

Cave sediments in the McCloud Limestone exhibit mineralogical, textural, and facies patterns that aid in characterizing a history of varied paleohydrologic and speleogenetic regimes. By evaluating the variability and consistencies of sediment mineralogy and texture in the seven study caves, the study was able to answer three research questions pertaining to cave sedimentation in the McCloud Limestone.

- What is the relationship between modes of cave development and the distribution, source, and transport mechanisms of clastic deposits of the caves of the McCloud Limestone?
- Can previously devised cave sediment classifications systems be used to characterize and classify the suites of sediments observed in the study caves of the McCloud Limestone?
- How does karstification and cave sedimentation in the McCloud Limestone relate to regional geologic context and geomorphic development?

The questions are addressed in the following sections with examples from the seven caves studied. Sedimentary relationships are substantiated by clay mineralogy and grain-size trends. Through study of these relationships, a set of facies associations has emerged that characterize distinct paleo-hydrogeologic, depositional regimes. The presence or lack of characteristic depositional regimes or facies associations in each cave further substantiates the differentiation between modes of cave genesis. These relations all together aid in describing the link between cave genesis and regional geomorphic development.

6.1 Cave-Sediment Classification

Sedimentation in the set of seven caves evaluated in this study follow facies associations related to influences from surficial processes such as colluviation and alluviation as well as patterns related to in-cave weathering and in-situ formation of authigenic products. Patterns of sedimentation appear as observable patterns within each cave but also manifest in mineralogical and textural patterns between caves and the surface, and between each cave. Prior studies on the use of lithofacies classifications in caves have been developed in strictly epigene caves and do not expressly address facies deposition in hypogene or polygenetic cave environments (Bosch and White, 2015; Trappe, 2010; Kukla and Ložek, 1958). This study uses modified facies terms as well as introduces new descriptive facies terms that can be used in similar karst environments.

Quantitative and empirical observations of sedimentary patterns from this study necessitated the use of updated facies classifications for the unique nature of polygenetic cave settings. This study introduces ‘infiltrate facies,’ ‘residuum facies,’ and ‘autogenic facies’ and separates ‘infiltrate facies’ from ‘entrance facies,’ ‘crack-filling facies,’ and ‘diamicton facies.’ The proposed ‘infiltrate facies’ and ‘autogenic facies’ are further distinguished from the Bosch and White (2015) ‘backswamp facies.’ The ‘entrance facies’ of Kukla and Lozek (1958) was introduced to describe deposits that consist of colluvium, wind-blown sediments, and freeze-thaw sloughing. It was observed that the ‘entrance facies’ is distinct from the newly proposed ‘infiltrate facies’ by degree and mode of transport and depositional extent. Trappe (2010) introduced the ‘crack-filling facies’ to describe epikarst soil infiltrate that may become mixed with autogenic weathering residuum. In this study ‘infiltrate facies’ was determined to be distinct from ‘entrance facies’ and ‘crack-filling facies’ by depositional setting and extent of sedimentation. Gillieon (1986) describes the ‘diamicton facies’ as being sedimentary facies

consisting of an unbedded and unsorted mixture of a broad range of grain sizes derived from violent flood events. This study distinguishes ‘infiltrate facies’ from ‘diamicton facies’ from a lower range of grain sizes and distinctive epikarstic alluvial transport. This study further distinguishes ‘infiltrate facies’ and ‘autogenic facies’ from ‘backswamp facies’ (Bosch and White, 2015). Bosch and White (2015) introduce ‘backswamp facies’ to describe facies that consist primarily of bedrock weathering residuum and infiltrate material being deposited with little to no lateral transport. However, epikarst infiltrate material was observed to be distinct from autogenic material both in terms of texture and mineralogy. Overall, caves in the McCloud Limestone exhibit distinct relationships between facies and paleo-hydrologic depositional environments. These relationships can be organized into three primary facies associations; epikarst-dominated, fluviially-dominated, and autogenic-dominated. The facies associations consist of characteristic sets of facies that are genetically linked to the paleo-hydrologic conditions of the resulting deposit.

The epikarst-dominated facies associations in the polygenetic caves of the McCloud are defined by entrance infiltrate from colluvial and alluvial (pluvial) processes, infiltration through enlarged joints and faults in the well-developed epikarst, and wind-blown clastic material through large-volume cave entrances (Herman et al., 2012; Williams, 2008). Pluvial in this case is defined by processes relating to the action of effects of rainfall (Jackson and Bates, 1984). Epikarst-dominated sedimentation largely forms entrance facies (Kukla and Ložek, 1958), crack-filling facies (Trappe, 2010), and infiltrate facies. The infiltrate facies is introduced to describe lithofacies with significant colluvial and alluvial influence, poor-stratification, very poor sorting, and low-degrees of weathering. Facies in the epikarst facies association are dominated by colluvial and alluvial (pluvial) processes and are distinct from fluvial facies.

The fluvial facies associations are characterized by fluvially-derived sediments and resulting facies. Fluvial processes largely form channel facies, thalweg facies, diamicton facies, slackwater facies, and backswamp facies (Bosch and White, 2015; Springer and Kite, 1997; Gillieson, 1986). Fluvially-dominated cave sedimentation in the McCloud Limestone is defined by flood-derived slackwater facies with a minor component of suspended and bedload-transported channel and thalweg facies (Bosch and White, 2015). Overall, channel and thalweg facies are rare in the set of McCloud caves studied as well as the larger set of caves that are known in the McCloud Limestone. Very few deposits of coarse-grain (>2 mm) dominant sediments are present in caves of the McCloud Limestone. Where they are present they can be attributed to flood-controlled sedimentation and are rarely associated with consistent channelization.

Autogenic-dominated facies associations in the McCloud Limestone are defined by autogenic bedrock residuum and authigenic mineral and mineraloid products. The lithofacies associations include the 'residuum facies' and the 'authigenic facies.' Bedrock weathering residuum is observable as autogenic grains of Fe-rich olivine (fayalite) and pitted and corroded quartz (Figure 5.27). The fayalite is a relatively resistant, high-temperature mineral, that likely did not form authigenically. The fayalite is likely eroding out of dikes of altered diorite in the Borning Room of Ancient Palace Cave. The resulting material would be described as 'residuum facies.' The 'authigenic facies' describes the ubiquitous authigenic clay in Ancient Palace and January Cave, the Fe-Mn imogolite-allophane nodules forming in extensively altered tephra in Lake Shasta Caverns, and the condensation corrosion-induced ferromanganese deposit (FMD) in Ancient Palace Cave. The autogenic facies association and resultant 'residuum facies' and 'authigenic facies' are characterized by mineralogy and grain-size distribution that is distinct

enough to split from the 'backswamp facies' classification. Bedrock weathering residuum and weathering by-products have been identified in many caves in both epigene and hypogene settings (White, 2007; Polyak and Guven, 2000; Foos et al., 2000). In epigene settings, weathering residuum is defined by insoluble residue left after the dissolution of bedrock and may consist of quartz sand, chert, and silicified fossil fragments (White, 2007). In hypogene settings, authigenic by-products are defined by unique clay minerals such as endellite, montomillonite, and palygorskite (Polyak and Guven, 2000; Foos et al., 2000) and ferromanganese corrosion residue induced by microbial action and condensation corrosion (Spilde et al., 2006; Northup and Lovoie, 2001; Dotson et al., 1999). The three depositional patterns and resultant facies (epikarst, fluvial, and autogenic) are evident within the seven caves that were analyzed in this study through depositional, mineralogical, and textural evaluation.

6.2 Epikarst-Dominated Facies

Epikarst-dominated sedimentation and resultant facies are a major component of material deposited in Rileys Cave and a minor component of material deposited in Pipevine Cave, Ellery Creek Cave, Tardis Cave, and January Cave. Epikarst sedimentation is not a major mode of transportation and deposition in Ancient Palace Cave or Lake Shasta Caverns, although it occurs locally closest to the entrance(s). In Rileys Cave, epikarst sedimentation is characterized by similarities in clay mineralogy and sediment texture between surface and in-cave sediments as well as pathways of deposition that do not directly involve fluvial or autogenic processes, but rather pluvial and/or gravity-driven processes. The resultant facies can be described as 'infiltrate facies.' Epikarst facies associations forms a minor component in Pipevine Cave, Ellery Creek Cave, Tardis Cave, and January Cave by clear infiltration through epikarst pathways

although for all cases outside of Rileys Cave, there is also distinct transport, sorting, and mineralogical variability.

In Rileys Cave, sediments are characterized as being very poorly sorted sandy silt consisting of Mg-chlorite (clinochlore), illite, and quartz. In-cave samples were collected from the current fill surface as well as paleofill deposits representing prior fill surfaces. All of the in-cave samples analyzed for clay mineral XRD contain Mg-chlorite, illite, and quartz as major constituents (Figure 5.35). Grab samples taken from the surface adjacent to the upper sinkhole entrance of the cave contain the same species of chlorite as well as illite and quartz (Figure 5.34) (Poppe et al., 2001; Moore and Reynolds, 1997). Grain size distribution of both the in-cave and surface samples indicate a low degree of transportation and sorting, although the in-cave samples are notably finely-skewed with an overall coarser mean size (Figures 5.36 – 5.38). The discrepancy between distribution geometry can be explained by the amount of colluvial and channelized pluvial transport that has occurred to emplace the material. The degree of similarity between surface and in-cave mineralogy and texture, as well as the presence of poor stratification and ubiquitous presence of paleofill levels and false floors, suggests that cave sedimentation occurred when passages were exposed to the surface through cliff-side erosion and subsequent colluvial and alluvial infiltration. Colluvial influence would be defined by gravity collapse and soil washdown by pluvial action (White, 2007). Therefore, cave sedimentation did not occur through direct fluvial or autogenic processes. The resulting classification of sedimentation in Rileys Cave would be called an ‘infiltrate facies’ from the high degree of colluvial and pluvial influence, poor-stratification, and very poor sorting.

The infiltrate facies in Rileys Cave is likely forming from the combination of gravity collapse and channelization and resulting alluviation of epikarstic, pluvial water. Since Rileys

Cave shows no evidence of fluvial influence on the sediments or geomorphology, sedimentation could only be occurring through the combination of colluvial and pluvial transport and deposition. The degree that clastic material is being accommodated in void space in unknown lower-level passages suggests that a major sedimentation event occurred in the distant past and the cave is slowly accommodating passage fill through epikarstic, pluvial water channelization, passage-fill incision and transport, and in-cave sink formation.

6.3 Fluvially-Dominated Facies

Fluvially dominated sedimentation and resultant facies associations are a major component of sedimentation in Pipevine Cave, Ellery Creek Cave, and Tardis Cave and a minor component in Riley's Cave and Lake Shasta Caverns. Fluvial sedimentation is not present in Ancient Palace Cave or January Cave. In Pipevine Cave and Ellery Creek Cave, fluvial transport and deposition is defined by flood-dominated facies and reworking by presumed slow-velocity flow regimes. In Tardis Cave, stream piracy and flood-dominated facies are apparent through the prevalence and extent of rounded and well-imbricated coarse material (>2 mm), clay mineralogy distinct from epikarst infiltrate, and associated paragenetic notches and dissolution features.

Fluvial sedimentation in Rileys Cave is evidenced by the channelization of epikarstic water and minor in-cave reworking and sorting. Minor channel facies are therefore present in Rileys Cave but the effect on the overall sedimentation is minimal. Fluvial sedimentation in Lake Shasta Caverns is present as multiple deposits of well-rounded and imbricated sand and gravel along with beds of relatively well-sorted and well-stratified sand and silt (Figure 3.16). The resulting facies in Lake Shasta Caverns are channel and slackwater facies. The fluvial facies in

Lake Shasta Caverns are concentrated in passages at close proximity to a presumed collapsed entrance and are not well distributed throughout the cave.

In Pipevine Cave, sedimentation is characterized by scant entrance passage sediment and a singular deposit of well-stratified and very poorly-sorted sand, silt, and clay in the lower chamber. Fine-grained material, where exposed, shows evidence of deposition in slow moving or stagnant water by a higher degree of stratification and sorting. The exposed stratigraphic section in the lower chamber exhibits a range of sedimentary structures, clay mineralogy, and grain-size characteristics suggesting temporal shifts in provenance and depositional energy. Fine-grained material in the entrance room consists primarily of very poorly sorted sandy silt that is largely quartz and clinochlore (Mg-chlorite). Very little illite was detected in the entrance room sample according to the low relative peak intensity. Samples collected from the lower chamber passage fill consist of interstratified illite-chlorite, illite, and quartz with a distinct bed of vermiculite and kaolinite (Figures 5.16 to 5.19). The varied clay mineralogy and grain-size distribution between the entrance passage and lower chamber suggests the mineral provenance and transport mechanisms are notably different. Current cave sedimentation and resulting facies are dominated by epikarst infiltration through vadose seepage and channelization seen throughout the cave, but there is no clear fluvial input or output. Significant vadose water channelization and vertical transport occur during large-volume rain events, so epikarst infiltration through channelization is likely providing enough suspended-load transport from well-developed epikarst fills overlying the cave. The channelized, alluvial infiltrate is then deposited in a low-flow pool in the lower chamber. Transport, sorting, and subsequent deposition is occurring through in-cave fluvial processes so the overall facies association can be described as fluvially dominated with epikarst influence. The material in the lower chamber can be described as a backswamp facies due to low

lateral transport, low-flow depositional conditions, and mixture of epikarst infiltrate and weathering residuum. Ellery Creek Cave preserves a similar well-stratified, large-volume passage fill that shares genetic similarities with the Pipevine Cave fill but shows notable differences.

Sedimentation in Ellery Creek Cave is characterized by flood-dominated deposition and incision and reworking of in-cave sediments. Facies present in Ellery Creek Cave are slackwater and channel facies with minor infiltrate facies. Sediments in Ellery Creek Cave display a range in mineralogy and texture but are mostly composed of very poorly sorted sandy quartz silt with a distinct clay mode of vermiculite, illite and kaolinite (Figures 5.1 to 5.7). Both samples collected from Boring 13 in the Sump Room passage fill show little variation in vermiculite, illite, kaolinite, and quartz through the depth of the boring, although sample size is minimal. Overall, the sandy silt passage fill in the Sump Room shows variation in depositional energy through shifts in stratigraphic structure and grain-size distribution, but provenance and clay mineralogy appear consistent.

Strata in the passage fill ranges from thinly laminated with one to two mm laminations to massively bedded with minimal structure. Variability in grain size with consistency in clay mineralogy suggests changes in depositional energy but consistency in provenance. The sample collected at the lower entrance of Ellery Creek Cave shows marked difference in mineralogy and grain-size distribution with an overall lack of vermiculite and shared presence of illite and quartz. The entrance sample is notably coarser and relatively well sorted compared to material in the Sump Room passage fill, so a varied mode of deposition is likely. The fine-grained material in the Sump Room and elsewhere in the cave is therefore likely entering the cave as suspended

and bed load through the Sump Room fluvial inlet as well as reworked material coming through epikarst inlets.

Charcoal and wood fragments are common throughout the Sump Room passage fill in Ellery Creek Cave and were carbon dated to establish time constraints on deposition. The sample collected towards the base of the boring and the sample collected at approximately half-depth gave the same radiocarbon date of $12,500 \pm 40$ yr BP (see Appendix II). The two dates were converted from conventional radiocarbon age to calendar year through the “High-Probability Density Range Method” (BeRC, 2015). The similarity in radiocarbon age of the two wood fragments suggests either that deposition occurred rapidly during a series of significant sedimentation events or charcoal and wood fragments are being reworked and redeposited. Charcoal and wood fragments are preserved as individual fragments, as well as well-defined strata ranging in thickness from one to eight cm. One would expect more individual fragments and less stratification if charcoal and wood fragments are strictly reworked, so the former hypothesis of a singular or a series of large-scale sedimentation events around 12,500 years ago is more likely.

Two likely causes of such a large-scale event would be a period of increased biomass and slight warming prior to the onset of Younger Dryas cooling (Cowan, 2022; Vacco et al., 2005; Barron et al., 2003) or continent-wide forest fires as a result of the hypothesized Younger Dryas impact event approximately 12,800 yr BP (Holliday et al., 2023; Powell, 2022; Scott et al., 2011). Regional lake cores records suggests a cool and dry period of lower relative biomass productivity from 16 to 14.7 ka followed by a period of increased biomass productivity and moisture from 14.6 to 12.9 ka (Barron et al. 2003). Vacco and others (2005) studied speleothem records from Oregon Caves National Monument and observed regional-wide cooling occurring at the onset of

the Younger Dryas approximately 12,900 yr BP. Cowan (2022) observed a shift from glacially-derived sediments to non-glacially-derived sediments at approximately $11,340 \pm 660$ yr BP through a notable increase in loss on ignition (LOI) and decrease in magnetic susceptibility. Increased biomass production and a shifting climate towards the onset of the Younger Dryas period could have produced large-scale forest fires and mass sedimentation, although no current record of large-scale biomass burning events are present in the Klamath Mountains at the start of the Younger Dryas (Cowan, 2022; Vacco et al., 2005; Barron et al., 2003). Large-scale biomass burning events have been noted elsewhere during this time and have been attributed to continent-wide forest fires initiated during the Younger Dryas impact event approximately 12,800 yr BP (Powell, 2022; Scott et al., 2011). The Younger Dryas Impact Hypothesis (YDIH) is intensely debated, however, and evidence is scant for catastrophic landscape and biosphere perturbation during this time (Holliday et al., 2023).

Sedimentation in Tardis Cave is characterized by flood and channelization-dominated fluvial facies and associated reworking of epikarst infiltrate. Clastic sediment in Tardis Cave shows the greatest range in grain-size distribution of the caves studied with fine clay to coarse gravel (Figure 5.12 to 5.14). Clay mineralogy also shows a great range with the dome infiltrate sample, TH5, consisting of Fe-chlorite, illite, and quartz, and samples collected from the singular boring in the Boxwork Room consisting of smectite, chamosite (Fe-chlorite), and illite (Figure 5.9 to 5.11). The singular boring conducted in the Boxwork Room shows evidence for periodic flooding with sequences of well-sorted sand and poorly sorted clayey sand with gravel (Figure 5.8). Mineralogical consistency through the depth of the boring suggests consistent provenance through depositional history (Figure 5.10 and 5.11). The differences in clay mineralogy observed could either be from differences in mineral provenance or a high degree of pedogenesis

occurring in the cave since deposition (Entrena et al., 2022). Both are likely in Tardis Cave due to the high degree of lateral transport that has occurred to emplace the sediments during flood events.

Flood events have also contributed greatly to cave-passage development through lateral and upwards paragenetic dissolution. Paragenesis is apparent through the prevalence of horizontal wall notches and upwards migrating cupulas. Ubiquitous clay, silt, sand, and gravel deposits throughout the cave have acted to shield the bedrock floor from downwards incision and redirect chemical aggressiveness upwards and laterally (Farrant and Smart, 2011; Renault, 1958). Paragenetic processes are also apparent in Lake Shasta Caverns where the emplacement of poorly sorted sand and gravel has similarly shielded the floor from downwards incision.

Fluvially dominated sedimentation and facies associations in Lake Shasta Caverns are not a dominant mode of sedimentation, although the effects are clearly seen in passages adjacent to the collapsed entrance at the south end of the Signature Room. A significant amount of rounded and poorly sorted sand and gravel was deposited in the Signature Room, Basement Room, and Spider Complex passages in a flood event strong enough to form distinct imbrication (Figure 3.16). The coarse material deposits throughout these rooms can be described as channel and slackwater facies. The evidence of a once large-volume fill is seen in floor, wall, and pocket deposits of well-stratified and well-imbricated coarse material that form paleo-fill levels at relatively high elevations in the passages mentioned. Of note is a ceiling passage fill upwards of 5 meters off the floor in the Champagne Room of the Spider Complex. The ceiling passage fill is composed of cemented sand and gravel and likely forms the floor of portions of the Basement and Signature Rooms. Coarse material (>2 mm) is only encountered in the aforementioned passages and not elsewhere in the cave. In the Signature Room and Basement Room, the coarse

material is capped by a deposit of well-stratified altered tephra. Since the deposition of thick sequences of silt, sand and gravel with a cap of altered tephra, subsequent fluvial incision must have occurred to erode a significant volume of coarse material and transport the material out of the cave. Cupulas and horizontal notches have formed proximal to the top surfaces of many clastic deposits in the Signature Room and Basement room and could be products of lateral and upwards dissolution from paragenetic forcing (Farrant and Smart, 2011).

6.4 Autogenic-Dominated Facies

Autogenic dominated facies are a major component of deposits in Ancient Palace Cave and January Cave and a minor component in Lake Shasta Caverns. Observable autogenic sedimentation is not present in the remaining four caves either due to epikarst or fluvial erosion and overprinting or the lack of processes that form such deposits.

Autogenic bedrock residuum and authigenic facies are major component of sedimentation in Ancient Palace Cave and January Cave by the ubiquitous presence of very fine-grained smectite, disordered kaolinite, and illite clay and localized deposits of Fe-Mn corrosion residue products. The deposits are very poorly sorted with sand-sized Fe-Mn nodules and altered diorite. Autogenic sedimentation in Ancient Palace Cave is also characterized by a distinct deposit of condensation corrosion and biologically mediated Fe-Mn corrosion residue formed as a result of high-degrees of in-situ weathering of altered diorite and limestone bedrock.

Authigenic facies in Lake Shasta Caverns is characterized by localized deposits of altered tephra to authigenic platy halloysite and Fe-Mn allophane-imogolite (Figure 5.41 to 5.48). Authigenic deposits in Ancient Palace Cave, January Cave, and Lake Shasta Caverns can be

described as authigenic facies due to distinct mineralogical and textural characteristics that separate autogenic facies from infiltrate facies in the backswamp facies classification.

Autogenic residuum facies in Ancient Palace Cave is characterized by ubiquitous deposits of often well-laminated dark red clay that consists of unique clay species and very fine mean grain size (Figure 5.31 and 5.32). The clay species present in the APC2 and APC4 red clay samples are smectite, illite, and disordered kaolinite (Figure 5.25). The APC2 and APC3 samples do not contain chlorite or quartz. The clay species observed at the entrance and above the cave are notably different with the presence of Fe-chlorite, illite, and quartz. Grain size distribution between fine-grain material inside and outside the cave suggests varied modes of deposition and transport. The sample collected at the entrance is notably coarser and more poorly sorted with distinct clay, silt, and sand mode (Figure 5.30). The very fine grain size observed with the in-cave samples suggests deposition in extremely slow-moving or completely stagnant water. Stokes Law is used to calculate settling velocity of a spheroidal particle in fluid (Lamb, 1895). Calculation of settling velocity using of a mean grain size of 0.22 microns, density of kaolinite of 2.65 g/cm^3 , and a presumed settling column of 2.5 meters yields a settling time of 2.3 years (Equation 1) (Lamb, 1895). Very fine grain clay consisting mostly of smectite, illite, and disordered kaolinite, with a lack of detrital quartz and chlorite, is suggestive of a non-surficial, autogenic origin. Similar clay species have been identified as bedrock weathering residuum from Lechuguilla Cave (Northup and Lovoie, 2001; Polyak and Guven, 2000). The APC3 Fe-Mn corrosion residue collected in the Borning Room is another autogenic facies deposit in Ancient Palace Cave, that shows a high-degree of in-situ alteration and corrosive morphology.

The APC3 Fe-Mn deposit, or ferromanganese deposit (FMD), is present in the Borning Room as massive deposits and thin wall coatings (Figure 5.23). The Fe-Mn deposit consists of

pitted and corroded quartz, opal-A, Fe-Mn oxides/hydroxides, alunite, kaolinite, smectite, calcite, and fayalite (Figure 5.26 to 5.29). Similar ferromanganese deposits, except for the occurrence of fayalite, have been identified as ferromanganese corrosion residue products in caves in New Mexico and South Dakota and have been attributed formation to microbially induced bedrock corrosion and subsequent oxidization of iron and manganese (Spilde et al. 2006; Northup and Lovoie, 2001; Dotson et al., 1999). Iron and manganese oxides are common in cave environments and form as coatings on walls and speleothems, soft deposits in clastic material, and consolidated crusts. Oxidation of iron and manganese can occur through abiotic and biotic mechanisms and is largely controlled by pH and Eh and changes from anaerobic to aerobic conditions (Kotula et al., 2019; Winkler et al., 2016; White et al., 2009; Northup and Lovoie, 2001; Hill, 1982). Bosak et al (2005) describe the occurrence of massive Mn-oxide/hydroxide deposits in close association with allophane and halloysite. Bosak and others (2005) attributed the formation of Mn-oxides to microbial precipitation towards the lower depths of a water column. They further attribute the formation of allophane to low pH conditions produced by the weathering of sulphide minerals (Bosak et al. 2005). Grain size distribution of the Fe-Mn corrosion residue indicates a mesokurtic distribution around a mean grain size of 11.25 microns (Figure 5.33). The high angularity of non-opalized grains suggests minimal transport (Figure 5.27) although the moderate degree of sorting suggests some degree of sorting mechanism.

Sedimentation in January Cave is characterized by notably similar depositional patterns, clay mineralogy, and grain size distribution to deposits encountered in Ancient Palace Cave. The lower chamber of January Cave preserves chemically and morphologically identical very fine dark red clay as well as entrance passage material that consists of very poorly sorted sandy quartz silt with a clay mode of Fe-chlorite and illite (Figures 5.53 to 5.56). The very fine grain

clay collected from the lower chamber contains smectite, illite, and disordered kaolinite and does not contain quartz (Figure 5.54). The similarities in clay mineralogy, grain-size distribution, and overall lack of quartz between the Ancient Palace Cave and January Cave lower chamber samples suggests similar if not identical depositional conditions and provenance. The lack of detrital quartz in both clay samples further suggests the clay material is an authigenic weathering product and not detrital. Both dark red clay deposits are described here as autogenic facies (Figure 5.24 and 5.55).

Autogenic sedimentation in Lake Shasta Caverns is characterized by extensively altered tephra that has chemically weathered in-situ to halloysite and Fe-Mn imogolite and allophane. At least three separate deposits of altered tephra were identified throughout the Basement Room and Signature Room. The tephra observed are in distinctly different deposition conditions with two deposits being clearly fluvially derived, as they are strongly associated with rounded and imbricated siliciclastics. The other two localities are heavily-calcified floor deposits in the Signature Room and discrete pocket fills in the Basement Room. Depositional conditions for the pocket and floor deposits are less clear, but little evidence exists to suggest they are fluvially-derived. The two pocket and floor deposits are non-stratified with little to no association with fluvial siliciclastics. The heavily-calcified floor deposit in the Signature Room, sample LSC3, contains distinct silt-sand size nodules of Fe-Mn imogolite-allophane that has precipitated as an interstitial matrix within an agglomeration of tephra shards. The agglomerated shards have since eroded away and the angular, brecciated matrix is left. In some cases, the angular voids are partially filled by platy kaolinite (Figure 5.46). Precipitation of imogolite and allophane in karst environments occurs through the action of acidic water on siliciclastic sediments (Onac, 2019, Adriaens et al., 2017). The precipitation of allophane in a solution saturated with Al and Si

begins at a pH of 4.8 and often the formation of a semi-crystalline gel phase is kinetically favored over a more crystalline phase in low-pH conditions (Adriaens et al., 2017). Allophane is commonly associated with halloysite in volcanic soils although no halloysite or allophane was encountered in any of the surface samples collected (Brydon-Shimoda, 1972). The observed tephra shards have been partially to totally kaolinized to halloysite through intense in-situ weathering. Halloysite has been identified in karst environments associated with low-pH induced by the sulphide oxidation (Onac and Forti, 2019; Bosak et al., 2005; Adriaens et al., 2017) as well as by-products of sulfuric-acid speleogenetic processes in known hypogene caves (Polyak and Guven, 2000). The presence of Fe-Mn allophane and halloysite in the altered tephra deposits of Lake Shasta Caverns suggests low-pH alteration of siliciclastic material post-deposition and in-situ weathering. Furthermore, the presence of corrosive surface texture on kaolinized tephra shards suggests aggressive corrosive acidification indicative of chemical weathering and low-pH conditions (Figure 5.43) (Shackley, 1972).

6.5 Lithofacies Associations and Paleo-Depositional Environments

Facies relationships of sediments in caves of the McCloud Limestone have provided a useful framework for evaluating modes of cave genesis and paleohydrology in a hypogene and epigene setting. The three lithofacies associations observed in the McCloud Limestone karst are epikarst-dominated, fluvially-dominated, and autogenic-dominated. Describing caves in the McCloud Limestone by the set of facies associations has led to a descriptive tool for studying paleo-hydrogeologic conditions in a polygenetic karst setting. Patterns of depositional energy and allogenic input emerge when caves are grouped by facies associations (Table 6.1). Broadly, caves in the McCloud Limestone that primarily preserve lithofacies associated with corrosion-

residue formation and deposition of very fine-grained autogenic clay show more prevalent hypogene morphologies than those with epigenic fluviually derived clastic material, for instance (Figures 3.12, 3.16, 5.25, 5.41). Sediments that show strong fluvial influence tend to associate closely with classic epigenic and paragenetic forms (Figure 3.7 and 3.8). Examples of this can be seen in Ellery Creek Cave and Tardis Cave with the presence of phreatic flood mazes and canyon incision in close association with poorly sorted, coarse-grained clastic material (Figures 3.7, 3.8, 5.8).

Table 6.1: Facies exposed at each study cave (listed in ascending order of elevation) and facies associations shown in color. Epikarst-dominated (green), Fluvially-dominated (blue), and Autogenic-dominated (red) (Source: Author).

Cave Name	Epikarst			Fluvial					Autogenic	
	Entrance	Crack-filling	Infiltrate	Channel	Thalweg	Diamicton	Slackwater	Backswamp	Authigenic	Residuum
ElleryCr	X			X			X			
Tardis	X	X		X			X			
Pipevine	X	X						X		
APC	X								X	X
Rileys	X		X	X			X			
LSC	X			X			X		X	
January	X		X							X

Grouping caves in the McCloud Limestone by speleogenetic and sedimentary origin suggest development of caves representing both epigene and hypogene end members, as well as the spectrum of modes in-between. From a facies perspective, the purely epigenic caves of the

McCloud Limestone are Ellery Creek Cave, Tardis Cave, and Rileys Caves. The purely hypogenic caves, from an autogenic facies perspective, are Ancient Palace Cave and January Cave. Lake Shasta Caverns exhibits both epigenic and hypogenic facies associations, so can therefore be described as polygenetic (Table 6.1).

The limitations of describing cave genesis by way of facies associations is that facies are typically overprinted or eroded through multiple depositional and erosional phases during speleogenesis, and exploration bias may restrict total assessment of the possible spectrum of depositional conditions. Cave sediments are especially prone to erosion from high-velocity, turbulent flows during epigenic flood events, so long-time preservation of autogenic facies are less likely (Springer, 2019; Herman et al., 2012). Exploration bias is inherent in cave exploration in that the totality of a cave system is often largely unknown from burial or collapse and inaccessible to exploration and study (Palmer, 2006; Gillieson, 1986). Overall, facies relationships and associations have aided in the description of polygenetic cave genesis and resulting sedimentation in a montane karst setting.

6.6 Trends in Clay Mineralogy

Clay mineralogy in the McCloud Limestone is immensely varied with many patterns and unique occurrences present in the set of cave and surface samples analyzed. Overall, clay mineralogy between surface and in-cave samples show marked similarities, although unique authigenic clay species were identified in several caves. Clay species present in surface samples are chlinochlore and chamosite, vermiculite, and illite. Clay species present in cave deposits are mixed layer clays, smectite, vermiculite and kaolinite. Mixed layered clays, smectite, and kaolinite were not detected in the surface material collected. In most instances, the set of clay

minerals detected on the surface were also detected in cave deposits. Clays observed in the caves and surface samples collected exhibited varying degrees of in-situ pedogenic weathering. Clay species in differing stages of weathering is suggestive of varied intensities of weathering conditions in caves and/or temporal and spatial shifts in clay mineral provenance. Surface and entrance passage samples on the other hand do not show a high degree of pedogenic weathering.

The suite of observed clay species on the surface are predominately Fe and Mg-chlorite and illite. The presence of Fe and Mg-chlorite in a majority of the surface and cave samples is likely derived from hydrothermally altered diorite. Fe and Mg-chlorite were identified as major components of diorite analyzed as part of petrographic study on altered diorite associated with Lake Shasta Caverns (Spain, 2022). The spatial distribution of Mg-chlorite and Fe-chlorite suggests that Mg-chlorite is more common towards the northern portion of the study area and Fe-chlorite common in the central and southern portions (Table 6.2). Illite is present as a major fraction in all surface samples and a minor fraction in the samples collected from surface and entrance passages of Pipevine and Ancient Palace Cave (Table 6.2). Under non-aqueous surface conditions, pedogenic evolution involves the weathering of illite to vermiculite, smectite mixed layers, smectite, kaolinite, and amorphous compounds like allophane and imogolite. Illite is the common parent material for the pedogenic weathering of vermiculite and smectite (Entrena et al., 2022; Iacoviello and Martini, 2012; Velde, 1995). The lack of pedogenic weathering products in the surface and entrance passage samples suggests a low degree of pedogenic weathering on the surface. Clay species observed in various cave environments show a marked difference in the degree of weathering by the species of clays present on the surface and in-cave (Table 6.2). The suite of observed clay species in cave samples includes Fe and Mg-chlorite, illite, vermiculite, smectite, kaolinite, disordered kaolinite, and interstratified chlorite-illite (Table 6.2).

Overall, variability in clay species observed in caves is localized and genetic trends are illusive to define, but two trends emerge that can elucidate the origin of certain clay deposits encountered. Both Ancient Palace Cave and January Cave preserve extensive deposits of very fine-grained red clay in the lower chambers. In both cases, the red clay consists of smectite, illite, and disordered kaolinite and no detrital quartz (Figure 5.25 and 5.54). The lack of detrital quartz and Fe and Mg-chlorite and the very-fine grain size and presence of disordered kaolinite and smectite suggests that the material is authigenic in both cases.

Table 6.2: Clay species present in surface and in-cave samples. Cave samples are combined. (Entrance/surface) (Source: Author).

Clay Species	Quartz	Illite	Mg-chlorite	Fe-chlorite	Mixed layer	Smectite	Vermiculite	Kaolinite
Ellery Cr-E	X	X	X					
Ellery Cr	X	X				X	X	X
Tardis-E	X	X		X				
Tardis	X	X		X		X		
Pipevine-E	X	X	X					
Pipevine	X	X			X		X	X
APC-E	X	X		X				
APC		X			X	X		X
Rileys-E	X	X	X					
Rileys	X	X	X					
LSC-E	X	X		X				
LSC	X	X		X				X
January-E	X	X		X				
January		X				X		X

Vermiculite preserved in Ellery Creek Cave and Pipevine Cave is a trend that can be described by high-degrees of pedogenic weathering in both caves. Vermiculite is a weathering product of mica and illite, but the weathering process requires non-aqueous conditions over a significant period of time (Entrena et al., 2022; Velde, 1995). Therefore, the presence of

vermiculite in Pipevine Cave and Ellery Creek Cave are indicative of the relative length of time illite-rich sediments have been subject to pedogenic processes and/or the degree of weathering in these environments is much higher. Rileys Cave, on the other hand, does not preserve any evolved pedogenic species so it can be assumed that the illite-rich material was emplaced relatively recently or the conditions for pedogenic evolution are not present. Rileys Cave does not show evidence for significant standing water over long periods of time, so the latter case is more likely. Overall, clay species present in caves of the McCloud Limestone are notably varied although share some similarities. Those similarities can be crucial for describing the depositional conditions that these deposits were formed in.

6.7 Trends in Grain-Size Distribution

Overall, trends in grain size distribution suggest varying depositional and paleohydrologic patterns acting on the genesis, transport, and deposition of sediments in the polygenetic caves of the McCloud Limestone. Grain-size analysis of 57 samples was conducted to elucidate the degree of sorting, mean grain size, skewness, and kurtosis in the set of seven caves studied. Trends emerged through study of grain-size distribution that further aided in classifying sediments by depositional mode and energy. Prior to plotting on a set of ternary and bivariate plots and evaluating for statistical relationships, grain size samples were determined to be epikarst-dominated, fluvially-dominated, or autogenic-dominated by the depositional setting of the deposit, lithofacies classification, grain size distribution statistics, and clay mineralogy. Statistical analysis of median grain sizes through KW, Dunn's, and MWU tests were employed on median grain size data in an attempt to provide statistical significance to the three classifications. Further, bivariate and ternary plots between mean grain size, sorting, and sand-

silt-clay content reveal trends that group the 57 samples by characteristic sorting behavior and clay content (Figure 6.1 and 6.2). These trends further support differentiation of facies associations by respective depositional settings and energies.

Overall, grain size distributions for epikarst-dominated sedimentation show the lowest degree of sorting with distinct polymodal behavior and high relative clay content. Fluvially dominated sediments show higher degrees of sorting along a range of grain sizes and clay content. Autogenic sedimentation displays a range of sorting and grain sizes but can be separated into two distinct groups, relatively poorly-sorted, very fine-grained authigenic clay and well-sorted, authigenic and autogenic weathering residuum and corrosion residues (Figures 6.1 and 6.2).

Grain size distributions of material sampled from lithofacies in the epikarst facies association are predominantly very poorly sorted and polymodal with a distinct clay or sand mode (Figure 6.1). In general, samples analyzed from entrance facies, infiltrate facies, and crack-filling facies are composed of fine sandy coarse silt with a distinct sand mode (Figure 5.7, 5.20, 5.50) or finely skewed fine silt with a distinct clay mode (Figure 5.12, 5.30, 5.36, 5.57). The two types of sorting characteristics are loosely defined and some epikarst facies samples exhibit both clay and sand modes and fine skewness (Figure 5.13). The two broad trends in grain size distribution could suggest two primary types of transport and sorting mechanisms acting on epikarst facies, colluvial and pluvial transport. Colluvial (gravity-driven) transport is generally

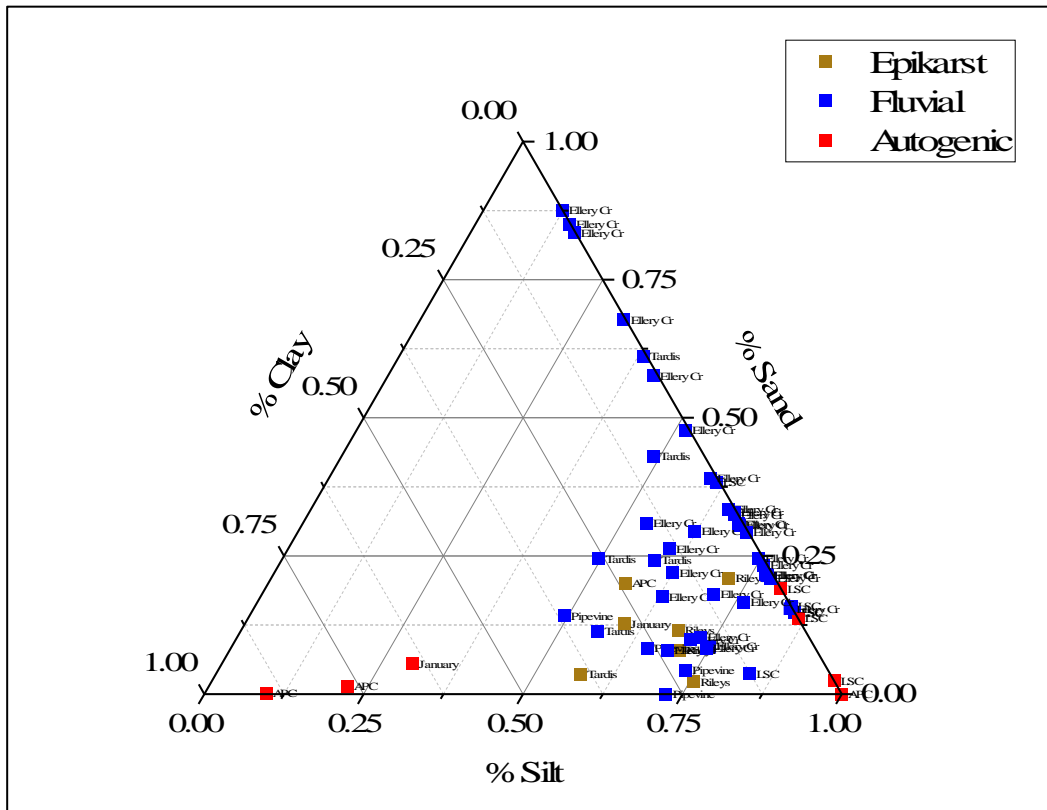


Figure 6.1: Sand-silt-clay ternary plot of material sampled from seven cave sites and associated entrances (Source: Author).

not an efficient transport mechanism for clay and silt-sized particles, because fine particles largely require suspension in water for transport, as well as a high boundary shear stress (Herman et al., 2012; Hjulström, 1955). Channelized pluvial transport, as distinctly seen in Rileys Cave, may have enough boundary shear stress to move fine particles during heavy rain events and may also skew the distribution geometry to a finer particle size. The same is true for the transport of material coarser than sand size (Hjulström, 1955). When plotted on a bivariate plot between mean grain size and sorting, the epikarst facies analyzed displays variable sorting despite a consistent mean grain size. This relationship has been attributed to sediments in a colluvial setting where localized sorting is occurring through pluvial action (Mycielska and Kudwikowska, 2011). Grain size distributions for epikarst facies are generally distinct from

fluvial facies by having a limited grain size range, relatively poor sorting, and higher overall clay content (Figure 6.1).

Samples analyzed from deposits in the fluvial facies association showed a higher overall range in grain size (1.35 – 590 μm), and sorting (1.1 – 3.7 ϕ), as well as symmetrical skewness of the primary mode (Figure 6.1). The fluvial lithofacies observed in the set of McCloud Caves were primarily slackwater and channel facies with minor backswamp facies (Table 6.1). The slackwater and backswamp facies were predominately bimodal fine silt with well sorted, symmetrical silt mode and distinct clay mode (Figure 5.5, 5.6, 5.21). The channel facies ranged from silt to coarse sand with little to no clay (Figure 6.1). The lack of clay in channel facies deposits can be explained by the relationship between grain size, settling velocity, boundary shear stress (Herman et al., 2012; Hjulström, 1955; Lamb, 1895). Once in suspension, clay particles are more easily transported, rather than deposited, because the clay's slow relative settling velocities cannot overcome turbulent water velocity (Lamb, 1895). Because of this, clay in suspension is often transported away from zones of storage. The low overall clay content in fluvial facies observed in the McCloud suggests that water velocities were high enough to transport suspended load away from the cave environment (Hjulström, 1955). Plotted on a bivariate plot with mean grain size and sorting, distributions for fluvial facies samples shows an overall decrease in sorting through a decrease in mean grain size. This is due to the accumulation of suspended load after a flood or silt deposition after a sand storm (Mycielska and Kudwikowska, 2011). This is in contrast to the epikarst grain size relationship of variable sorting despite a consistent mean grain size.

Contrary to distributions for both epikarst and fluvial facies associations, samples analyzed from the autogenic facies association fall into two groups of grain size characteristics.

Grain size distributions of samples analyzed from the autogenic facies association show two distinct groups of distributions (Figure 6.2). One group shares a distribution of very coarse skewed and polymodal, very fine-grained clay (Figure 5.31, 5.32, 5.58), and the other group consists of symmetrical and mesokurtic, well sorted silt (Figure 5.33 and 5.52). The set of samples that consists of very-fine grained clay is very coarse-skewed with one primary clay mode and two to three lesser modes of silt and sand. According to mineralogical analysis, the very-fine grained material primarily consists of authigenic smectite, illite, and disordered kaolinite (Figure 5.25 and 5.55). Mineralogy of the silt and sand modes were not identified, but the likely mineralogy would ferromanganese nodules or clasts of bedrock residuum according to observations elsewhere in the study area. The second group of distributions in the autogenic facies samples showed some of the best sorting in total sample population (Figure 6.2), as well as displayed exclusively unimodal geometry (Figure 5.33 and 5.52). The high degree of sorting could be a result of uniform transport mechanisms across samples and caves, but the genetic history of both of the silt-sized particles, ferromanganese deposits in APC, and altered tephra from LSC, are notably different (Figure 5.27 and 5.43). This could suggest that another mechanism is involved in the control of grain size distribution, such as mineralogical stability and growth conditions through a unique cave microclimate. To further elucidate differences and similarities in grain size statistics between facies associations, the non-parametric statistical analyses using KW, Dunn's, and MWU tests were employed.

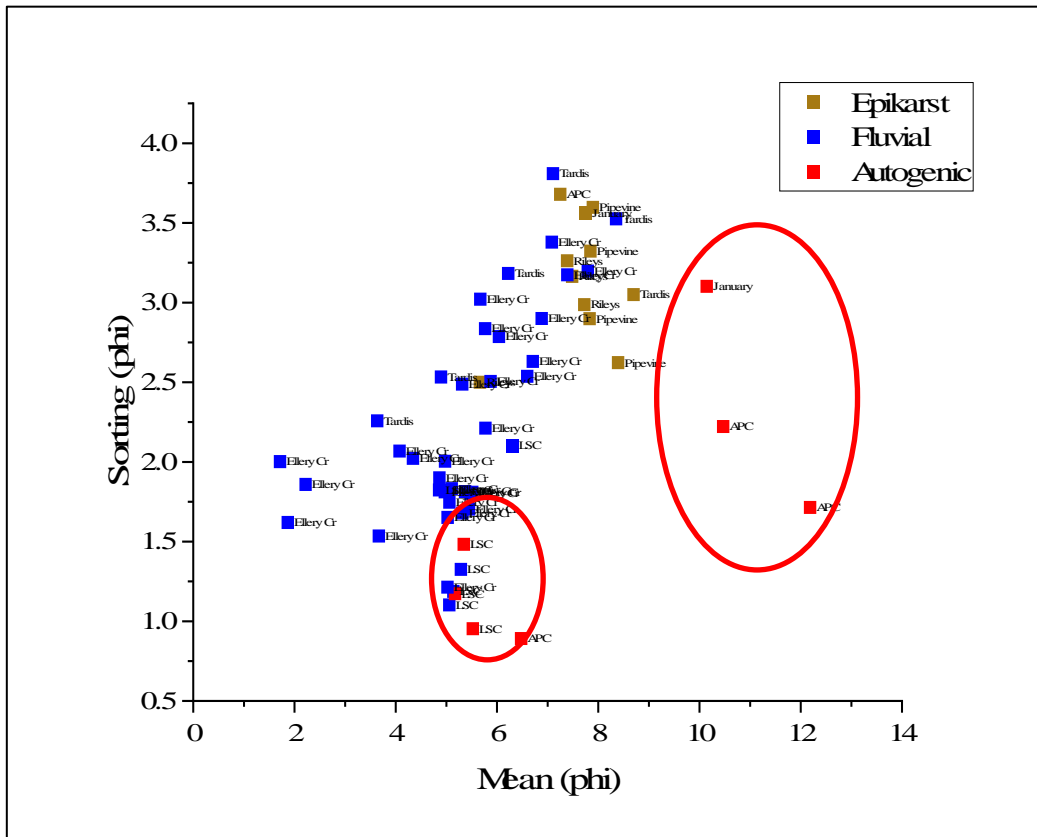


Figure 6.2: Bivariate plot of mean grain size (phi) vs sorting (phi) of sediments sampled from seven cave sites and associated entrances. Two groups of autogenic facies are marked with the right group being authigenic clay and the left group being silt-sized weathering residuum (Source: Author)

The KW analysis was conducted to determine whether all three of the lithofacies association groups (epikarst, fluvial, and autogenic) have different median grain sizes from the grouped size distributions. Results from these analyses quantify the facies association classification scheme by providing numerical significance to similarities and differences between each facies association group. Prior to running the analyses, fluvial samples finer than the overall median grain size of the group were removed. This accounted for the episodic nature of fluvial deposition with an intentional disregard for low-velocity slackwater and backswamp conditions. Inclusion of data that are coarser than the median is representative of higher-velocity transport

conditions (Hjulström, 1955; Lamb, 1895). Since a majority of fluvial samples analyzed are associated with high-velocity transport conditions, those conditions were determined to be representative of the fluvial facies association.

The results of the KW test indicate a significant difference between all three groups with a p -value = <0.0001 , so the null hypothesis is rejected, meaning the groups are significantly different (Table 6.3); however, a subsequent Dunn's test revealed that samples in the epikarst and autogenic groups are not significantly different (Table 6.3). This could be due to similar depositional mechanisms between the two groups, or could be due to similar sorting mechanisms occurring at a local-scale, such as gravity-driven transport. A subsequent MWU test was conducted to reduce potential Type I errors caused by relatively low sample sizes per group and intervariation within the sample set. The results of the MWU test indicate that each pair of facies associations are significantly different from each other with p -values of <0.001 (Epikarst-Fluvial), 0.0067 (Epikarst-Autogenic), and 0.0012 (Fluvial-Autogenic) (Table 6.3) (Dunn, 1964; Kruskal and Wallis, 1952; Mann and Whitney, 1947). The difference in statistical significance between the KW and MWU tests could be attributed to the varying sample sizes between the three facies groups and broad range in median values between the facies groups (see Appendix IV for median grain size data). In general, the statistical test results strongly suggest that the facies association groups are distinct, thus support the likelihood of a difference in depositional mechanism and resulting lithofacies.

Table 6.3: Results from KW, Dunn's, and MWU statistical tests done on median grain size data from 57 samples (see Appendix IV for median grain size data) (Source: Author).

Kruskal and Wallis				
	H (Chi-Square)	Degrees of Freedom (DF)	<i>p</i> -value	
Median	31.01	2	<0.0001	
Dunn's Test				
	z-score	<i>p</i> -value		
Autogenic-Epikarst	-0.92	1		
Autogenic-Fluvial	-3.99	1.95E-4		
Epikarst-Fluvial	-4.51	<0.0001		
Mann-Whitney U Test				
	# of samples	U number	<i>p</i> -value	
Autogenic-Epikarst	15	43	0.0067	
Autogenic-Fluvial	35	124	0.0012	
Epikarst-Fluvial	43	0	<0.0001	

6.8 Multi-stage Polygenetic Development

Polygenetic caves and cave regions have been described by Piccini and others (2007) and Forti and others (2006) in Coahuila, Mexico, Palmer (2007) in South Dakota, USA, by Burgess and others (2023) in Indiana, USA, and by Kambesis and Machel (2013) in Barbados.

Speleogenetic history, geomorphic context, and source and transport of aggressive karst solvents in all cases of polygenetic cave development are unique and depend on regional hydrology and geology. The hypogenic caves of Coahuilla, Mexico formed from slow-moving, rising thermal waters with relatively low chemical aggressiveness (Piccini et al., 2007; Forti et al., 2006). This combination results in monogenic hydrothermal caves as described by Dubyansky (1995) in Budapest, Hungary. The resulting hypogenic morphology is a large basal chamber with

secondary conduits departing upwards (Dublyansky, 1995). This type of development requires concentrated, slow-moving rising water and typically results in medium-sized caves with large basal chambers (Piccini et al., 2007; Dubyansky, 1995). The epigenic caves of Coahuilla, Mexico show evidence of meteoric-influenced phreatic and vadose morphologies such as rounded niches, scallops, and vadose canyon incision. Elsewhere, polygenetic caves described in South Dakota, Indiana, and Barbados, have been attributed to either multistage polygenetic development (Palmer, 2007) or concurrent polygenetic development with hydrogen sulfide oxidation occurring concurrently with epigenic fluvial processes (Burgess et al., 2023).

Epigenic overprinting is present in Pipevine Cave and Rileys Cave as indicated by vadose morphologies and epigenic sedimentation. Epigenic overprinting and resulting sedimentation in Pipevine Cave is seen as a one-half to one-meter-deep, stair stepping vadose canyon incision in the floor of a down-trending phreatic passage oriented at a roughly 80 degree slope. The initial incision point for the canyon is formed at the base of an aggressive drip location that appears to be channelized epikarst infiltration. Localized transport, sorting, and rounding is occurring here, but the input does not appear to be a major contributor to the formation of the cave and primary storage zones. Pipevine exhibits primarily hypogenic morphologies and the only evident vadose morphology is the epigenic overprint. Rileys Cave shows evidence for a primarily hypogenic origin through the lack of epigenic morphologies and fluvial facies, but localized transport and sorting of extensive epikarst facies is evident throughout the cave. Tardis Cave and Ellery Creek Cave exhibit primarily epigenic passage morphologies and cave sediment that hint at a strictly epigenic development, regardless of the geographic proximity to strictly hypogenic caves such as Ancient Palace Cave and January Cave.

Ancient Palace Cave exhibits notably similar morphology to monogenic hydrothermal caves in Coahuilla, Mexico and Budapest, Hungary (Piccini et al., 2007; Dubyansky, 1995). Ancient Palace Cave and January Cave consists of a singular, large-volume basal chamber with numerous secondary conduits that, in most cases, ascend upwards to rounded bedrock terminations. As with hypogenic caves with similar origin in Hungary and Mexico, the singular entrances at Ancient Palace Cave and January Cave are situated at the highest known point where the hillside erosional surface has intersected the highest rising passages. Sedimentation patterns in Ancient Palace Cave and January Cave support a hypogenic origin based on the presence of clay-rich bedrock residuum and Fe-Mn corrosion residues and overall lack of detrital clastic material like quartz and chlorite. Similar to hypogenic caves in Coahuilla, Mexico, the hypogenic caves of the McCloud Limestone are situated in proximity to caves of epigenic origin. In Lake Shasta Caverns, multi-stage hypogene and epigene development is evident through the emplacement and subsequent low-pH alteration of fluvially transported tephra, as well as through the presence of condensation-corrosion-induced bedrock scour features incising through allogenic and chemical sediments. The occurrence of altered tephra in Lake Shasta Caverns is strongly associated with deposits of well-imbricated and well-stratified coarse-grain sediments that are indicative of long-lasting fluvial flow. In some instances, the altered tephra is incorporated in deposits of fluvial sediments as distinct interbeds. The presence of allophane and spheroidal halloysite in the altered tephra suggests in-situ weathering in low-pH solutions as low as 4.8 (Adriaens et al., 2017). Since much of the clastic material that is associated with the altered tephra has eroded away leaving only disjunct wall, floor, and ceiling pockets, one can assume that after deposition of the fluvial clastic and tephra, there were multiple episodes of fluvial erosion and transport as well as hypogenic episodes of low-pH alteration. This is

supported by the presence of a condensation-corrosion ablation rim in the upper level, Cathedral Room, portion of the cave (Figure 6.3). Ablation rims, or air scallops, form primarily as the result of closed-cell convection of warm vapor rising from a pool of thermal water. Vapor charged with carbonic acid or sulfuric acid condenses on cooler cave walls as it rises and results in contact dissolution (Dublyansky and Spotl, 2018; Audra and Palmer, 2015; Ford and Williams, 2007).

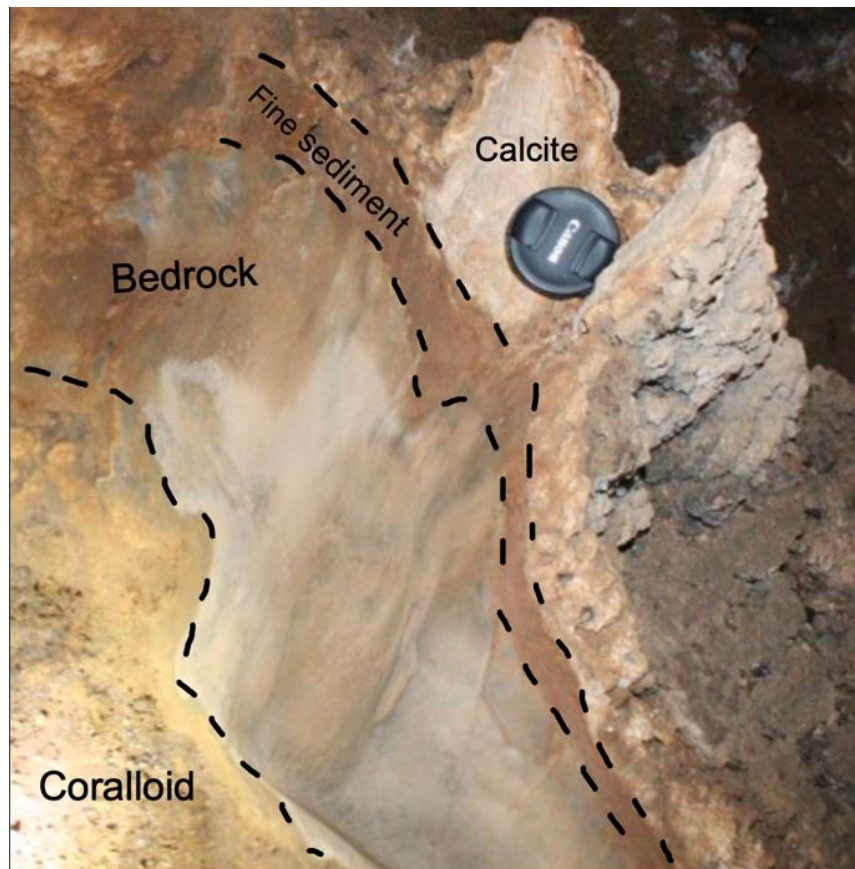


Figure 6.3: Smooth ablation rim incising through limestone bedrock, fine clastic sediment, and calcite flowstone. (Source: Despain, 2021)

The presence of a stable pool of thermal waters in the lower portions of Lake Shasta Caverns is evident in numerous horizontal pool notches in the Signature Room and Basement Room. Corrosion notches are present in many caves both hypogenic and epigenic and typically

form when a pool of water is almost entirely static, and the smallest perturbation to fluid density gradients can cause internal convection and supply of H⁺ ions to the walls of the pool surface. In hypogenic and hydrothermal settings, pool notches are attributed to the oxidation of hydrogen sulfide at the pool-water surface (Audra and Palmer, 2015; Palmer, 2013; Ford and White, 2007)

Pool notches in Lake Shasta Caverns could be attributed to static pool levels that are not related to thermal waters, but the presence of thermal convection dissolution, altered allogenic deposits, and many hypogenic cave morphologies suggests the static pools present in the Basement Room and Signature Room were thermal in origin. In the case for Lake Shasta Caverns, a pool of thermal water would have been present in passages below the Cathedral Room (i.e the Basement or Signature Rooms) and supplying rising and convecting vapor to overlying passages. The suspected temperature range for the thermal pools is not evident, but the source of the thermal fluids could be from regional volcanic centers or deep circulating groundwater (Audra and Palmer, 2015). The proximity to regional volcanic centers supports a volcanogenic thermal source for circulating groundwater (Hildreth, 2007). In summary, caves in the McCloud Limestone preserve sediments and associated morphologies that show evidence for multi-stage speleogenesis, punctuated by depositional events, through time.

6.9 Regional Context

Caves and cave sediments within the McCloud Limestone display numerous indications of influence from hydrothermal and/or chemically aggressive sulfuric-acid hypogenic fluids. The McCloud Limestone and Shasta Lake physiographic region is situated within 30 kilometers of the Mt. Shasta and Mt. Lassen volcanic centers (Figure 6.4). Additionally, the McCloud

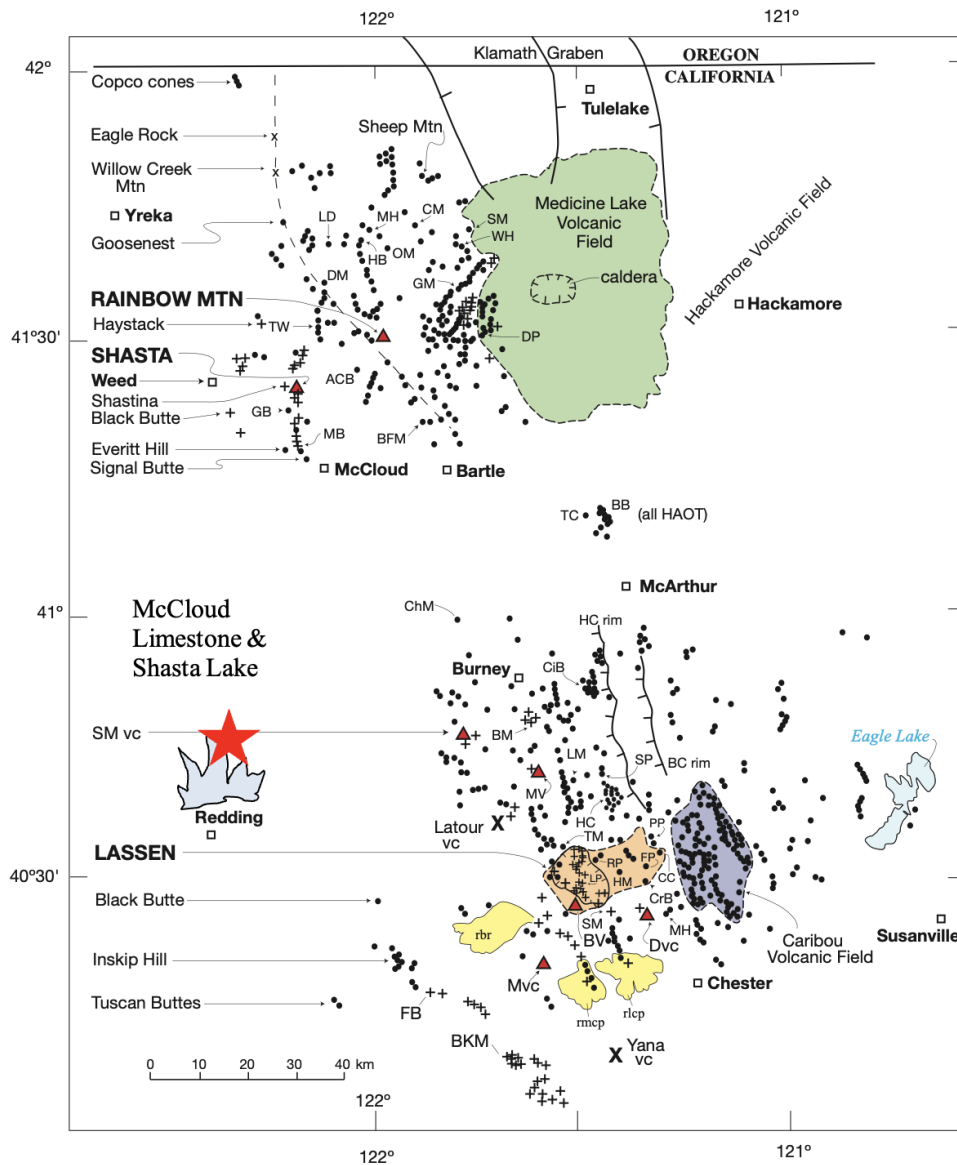


Figure 6.4: Modified map of regional volcanic centers in relation to Shasta Lake and the McCloud Limestone (Source: Hildreth, 2007).

Limestone is situated within 10 kilometers of massive, pyrite-rich volcanogenic sulfide deposits (VMS) of the Balaklala Rhyolite and massive sulfide shear-zone mineralization of the Bully Hill Rhyolite (Albers and Roberson, 1961; Nordstrom and Alpers, 1999). The geographic proximity to two large-scale volcanic centers and large-scale massive sulfide deposits suggests that hydrothermal fluids could have originated from both or either of the volcanic centers and interacted with massive sulfide deposits to generate highly aggressive hypogenic fluids. The evidence of multiple stages of influence from low-pH thermal water comes with the presence of extensively altered tephra that has been altered to Fe-Mn-rich halloysite, allophane, and imogolite (Adriaens et al., 2017; Lowe, 1986; Fieldes, 1955), as well as the presence of condensation-corrosion ablation rims caused by the convection of rising vapor off a thermal pool in Lake Shasta Caverns (Audra and Palmer, 2015; Ford and Williams, 2007). Caves in the McCloud Limestone are lacking in sulfate mineralogy, however. Deposits of sulfates such as gypsum are common byproducts of sulfuric-acid-speleogenesis (SAS) (Hill and Forti, 1986), although sulfates are not present in any known caves in the McCloud Limestone. This may be due to a deep and well-developed epikarst and overall wet climate, but could also be a sign of a lack of regional SAS hydrogeology (Despain et al., 2022). Regardless, multi-stage speleogenesis can erase evidence of SAS byproducts through multiple stages of chemically-aggressive dissolution and periods of high pluvial activity (high rainfall).

Multiple stages involving the ingress of thermal waters could be explained by the periodicity of regional volcanic events and associated hydrothermal systems, as well as proximity to sources of oxidized massive sulfides (Nordstrom and Alpers, 1999). The effects of hydrothermal systems are well documented in volcanic rocks from the Dittmar Volcanic Center (2.4 - 1.3 Ma) situated in the Mt. Lassen Volcanic Center (Clynne and Muffler, 2017), and

regional structures and faults could have migrated those fluids to the McCloud Limestone karst. The timing of cave development in the McCloud Limestone has remained undefined, but certain stratigraphic correlations can be made that can aid in applying a minimum time constraint.

An attempt to constrain a minimum age for Lake Shasta Caverns can look to lateral correlation with the Tuscan Formation. The Tuscan Formation is a wide-spread Pliocene-age volcanic debris-flow consisting of tuff breccia, air-fall tuff, basaltic and andesitic lava flows, and siliciclastic sediments. The Tuscan Formation was mapped to an extent of 5,000 km² with an approximate volume of 1,200 km³ and extends from south of Chico to the low-lying regions immediately south of Shasta Lake (Figure 6.5) (Hildreth, 2007; Hamusek-McGann, 1995; Helley and Hardwood, 1985). Albers and Robertson (1961) identified a paleo-high stand deposit in the vicinity of Lake Shasta Caverns at approximately 520 meters that consists of spongy, transported limonite. The deposit was further correlated to outcrops of Tuscan Formation immediately south of Shasta Lake at a similar elevation. They further note that the Tuscan Formation was deposited on an area of low-relief at approximately 520 meters (Albers and Robertson, 1961). The elevation of Lake Shasta Caverns is approximately 580 meters. Considering the extent of paleo-high stands adjacent to Lake Shasta Caverns, lateral correlation with the Tuscan Formation, and the extent of siliciclastic and fluvially transported tephra deposits in Lake Shasta Caverns at approximately the same elevation of large volumes of volcanic debris-flows of the Tuscan, it is therefore possible that the siliciclastic material observed in Lake Shasta Caverns originated from the Tuscan Formation debris-flows. The Tuscan Formation ranges in age from 2.5 – 3.5 Ma (Clynne and Muffler, 2017; Helley and Harwood, 1985). If the tephra-rich siliciclastic material originated from the Tuscan volcanic event, it would apply a minimum age of Lake Shasta Caverns to 2.5 – 3.5 Ma.

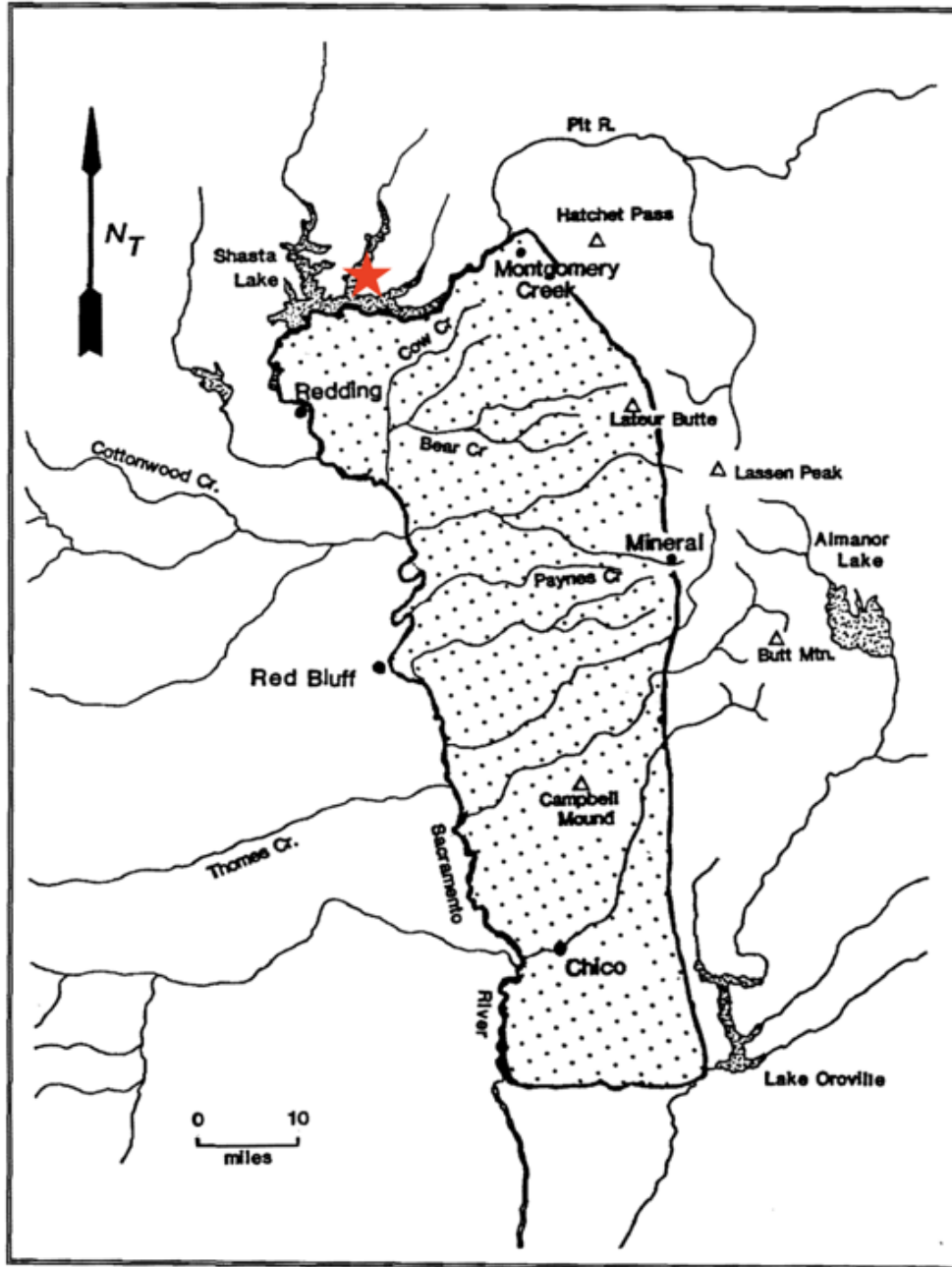


Figure 6.5: Modified map of the extent of the Tuscan Formation with Lake Shasta Caverns marked (Source: Hamusek-McGann, 1995).

Lake Shasta Caverns, and other caves of the McCloud Limestone, that form in epiphreatic settings can therefore act as paleo-high stand markers for evaluating regional geomorphic development. Albers and Robertson (1961) concluded that local uplift and

subsequent downcutting of the Pit River since the deposition of the Tuscan has been 35 meters measured from the base of the Tuscan Formation adjacent to the Pit River at approximately 366 meters and the base of the Pit River valley at approximately 251 meters. This conclusion indicates an approximate maximum incision rate of approximately $0.03 \text{ mm/yr} - 0.05 \text{ mm yr}^{-1}$ using an approximate age of 2.5 – 3.5 Ma for the Tuscan Formation (Clynne and Muffler, 2017; Helley and Harwood, 1985; Albers and Robertson, 1961).

In the western and central Klamath mountains, Anderson (2008) modeled Pleistocene uplift using river incision profiles and concluded an incision rate of 0.4 mm/yr beginning at 5 Ma with an increase to 2.9 mm yr^{-1} by 0.7 Ma. In the southern Sierra Nevada Mountains, Stock and others (2005) evaluated numerous cave sediment proxies to establish a maximum incision rate of approximately $0.03 - 0.05 \text{ mm yr}^{-1}$. Similarities between the maximum incision rates in the eastern Klamath Mountains region and southern Sierra Nevada range suggests the eastern Klamath region has shared a similar tectonic history to portions of the Sierra Nevada range. The lower relative incision rate for the eastern Klamath Mountain further suggests that late Pleistocene ($<0.7 \text{ Ma}$) uplift in the eastern Klamath range has been minimal.

6.10 Limitations

Limitations of this study include exploration and observation bias, collection bias, and biases related to the simplification of deposition conditions. Overall, this study paid close attention to documenting the present sediment-storage conditions and inputs and outputs, but caves are inherently subject to exploration and observation bias. Exploration and observation bias occurs when cave surveyors have not or are unable to explore all reaches of the cave, whether it be from passage constrictions, vertical relief, or passage collapse or sedimentation.

Exploration bias is of concern because there may be sedimentary pathways and storage zones that evade documentation. Additionally, duplicate samples were not collected for most corings or grab samples, due to time and logistical constraints, and to minimize disturbance to the cave itself. Trenches were avoided for this same reason, so reproducibility of the results is limited to in-core and replicate single-sample analyses.

The caves chosen for this study were selected because exploration has continued to a degree to that cavers can say there are no longer any major continuing passages. This cannot be said for certain, as caves are inherently a black box, but this can be said with a certain degree of confidence for the seven chosen cave sites. Collection bias, on the other hand, may have occurred during the sampling process when the author chose specific sampling sites to represent diagnostic sedimentary deposits at each cave. Collection bias, in this case, was avoided by collecting samples from any and all representative deposits in a specific cave and subsequently identifying a subset of samples that represent the overall sedimentary conditions. Lastly, this study may have been subject to simplification bias related to concluding the paleo-hydrologic depositional conditions in each study cave. Since this study was limited by the tools and methods employed, the conclusions are, therefore, limited by the quantitative data produced. This study did not employ any hydrologic or isotopic methods, so cannot pose theories on current hydrologic regimes and isotopic signatures. To combat this, special focus on sedimentary characteristics were utilized to evaluate transport mechanisms and provenance.

7. Conclusions

The evaluation of seven closely-spaced caves formed in the McCloud Limestone revealed that sedimentation characteristics, in concert with morphologic observations, can provide insight into the paleo-hydrogeologic and speleogenetic history of polygenetic karst development. The study of clastic sedimentation in the McCloud caves provided a framework for evaluating the diversity of observed clay mineralogies and grain size distributions in the context of paleo-hydrology and cave development. Three facies associations were characterized and include epikarst-dominated, fluvially-dominated, and autogenic-dominated. The resulting facies aided in

the distinction between hypogenic and epigenic modes of paleo-hydrology and provenance. The three research questions this study addressed are as follows:

- What is the relationship between modes of cave development and the distribution, source, and transport mechanisms of clastic deposits of the caves of the McCloud Limestone?
- Can previously devised cave sediment classifications systems be used to characterize and classify the suites of sediments observed in the caves of the McCloud Limestone?
- How does karstification and cave sedimentation in the McCloud Limestone relate to regional geologic context and geomorphic development?

To initiate appropriate descriptive procedure, updated facies were utilized to characterize facies observed in this study. Facies such as the ‘infiltrate facies,’ ‘autogenic facies,’ and ‘residuum facies’ are largely specific to hypogene and polygenetic karst regions. Fluvial processes will sort and transport these facies resulting in fluvially-dominated sedimentation and associated facies. Caves that displayed autogenic-dominated sedimentation also showed evidence of hypogene morphologies. Caves that exhibited strong fluvially-dominated facies associations showed notable epigenic morphologies. Caves that exhibit both autogenic- and fluvial- or epikarst-dominated facies associations showed evidence of both epigene and hypogene cave development, thus identifying them as polygenetic. Further, statistical relationships between the median grain size of the samples studied suggests that depositional mechanisms between the three facies associations are significantly different. From these relationships, it is reasonable to assume that a clear relationship exists between modes of cave genesis and the distribution, source, and transport mechanisms of clastic sediments in the McCloud Limestone; therefore,

study of cave sedimentation through facies relationships, mineralogical variability, and grain size distribution can further the descriptive differentiation of types of cave development in a polygenetic setting.

Through evaluation of the diversity in cave sediments, evidence of multi-stage hypogene and epigene development, as well as indications of significant hydrologic fluctuations and massive sedimentation events, were interpreted. The relationship between cave deposits and regional volcanic events and stratigraphic markers has provided time constraints for the development of the McCloud Caves and establishes a likely minimum age for Lake Shasta Caverns to 2.5 – 3.5 Ma (Clynne and Muffler, 2017; Helley and Harwood, 1985). Further time constraints on epigenic flood sediments in Ellery Creek Cave suggests successive flood events and associated mass sedimentation likely a result of increased biomass and slight warming prior to the onset of Younger Dryas cooling (Cowan, 2022; Vacco et al., 2005; Barron et al., 2003), or continent-wide forest fires as a result of the hypothesized Younger Dryas impact event (Holliday et al., 2023; Scott et al., 2011; Powell, 2022). Studying the diversity, extent, and sedimentary evolution of cave sediments in a set of seven polygenetic caves in the McCloud Limestone has allowed for greater insight into the geomorphic development of the Eastern Klamath physiographic region and provided a framework for studying polygenetic caves elsewhere.

Works Cited

Aalto, K. R. (1992) "Late Cenozoic Sediment Provenance and Tectonic Evolution of the Northernmost Coast Ranges, California," *Field Guide to the Late Cenozoic Subduction Tectonics & Sedimentation of North Coastal California*.

- Aalto, K. R. (2006) “The Klamath peneplain: A review of J.S. Diller’s classic erosion surface,” *Geological Studies in the Klamath Mountains Province, California and Oregon: A volume in honor of William P. Irwin*. Geological Society of America, pp. 451–463.
- Adriaens R, Ronchi B, Mertens G, Hollanders S, Elsen J, Dusar M, Vandenberghe N (2017) “Halloysite occurrence at the karstified contact of Oligocene sands and Cretaceous calcarenites in Hinnisdael quarries, Vechmaal (NE of Belgium),” *Geologica Belgica*, 20(1–2), pp. 43–52. doi: 10.20341/gb.2017.002.
- Albers, J. P. and Robertson, J. F. (1961) “Geology and ore deposits of east Shasta copper-zinc district, Shasta County, California,” *Professional Paper. U.S. Geological Survey*. doi: 10.3133/pp338.
- Almquist, K. D. (2011) *The Weathering of Volcanic Ash and Resultant Clay Minerals in a Terrestrial and Marine Environment: North Island, New Zealand*. Masters Thesis. North Carolina State University.
- Anderson, T. K. (2008) Inferring bedrock uplift in the Klamath Mountains Province from river profile analysis and digital topography. Masters Thesis. Texas Tech University.
- ASTM (2014) *ASTM D1586: Standard Test Method for Standard Penetration Test (SPT) and Split-Barrel Sampling of Soils*.
- Audra, P. and Palmer, A. N. (2015) “Research frontiers in speleogenesis. Dominant processes, hydrogeological conditions and resulting cave patterns,” *Acta Carsologica*, 44(3). doi: 10.3986/ac.v44i3.1960.
- Audra, P., Bigot, J.-Y. and Mucochain, L. (2003) “Hypogenic caves in Provence (France): Specific features and sediments,” *Acta Carsologica*, 31(3), pp. 33–50.
- Bahadorinia, S. *et al.* (2016) “The morphology and development of Kalahroud Cave, Iran,” *International Journal of Speleology*, 45(3), pp. 243–257. doi: 10.5038/1827-806x.45.3.2008.
- Bailey, G. and Thomas, G. (1987) “The use of percussion drilling to obtain core samples from rock-shelter deposits,” *Antiquity*, 61(233), pp. 433–439. doi: 10.1017/s0003598x00072987.
- Barron, J. A. *et al.* (2003) “High-resolution climatic evolution of coastal northern California during the past 16,000 years: climatic evolution of coastal California,” *Paleoceanography*, 18(1). doi: 10.1029/2002pa000768.
- BeRC (2015) *Radiocarbon dating results calibration - beta Analytic, Carbon Dating Service, AMS Miami - Beta Analytic*. Beta Analytic. Available at:

- <https://www.radiocarbon.com/calendar-calibration-carbon-dating.htm> (Accessed: July 11, 2024).
- Birle J D, Gibbs G V, Moore P B, Smith J V (1968) Crystal structures of natural olivines, *American Mineralogist*, 53, 807-824
- Black, J. H. and Raines, M. G. (1978) "Soil sampler with retrievable liner," *Journal of Soil Science*, 29(2), pp. 271–276. doi: 10.1111/j.1365-2389.1978.tb02057.x.
- Blakely, Richard J; Jachens, Robert C; Simpson, Robert W; Couch, Richard W; (1985) "Tectonic setting of the southern Cascade Range as interpreted from its magnetic and gravity fields," *Geological Society of America bulletin*, 96(1), p. 43. doi: 10.1130/0016-7606(1985)96<43:tsotsc>2.0.co;2.
- Blott, S. J. and Pye, K. (2001) "GRADISTAT: a grain size distribution and statistics package for the analysis of unconsolidated sediments," *Earth surface processes and landforms*, 26(11), pp. 1237–1248. doi: 10.1002/esp.261.
- Bosak, P. (2008) "Karst processes and time," *Geologos*, 14(1), pp. 19–36.
- Bosak, Pavel; Bella, Pavel; Vaclav, Cilek; Ford, Derek C; Hercman, Helena; Kadlec, Jaroslav; Osborne, Armstrong; Pruner, Petr (2005) "Ochtina Aragonite Cave (Slovakia): morphology, mineralogy and genesis," *Speleogenesis and Evolution of Karst Aquifers*, 3(2), pp. 1–16.
- Bosch, R., White, W. (2015) *Lithofacies and Transport of Clastic Sediments in Karstic Aquifers*. Masters Thesis. The Pennsylvania State University.
- Bruker (2018). *DIFFRAC.EVA: software to evaluate X-ray diffraction data*. Version 4.3. <https://www.bruker.com/eva>
- Brydon, J. E. and Shimoda, S. (1972) "Allophane and other amorphous constituents in a podzol from Nova Scotia," *Canadian Journal of Soil Science*, 52(3), pp. 465–475. doi: 10.4141/cjss72-058.
- Bunnell, D. (2023) Ancient Palace Cave photos [Photograph].
- Bunnell, D. (2023) Tardis Cave photos [Photograph].
- Burgess, Sarah, Florea, Lee, and Branam, Tracy. (2023) "Divergent Geochemical Pathways of Carbonate Aquifer Evolution in a Classic Karst Terrain: (1) Polygenetic Cave Development Identified Using Longitudinal Groundwater Geochemistry" *Water*, 15(19), pp. 3410. <https://doi.org/10.3390/w15193410>

- Butzer, K. W. (1981) “Cave sediments, upper Pleistocene stratigraphy and mousterian facies in Cantabrian Spain,” *Journal of Archaeological Science*, 8(2), pp. 133–183. doi: 10.1016/0305-4403(81)90022-4.
- Canti, M. G. and Meddens, F. M. (1998) “Mechanical coring as an aid to archaeological projects,” *Journal of Field Archaeology*, 25(1), pp. 97–105. doi: 10.1179/jfa.1998.25.1.97.
- Carter, M. and Bentley, S. P. (2016) *Soil properties and their correlations*. 2nd ed. Standards Information Network.
- Churchman, J., Pasbakhsh, P., Lowe, D., and Benny, T. (2016) “Unique but diverse: some observations on the formation, structure and morphology of halloysite,” *Clay Minerals*, 51(3), pp. 395–416. doi: 10.1180/claymin.2016.051.3.14.
- Clynne, M. A. and Muffler, P. L. J. (2017) “Geologic Field-Trip Guide to the Lassen Segment of the Cascades Arc, Northern California,” *USGS Scientific Investigations Report 2017–5022–K2*.
- Collcutt, S. N. (1979) “The analysis of quaternary cave sediments,” *World Archaeology*, 10(3), pp. 290–301. doi: 10.1080/00438243.1979.9979738.
- Courty, M.A., Goldberg, P. and Macphail, R. (1990) “Soils and micromorphology in archaeology,” *Soil Science*, 150(6), p. 904. doi: 10.1097/00010694-199012000-00014.
- Cowan, A. P. (2022) *Late Quaternary Glacier Fluctuations at Picayune Lake, Northern California*. Masters Thesis. California State Polytechnic University, Humboldt.
- Demirmen, F. and Harbaugh, J. W. (1965) “Petrology and origin of Permian McCloud Limestone of northern California,” *Journal of Sedimentary Research*, 35(1), pp. 136–154.
- Despain, J. (2022a) *Ancient Palace Cave Map*. CRF Klamath Mountains Project
- Despain, J. (2022b) *Lake Shasta Caverns Map*. CRF Klamath Mountains Project
- Despain, J. (2022c) *Tardis Map*. CRF Klamath Mountains Project
- Despain, J. and Veerkamp, H. (2024a) *January Cave Map*. CRF Klamath Mountains Project
- Despain, J. and Veerkamp, H. (2024b) *Ellery Creek Cave Map*. CRF Klamath Mountains Project
- Despain, J., Veerkamp, H. and Lathrop, N. (2022) *CRF Klamath Mountains Project 2019-2021*. Cave Research Foundation Newsletter
- Despain, J. (2024) Ancient Palace Cave photos [Photograph]

- Despain, J. (2021) Lake Shasta Caverns photos [Photograph]
- Diller, J. S. (1902) *Topographic development of the Klamath mountains*. Denver, CO: United States Geological Survey.
- DOI (2013) Shasta Lake Water Resource Investigation - US Department of the Interior.
- Dublyansky, Y. V. (1995) "Speleogenetic history of the Hungarian hydrothermal karst," *Environmental Geology*, 25(1), pp. 24–35. doi: 10.1007/bf01061827.
- Dublyansky, Y. V. and Spotl, C. (2018) "Morphological effects of condensation-corrosion speleogenesis at Devils Hole Ridge, Nevada" *Hypogene Cave Morphologies*. Karst Waters Institute Special Publication. pp. 18-43
- Ecology and Environment, Inc. (1997) *Soil Sampling : Standard Operating Procedure*.
- Entrena, Ana, Fornós, Joan J., Auqué, Luis F., Gràcia, Francesca, Laita, Elisa (2022) "Mineralogical and sedimentological characterization of the clay-rich sediments from Ases cave (Cova dets Ases, Mallorca, Spain): Origin and classification," *Minerals (Basel, Switzerland)*, 12(11), p. 1473. doi: 10.3390/min12111473.
- Evans, J. R. (1977) "Economic Geology of the McCloud Limestone," California Division of Mines and Geology, 30(6), pp. 121–144.
- Farrand, W. R. (2001) "Sediments and stratigraphy in rockshelters and caves: A personal perspective on principles and pragmatics," *Geoarchaeology*, 16(5), pp. 537–557. doi: 10.1002/gea.1004.
- Farrant, A. R. and Smart, P. L. (2011) "Role of sediment in speleogenesis; sedimentation and paragenesis," *Geomorphology (Amsterdam, Netherlands)*, 134(1–2), pp. 79–93. doi: 10.1016/j.geomorph.2011.06.006.
- Feranec, R. S. (2009) "Implications of radiocarbon dates from Potter Creek Cave, Shasta County, California, USA," *Radiocarbon*, 51(3), pp. 931–936. doi: 10.1017/s0033822200034007.
- Fieldes, M. (1955) "Clay mineralogy of New Zealand. Pt. 2 Allophane and related mineral colloids," *N.Z. Journal of Science and Technology*, Sect. B(37), pp. 336–350.
- Folk, R. L. (1980) *Petrology of Sedimentary Rocks*. pp. 39-61. Austin, Tex: Hemphill Pub. Co.
- Folk, R.L. and Ward, W.C. (1957) A Study in the Significance of Grain-Size Parameters. *Journal of Sedimentary Petrology*, 27, pp.3-26.

- Foos, A.M., Sasowsky, I.D., LaRock, E.J., Kambesis, P.N. (2000) “Detrital Origin of a Sedimentary Fill, Lechuguilla Cave, Guadalupe Mountains, New Mexico.” *Clays Clay Miner.* 48, 693–698 (2000). <https://doi.org/10.1346/CCMN.2000.0480610>
- Forbes, M., Well, R. and Bestland, E. A. (2007) “Stable isotope investigation of cave and surface sediments in the Naracoorte region: evidence for a local aeolian source,” *Geomorphology*, 86, pp. 369–392.
- Ford, D. and Williams, P. D. (2007) *Karst Hydrogeology and Geomorphology*. 1st ed. Nashville, TN: John Wiley & Sons.
- Forti, P., Galli, E. and Rossi, A. (2006) “Peculiar minerogenetic cave environments of Mexico: The cuatro ciénegas area,” *Acta Carsologica*, 35(1). doi: 10.3986/ac.v35i1.245.
- Furlong, E. L. (1906) “The exploration of Samwel Cave,” *American Journal of Science*, s4-22(129), pp. 235–247. doi: 10.2475/ajs.s4-22.129.235.
- Gardner, M. C. (1964) *Cenozoic volcanism in the High Cascade and Modoc Plateau provinces of northeast California*. The University of Arizona. <https://repository.arizona.edu/handle/10150/565614>
- Gary, M.O. and Sharp, J. M. (2006) “Volcanogenic karstification of Sistema Zacatón, Mexico,” in *Perspectives on Karst Geomorphology, Hydrology, and Geochemistry - A Tribute Volume to Derek C. Ford and William B. White*. Geological Society of America, pp. 79–89.
- Gee, G. W. and Or, D. (2002) “2.4 Particle-Size Analysis,” in *SSSA Book Series*. Madison, WI, USA: Soil Science Society of America, pp. 255–293.
- Gilli, E. (2014) “Volcanism-induced karst landforms and speleogenesis, in the Ankarana Plateau (Madagascar). Hypothesis and preliminary research,” *International Journal of Speleology*, 43(3), pp. 283–293. doi: 10.5038/1827-806x.43.3.5.
- Gillieson, D. (1986) “Cave sedimentation in the new Guinea highlands,” *Earth Surface Processes and Landforms*, 11(5), pp. 533–543. doi: 10.1002/esp.3290110508.
- Gillieson, D. (1996) *Caves: Processes, Development and Management*. John Wiley & Sons.
- Gonzalez, M. (2014) *Statal Geometries of Tuscan Deposits in Big Chico Creek Canyon Outcrops and in the Subsurface Underlying Chico, California*. California State University, Chico.
- Granger, D. E., Fabel, D. and Palmer, A. N. (2001) “Pliocene–Pleistocene incision of the Green River, Kentucky, determined from radioactive decay of cosmogenic ^{26}Al and ^{10}Be in Mammoth Cave sediments,” *Geological Society of America bulletin*, 113(7), pp. 825–836. doi: 10.1130/0016-7606(2001)113<0825:ppiotg>2.0.co;2.

- Guffanti, Marianne; Clynne, Michael A; Smith, James G; Muffler, L J P; Bullen, Thomas D (1990) "Late Cenozoic volcanism, subduction, and extension in the Lassen Region of California, southern Cascade Range," *Journal of Geophysical Research*, 95(B12), p. 19453. doi: 10.1029/jb095ib12p19453.
- Hacker, B.R, Donato, M.M., Barnes, C.G., McWilliams, M.O, Ernst, W.G (1995) "Timescales of orogeny: Jurassic construction of the Klamath Mountains," *Tectonics*, 14(3), pp. 677–703. doi: 10.1029/94tc02454.
- Haggart, J. W. (1986) "Cretaceous stratigraphic sequences of north-central California suggest a discontinuity in the Late Cretaceous forearc basin," *Geology*, 14(10), p. 860. doi: 10.1130/0091-7613(1986)14<860:cssonc>2.0.co;2.
- Hamusek-McGann, B. (1995) "The Tuscan Obsidian Source of Northern California: Archaeological Implications and Geochemical Variability," *Proceedings of the Society for California Archae*, 8, pp. 13–32.
- Harper, G. D. and Wright, J. E. (1984) "Middle to Late Jurassic tectonic evolution of the Klamath Mountains, California-Oregon," *Tectonics*, 3(7), pp. 759–772. doi: 10.1029/tc003i007p00759.
- Hauselmann, A. D., Hauselmann, P. and Petroniu-Onac, B. (2010) "Speleogenesis and deposition of sediments in Cioclovina Uscata Cave, Sureanu Mountains, Romania," *Environmental Earth Science*, 61, pp. 1561–1571.
- Helley, E.J., and Harwood, D.S., (1985) Geologic map of the late Cenozoic deposits of the Sacramento Valley and northern Sierra Foothills, California: U.S. Geological Survey Miscellaneous Field Studies Map MF 1790, 5 sheets, scale 1:62,500, pamphlet 24 p.
- Herman, E. K., Toran, L. and White, W. B. (2012) "Clastic sediment transport and storage in fluviokarst aquifers: an essential component of karst hydrogeology," *Carbonates and Evaporites*, 27(3–4), pp. 211–241. doi: 10.1007/s13146-012-0112-7.
- Hildreth, W. (2007) "Quaternary Magmatism in the Cascades - Geologic Perspectives," *U.S. Geological Survey Professional Paper 1744*, 125. Available at: [<http://pubs.usgs.gov/pp/pp1744/>].
- Hill, C. A. and Forti, P. (1986) *Cave Minerals of the World*. 2nd ed. Huntsville, AL: National Speleological Society.
- Hjulström, F. (1955) "Transportation of detritus by moving water," in *Recent Marine Sediments*. SEPM (Society for Sedimentary Geology), pp. 5–31.
- Holliday, Vance T; Daulton, Tyrone L; Bartlein, Patrick J; Boslough, Mark B; Breslawski, Ryan P; Fisher, Abigail E; Jorgeson, Ian A; Scott, Andrew C; Koeberl, Christian; Marlon,

- Jennifer R; Severinghaus, Jeffrey; Petaev, Michail I; Claeys, Philippe (2023) “Comprehensive refutation of the Younger Dryas Impact Hypothesis (YDIH),” *Earth-science Reviews*, 247(104502), p. 104502. doi: 10.1016/j.earscirev.2023.104502.
- Horton, J., Butler, L., Overton, D.D., Garcia, D. (2015) “Variability of samples from various drilling and sampling methods,” *Proceedings Tailings and Mine Waste*.
- Humboldt Mfg, Inc. (2022) *H-4202A : Dynamic Cone Penetrometer Set - Manual*.
- Iacoviello, F. and Martini, I. (2013) “Clay minerals in cave sediments and terra rossa soils in the Montagnola Senese karst massif (Italy),” *Geological Quarterly*, 57(3). doi: 10.7306/gq.1111.
- Irwin, W. P. (1989) “Terranes of the Klamath mountains, California and Oregon,” *Tectonic Evolution of Northern California: Sausalito to Yosemite National Park, California*. June 28–July 7, 1989. Washington, D. C.: American Geophysical Union, pp. 19–32.
- Jackson, J. A. and Bates, R. L. (1984) *Dictionary of Geological Terms*. 3rd ed. American Geological Institute.
- Jenkinson, R.D.S., Gilbertson, D.D. and Griffin, C.M. (1983) “A hydraulic ram method for obtaining ‘undisturbed’ core samples from Quaternary cave sediments,” *Proceedings of the Geologists’ Association. Geologists’ Association*, 94(2), pp. 187–190. doi: 10.1016/s0016-7878(83)80010-8.
- Jillavenkatesa, A., Dapkunas, S. J. and Lum, L.-S. H. (2001) “Particle Size Characterization,” *National Institute of Standard (Special Publication 960-1)*.
- Kambesis, P. N. and Machel, H. G. (2013) “Caves and Karst of Barbados,” in *Coastal Karst Landforms*. Dordrecht: Springer Netherlands, pp. 227–244.
- Kasich, J. R., Taylor, M. and Butler, C. (2017) “Drilling and Subsurface Sampling,” in *Technical Guidance Manual for Hydrogeological Investigations and Ground Water*.
- Kruskal, W. H. and Wallis, W. A. (1952) “Use of ranks in one-criterion variance analysis,” *Journal of the American Statistical Association*, 47(260), p. 583. doi: 10.2307/2280779.
- Klimchouk, A. (2015) “The Karst paradigm: Changes, trends and perspectives,” *Acta Carsologica*, 44(3). doi: 10.3986/ac.v44i3.2996.
- Klimchouk, A. (2017) “Types and Settings of Hypogene Karst,” in *Hypogene Karst Regions and Caves of the World*. Cham: Springer International Publishing, pp. 1–39.

- Klimchouk, A. (2023) “Hypogene speleogenesis related to porphyry magmatic intrusions and its influence on subsequent karst evolution in the Peruvian high Andes,” Preprint.
- Knapp, E.P., Terry, D.O., Harbor, D.J., Thren, R.C. (2004) “Reading Virginia’s paleoclimate from the geochemistry and sedimentology of clastic cave sediments,” in *Studies of Cave Sediments*. Boston, MA: Springer US, pp. 95–106.
- Kotula, Piotr; Andreychouk, Viacheslav; Pawlyta, Jacek; Marynowski, Leszek; Jendrzewska, Izabela (2019) “Genesis of iron and manganese sediments in Zoloushka Cave (Ukraine/Moldova) as revealed by $\delta^{13}\text{C}$ organic carbon,” *International Journal of Speleology*, 48(3), pp. 221–235. doi: 10.5038/1827-806x.48.3.2255.
- Kukla J., Ložek V., K (1958) “promlematice vyzkumu jeskynnich vyplni (To the problems of investigation of the cave deposits)” *Československy Kras*, 11, 19-83.
- Kurecic T.B., Neven, W., Wacha, L., Bakrac, K., Grizela, A., Tresic Pavicic, D., Lüthgens, C., Sironic, A., Radovic, S., Redovnikovic, L., and Fiebig, M. (2021) “Changes In Cave Sedimentation Mechanisms During The Late Quaternary: An Example From The Lower Cerovac’ka Cave, Croatia”. *Front. Earth Sci.* 9:672229. doi: 10.3389/feart.2021.672229
- Lamb, H. (1895) *Hydrodynamic*. Cambridge [Eng.] : University Press,.
- Laureano, Fernando V; Karmann, Ivo; Granger, Darryl E; Auler, Augusto S; Almeida, Renato P; Cruz, Franciso W; Stricks, Nicolás M; Novello, Valdir F (2016) “Two million years of river and cave aggradation in NE Brazil: Implications for speleogenesis and landscape evolution,” *Geomorphology (Amsterdam, Netherlands)*, 273, pp. 63–77. doi: 10.1016/j.geomorph.2016.08.009.
- Le Ba, T; Alkurdi, A. H; Lukács, I. V; Molnár, J; Wongwises, S.; Gróf, G.; Szilágyi, I. M. (2020) “A novel experimental study on the rheological properties and thermal conductivity of halloysite nanofluids,” *Nanomaterials (Basel, Switzerland)*, 10(9), p. 1834. doi: 10.3390/nano10091834.
- Lowe, D. J. (1986) “Controls on the rates of weathering and clay mineral genesis in airfall tephra: A review and New Zealand case study,” in Colman, S. M. and Dethier, D. P. (eds.) *Rates of Chemical Weathering of Rocks and Minerals*. Academic Press (Orlando).
- Lomuscio, S (2021) “Getting Started with the Kruskal-Wallis Test” *UVA Library StatLab*. <https://library.virginia.edu/data/articles/getting-started-with-the-kruskal-wallis-test> (accessed July 11, 2024).
- Mann, H. B. and Whitney, D. R. (1947) “On a Test of Whether one of Two Random Variables is Stochastically Larger than the Other,” *The Annals of Mathematical Statistics*, 18(1), pp. 50–60. doi: 10.1214/aoms/1177730491.

- Mankinen, E. A., Irwin, W. P. and Grommé, C. S. (1989) “Paleomagnetic study of the Eastern Klamath terrane, California, and implications for the tectonic history of the Klamath Mountains Province,” *Journal of Geophysical Research*, 94(B8), pp. 10444–10472. doi: 10.1029/jb094ib08p10444.
- Martini, I. (2011). “Cave clastic sediments and implications for speleogenesis: new insights from the Mugnano cave (Montagnola Senese, northern Apennines, Italy)” *Geomorphology* 134, 452–460. <https://doi.org/10.1016/j.geomorph.2011.07.024>.
- Miller, M. (1989) “Intra-arc sedimentation and tectonism: late Paleozoic evolution of the Eastern Klamath Terrane, California”: *GSA Bulletin* 101 v. 2, p. 170–187.
- Moore, D. M. and Reynolds, R. C. (1997) *X-ray diffraction and the identification and analysis of clay minerals*. 2nd ed. New York, NY: Oxford University Press.
- Moss, C. and Merguerian, C. (2010) *Evidence for Multiple Glacial Advances and Ice Loading From a Buried Valley in Southern Manhattan*.
- Munsell, A. H. (2020) *A color notation*. Outlook Verlag.
- Mycielska-Dowgiałło, E. and Ludwikowska-Kędzia, M. (2011) “Alternative interpretations of grain-size data from Quaternary deposits,” *Geologos*, 17(4). doi: 10.2478/v10118-011-0010-9.
- Nehme, C., Jaillet, S., Delannoy, J.J., Azouni, M., Stephan, R., Comaty, T. (2014) “Subsurface flux adjustments and speleogenesis as inferred from sediment traps in major Lebanese cave systems,” *Acta Carsologica*, 44(1). doi: 10.3986/ac.v44i1.1149.
- Nordstrom, D. K. and Alpers, C. N. (1999) “Negative pH, efflorescent mineralogy, and consequences for environmental restoration at the Iron Mountain Superfund site, California,” *Proceedings of the National Academy of Sciences of the United States of America*, 96(7), pp. 3455–3462. doi: 10.1073/pnas.96.7.3455.
- North State Resources, Inc. (2010) Upper Sacramento River Watershed Assessment and Management Strategy.
- Northup, D. E and Lavoie, K. H. (2001) “Geomicrobiology of caves: A review,” *Geomicrobiology Journal*, 18(3), pp. 199–222. doi: 10.1080/01490450152467750.
- O’Dowd, C. (2017) *Analysis of volcanic ash*. Eastern Michigan University.
- Onac, B. and Forti, P. (2011) “Minerogenetic mechanisms occurring in the cave environment: an overview,” *International Journal of Speleology*, 40(2), pp. 79–98. doi: 10.5038/1827-806x.40.2.1.

- Onac, B. P. (2019) “Minerals in caves,” in *Encyclopedia of Caves*. Elsevier, pp. 699–709.
- OriginLab Corporation (1992) *OriginPro*. Available at: <https://www.originlab.com/origin>.
- Oster, J. L., Weisman, I. E. and Sharp, W. D. (2020) “Multi-proxy stalagmite records from northern California reveal dynamic patterns of regional hydroclimate over the last glacial cycle,” *Quaternary science reviews*, 241(106411), p. 106411. doi: 10.1016/j.quascirev.2020.106411.
- Palmer, A. N. (1991) “Origin and Morphology of Limestone Caves,” *Geological Society of America bulletin*, 103(1), pp. 1–21. doi: 10.1130/0016-7606(1991)103<0001:oamolc>2.3.co;2.
- Palmer, A. N. (2006) *Cave Geology*. Cave Books.
- Palmer, A. N. (2013) “Sulfuric Acid Caves: Morphology and Evolution,” *Treatise on Geomorphology*. Elsevier, pp. 241–257.
- Palmer, A.N., (2011), “Distinction between epigenic and hypogenic maze caves,” *Geomorphology*, Volume 134, Issues 1–2, p. 9-22, ISSN 0169-555X, <https://doi.org/10.1016/j.geomorph.2011.03.014>.
- Parés, J M; Campaña, I; Duval, M; Sier, M J; Ortega, A I; López, G I; Rosell, J (2020) “Comparing depositional modes of cave sediments using magnetic anisotropy,” *Journal of Archaeological Science*, 123(105241), p. 105241. doi: 10.1016/j.jas.2020.105241.
- Pasini, G. (2009) “A terminological matter: paragenesis, antigravitative erosion or antigravitational erosion?,” *International Journal of Speleology*, 38(2), pp. 129–138. doi: 10.5038/1827-806x.38.2.4.
- Piccini, Leonardo; Forti, Paolo; Giulivo, Italo; Mecchia, Marco (2007) “The polygenetic caves of Cuatro Ciénegas (Coahuila, Mexico): morphology and speleogenesis,” *International Journal of Speleology*, 36(2), pp. 83–92.
- Pickle, J. D. (1985) *Dynamics of clastic sedimentation and watershed evolution within a low-relief karst drainage basin*. Masters Thesis. University of New Mexico.
- Pinter, N. *et al.* (2011) “The Younger Dryas impact hypothesis: A requiem,” *Earth-science Reviews*, 106(3–4), pp. 247–264. doi: 10.1016/j.earscirev.2011.02.005.
- Polk, Jason S; van Beynen, Philip; Asmerom, Yemane; Polyak, Victor J (2013) “Reconstructing past climates using carbon isotopes from fulvic acids in cave sediments,” *Chemical Geology*, 360–361, pp. 1–9. doi: 10.1016/j.chemgeo.2013.09.022.

- Polyak, V. J. and Guven, N. (2000) “Clays in Caves of the Guadalupe Mountains, New Mexico,” *Journal of Cave and Karst Studies*, 62(2), pp. 120–126.
- Polyak, V.J., McIntosh, W.C., Guven, N., and Provencio, P (1998) “Age and Origin of Carlsbad Cavern and Related Caves from $^{40}\text{Ar}/^{39}\text{Ar}$ of Alunite,” *Science* (New York, N.Y.), 279(5358), pp. 1919–1922. doi: 10.1126/science.279.5358.1919.
- Poppe, L.J., Paskevich, V.F., Hathaway, J.C., and Blackwood, D.S (2001) *A Laboratory Manual for X-Ray Powder Diffraction, U.S. Geological Survey Open-File Report 01-041*. Available at: <https://pubs.usgs.gov/of/2001/of01-041/index.htm>.
- Putz, H. and Brandenburg, K. (2024) *Match! - Phase Analysis using Powder Diffraction, Crystalimpact.de*. Available at: <https://www.crystalimpact.de/match>.
- Reading, H. G. (ed.) (1996) *Sedimentary environments: Processes, facies and stratigraphy*. 3rd ed. Philadelphia, PA: Blackwell Science.
- Renault Ph., (1958) “Eléments de spéléomorphologie karstique”. *Annales de Spéléologie*, **13(1-4)**: 23–48.
- Renne, P. R., Becker, T. A. and Swapp, S. M. (1990) “ $^{40}\text{Ar}/^{39}\text{Ar}$ laser-probe dating of detrital micas from the Montgomery Creek Formation, northern California: Clues to provenance, tectonics, and weathering processes,” *Geology*, 18(6), p. 563. doi: 10.1130/0091-7613(1990)018<0563:aalpdo>2.3.co;2.
- Salomon, J.N. (2003) “Karst system response in volcanically and tectonically active regions” *Annals of Geomorphology; Karst in a Changing World*, supplement volume 131, p. 89-112.
- Sanborn, A. F. (1960) *Geology and paleontology of the southwest quarter of the Big Bend quadrangle, Shasta county, California; No.63*. Hassell Street Press.
- Sasowsky, I. D. (2007) “Clastic sediments in caves – imperfect recorders of processes in Karst,” *Acta Carsologica*, 36(1). doi: 10.3986/ac.v36i1.216.
- Sasowsky, I. D. and Mylorie, J. (2003) *Studies of cave sediments: Physical and chemical records of paleoclimate*. New York, NY: Kluwer Academic/Plenum.
- Shackley, M. L. (1972) “The use of textural parameters in the analysis of cave sediments,” *Archaeometry*, 14(1), pp. 133–145. doi: 10.1111/j.1475-4754.1972.tb00058.x.
- Sinclair, W. J. (1904) *The Exploration of Potter Creek Cave*. Berkeley: University of California Press.

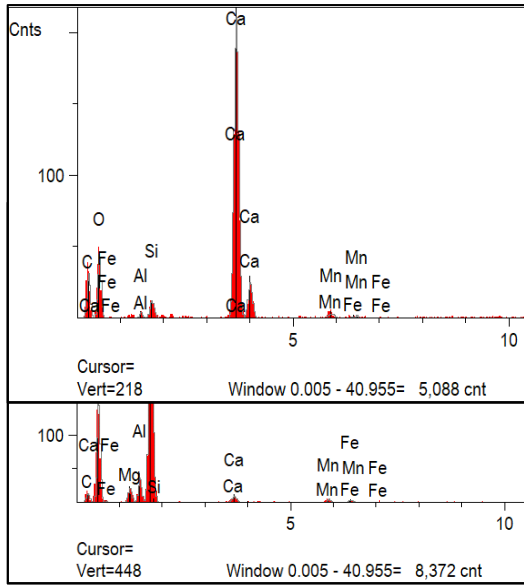
- Skinner, J. W. and Wilde, G. L. (1965) "Permian Biostratigraphy and Fusulinid Faunas of the Shasta Lake Area, Northern California," *Protozoa*, 6, pp. 1–98.
- Smith, J. P. (1894) "The Metamorphic Series of Shasta county, California," *The Journal of Geology*, 2(6), pp. 588–612. doi: 10.1086/607023.
- Spain, R. (2022) *Evaluation of Alterations in Intrusive Igneous Rocks: Lake Shasta Caverns, California*. Masters Thesis. Fort Hays State University.
- Spilde, M., Northrup, D. E. and Boston, P. J. (2006) "Ferromanganese deposits in the caves of the Guadalupe Mountains," *Caves and Karst of Southeastern New Mexico*. pp. 161-165
- Springer, G. S. (2019) "Clastic sediments in caves," *Encyclopedia of Caves*. Elsevier, pp. 277–284.
- Springer, G. S. and Kite, J. S. (1997) "River-derived slack water sediments in caves along Cheat River, West Virginia," *Geomorphology* (Amsterdam, Netherlands), 18(2), pp. 91–100. doi: 10.1016/s0169-555x(96)00022-0.
- Stock, G. M., Riihimaki, C. A. and Anderson, R. S. (2006) "Age Constraints on Cave Development and Landscape Evolution in the Bighorn Basin of Wyoming, USA," *Journal of Cave and Karst Studies*, 68(2), pp. 76–84.
- Stock, G.M., Granger, D.E., Sasowsky, I.D., Anderson, R.S., Finkel, R.C. (2005) "Comparison of U–Th, paleomagnetism, and cosmogenic burial methods for dating caves: Implications for landscape evolution studies," *Earth and Planetary Science Letters*, 236(1–2), pp. 388–403. doi: 10.1016/j.epsl.2005.04.024.
- Stratford, D. J. (2011) "Cave excavation: some methodological and interpretive considerations," *Cave and Karst Science*, 38(3).
- Temovski, M., Pruner, P., Hercman, H., Bosák, P. (2016) "A cave response to environmental changes in the Late Pleistocene: a study of Budimirica Cave sediments, Macedonia," *Geologia Croatica*, 69(3), pp. 307–316. doi: 10.4154/gc.2016.29.
- Tobin, B. (2007) "An Analysis of Base-Level Conduit Sedimentation in South Central Kentucky," Master Theses & Specialist Projects, (383), <https://digitalcommons.wku.edu/theses/383/>.
- Trappe, M. (2010) "Actualist approaches to the systematics and facies relations of clastic karst deposits," *Geodinamica Acta*, 23(1–3), pp. 41–48. doi: 10.3166/ga.23.41-48.
- Trask, J. B. (1855) *Geology of the Coast Mountains*.
- USBR (2001) Engineering Geology Field Manual, V. 2. U.S. Bureau of Reclamation.

- USDA-Shasta-Trinity National Forest (1998) McCloud Arm Watershed Analysis.
- Vacco, David A; Clark, Peter U; Mix, Alan C; Cheng, Hai; Edwards, R Lawrence (2005) “A speleothem record of Younger Dryas cooling, Klamath Mountains, Oregon, USA,” *Quaternary Research*, 64(2), pp. 249–256. doi: 10.1016/j.yqres.2005.06.008.
- Velde, B. (1992) *Introduction to Clay Minerals: Chemistry, origins, uses and environmental significance*. London, England: Chapman and Hall.
- W.B. White, C. Vito, and B.E. Scheetz (2009) “The mineralogy and trace element chemistry of black manganese oxide deposits from caves,” *Journal of Cave and Karst Studies*, 71(2), p.p. 136–143.
- White, E.L. and White, W.B. (1968), “Dynamics of sediment transport in limestone caves”, *National Speleological Society Bulletin*. 30, p.p. 115-129.
- White, W. B. (2007) “Cave Sediments and Paleoclimate,” *Journal of Cave and Karst Studies*, 69(1), pp. 76–93.
- White, W.B., Culver, D.C., Herman, J.S., Kane, T.C., Mylroie, J.E. (1995) “Karst Lands,” *American Scientist*, 83(5), pp. 450–459.
- Williams, P. (2008) “The role of the epikarst in karst and cave hydrogeology: a review,” *International Journal of Speleology*, 37(1), pp. 1–10. doi: 10.5038/1827-806x.37.1.1.
- Winkler, T. S. *et al.* (2016) “Detrital cave sediments record Late Quaternary hydrologic and climatic variability in northwestern Florida, USA,” *Sedimentary Geology*, 335, pp. 51–65. doi: 10.1016/j.sedgeo.2016.01.022.
- Woodside, J., Peterson, E. and Dogwiler, T. (2015) “Longitudinal profile and sediment mobility as geomorphic tools to interpret the history of a fluvio-karst stream system,” *International Journal of Speleology*, 44(2), pp. 197–206. doi: 10.5038/1827-806x.44.2.9.
- Yang, T., Liu, X., Wang, L., Bai, P., Li, J. (2020) “Simulating hydropower discharge using multiple decision tree methods and a dynamical model merging technique,” *Journal of Water Resources Planning and Management*, 146(2), p. 04019072. doi: 10.1061/(asce)wr.1943-5452.0001146.

Appendix I: EDS Results

Elt.	Line	Intensity (c/s)	Atomic %	Conc.	Units	Error 2-sig	MDL 3-sig
C	Ka	10.05	30.98	20.29	wt. %	2.87	2.555
O	Ka	15.20	54.02	47.14	wt. %	4.62	2.098
Al	Ka	1.44	0.30	0.44	wt. %	0.26	0.348
Si	Ka	5.19	0.87	1.34	wt. %	0.28	0.276

Figure 5.27: APC3 Black Fines - Scan 1 – Authigenic calcite with well-developed facets and striations

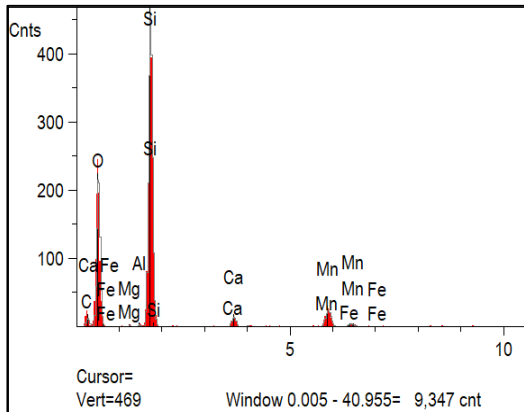


Ca	Ka	94.82	13.13	28.71	wt.%	1.10	0.341
Mn	Ka	0.00	0.00	0.00	wt.%	0.00	0.000
Fe	Ka	0.96	0.22	0.66	wt.%	0.37	0.424
			99.53	98.59	Wt.%		Total

Figure 5.27: APC3 Black Fines - Scan 2 – Corroded and pitted quartz with accessory oxide coatings

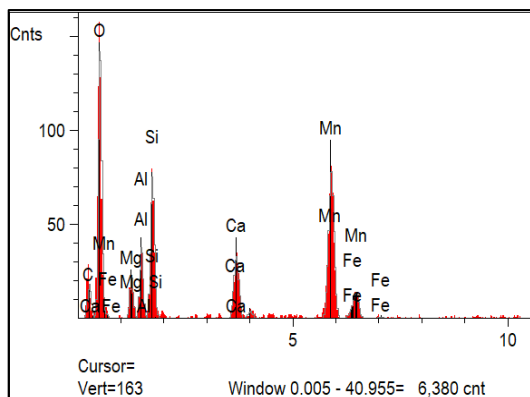
Elt.	Line	Intensity (c/s)	Atomic %	Conc.	Units	Error 2-sig	MDL 3-sig
C	Ka	5.25	28.57	19.96	wt.%	4.64	5.177
O	Ka	50.28	53.08	49.40	wt.%	2.63	1.012
Mg	Ka	8.70	1.21	1.71	wt.%	0.26	0.233
Al	Ka	13.24	1.42	2.23	wt.%	0.28	0.247
Si	Ka	159.42	14.84	24.25	wt.%	0.72	0.218
Ca	Ka	4.86	0.41	0.95	wt.%	0.20	0.183
Mn	Ka	2.29	0.26	0.83	wt.%	0.28	0.306
Fe	Ka	1.63	0.21	0.67	wt.%	0.30	0.357
			100.00	100.00	Wt.%		Total

Figure 5.27: APC3 Black Fines - Scan 3 – Well-rounded and spheroidal opal-A



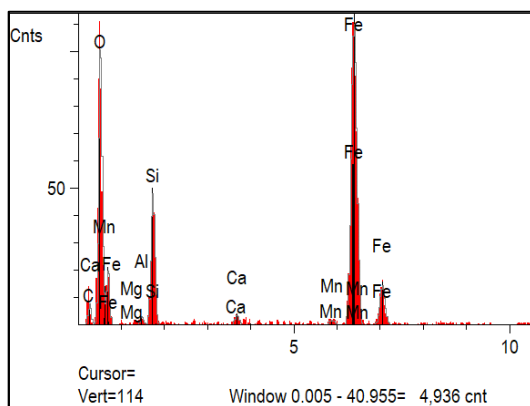
Elt.	Line	Intensity (c/s)	Atomic %	Conc.	Units	Error 2-sig	MDL 3-sig
C	Ka	4.71	21.50	14.64	wt.%	3.69	4.203
O	Ka	74.62	61.77	56.03	wt.%	2.42	0.781
Mg	Ka	0.87	0.12	0.17	wt.%	0.18	0.258
Al	Ka	1.35	0.14	0.21	wt.%	0.17	0.238
Si	Ka	168.10	14.43	22.97	wt.%	0.66	0.200
Ca	Ka	6.35	0.49	1.11	wt.%	0.19	0.163
Mn	Ka	13.32	1.40	4.36	wt.%	0.45	0.195
Fe	Ka	1.36	0.16	0.51	wt.%	0.22	0.227
			100.00	100.00	Wt.%		Total

Figure 5.27: APC3 Black Fines - Scan 4 – Manganese oxides/hydroxide with unknown aluminosilicate (near 1:2 Al:Si) and calcite



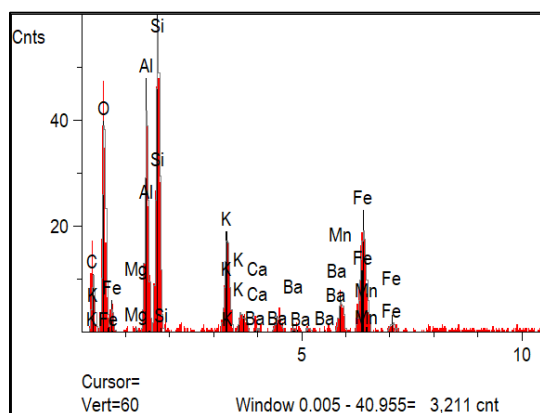
Elt.	Line	Intensity (c/s)	Atomic %	Conc.	Units	Error 2-sig	MDL 3-sig
C	Ka	6.85	27.36	17.44	wt.%	3.66	4.190
O	Ka	48.03	56.24	47.75	wt.%	2.63	1.147
Mg	Ka	8.14	1.84	2.37	wt.%	0.37	0.317
Al	Ka	13.05	2.21	3.16	wt.%	0.38	0.316
Si	Ka	27.08	3.82	5.70	wt.%	0.44	0.285
Ca	Ka	16.44	1.70	3.62	wt.%	0.36	0.222
Mn	Ka	42.32	6.21	18.11	wt.%	1.06	0.441
Fe	Ka	3.81	0.62	1.85	wt.%	0.44	0.420
			100.00	100.00	Wt.%		

Figure 5.29: APC3 Black Fines - Scan 1 – Fayalite (Fe₂SiO₄)



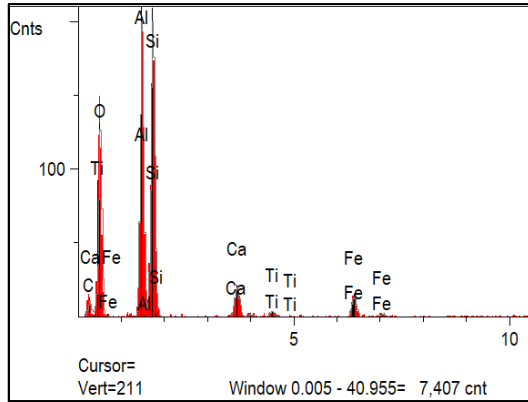
Elt.	Line	Intensity (c/s)	Atomic %	Conc.	Units	Error 2-sig	MDL 3-sig
C	Ka	2.59	20.36	10.71	wt.%	4.56	5.912
O	Ka	35.29	56.46	39.54	wt.%	2.54	1.143
Mg	Ka	0.27	0.13	0.14	wt.%	0.32	0.463
Al	Ka	1.32	0.45	0.54	wt.%	0.33	0.427
Si	Ka	18.03	4.86	5.97	wt.%	0.56	0.358
Ca	Ka	1.81	0.32	0.57	wt.%	0.27	0.331
Mn	Ka	1.32	0.32	0.77	wt.%	0.46	0.603
Fe	Ka	60.04	17.08	41.76	wt.%	2.03	0.737
			100.00	100.00	Wt.%		

Figure 5.29: APC3 Black Fines - Scan 2 – Manganese oxide/hydroxide coated alunitite



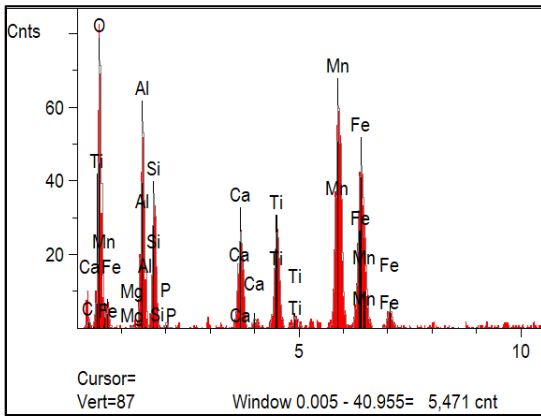
Elt.	Line	Intensity (c/s)	Atomic %	Conc.	Units	Error 2-sig	MDL 3-sig
C	Ka	3.53	36.74	22.98	wt.%	7.27	8.771
O	Ka	13.54	43.37	36.14	wt.%	3.86	2.178
Mg	Ka	0.20	0.10	0.12	wt.%	0.32	0.467
Al	Ka	14.78	5.25	7.37	wt.%	0.77	0.477
Si	Ka	20.42	6.55	9.58	wt.%	0.83	0.459
K	Ka	8.16	1.90	3.87	wt.%	0.57	0.444
Ca	Ka	2.05	0.50	1.03	wt.%	0.38	0.412
Mn	Ka	3.08	1.01	2.90	wt.%	0.72	0.608
Fe	Ka	10.76	3.96	11.52	wt.%	1.35	0.655
Ba	La	1.91	0.62	4.47	wt.%	1.72	1.914
			100.00	100.00	Wt.%		

Figure 5.43: LSC3 Yellow Fines - Scan 1 – Halloysite/kaolinite with accessory oxide and calcite coating



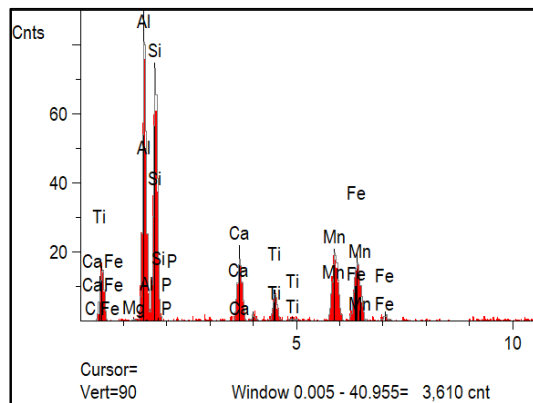
Elt.	Line	Intensity (c/s)	Atomic %	Conc.	Units	Error 2-sig	MDL 3-sig
C	Ka	2.29	26.38	17.57	wt.%	4.80	5.354
O	Ka	22.18	51.36	45.57	wt.%	2.85	1.193
Al	Ka	43.06	9.75	14.58	wt.%	0.65	0.238
Si	Ka	43.10	10.04	15.64	wt.%	0.69	0.255
Ca	Ka	5.88	1.05	2.33	wt.%	0.31	0.215
Ti	Ka	1.50	0.29	0.77	wt.%	0.24	0.242
Fe	Ka	4.20	1.14	3.52	wt.%	0.55	0.398
			100.00	100.00	Wt.%		

Figure 5.46: LSC3 Yellow Fines - Scan 1 – Fe-Mn allophane-imogolite nodule with ilmenite and calcite



Elt.	Line	Intensity (c/s)	Atomic %	Conc.	Units	Error 2-sig	MDL 3-sig
C	Ka	0.94	10.07	4.71	wt.%	4.60	6.490
O	Ka	20.60	53.67	33.46	wt.%	2.83	1.326
Mg	Ka	0.46	0.25	0.24	wt.%	0.35	0.495
Al	Ka	20.38	7.98	8.39	wt.%	0.75	0.501
Si	Ka	12.46	4.24	4.64	wt.%	0.57	0.472
P	Ka	0.80	0.25	0.30	wt.%	0.32	0.459
Ca	Ka	12.35	2.71	4.23	wt.%	0.50	0.370
Ti	Ka	13.19	3.06	5.71	wt.%	0.64	0.419
Mn	Ka	32.25	10.04	21.50	wt.%	1.43	0.561
Fe	Ka	22.28	7.73	16.83	wt.%	1.37	0.654
			100.00	100.00	Wt.%		

Figure 5.46: LSC3 Yellow Fines - Scan 2 – Platy halloysite/kaolinite with accessory oxide and calcite coating



Elt.	Line	Intensity (c/s)	Atomic %	Conc.	Units	Error 2-sig	MDL 3-sig
C	Ka	0.00	0.00	0.00	wt.%	0.00	0.000
O	Ka	2.20	20.01	10.16	wt.%	2.86	2.108
Mg	Ka	0.45	0.54	0.42	wt.%	0.45	0.598
Al	Ka	29.68	26.98	23.09	wt.%	1.60	0.645
Si	Ka	26.73	26.13	23.29	wt.%	1.71	0.722
P	Ka	0.00	0.00	0.00	wt.%	0.00	0.000
Ca	Ka	8.46	5.43	6.91	wt.%	1.00	0.764
Ti	Ka	3.75	2.53	3.85	wt.%	0.90	0.810
Mn	Ka	11.16	9.58	16.70	wt.%	1.92	0.891
Fe	Ka	9.23	8.80	15.58	wt.%	1.99	1.033
			100.00	100.00	Wt.%		

Appendix II: Radiocarbon Dates from EC13

BetaCal 5.0

Calibration of Radiocarbon Age to Calendar Years

(High Probability Density Range Method (HPD): INTCAL20)

(Variables: $\delta^{13}C = -24.0$ o/oo)

Laboratory number **Beta-685193**

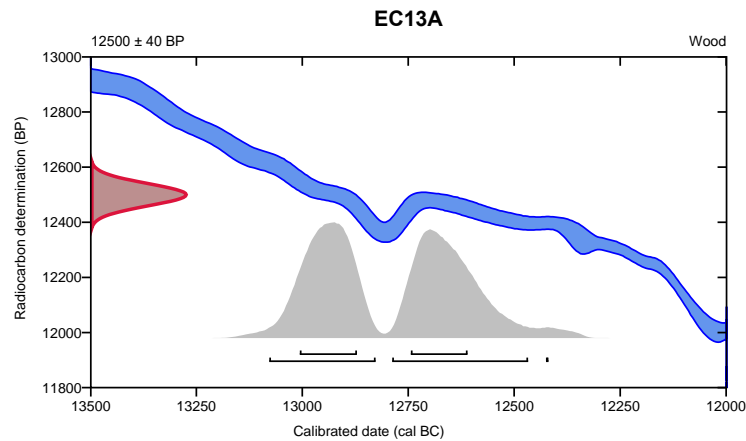
Conventional radiocarbon age **12500 ± 40 BP**

95.4% probability

(49%)	12790 - 12469 cal BC	(14739 - 14418 cal BP)
(46.2%)	13080 - 12829 cal BC	(15029 - 14778 cal BP)
(0.2%)	12427 - 12421 cal BC	(14376 - 14370 cal BP)

68.2% probability

(35.6%)	13008 - 12873 cal BC	(14957 - 14822 cal BP)
(32.6%)	12746 - 12612 cal BC	(14695 - 14561 cal BP)



Database used
INTCAL20

References

References to Probability Method

Bronk Ramsey, C. (2009). Bayesian analysis of radiocarbon dates. *Radiocarbon*, 51(1), 337-360.

References to Database INTCAL20

Reimer, et al., 2020, *Radiocarbon* 62(4):725-757.

Beta Analytic Radiocarbon Dating Laboratory

4985 S.W. 74th Court, Miami, Florida 33155 • Tel: (305)667-5167 • Fax: (305)663-0964 • Email: beta@radiocarbon.com

BetaCal 5.0

Calibration of Radiocarbon Age to Calendar Years

(High Probability Density Range Method (HPD): INTCAL20)

(Variables: $\delta^{13}C = -24.6$ o/oo)

Laboratory number **Beta-685194**

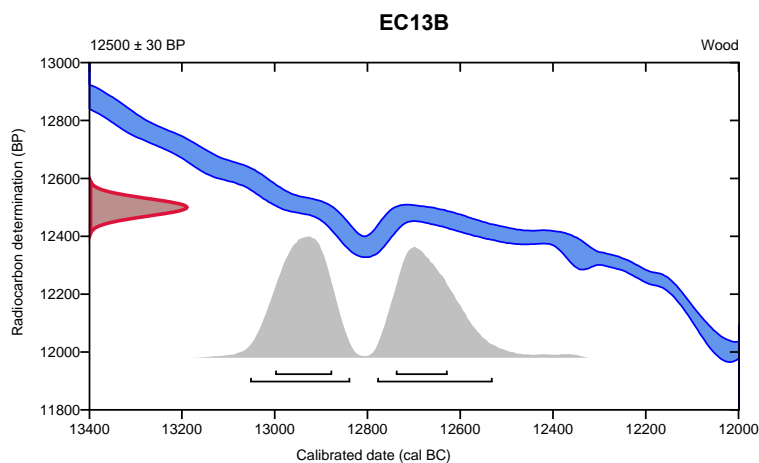
Conventional radiocarbon age **12500 \pm 30 BP**

95.4% probability

(48.5%)	13055 - 12839 cal BC	(15004 - 14788 cal BP)
(46.9%)	12781 - 12532 cal BC	(14730 - 14481 cal BP)

68.2% probability

(37.3%)	13001 - 12878 cal BC	(14950 - 14827 cal BP)
(30.9%)	12741 - 12629 cal BC	(14690 - 14578 cal BP)



Database used

INTCAL20

References

References to Probability Method

Bronk Ramsey, C. (2009). Bayesian analysis of radiocarbon dates. *Radiocarbon*, 51(1), 337-360.

References to Database INTCAL20

Reimer, et al., 2020, *Radiocarbon* 62(4):725-757.

Beta Analytic Radiocarbon Dating Laboratory

4985 S.W. 74th Court, Miami, Florida 33155 • Tel: (305)667-5167 • Fax: (305)663-0964 • Email: beta@radiocarbon.com

Appendix III: Standard Operating Procedure for Clay Mineral XRD Analysis with a Bruker D2 Phaser XRPD

Table of Contents

1 – General Information	
1.1 – Purpose.....	2
1.2 – Background.....	2
1.3 – Safety.....	2
2 – Sample Perpetration	
2.1 – Bulk Samples.....	3
2.2 - Gravity-Settled Glass Mounts – Bulk Samples.....	4
2.3 - Gravity-Settled Glass Mounts – Clay Fraction.....	5
2.4 – Oriented Glass Slides – Syringe Method.....	5
3 – Bruker D2 Phaser X-Ray Powder Diffractometer	
3.1 – Kiln Setup.....	8
3.2 – Instrument Setup.....	9
3.3 – Data Collection Setup.....	11
3.4 – Data Collection.....	12
3.5 – Data Interpretation – Match! XRD Software.....	13

Works Cited

- Poppe, L. J. *et al.* (2001) *A Laboratory Manual for X-Ray Powder Diffraction, U.S. Geological Survey Open-File Report 01-041*. Available at: <https://pubs.usgs.gov/of/2001/of01-041/index.htm>.
- Moore, D. M. and Reynolds, R. C. (1997) *X-ray diffraction and the identification and analysis of clay minerals*. 2nd ed. New York, NY: Oxford University Press.

1 General Information

1.1 Purpose

Procedures described in this SOP will allow personnel to prepare and perform XRPD analysis on fine-sediment samples utilizing a Bruker D2 Phaser. This SOP will review preparation procedures for separating a clay fraction, preparing glass slide and oriented mounts, and taking samples through heat treatment and treatment with ethylene glycol. Secondly, this SOP will review the Bruker D2 Phaser XRPD and proper instrument setup and operation. Lastly, data interpretation will be reviewed with a focus on clay mineral identification using Match! XRD Software and the USGS XRD Lab Manual.

1.2 Background

X-ray powder diffraction is a rapid, non-destructive scientific method that utilizes x-ray diffraction to identify structural information of powder and microcrystalline materials. Structural information, or atomic spacing, is determined by the diffraction of x-rays through a crystal lattice. X-rays are produced by an x-ray diffractometer at a known wavelength and frequency and are either reflected off the material surface or enter the crystal lattice and are diffracted at a specific wavelength. The diffractogram that is produced is specific to the crystal structure of the material and thus the mineral(s) present in the sample. To identify the mineral(s) present, one must compare the diffractogram to a database of known patterns or interpret pattern behavior after heat treatment and chemical treatment. The most common database of reference patterns is the Powder Diffraction File (PDF) compiled by the International Centre for Diffraction Data (ICDD). The PDF consists of over 200,000 diffraction patterns that are used for pattern identification. Certain minerals, such as clay minerals, have broad peaks that are not easily identifiable using pattern correlation using the PDF. Instead, one must prepare glass slide mounts and obtain x-ray diffractograms after heat treatment and ethylene glycol chemical treatment. Heat and chemical treatment affect atomic spacing by collapsing or swelling the crystal structure in characteristic manners. Behavior of clay mineral spacing through heat and chemical treatment is well understood and summarized by the USGS XRD Lab Manual through the 'Clay Mineral Identification Flow Diagram'. Clay minerals and fine sediments are one of the many materials identifiable by X-ray diffraction. X-ray diffraction is used by many workers in field such as mineralogy, metallurgy, forensic science, chemistry, physics, and pharmaceutical sciences.

1.3 Safety

X-ray powder diffraction uses x-ray radiation to identify structural information of crystalline materials. X-ray radiation is ionizing radiation that transmits enough energy to ionize atoms and damage molecular bonds. High doses of x-ray radiation can cause skin tissue damage and lower doses can lead to increased cancer risk. The Bruker D2 Phaser is equipped with enough radiation protection to prevent x-ray radiation from affecting the user. For instance, the autolocking main door needs to be closed before the instrument can emit radiation. The autolocking main door indicates when x-rays are being generated by a yellow light bar at the top of the door. Before using the instrument, all users must complete the online radiation safety

course through the lab manager.

2 Sample Preparation

Equipment Needed for Sample Preparation

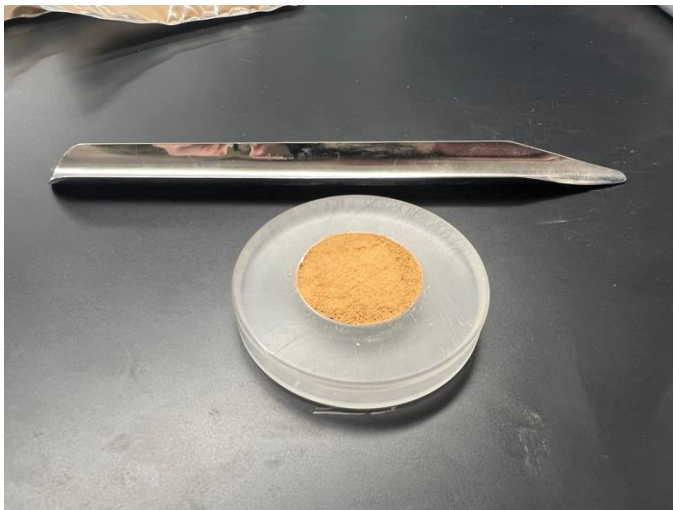
- (2-3) 1000 mL beakers
- (2-3) 25 mL beakers
- (2-3) Beaker labels
- (1) Pen/pencil
- (1) Small metal spatula/spoon
- (1) Plastic pipette
- (1) Mortar & pestle
- (12+) Kim wipes
- (3+) 26x26mm glass slides
- (1) Benchtop lab mixer
- (1) Benchtop scale
- (100g+) Sodium hexametaphosphate powder
- (3 liters+) DI water

2.1 Bulk Samples

- 1) Air-dry sample in preparation for scanning.
- 2) Remove any obvious organics before sample preparation.
- 3) First sieve the sample with a No. 18 (1mm) sieve to remove large clasts that cannot easily be ground. Use the sieve tray to collect sieved material.



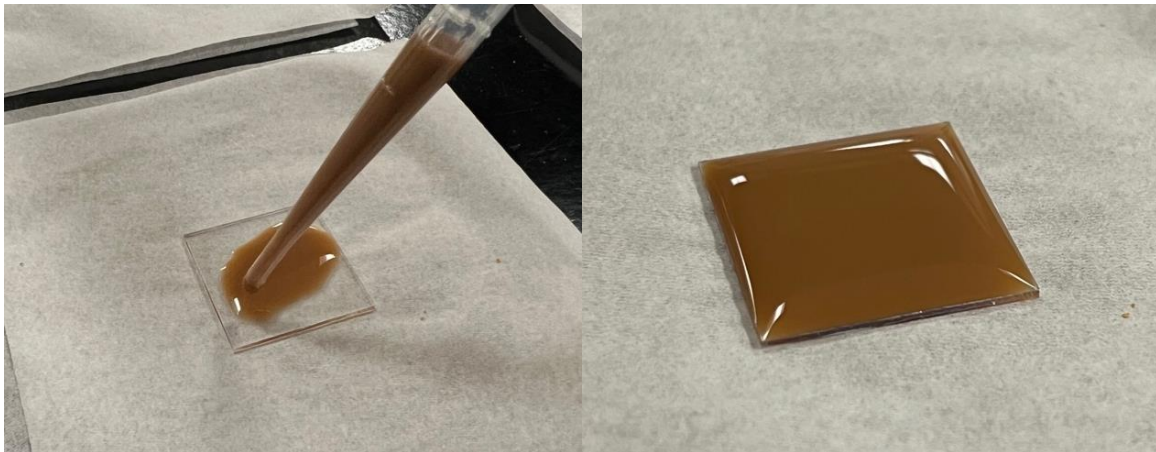
- 4) Use the mortar and pestle to gently grind the sieved sample to an approximate grain size of fine to very-fine sand.
- 5) Sieve the ground sample with a No. 80 (180 micron) sieve to homogenize the sample to 180 micron (fine sand) or less.
- 6) Prepare no less than approximately 10 g of air-dried sample in a plastic sample bag and label accordingly.
- 7) When in the XRD lab, proceed to section 3.2 to turn on the Bruker D2 Phaser.
- 8) Once the Bruker D2 Phaser is turned on and ready to scan a sample, grab a silicon sample holder and metal scrapper. Make sure the silicon holder and metal scrapper are clean and dry.
- 9) Carefully pour dried powder sample into the sample holder being careful not to pour too much sample into the holder. Remove any grain agglomerations.
- 10) Use the metal scrapper to gently scrape the powder flat in the sample holder. The powder must be flush with the sample holder surface. Be careful to not pack the powder in the sample holder and use a Kim Wipe to clean excess powder around the outside rim of the sample holder.



- 11) When the D2 Phaser is ready, place the filled sample holder into the instrument and begin the scan. Proceed to section 3.2 onwards for scan setup, etc.

2.2 Gravity-Settled Glass Mounts – Bulk Samples

- 1) Prepare a 1000 mL beaker, approximately 400 mL of distilled ionized water, 20-30 mg of sodium hexametaphosphate, and approximately 3-4 g the fine-sediment sample.
- 2) Pour approximately 400 mL of DI water into the 1000 mL beaker and place approximately 4-5 g of sample (dry or moist) into the water. Break up clay-rich samples to 2-3 cm diameter chunks with clean hands or a metal spatula.
- 3) Place 20-30 mg of sodium hexametaphosphate into the water and sample mixture and place the mixture under the mechanical mixer.
- 4) Mix the sample in the mechanical mixer for 15-20 minutes or until all aggregates are totally separated.
- 5) While sample is mixing, prepare three 26x26 mm glass slides, three Kim Wipes, and a clean pipette.
- 6) While sample is mixing, carefully pipette small amounts of mixture onto three separate glass slides until the glass slide is covered with sample. This usually takes about 1-1.5 mL of liquid depending on the concentration of suspended fines. Be careful not to break surface tension over the edge of the slide and try to homogenize the mixture throughout the slide.



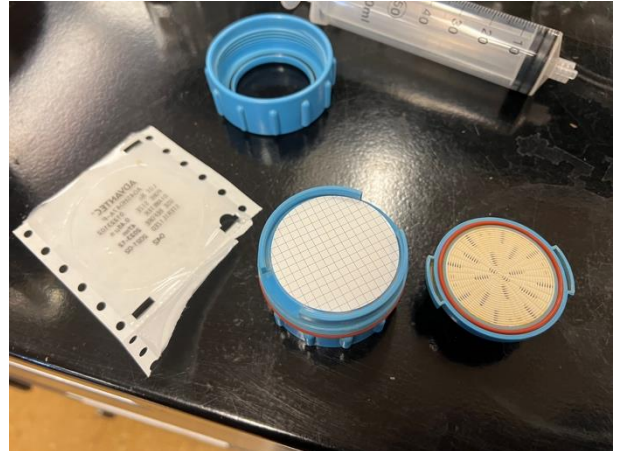
- 7) Let glass slide dry overnight under room temperature and be careful not to move the slides while drying.

2.3 Gravity-Settled Glass Mounts – Clay Fraction

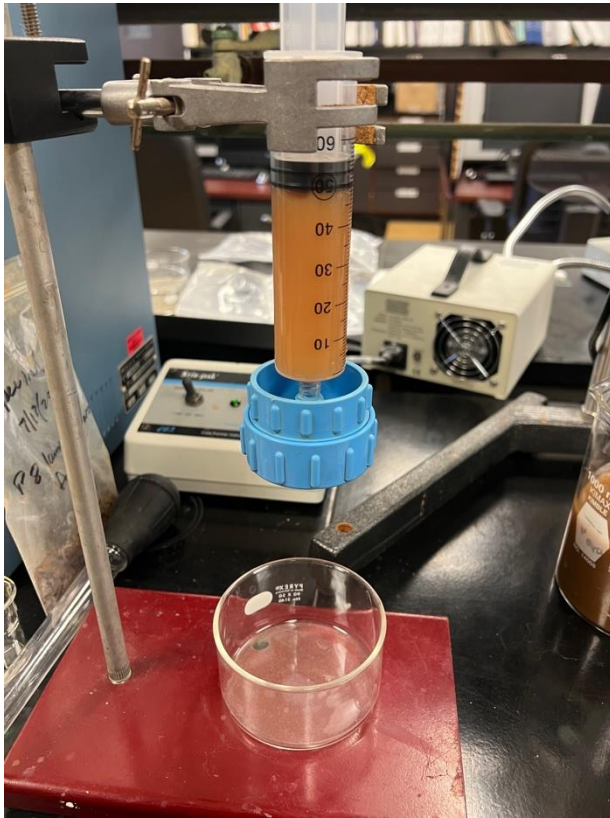
- 1) Repeat steps 1-5 of section 2.2 to prepare a mixture of suspended fine material and sodium hexametaphosphate dispersant.
- 2) Set the mixture aside for approximately 1 hour at room temperature to allow for the silt and sand fractions to settle out of suspension. With a non-permanent marker or label, mark 5 cm below the surface of the mixture. The clay fraction will be in suspension above this 5 cm mark.
- 3) Repeat steps 6 & 7 of section 2.2 to prepare three glass slides.

2.4 Oriented Glass Mounts – Syringe Method

- 4) Repeat the process for preparing a suspended mixture by following steps 1-5 in section 2.2.
- 5) Prepare a 75 mL plastic syringe, 0.47 micron filter (gridlines facing upwards, see photo), filter holder (gridlines facing upwards, see photo), syringe clamp on a pipette stand, and small beaker to collect ~50 mL of drip water.

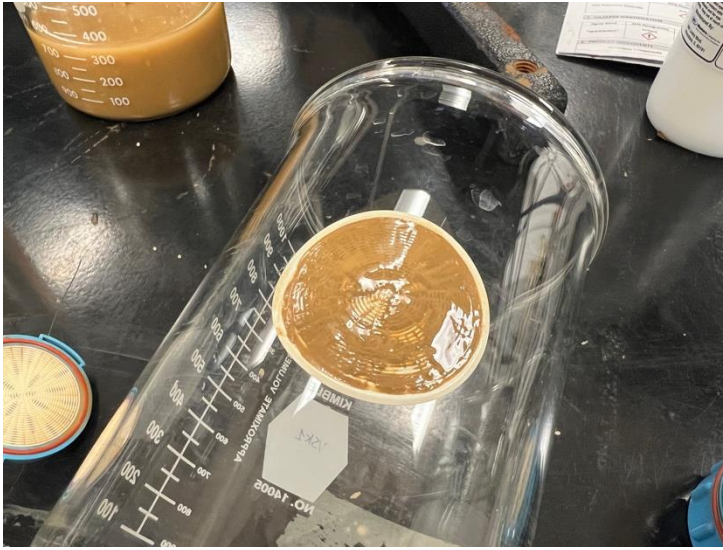


- 6) While sample is mixing, pull approximately 50 mL from the mixture using the plastic syringe and attach the filter holder to the syringe. Place the syringe and filter holder into the syringe clamp on the pipette stand and place a small beaker underneath the filter.



- 7) Begin filtering the sample mixture through the filter and be careful not to apply too much force on the syringe. Because of the fine particle-size, it will be challenging to filter the mixture. Be patient.
- 8) Prepare a 1000 mL beaker and place it on its side on the lab bench.
- 9) Once approximately 50 mL has been passed through the filter, remove the filter holder from the syringe and set it aside.
- 10) Prepare a 1000 mL beaker and place it on its side on the lab bench. This will provide a smooth surface to peel the filtered material off the filter and onto a glass slide.
- 11) Unscrew the filter holder and carefully peel the filter off the holder. Be careful not to disturb the filtered sediment more than necessary. Extra care is needed in this step.

12) Drape the filter over the side of the beaker with the filtered sediment facing upwards.



13) Take a clean glass slide and carefully peel/transfer the filtered sediment onto the glass slide. Be careful not to smear the glass slide and the filtered sediment or it will damage the integrity of the oriented grains. At least half of the central portion of the glass slide needs to be covered in material. the entire slide does not need to be covered.



- 14) Prepare three of these oriented glass slides by repeating steps 2-11. Let glass slides air-dry overnight in preparation for scanning.



3 Bruker D2 Phaser X-Ray Powder Diffractometer

Equipment Needed for Operating the Bruker D2 Phaser

- (3+) Prepared 26x26mm glass slides
- (1) Glass slide sample holder (picture)
- (1) Bulk sample holder (picture)
- (1) Small metal spatula
- (5+) Kim wipes
- (1) Ethylene glycol dropper
- (1) Metal tongs
- (1) Kiln for heat treatment

3.1 Kiln Setup

- 1) If you are proceeding with clay mineral identification, go to the kiln and start the setup procedure before turning on the Bruker D2 Phaser. The kiln is at the left end of the lab bench along the window in G019.
- 2) Follow the procedure below to turn the kiln to 400 C to start. You will need to turn the kiln to 550 C in later steps, but for now let the kiln pre-heat to 400 C.



Ramp-Hold Programming

Use these instructions for your first firings. Later you may prefer "Ramp-Hold Shorthand Instructions," page 31.

As the program prompts for segments, rate, temperature, etc., you will see values from the last firing. To use these again, press **ENTER**. To control cooling, set the segment to a lower temperature than that of the preceding segment.

To fire without Alarm or Delay: Follow steps 1 through 7. Then press **START** once.

- 1 Apply power to the kiln. **8888** then **Idle** will appear. (Press **ENTER** **Idle** does not appear.)
- 2 Press **4** **USER** will appear. Enter a number from 1 to 4.
- 3 Press **ENTER** **RA** will appear. Enter firing rate for segment 1 (temperature change per hour: from 1 to 9999).
- 4 Press **ENTER** **FR** (or **CR**) will appear. Enter the target temperature of segment 1.
- 5 Press **ENTER** **Hd** will appear. Enter segment 1 hold time in hours/minutes (e.g. 12 hours, 30 minutes = 12.30). No hold = 0.
- 6 Press **ENTER** **FN** appears, and you have an AOP receptacle on your kiln, select ON or OFF. Press **ENTER**. (For more details on AOP, see AOP option, page 20.)
- 7 Continue entering values for the segments needed. When **RA** appears for the first segment you don't need, press **0**, then **ENTER** **Idle** will appear.
- 8 **To set Alarm:** press **7** **ALARM** will appear. Enter alarm temperature. (Enter **0** to turn alarm off.) Then press **ENTER** **Idle** will appear.
- 9 **To set Delay:** press **3** **DELA** will appear. Enter delay time (i.e. 12 hours, 30 minutes = 12.30). Then press **ENTER** (Delay zeroes opt after each completed firing.) **Idle** will appear.
- 10 **To start program,** press **ENTER** once. **STRT** will appear, then kiln temperature. If a delay was programmed, **STRT** will appear, then time remaining until start. To stop the firing, press **STOP**.

We recommend using Program Review (page 6) before firing. When program fires to completion, **CPLT** will appear. Press **ENTER** **Idle** will appear. To shut off the alarm when it sounds during a firing, press **ENTER**.

User Programs (USER)

When you enter Ramp-Hold mode, the first prompt to appear is **USER** meaning, "Select one of your programs." You, the user, can make your own firing schedules and store them in memory. A firing schedule, or program, is the segments needed for a firing. To make a segment, you will need three facts:

- rate (how fast temperature changes in degrees per hour)
- target temperature
- hold, if any

The controller can retain four user programs in memory even when power is turned off. User programs are numbered from 1 through 4. User program #1 can have up to 20 segments. User programs #2 - #4 can have ten segments each. You don't have to use all 20 or all 10 segments—only the number needed per firing. Often one segment is all you will need. A User program can be as simple as a single ramp.

When using Ramp-Hold for the first time, press **1** when **USER** appears. Your first firing will be stored as User Program #1.

Each time you store another program, select another available number, such as 2, at the **USER** prompt. Adding a program to a user number over-writes any existing program stored there. Write down your User Programs.

Note: If you don't need all the segments available in a User program, zero out the unused segments. First, enter values for the segments needed. At the

Segment	Rate %	Temp °C	Hd H
1	100	350	—
2	180	950	2.0
3	350	2250	2.0
4	9999	2100	10
5	65	1910	40

Write down each program stored in memory. Before firing, use Program Review to be sure everything is correct.

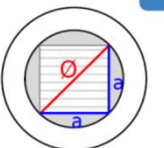
RA prompt for the segment you don't need, press **0**, then **ENTER**. The display will return to **Idle**.

Note: For repeat firings that you don't want to inadvertently change, see Program Lock, page 20.

3.2 Instrument Setup

- 3) Begin by signing into the lab sign-in sheet next to the instrument.
- 4) Go to the back of the instrument and turn the silver key clockwise and power button on, in that order.
- 5) Log into the Lab Manager account using the password 'Bruker.'
- 6) If taking a measurement, open the Diffrac.Measurement icon on the icon bar and click OK when the password prompt is displayed.
- 7) Open the instrument hood by pulling out on the central black knob. This is the door handle and will auto-lock when the scan is in process.
- 8) Set the divergence slit according to the sample size and 2theta starting angle. In this case, for a starting angle of 3 degrees and square glass slide dimension of 26x26mm use the 0.2 mm divergence slit. Other divergence slit sizes are in the keyboard drawer. When installed, the number on the divergence slit should be facing upwards.

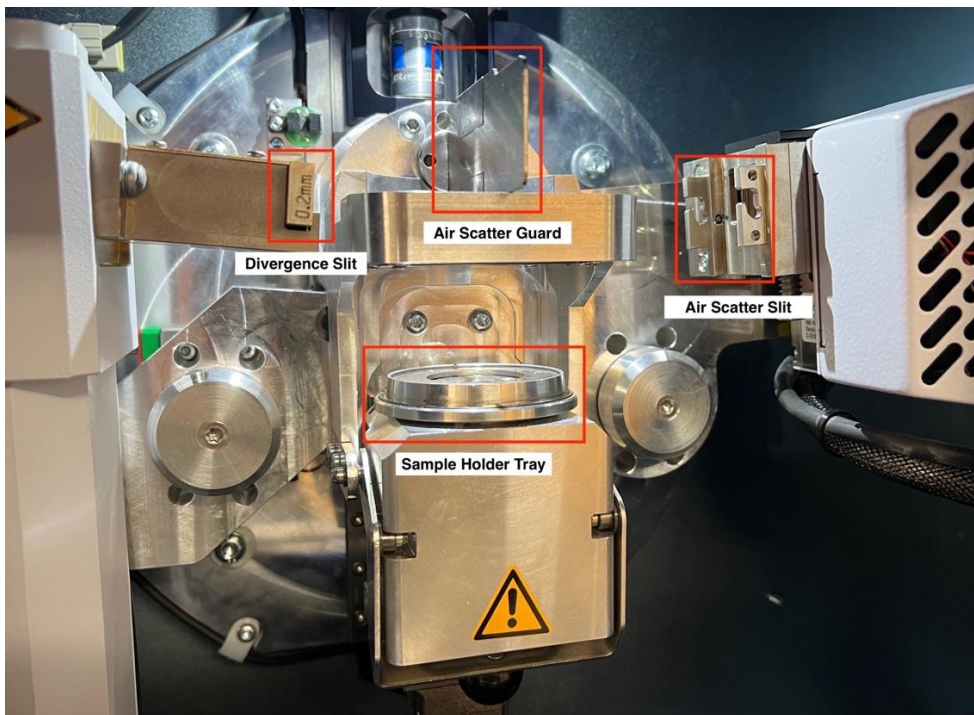
Fixed slit for different starting angles



Choose the column depending on the start angle

Fixed slit for a given starting angle 2θ and sample size		1	2	3	5	7.5	10	15	20
sample (mm)									
a	ϕ	Correct fixed slit (in mm)							
7.1	10.0	-	0.05	0.1	0.2	0.2	0.4	0.6	0.6
14.1	20.0	0.05	0.1	0.2	0.4	0.6	0.6	1	1
17.7	25.0	0.1	0.2	0.2	0.4	0.6	1	1	2
21.2	30.0	0.1	0.2	0.2	0.6	0.6	1	1	2
28.3	40.0	0.1	0.4	0.4	0.6	1	1	2	2

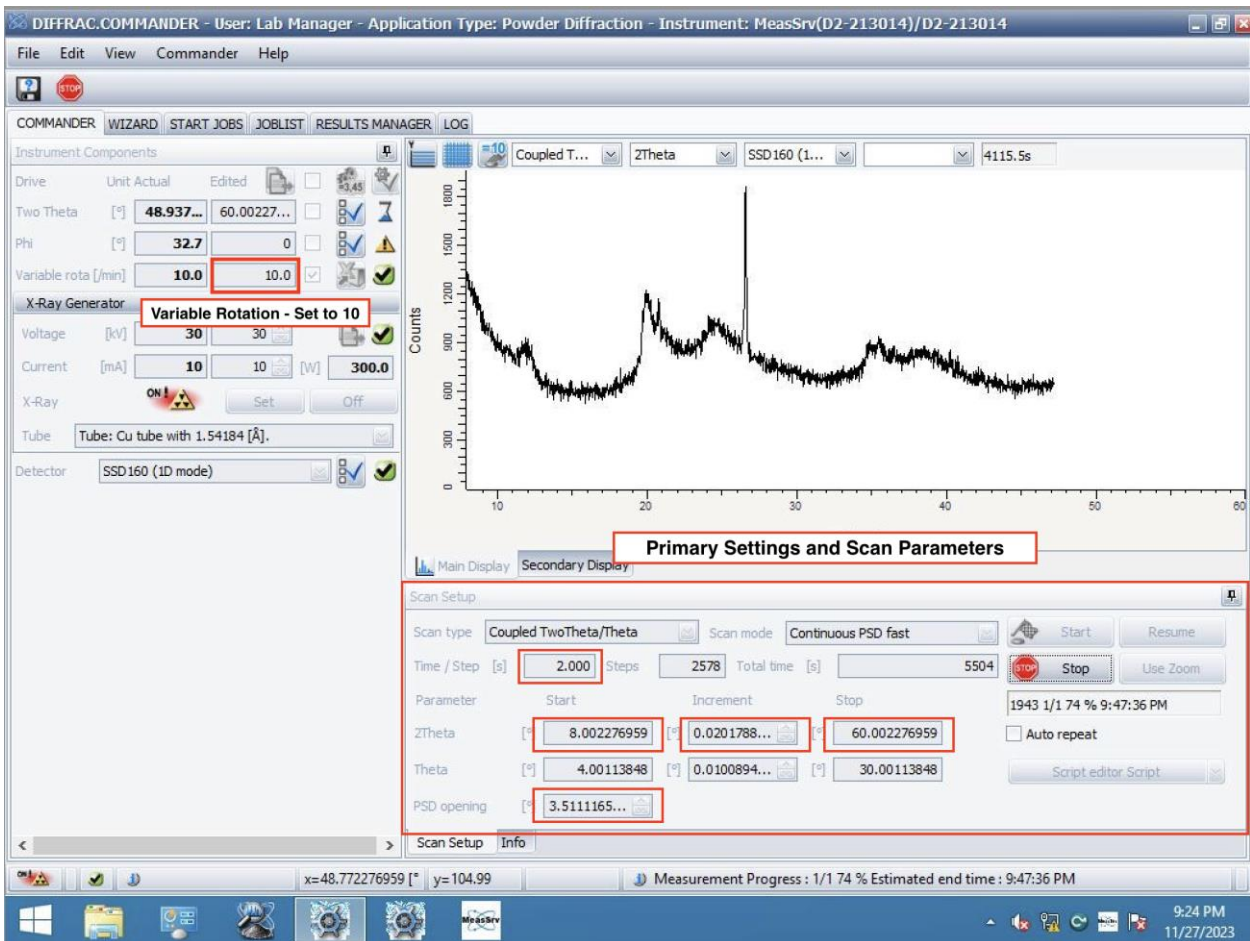
Choose the row depending on the sample size



- 9) Place the air scatter screen above the sample tray to 1 mm spacing.
- 10) Confirm that the beam stop is removed. The beam stop is a thin strip of black metal at the right side of the sample tray. Remove the beam stop with the small allen key in the keyboard drawer. The beam stop allows for collection at smaller starting angles.
- 11) Pull down on the black central handle to lower the sample holder tray.
- 12) Place the sample holder in the tray and gently push the tray back into position. Make sure the tray is fully seated in position.
- 13) Close the hood after confirming that all components are in place.
- 14) Open Diffrac.Measurement to begin the data collection process.

3.3 Data Collection Setup

- 1) Familiarize yourself with the general layout of the Diffrac.Measurement. The primary settings and scan parameters will be in the 'scan setup' window highlighted in red.



- 2) Set the variable rotation to 10 degrees/min, as seen in the highlighted box to the upper left. This will rotate the sample to allow for a scanning of more individual mineral grains.
- 3) The scanning parameters you will need to input/change before scanning are step time (seconds), step increment (degrees), PSD opening (degrees), and starting and ending 2theta angle (degrees). These settings will depend on the material you are scanning and the quality/resolution of the scan you are looking to produce.
- 4) The step time (written as Time / Step in the scan setup window) will depend on the desired resolution of the scan. Typically, the step time will be setup for 1 second/step for clay analysis. A step time of 2 seconds/step is useful for especially amorphous material, such as amorphous aluminosilicates (allophane/imogolite) or opal materials. A step time less than 1 second is useful in quick analysis and not typically used in publications.

- 5) Since clays have most of their diagnostic reflections at low 2θ angles, set the starting 2θ angle to 3 degrees 2θ . Most clays do not have strong peaks at higher angles, so set the ending 2θ angle to 40 degrees 2θ .
- 6) The step increment (in between the starting and ending 2θ) should be set to 0.02 degrees. The step increment sets the degrees covered during each step time. Generally, the lower the step increment the higher the scan resolution will be, with 0.02 degrees being the lowest step increment possible.
- 7) Generally, the PSD opening controls the area of the sample that is exposed to X-ray radiation. If the starting 2θ angle is less than 10 degrees, the PSD opening should be set to half the starting 2θ angle. If the starting angle is 10 degrees or above, the PSD opening should be set to 4.8 degrees.
- 8) Once all the necessary parameters are set, proceed to placing the glass slide and sample holder on the sample holder tray and push the sample holder tray up into position.

3.4 Data Collection

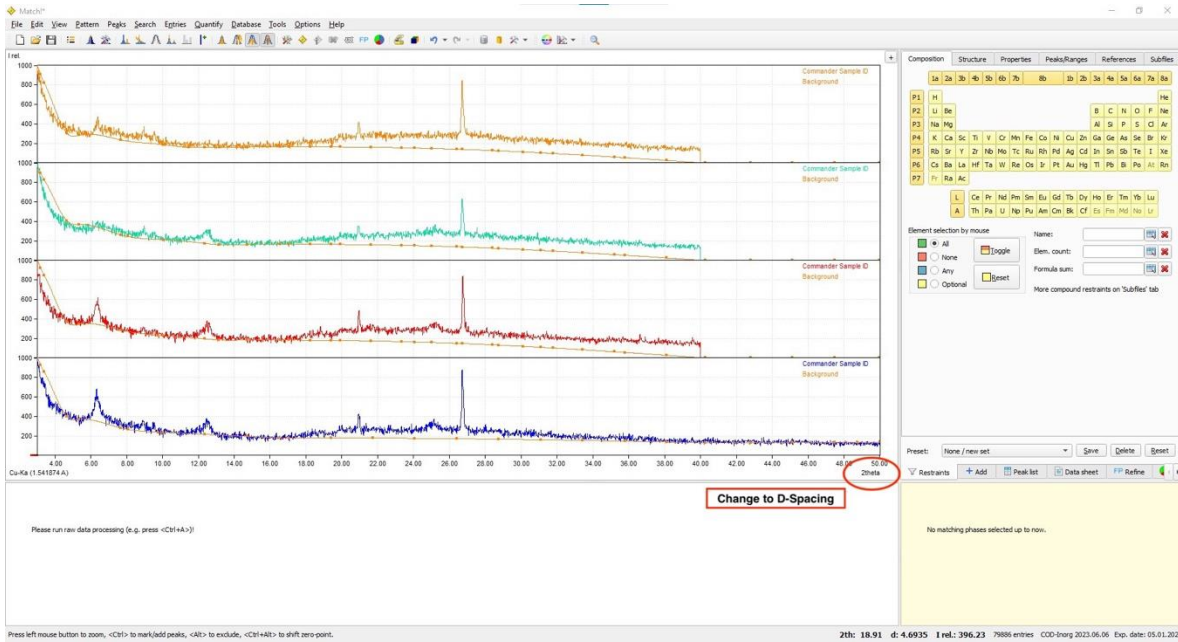
- 1) Once the proper scan parameters are set and sample is loaded, close the instrument door and begin the first scan by pressing the 'start' button in the 'scan setup' pane.
- 2) If you are scanning for clay mineralogy there will be three slides and four scans. One slide will be used for both the untreated and the ethylene glycol scans, and the other two slides will be used for heat treatment to 400 and 550 C. The first scan will be on an untreated, room-temperature glass mount. The second will be on after ethylene glycol treatment, one after heating to 400 C, and one after heating to 550 C. You cannot use the glass slide heated to 400 C for the 550 C scan; the two slides must be heated separately.
- 3) If the oven is pre-heated to 400 C, place one of the heat treatment slides into the oven and heat the slide for at least 30 minutes. Scanning the untreated slide at a 1 second step time usually takes around 30 minutes.
- 4) After the scan of the untreated slide is complete, press the 'stop' button in the scan setup window and turn off the X-ray emitter by pressing the 'off' button in the 'X-ray generator' window below the 'variable rotation' button. Save the file in .raw format by clicking 'save result' in the file tab.
- 5) Once the X-ray emitter is off and the yellow bar light is turned off, open the primary door and remove the untreated glass slide and sample holder.
- 6) If the 400 C heat treatment slide has been in the oven for at least 30 minutes, proceed to carefully removing it from the oven with metal tongs and place it in a glass dish to cool for 1-2 minutes.

- 7) Once the 400 C glass slide is cool to the touch, proceed to carefully placing it on the sample holder and put the slide and holder into the sample holder tray. Close the main door and begin a new scan. Before beginning a new scan, make sure the previous scan is saved in .raw format.
- 8) While the 400 C scan is in progress, proceed to turning the kiln temperature up to 550 C for the next heat treatment.
- 9) While the kiln is pre-heating to 550 C, place the previously scanned untreated glass slide onto a Kim wipe for ethylene glycol treatment.
- 10) Use a dropper of ethylene glycol to drop a single drop in the middle of the untreated glass slide. Let the single drop absorb throughout the slide. Place a second small drop if the first drop does not soak the entire slide. Gently soak up any extra ethylene glycol with a clean Kim wipe. The slide should not be overly wet. (picture)
- 11) When the 400 C scan is complete, save the file and remove the sample from the sample holder tray. Replace the 400 C glass slide with the ethylene glycol treated slide and begin the third scan.
- 12) Once the kiln is pre-heated to 550 C, place the third remaining glass slide into the kiln and heat the slide for at least 30 minutes.
- 13) Complete the fourth scan (550 C) after the ethylene glycol-treated slide is complete and the file is saved.
- 14) Once all four scans are complete, remove the 550 C glass slide and sample holder from the instrument and close the main door.
- 15) Make sure all four files are saved in .raw file format and transfer the data to an external usb drive. The usb connections are in the back of the instrument to the left of the silver key.
- 16) Once all data is transferred proceed to shutting down the computer. The screen will prompt you when it is safe to switch off the instrument. Go to the back of the instrument and turn the power button off and silver key counterclockwise.
- 17) To turn off the kiln simply unplug it from the wall outlet.

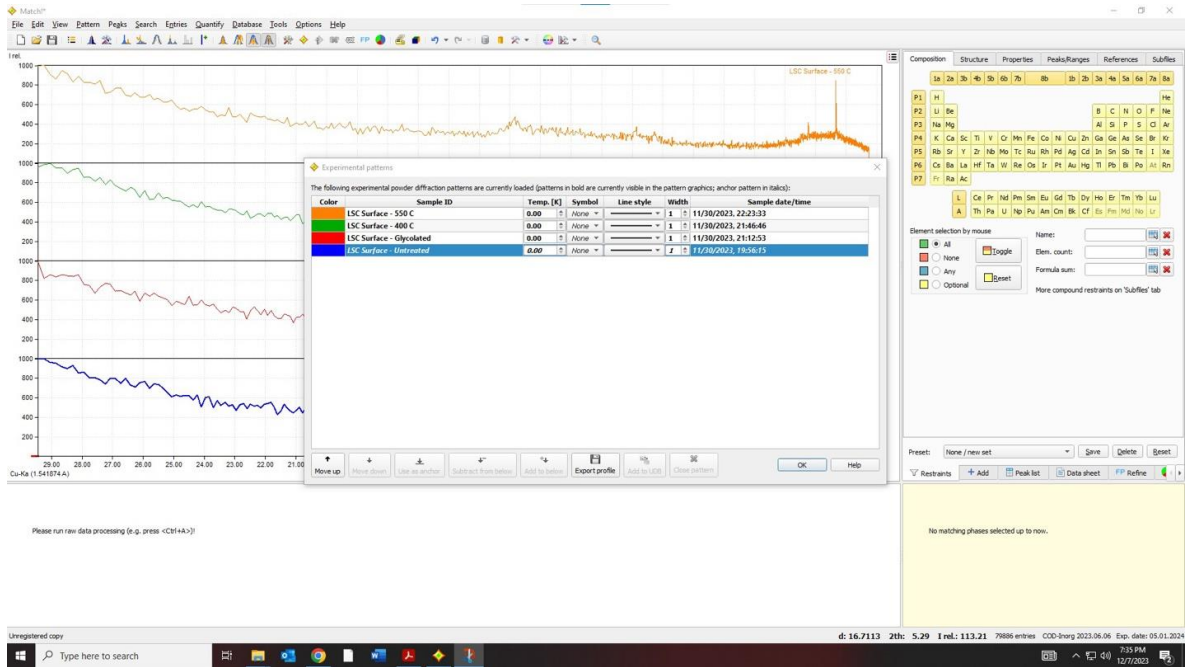
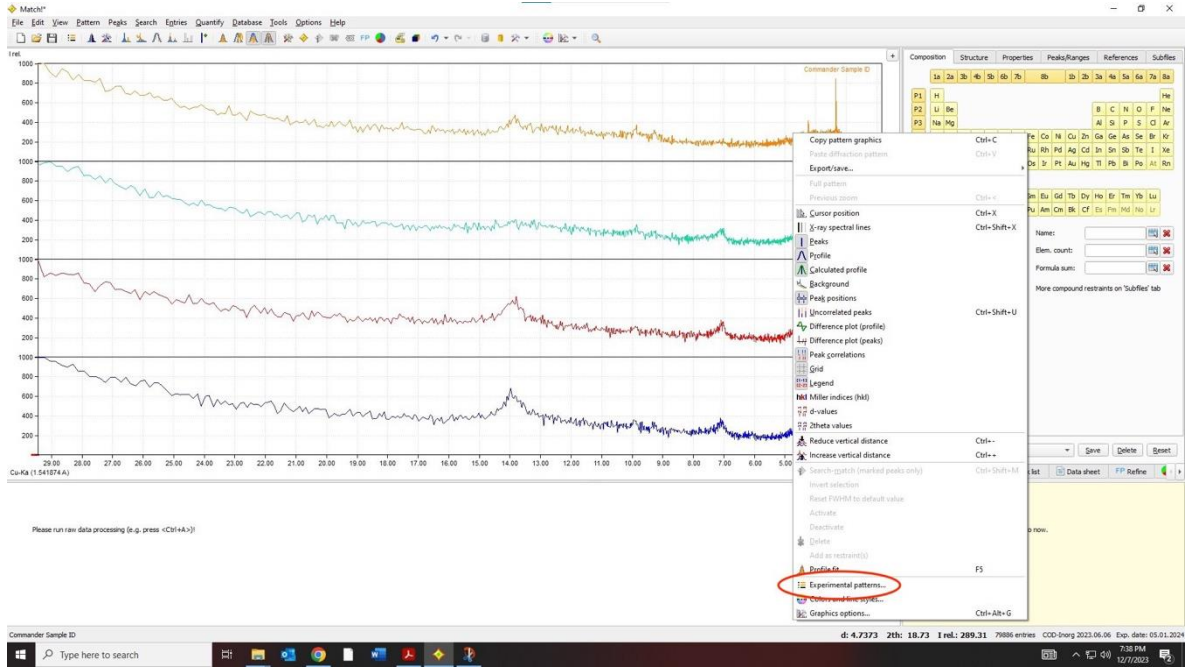
3.5 Data Interpretation – Match! XRD Software

- 1) Once all four scans (untreated, ethylene glycol, 400C, and 550 C) are complete and saved in .raw format, transfer the files to a personal computer and download the software ‘Match!’ at <https://www.crystalimpact.com/match/>.

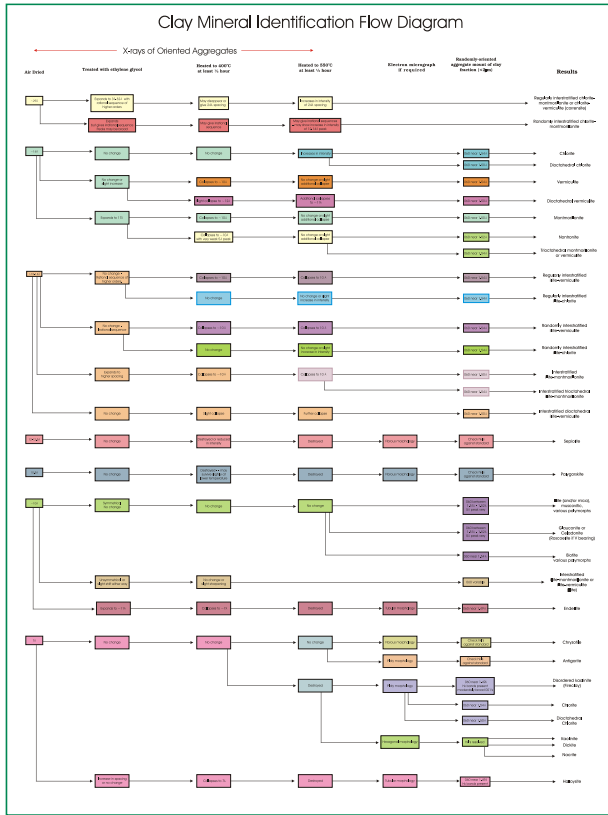
- 2) Go to the 'USGS XRD Lab Manual' website and download the 'Clay Mineral Identification Flow Diagram' at <https://pubs.usgs.gov/of/2001/of01-041/htmldocs/flow/index.htm>. This flow diagram enables one to identify clay minerals through the behavior of diagnostic diffraction peaks.
- 3) Open all four XRD scans in Match! by simply dragging the .raw file onto the main graphical window in Match!. First change the X-axis to D-Spacing from 2theta by clicking on the '2theta' label at the lower right of the graphical window.



- 4) Label the scans accordingly by right clicking on the 'Commander Sample ID' label and clicking on 'Experimental Patterns' option.



- 5) Now that all your scans are properly labeled and the X-axis is set to D-Spacing, open the ‘USGS Clay Mineral ID Flow Diagram’ to begin the identification process.



- 6) Firstly, identify the most prominent peaks in the four diffractograms. The peaks from 7A to 14A D-Spacing are the most relevant peaks in clay mineral identification. Peaks at lower or higher D-spacing, minus peaks around 29A, are not as relevant and could be ignored during clay mineral identification.
- 7) Evaluate how the peaks behave through the four scans and note if they remain in position, shift to another position, and/or collapse. For instance, the 14A peak in the four scans visible in the above images remains in position at 14A through treatment with ethylene glycol but heating to 400 C and 550C collapses the peak to a lower, ~10A D-spacing. This would suggest that vermiculite is present in the sample. Follow this procedure for other remaining peaks to identify that clay minerals are present.

Appendix IV: Grain Size Data

Cave Name	Sample	Facies Association	Median (mm)
APC	Borning Room	Autogenic	0.148
APC	Jaded River	Autogenic	0.224

January	JH-C9	Autogenic	0.224
Tardis	Red Fines	Fluvial	5.383
Tardis	TH5	Epikarst	6.181
Pipevine	P3	Fluvial	10.74
APC	Black Fines	Autogenic	12.33
EC13	183-193	Fluvial	14.16
PV	P10	Fluvial	14.16
EC11	63-90	Fluvial	16.26
Pipevine	P3	Fluvial	16.26
EC13	43-60	Fluvial	18.67
Pipevine	P8	Fluvial	18.67
LSC	LSC2	Epikarst	21.43
EC	EC1	Epikarst	24.61
January	JH3	Epikarst	24.61
LSC	LSC3	Epikarst	24.61
Rileys	R4	Epikarst	24.61
EC13	2-10	Fluvial	28.25
PV	PV1	Epikarst	28.25
Rileys	R2	Epikarst	28.25
Rileys	R3	Epikarst	32.44
EC12	90-102	Fluvial	37.24
EC13	208-226	Fluvial	37.24
LSC	LSC1	Epikarst	37.24
Rileys	R6	Epikarst	37.24
EC12	19-25	Fluvial	42.76
EC13	75-83	Fluvial	42.76
EC13	120-150	Fluvial	42.76
EC13	158-173	Fluvial	42.76
EC13	90-103	Fluvial	42.76
LSC	Spider White	Fluvial	42.76
LSC	Spider Upper	Fluvial	42.76
LSC	Spider Brown	Fluvial	42.76
LSC	LSC4	Fluvial	42.76
EC11	12-17	Fluvial	49.09
EC12	38-42	Fluvial	49.09
EC12	102-121	Fluvial	49.09
EC12	121-138	Fluvial	49.09
EC13	108-120	Fluvial	49.09

LSC	LSC5	Fluvial	49.09
EC11	120-138	Fluvial	56.37
EC11	138-148	Fluvial	56.37
EC12	49-60	Fluvial	56.37
EC12	82-90	Fluvial	56.37
EC12	138-148	Fluvial	56.37
EC13	34-37	Fluvial	56.37
EC13	83-90	Fluvial	56.37
Tardis	0-12	Fluvial	56.37
EC11	52-60	Fluvial	74.31
EC12	78-82	Fluvial	74.31
LSC	Spider Sands	Fluvial	74.31
EC13	65-75	Fluvial	112.5
EC13	103-108	Fluvial	112.5
EC12	42-49	Fluvial	390
EC12	25-31	Fluvial	447.7
EC11	17-33	Fluvial	590.2

Copyright Permission

Name: Lathrop, Niles Ward

Email (to receive future readership statistics): nlwlathrop@gmail.com

Type of document: ['Thesis']

Title: Polygenetic Cave Sedimentation and Speleogenesis in the McCloud Limestone of Northern California

Keywords (3-5 keywords not included in the title that uniquely describe content): cave sediments, polygenetic karst, hypogene, karst, lithofacies, McCloud Limestone

Committee Chair: Dr. Patricia Kambesis

Additional Committee Members: Dr. Jason Polk, Dr. Micheal May, Dr. John Tinsley, Joel Despain

Select 3-5 TopSCHOLAR® disciplines for indexing your research topic in TopSCHOLAR®: Speleology, Geology, Sedimentology, Geomorphology, Stratigraphy

Copyright Permission for TopSCHOLAR® (digitalcommons.wku.edu) and ProQuest research repositories:

I hereby warrant that I am the sole copyright owner of the original work.

I also represent that I have obtained permission from third party copyright owners of any material incorporated in part or in whole in the above described material, and I have, as such identified and acknowledged such third-part owned materials clearly. I hereby grant Western Kentucky University the permission to copy, display, perform, distribute for preservation or archiving in any form necessary, this work in TopSCHOLAR® and ProQuest digital repository for worldwide unrestricted access in perpetuity.

I hereby affirm that this submission is in compliance with Western Kentucky University policies and the U.S. copyright laws and that the material does not contain any libelous matter, nor does it violate third-party privacy. I also understand that the University retains the right to remove or deny the right to deposit materials in TopSCHOLAR® and/or ProQuest digital repository.

['I grant permission to post my document in TopSCHOLAR and ProQuest for unrestricted access.']

The person whose information is entered above grants their consent to the collection and use of their information consistent with the Privacy Policy. They acknowledge that the use of this service is subject to the Terms and Conditions.

['I consent to the above statement.']